Novel Super-resolution Optical Microscopy Methods for Single-molecule Biophysics

Helen Louise Miller

Doctor of Philosophy

University of York

Physics

June 2017

Abstract

Super-resolution microscopy is a relatively new and rapidly growing field. Development has been largely technology-driven, with high power lasers, higher resolution CCD cameras, and increasing computing power all enabling new biological questions to be explored. Single-molecule imaging is the tool of choice for studying systems where heterogeneity is present; ensemble methods can average away the interesting behaviour and lead to false conclusions. This thesis develops and optimises bespoke fluorescence microscopy for application to three biological questions, each pushing a limit of super-resolution imaging.

Super-resolution imaging of lambda DNA labelled with the intercalating dye YOYO-1 and the minor groove binder SYTO-13 at localisation precisions of 40 nm and 62 nm respectively has been achieved in preparation for combined fluorescence imaging and magneto-optical tweezers experiments. The combination of these two methods is challenging as both operate with low tolerances.

Single-molecule tracking was used to measure the diffusion coefficients of the chemokines CXCL13 and CCL19 at extremely high temporal resolution. Single-molecule imaging was found to have advantages over the ensemble techniques of FRAP and FCS for measuring the diffusion coefficient of the test molecule; Alexa Fluor 647 labelled bovine serum albumin. The diffusion coefficients of the two chemokines, CXCL13 and CCL19 were found by single particle tracking at sub-millisecond timescales in a collagen matrix to be $6.2\pm0.3\,\mu m^2 s^{-1}$ and $8.4\pm0.2\,\mu m^2 s^{-1}$. Further, CXCL13 was tracked in B cell follicle regions of *ex vivo* lymph node tissue sections at $\sim$2 millisecond timescales, giving a diffusion coefficient of $6.6\pm0.4\,\mu m^2 s^{-1}$.

Fluorescence microscopy was used to elucidate the stoichiometry of YOYO-1 on DNA origami tiles after treatment with low temperature plasma. Undamaged tiles were found to have a mean stoichiometry of 67.4±25.2 YOYO-1 molecules and a model of LTP damage to DNA origami tiles was proposed.

Contents

List of Tables

List of Figures

Acknowledgements

Many of the experiments contained in this thesis have been collaborative works, and I would like to thank the people involved for their invaluable contributions. Firstly, to Prof. Mark Leake, my supervisor, for allowing me to follow this highly collaborative path, and to Dr. Peter O'Toole, my second supervisor for keeping the challenges in perspective. I would like to thank Dr. Adam Wollman for his advice and discussions on every project I have worked on, and Zhaokun (Jack) Zhou, thank you for your eternal optimism as we worked through our studies together. Thank you to my collaborators who have made the experiments possible: Jason Cosgrove, Prof. Sonia Antoranz Contera, Dr. Adam Hirst, Sandra Schröter and Dr. Katherine Dunn, and to the people who have brightened each day: Dr. Laurence Wilson, Dr. Sviatlana Shashkova, Jack Shepherd, Katie Thornton, Nicola Farthing and Rachel Findlay. I would also like to thank the Biological Physical Sciences Institute (BPSI) at the University of York for funding my work. Finally I would like to my parents and my partner, Jamie.

Declaration

I declare that this thesis is a presentation of original work and I am the sole author except for the specific contributions of collaborators detailed below. This work has not previously been presented for an award at this, or any other, University. All sources are acknowledged as references.

The HEK293T cells shown in the introduction were a gift from Karen Hogg and Peter O'Toole in the biology technology facility at the University of York.

Adam Wollman wrote ADEMs code introduced in the methods chapter which I used to track images in all three projects, and provided Matlab code which I modified for some of the further analysis work.

The infrared filter box used in the design of the single molecule microscope in the optical methods chapter was designed and built by Oliver Harriman during his PhD studies.

In the DNA immobilisation and tethering chapter Adam Wollman designed the sequence used to extend the lambda DNA and Zhaokun Zhou modelled the photoblinking behaviour of YOYO-1 bound to DNA.

In the project measuring the diffusion coefficients of chemokines Jason Cosgrove performed the agent-based modelling and prepared the biological samples. Microscopy for this project was performed with both Jason Cosgrove and myself present. Peter O'Toole and Jo Marrison in the biology technology facility at the University of York provided technical help in acquiring SHIM, FCS and FRAP data. Chris Power of Carl Zeiss LtD. provided technical help setting up FCS on the Zeiss LSM 880 in the biology technology facility at the University of York. Andrew Leech in the biology technology facility at the University of York collected and analysed the HPLC data on BSA-AF647. Adam Wollman performed the overlap probability calculation.

In the DNA origami chapter Sonia Antoranz Contera acquired the AFM images. Katherine Dunn designed the biotin strand modifications to the DNA origami tile. Adam Hirst and Sandra Schröter operated the plasma jet for inflicting DNA damage. Steve Johnson developed the biotin-avidin surface immobilisation protocol used for microscopy of the DNA origami.

The image of yeast in appendix A was taken by Adam Wollman and Erik

Hedlund. The pH microscope work in appendix B was performed with Adam Wollman, and he performed the image analysis. The protocols described in appendix E were developed by Katherine Dunn.

List of publications arising from this PhD studentship

1. Superresolution imaging of single DNA molecules using stochastic photoblinking of minor groove and intercalating dyes, *H. Miller, Z. Zhou, A.J.M. Wollman, M.C. Leake*, Methods *(San Diego, Calif.)* (2015), 88, p81-88

2. Probing DNA interactions with proteins using a single-molecule toolbox: inside the cell, in a test tube and in a computer, *A.J.M. Wollman, H. Miller, Z. Zhou and M.C. Leake*, Biochem. Soc. Trans. (2015), 43, 2, p.139-145

3. Developing a New Biophysical Tool to Combine Magneto-Optical Tweezers with Super-Resolution Fluorescence Microscopy, *Z. Zhou, H. Miller, A.J.M. Wollman and M.C. Leake*, Photonics (2015), 2, 3, p.758-772

4. Designing a single-molecule biophysics tool for characterizing DNA damage for techniques that kill infectious pathogens through DNA damage effects, *H. Miller, A.J.M. Wollman and M.C. Leake*, Adv Exp Med Biol (2016), 915, p.115-27

5. An automated image analysis framework for segmentation and division plane detection of single live Staphylococcus aureus cells which can operate at millisecond sampling time scales using bespoke Slimfield microscopy, *A.J.M. Wollman*, H. Miller*, S. Foster, and M.C. Leake*, Phys. Biol. (2016), 13, 5

Under revision: Single-molecule techniques in biophysics: a review of the progress in methods and applications, *H. Miller*, Z. Zhou*, J. Shepherd, A.J.M. Wollman and M.C. Leake*

In preparation: Rapid single-molecule super-resolution microscopy in complex, heterogeneous environments, *H. Miller*, J. Cosgrove*, A.J.M. Wollman, P. O' Toole, M.C. Coles, M.C. Leake*

In preparation: DNA origami damage by low temperature plasma, *H. Miller et al.*

* These authors contributed equally to this work.

List of conference presentations arising from this PhD studentship

1. Bespoke super-resolution optical microscopy methods for single-molecule biophysics, *H. Miller, P. O'Toole and M.C. Leake*
Poster presentation at Microscience Microscopy Congress June/July 2014

2. Bespoke super-resolution optical microscopy methods for single-molecule biophysics, *H. Miller, P. O'Toole and M.C. Leake*
Poster presentation at the British Biophysical Society meeting July 2014

3. Super-resolution DNA imaging with intercalating and minor groove binding dyes, *H. Miller, Z. Zhou, A.J.M. Wollman, K.E. Dunn, S. Antoranz Contera, S. Johnson, A.M. Tyrrell, P. O'Toole and M.C. Leake*
Poster presentation at Microscience Microscopy Congress June/July 2015; Awarded "Life Sciences Session One Second Place"

4. Super-resolution DNA imaging with intercalating and minor groove binding dyes, *H. Miller, Z. Zhou, A.J.M. Wollman, K.E. Dunn, S. Antoranz Contera, S. Johnson, A.M. Tyrrell, P. O'Toole and M.C. Leake*
Poster presentation at Imaging Life (Sheffield) September 2015

5. Developing a single-molecule fluorescence tool to quantify DNA damage, *H. Miller, A.J.M. Wollman, K.E. Dunn, A.M. Hirst , S. Antoranz Contera, S. Johnson, D. O'Connell , P. O'Toole, A.M. Tyrrell, M.C. Leake*, Biophysical Journal, Volume 110, Issue 3 (2016), Supplement 1, p.164a
Poster presentation at BPS 60th Annual Meeting February/March 2016

6. Expanding the limits: combining sub-millisecond single-molecule nanoscale imaging and cellular level systems modelling, *H. Miller, J. Cosgrove, A.J.M. Wollman, P. O'Toole, M.C. Coles, M.C. Leake*
Oral presentation at Frontiers in BioImaging July 2016

7. DNA origami as a single molecule fluorescence tool to quantify DNA damage, *H. Miller, A.M. Hirst, A.J.M. Wollman, S. Antoranz Contera, D. O'Connell, M.C. Leake*
Oral presentation at Physics meets Biology September 2016

8. Catching chemokines in the lymph node, *H. Miller*
Invited flash talk at Sheffield STORM symposium January 2017

9. Catching chemokines in the lymph node, *H. Miller, J. Cosgrove, A.J.M. Wollman, P. O'Toole, M.C. Coles, M.C. Leake*
Poster presentation at Microscience Microscopy Congress July 2017; Awarded "Frontiers in BioImaging Second Place"

* These authors contributed equally to this work.

To B.M., J.M., & J.P.

Chapter 1

Introduction

1.1 Single-molecule Super-resolution Fluorescence Microscopy

Fluorescence microscopy is an attractive tool to study biological processes because it is minimally perturbative to the experimental environment [1]. However, optical diffraction places a fundamental limit on the size of objects one can directly observe with the microscope, spreading out light from a point source to a blob several hundred nanometres in diameter. Many biological molecules and systems are simply too small to be imaged directly. Fluorescent tags and dyes allow molecules of interest to be labelled, and then separated from the rest of the molecules by using a low spatial density, or by switching on only a few molecules at a time. Images of single molecules are acquired, which are a convolution of the response function of the imaging system and the fluorophore emission. This convolution is mathematically well-defined as a Bessel function, and numerically well-approximated by a Gaussian function. If only one fluorescently labelled molecule is present in an image, its' position can be found by numerically fitting the diffraction-limited spot of light to find the centre to within a few tens of nanometres, if enough photons are collected (see figure 1.1). By combining the individual localisations from all frames of an image stack a super-resolved image can be produced. There are different methods to acquire single molecule images; some, such as photoactivated localisation microscopy (PALM) and stochastic optical reconstruction microscopy (STORM) [2][3][4] use stochastic fluorophore photoactivation/switching, but others use the intrinsic photoblinking of fluorophores to achieve spatial separation.

The importance of circumnavigating the optical diffraction limit was recognised with the 2014 Nobel prize in chemistry, awarded to Stefan Hell,

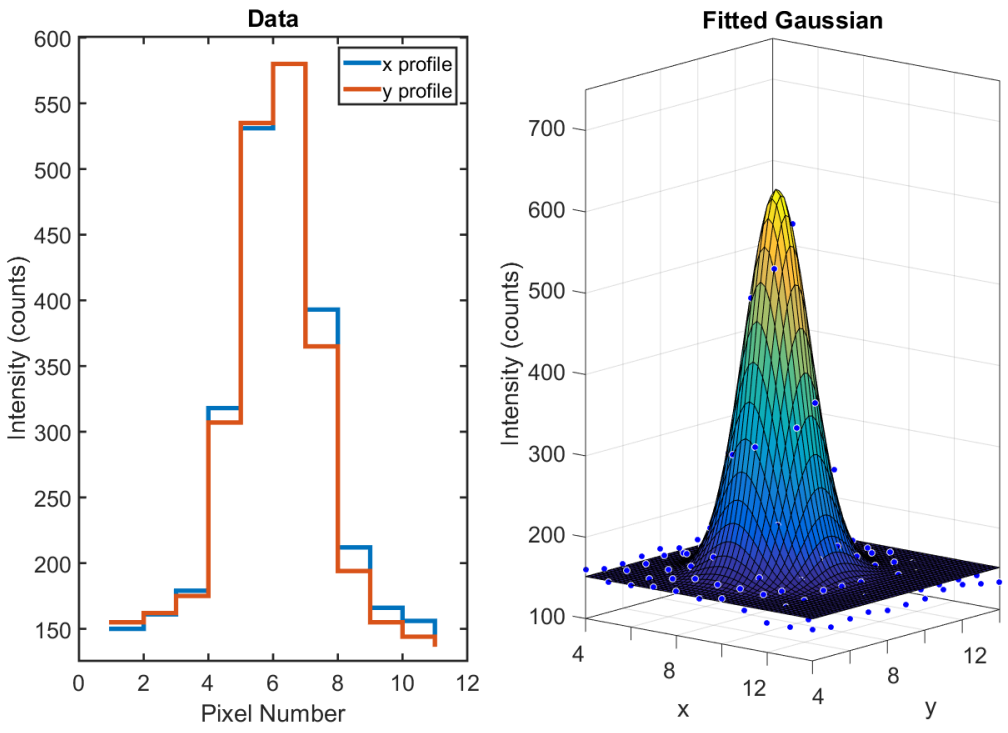

Figure 1.1: Gaussian fitting to a pixelated image of a fluorescent bead. Left: the intensity recorded per pixel in two lateral directions. Right: Gaussian fit (surface) to data points (blue).

Eric Betzig, and William Moerner "for the development of super-resolved fluorescence microscopy", the technique that forms the basis of this thesis. The developments that earnt them this honour are briefly presented here, based upon the scientific publications referenced, and the accounts in, the Nobel lectures of the laureates [5][6][7]. Single molecules of DNA had been imaged in 1956 using electron microscopy [8]; but different proteins cannot be distinguished in the electron microscope. All proteins look the same due to their similar electron content; heavy metals can be used as contrast agents but are often toxic and have a tendency to precipitate (see for example [9]).

Moerner and Kador were the first people to detect single molecules in solids at cryogenic temperatures in 1989 looking at pentacene in a *p*-terphenyl crystal using Stark or ultrasonic secondary modulation on frequency modulated spectroscopy [10] (building on the work of Hirschfeld [11] who detected single globulin molecules in aqueous phase). In this method small local defects change the emission spectrum and convert the frequency modulation to amplitude modulation. Orrit and Bernard [12] made an extremely important development by recording the fluorescence emitted in the same system to detect single molecules at a higher signal-to-noise ratio (Rotman [13] had previously inferred the presence of single enzyme molecules via fluorescence,

but this was the first use of fluorescence of the single molecule being studied). Ambrose and Moerner [14] were the first to map out the fluorescence emission profile of a single fluorophore.

Around the same time Betzig was developing near-field scanning optical microscopy (NSOM) with the aim of achieving electron microscopy level resolution in a light microscope, based on ideas demonstrated by Ash and Nicholls in 1972 with microwaves [15]. NSOM uses a small aperture, say 30 nm in diameter, and visible light travels through it. Very close to the aperture is the near-field range where diffraction has not occurred yet, and placing a detector here will beat diffraction. To image an area the light source and detector must be scanned across the sample. Betzig developed this technique to a resolution of 12 nm [16], and in 1993 was the first to demonstrate super-resolution fluorescent imaging of cells [17].

Shortly afterwards, Betzig made the first room temperature observation of single fluorescent molecules [18]. He realised that to image single molecules inside a cell required a method of turning them on and off controllably to reduce the density of 'on' molecules to be less than one per diffraction limited volume. Established centroid fitting algorithms [19] could then be used to build up an image of all the fluorophores.

The development of fluorescent proteins [20] which could be genetically encoded in cells, thereby eliminating background fluorescence signal caused by inefficient labelling provided the opportunity to achieve the required control over the fluorescent emission. This work was recognised with the Nobel Prize in Chemistry in 2008 for Osamu Shimomura, Roger Tsien and Martin Chalfie. Many variants of GFP with different properties were developed, but the work by Patterson [21] developed photoactivatable tags that provided the control to reduce the number of molecules in the diffraction limited volume, as Betzig had envisaged, and together they demonstrated photoactivated localisation microscopy (PALM) in 2006 [3]. Both Moerner and Betzig focussed on applying these techniques and variations on the method used to turn off random subsets of molecules to answer biological questions (see for example [22][23][24][25]).

Almost separate from these developments Stefan Hell developed stimulated emission depletion (STED) microscopy. He applied the process of stimulated emission used in lasers [26] to reduce the number of emitting molecules in a diffraction-limited laser focus to one. Stimulated emission allows the de-excitation of electrons at a wavelength longer than their fluorescence emission, such that dichroic mirrors or filters can be used to see only the fluorescence. By using a donut shaped depletion beam with a small

hole the sample can be scanned to pick up the locations of the single molecules one at a time, which was demonstrated in 2000 [27].

In recent years, Moerner has developed techniques which allow 3D imaging by modification of the point spread function (PSF) of the microscope, whilst Betzig has been developing structured illumination microscopy and lattice light sheet microscopy. Hell has developed a variant of STED called reversible saturable optical linear fluorescence transitions (RESOLFT) which uses lower de-excitation powers. These techniques are discussed in detail in section 1.2.

1.1.1 Single-molecule vs. ensemble measurements

Traditional biophysical techniques are based on ensemble measurements, such as protein mass spectrometry, in which many proteins are electrospray ionised to give an average value. However, ensemble methods mask heterogeneity and generally do not allow mechanistic insight; for example, looking at the average behaviour of four people in a car does not explain why it is moving. A biophysical example of this is myosin V; a molecular motor which is bound to actin most of the time, but it is the unbinding that allows translocation and the movement associated with a motor. Single-molecule methods allow the inspection not only of the average value of a parameter, but of the distribution of values around the average. When the distribution shows distinct clumps of events it can indicate, for example, the presence of different conformational or energetic states. If the average lies between them it may say something about the probability to be in either state. Single-molecule measurements go beyond simply calculating an average value of a quantity and can suggest explanations and mechanisms for observed behaviour.

Of the various methods available for investigating single molecules, fluorescence microscopy is attractive due to its relative non-invasiveness: fluorescent tags can be conjugated to proteins of interest with 100 % efficiency and can be imaged within the cell. By way of contrast, force transduction methods such as atomic force microscopy (AFM) or optical tweezers are limited by the physical extent of the probe which is introduced to the system under study. For example in AFM the surface profile recorded is a convolution of the profile of the actual surface and the shape of the tip used to probe it, so the best AFM data is acquired with atomically thin probes on relatively flat samples. The resolution limit in fluorescence microscopy is, by contrast, fundamental.

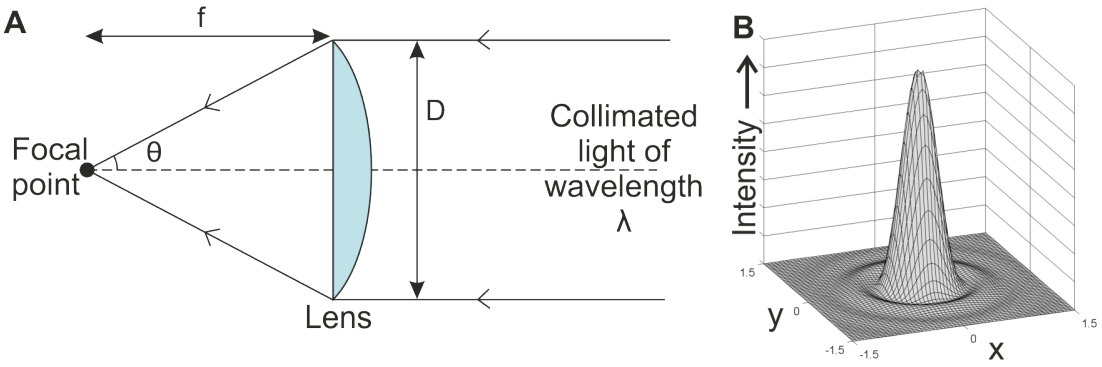

Figure 1.2: Focusing collimated light. (A) The geometry used to describe the numerical aperture of a lens. (B) The shape of the Airy function, showing a large central peak and subsidiary maxima.

1.1.2 The optical diffraction limit

Diffraction is the deviation of light from forward propagation when it passes through an aperture [28]. There are two often quoted versions of the diffraction limit; the Abbe and Rayleigh criteria. Whilst these two formulations are different, in particular their application to coherent and incoherent sources respectively, practically they are very similar. For coherent light sources with small separations the Abbe limit is formulated using Fourier theory of diffraction gratings, similar to an inverted Young's slits experiment, and gives the halfwidth Δx_{Abbe} of the smallest resolvable source as:

$$\Delta x_{Abbe} = \frac{\lambda}{2NA} \tag{1.1}$$

Where λ is the wavelength of light and NA is the numerical aperture of the focussing lens [28][29]. The numerical aperture of an objective is a measure of the amount of light it can collect, defined as $n \sin\theta = \frac{nD}{2f}$, as shown in figure 1.2. Here f is the focal length of the lens, n is the refractive index of the imaging medium between the focus in the sample and objective aperture, which might be air (n≈1), but can be increased using synthetic immersion oils (which generally have n≈1.515), and θ is the maximum half-angle of light that can be captured by the objective. The factor of two on the bottom of this equation comes from requiring only one first order spectrum to be collected, rather than both. Overall, the wavefront after the aperture is non-symmetric, which causes the image to become extended axially. In the axial direction the half-width Δz_{Abbe} is given by:

$$\Delta z_{Abbe} = \frac{2\lambda}{NA^2} \tag{1.2}$$

Thus the image of the point source in three dimensions is an oblate spheroid, sometimes called the "response function". The image is larger than the point source, being approximately half of the imaging wavelength in the lateral directions, and almost twice as large in the axial direction as in the lateral direction.

Classically the resolution is the distance at which two objects can be distinguished when their response functions overlap. When imaging a point source diffraction occurs at the edges of the back focal plane of the circular objective aperture, creating an Airy disk image. The Rayleigh criterion [28][29] states that two Airy functions can be resolved when the principal maximum of one Airy disk overlaps the first minimum of the second, and is given by:

$$\Delta x_{Rayleigh} \approx \frac{0.61\lambda}{NA} \tag{1.3}$$

For a high numerical aperture of 1.49 and wavelength of 475 nm, the lateral resolution achieved is just below 200 nm. Small improvements can be made by using shorter wavelengths, and there are other criteria such as the Sparrow limit [28] which allow more overlap of the two response functions. However, the resolution achieved is still far larger than many biological molecules of interest, for example in B form DNA the base pairs are only 3.4 Angstroms (1 Angstrom = 0.1 nm) apart [30]. Further, the ability to discern the degree of overlap of two response functions is limited by the pixelation of the recording media. Most image localisation algorithms cannot discern overlapping spots and simply centroid them as a single molecule. To study dense populations of molecules smaller than the diffraction limit the fluorescence must be controlled to ensure that emitting molecules are separated by at least the diffraction limit, or an image must be recorded before diffraction has occurred.

1.1.3 The physics of fluorescence emission

Fluorescence is the radiative emission of a photon as an electron in an excited singlet state decays to a lower energy state. Due to the inverse relation between energy, E, and wavelength, λ for a photon:

$$E = \frac{hc}{\lambda} \tag{1.4}$$

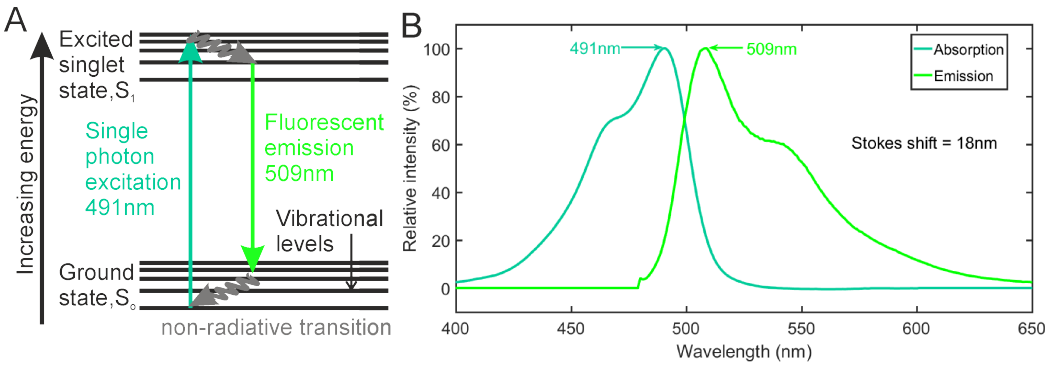

Figure 1.3: Fluorescence emission for YOYO-1 as a two-level system (A) Simplified Jablonski diagram for YOYO-1 as a two-level system showing excitation to the excited singlet state at 491nm and emission at 509nm. (B) Absorption and emission profiles of YOYO-1 showing the Stokes shift of 18nm between the peaks.

where h and c are Planck's constant and the speed of light respectively; emission occurs at a lower energy (longer wavelength) than the initial absorption. The wavelength difference is known as the Stokes shift, which usually arises when the electron undergoes non-radiative decay through vibrational levels before decaying to a high vibrational level of the ground state.

Consider as an example YOYO-1 [31]; a fluorescent dye used extensively in this thesis. An electron is promoted to a high vibrational level of the first excited state at a wavelength of 491 nm. After non-radiative decay through the vibrational levels fluorescence emission at the longer wavelength of 509 nm occurs to a high vibrational level of the ground state, as shown in figure 1.3A. This gives a Stokes shift of 18 nm between the absorption and emission peaks. The absorption and emission profiles are broadened due to the number of vibrational and rotational energy states available to the electron (A more detailed introduction to atomic structure can be found in [32]).

For maximum efficiency in exciting the fluorophore the illumination wavelength(s) chosen should be as close as practically possible to the excitation maximum of the fluorophore. Above the fluorescence emission of the molecule was simplified to a two level system, but for super-resolution imaging it is generally useful (in the stochastic methods) for a fluorophore to have a triplet state at a lower energy than the excited singlet state, from which the emission is non-radiative. Singlet and triplet states refer to the spin states of a molecule, and since spin is a conserved quantity transitions between the two systems are classically forbidden, and have a low probability of occurring. Since the rate constants governing the probability of a transition and fluorescence

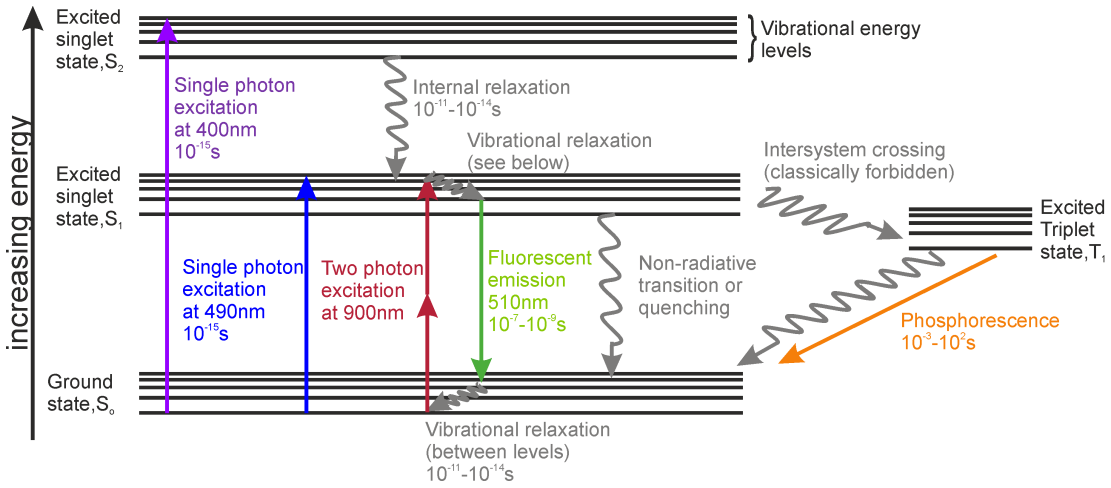

Figure 1.4: Jablonksi diagram of electronic transitions with typical timescales. Radiative transitions are colour coded spectrally to indicate relative energies of transitions. Non-radiative transitions are shown in grey.

lifetime are inversely proportional, the electron will spend a long time in the dark state, thus meaning it can be dark for a time before returning to the fluorescent state, a property known as photoblinking. If the molecule undergoes a physical change it will alter the electronic levels and so will likely convert the fluorophore into a state that is permanently dark under the original illumination wavelength. This is known as irreversible photobleaching [33]. A Jablonski diagram showing common excitation and decay modes is shown in figure 1.4.

Since each fluorophore has a different electronic configuration, the energy levels are different, and the probabilities of different transitions, and overlap of emission/excitation spectra of different fluorophores can be exploited to achieve control of the emitting population by different means. These mechanisms of control are the basis for many of the techniques to achieve super-resolution imaging.

The use of high laser intensities in super-resolution imaging can cause the production of highly reactive free radical species from the biological sample and buffer, for example from molecular oxygen [34][35]. Triplet oxygen is an efficient quencher of triplet states [36][37], so reduces the lifetime of the dark state. This can increase the photostability of the fluorescent dye by reducing the timescale of photoblinking behaviour to below the frame rate, allowing continuous localisation over more frames [38]. However, the reduction of lifetime of the triplet state is achieved by a reaction that produces reactive singlet oxygen which tends to oxidise chemical groups on the fluorescent molecule to photobleach it [39]. Many systems have been developed to mitigate these effects [39][40][41][42], but these are not used in this work.

1.1.4 Signal-to-noise ratio and localisation precision

The signal-to-noise ratio (SNR) is a measure of the relative power of the signal to be measured and the noise in the system (thermal, random fluctuations, shot noise etc). The term is used somewhat loosely in single-molecule fluorescence microscopy, although it is often taken as the ratio of the intensity in an area identified as a single molecule compared to an equal-sized area of background intensity. Low ratios are hard to detect and measure, with a ratio of one having signals at the level of noise. Careful filtering, for example using Chung-Kennedy filters [43] can be used to detect events that last for several frames even if they have a low signal to noise ratio in a single frame.

There are two main sources of noise in fluorescence images; shot noise from the photons emitted by the molecule that is being localised, and background from other sources, such as noise from the CCD used to record the image, or from out of focus fluorescent sources. One method to calculate the localisation precision Δx achievable in the system is to use the Thompson equation [44], which considers both regimes and uses a combined equation for situations in which both terms are present. The form of this equation is:

$$\langle (\Delta x)^2 \rangle = \frac{s^2 + \frac{a^2}{12}}{N} + \frac{4\sqrt{\pi} s^3 b^2}{aN^2} \tag{1.5}$$

where N is the number of photons from the fluorescent molecule, s is the standard deviation of the response function, a is the pixel size, and b is the background noise. This equation will underestimate the error and so overestimate the localisation precision in the case that both terms are present. For a high localisation precision the number of collected photons must be high, but the background noise level must be low, thus the SNR is linked to the level of localisation precision attainable in super-resolution fluorescence microscopy. When few photons are recorded above the background level the SNR is close to one and the localisation precision achieved is poor. Long integration times can be used to improve the SNR and the localisation precision, but this limits the temporal resolution that is achievable and thus limits the ability to study dynamic processes.

In practice localisation precision is usually calculated from experimental data rather than from theoretical considerations. For molecules which are stationary in time the localisation precision is usually calculated from the standard deviation of the centroid position in a series of measurements [45].

In single molecule tracking techniques the standard deviation of the series of localisations cannot be used as the localisation precision as the particle is moving. Instead, for Brownian motion, localisation precision is found by

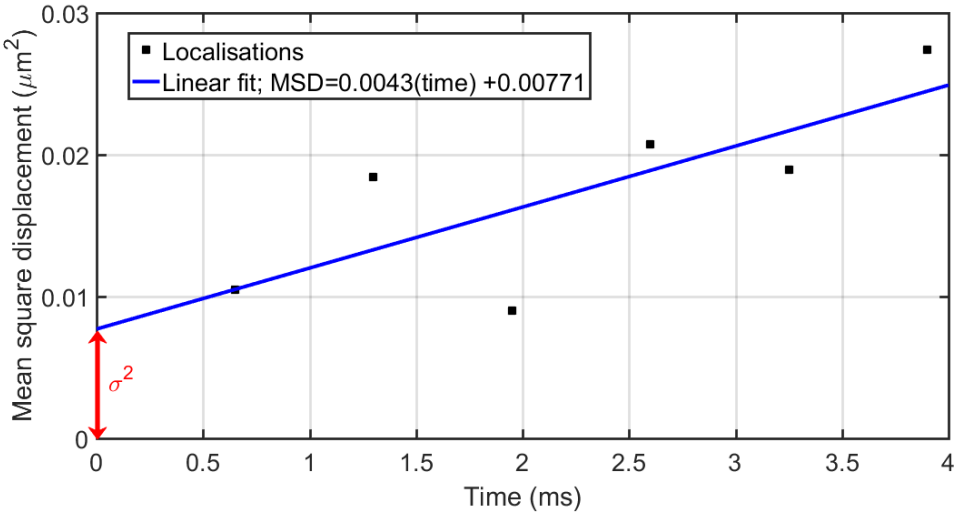

Figure 1.5: Method of calculating the localisation precision (σ) for a diffusing particle shown with simulated data of D=1.07 $\mu m^2 s^{-1}$. The data is shown with black squares and the linear fit is shown in blue.

plotting the mean square displacement between localisations and applying a linear fit to the data. The mean square displacement at time zero is the square of the localisation precision (see figure 1.5). Additional uncertainty can be introduced by motion blur if the image exposure time is long compared to the time taken for the molecule to move one pixel [46].

High temporal resolution is desired to study dynamic processes in single-molecule biophysics experiments, but the limited photon budget of fluorescent molecules often requires long acquisition times to increase the number of photons collected and improve the localisation precision.

1.1.5 Technical developments that have enabled super-resolution fluorescent imaging

Single-molecule super-resolution fluorescent imaging has been enabled by the development of highly sensitive detectors, narrowband light sources such as lasers, and the discovery and engineering of high photon budget fluorescent labels.

The optical detection of single fluorescent molecules at high temporal resolution requires extremely sensitive cameras. Electron multiplying charge-coupled device (emCCD) cameras can be cooled to -80°C to decrease thermal noise, and at low frame rates have very low read noise. However, as the frame rate is increased the read noise increases. CCD chips are multi-layered with the photon interaction region towards the back, relative

to incident light. Back-illumination technology (with incident photons approaching from what was previously used as the back of the CCD) increases the collection efficiency of emCCD cameras. Electron multiplying technology gives single-molecule sensitivity but also amplifies the shot noise from a fluorophore, and therefore halves the signal to noise ratio [47]. Scientific complementary metal oxide semiconductor (sCMOS) cameras have reached the sensitivity required to record single molecule emissions in the last few years [48][49], so camera choice now depends on application [50], but for single-molecule fluorescence microscopy back illuminated emCCDs are still the most popular choice.

Lasers provide a high power, single or narrowband wavelength excitation that can be selected to be near the excitation maximum of the fluorescent tag. The narrow band of laser illumination can be matched to the fluorophore to ensure the highest possible efficiency in exciting the fluorophore, so that less light is needed and no non-exciting but damage-causing light is illuminating the sample. This high specificity aids the separation of excitation and emission illumination with optical filters, such as dichroic mirrors, to improve the SNR during detection.

The fluorescent proteins used in early experiments generally had low photon yields and short lifetimes, and were limited to a few wavelengths. There are now a whole library of fluorescent proteins covering the entire visible spectrum with higher photon yields and longer lifetimes [51][52]. These modified fluorescent proteins enable longer observation times and faster image acquisition, and there have been similar improvements across all available types of fluorescent probes [53][54].

1.2 Super-resolution Fluorescence Microscopy Techniques

Many techniques have been developed to work around the optical diffraction limit and increasingly look further into the specimen beyond the surface, but they can be divided into two main categories: Illumination of a subset of molecules, such that the emitter concentration is low and many readings with different sets are used to build up an image, and methods which use non-linear intensity effects, or patterned/phased illumination.

Methods using illumination of subsets of the full population of molecules require that individual fluorescing molecules must be separated by more than the optical diffraction limit so that single molecule photon distributions can

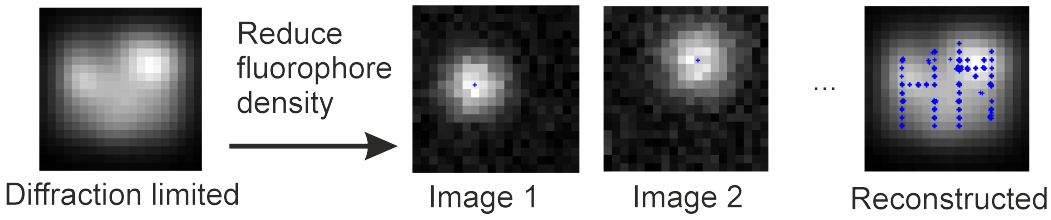

Figure 1.6: Localisation microscopy on the letters HM. Left: Diffraction limited image. Centre: Images of individual fluorophores and their found centres (note altered display levels for clarity). Right: Reconstruction of the letters.

be fitted to them (see figure 1.6). The localisations are then superposed, creating probability density maps of high spatial resolution. In the probability density map the intensity is proportional to the probability of there being an emitter there, as opposed to being a true image capturing all the fluorophores at once. Photophysical properties of fluorophores such as reversible photoswitching, photoblinking or photobleaching are key to the success of many super-resolution microscopy techniques.

1.2.1 Photoactivated localisation microscopy

One of the most widely adopted techniques is photoactivated localisation microscopy (PALM) [2][3]. The principle of this technique is to activate a small subset of photoactivatable fluorescent proteins in a region using a short pulse of a short wavelength laser, and to continuously monitor the fluorescence with a second, longer wavelength. When the number of emitters becomes low, another pulse of the short wavelength laser is applied to excite a different subset of molecules, and this process is repeated until an image of the structure is built up. Activating only a subset of the molecules at a time means that the individual emitters are separated by more than the classical diffraction limit. The single molecule emissions obtained are fitted with a Gaussian distribution, achieving localisation precisions of around 2-25 nm [3]. The technique generally suffers from low photon counts and a low SNR, so samples are often fixed and long acquisition times used, making the technique more useful for imaging structures than dynamic behaviour.

1.2.2 Stochastic optical reconstruction microscopy

Stochastic optical reconstruction microscopy (STORM)[4], similarly to PALM, uses photoactivatable dyes to achieve sub-diffraction localisation precision. This technique requires two fluorophores are paired together. For the case of

the Cy3-Cy5 photoswitch [4][55] a strong readout laser pulse (here red) is used to transfer the Cy5 into a dark state. A short low intensity recovery pulse (here green) is then used to turn a subset of the Cy5 back on, via Cy3. This subset of molecules is localised, and the process repeated to build up an image of the system.

In direct STORM (dSTORM) [56] the same optical process is applied to a single fluorophore, with a higher intensity recovery pulse instead of the second fluorophore. This was very quickly extended to require only a single wavelength with the use of an appropriate buffer [57][58].

The main advantage of the STORM techniques over PALM is that the molecules start in a fluorescent state which is then suppressed, simplifying practical implementation. Similarly to PALM, imaging cycle times are long and so the technique is usually unsuitable for dynamic processes, but the donor-acceptor switch or fluorophore can be cycled many times before irreversible photobleaching occurs, enabling a higher localisation precision to be achieved via averaging. Photoblinking dyes must be avoided as it is unclear if a single molecule is blinking or if the molecule has bleached and unbound and a new dye molecule has taken its place.

1.2.3 Stimulated emission depletion microscopy

Stimulated emission depletion (STED) uses a donut shaped second laser beam to decrease the area where fluorescence can occur, and can achieve single-molecule precision if the individual fluorophores are separated by distances larger than the size of the detection area. The excited state is depleted where the two beams overlap due to a preferable non-fluorescent transition induced by stimulated emission, the same process used in lasers. For a dye emitting at 400 nm a lateral resolution of 35 nm can be achieved [59]. The method is most effective when used with pulsed lasers which have pulses of shorter duration than the average lifetime of the spontaneous emission. The edges of the depleted area become sharper as the intensity of the STED beam is increased, so increasing the intensity increases the resolution.

1.2.4 Förster resonance energy transfer

For measuring very small distances Förster resonance energy transfer (FRET) is the method of choice [60][61]. Two fluorophores called the "donor" and "acceptor" are conjugated to a molecule that undergoes conformational change, or two molecules that will bind together, such that sometimes the

fluorophores are close to each other and sometimes they are not.

The fluorophores are chosen so that the donor's emission spectrum has significant overlap with the acceptor's absorption spectrum. This means energy can be transferred non-radiatively from the donor to the acceptor with a sixth power distance dependence, that is, in the range of one to ten nanometres. When the donor and the acceptor are spatially separated the fluorescence of the donor is seen, and when they are close together the fluorescence of the acceptor is seen. The use of alternating laser excitation (ALEX) to sequentially cause FRET and then excite only the acceptor enables a quantitative estimate of the FRET efficiency achieved to be made. This therefore allows estimation of the distance between the donor and acceptor [62].

1.2.5 Bleaching/blinking assisted localisation microscopy

In contrast to STORM and PALM which require activation of the dyes, bleaching/blinking assisted localisation microscopy (BaLM) [63] uses the intrinsic photobleaching and photoblinking properties of all fluorescent probes. All of the fluorophores are illuminated and emit in the first frame of the acquisition. Over time the fluorophores bleach or blink and their individual images can be found by subtracting each image from its predecessor and then performing the localisation. This technique works with all dyes and fluorescent proteins, and the technique itself does not limit the number of wavelengths that can be used, so the number of colour channels is determined solely by the researchers' ingenuity in separating them, unlike PALM which is quite tightly constrained. Burnette demonstrated the use of four Alexa dyes [63].

BaLM typically achieves a lower localisation precision than PALM at around fifty nanometres, because the many fluorophores in the imaging region contribute a high background signal.

1.2.6 Photoblinking reconstruction

In photoblinking reconstruction the required spatial separation between fluorophores is achieved using their intrinsic photoblinking once the initially emitting fluorophores have been driven into a dark state. This method is similar to STORM, but requires only one laser wavelength, simplifying practical implementation, but achieving similar general advantages. The method was first demonstrated with enhanced yellow fluorescent protein (eYFP) [23].

1.2.7 Methods to measure molecular turnover

Molecular diffusion can be studied using fluorescence recovery after photobleaching (FRAP) [64][65][66] and fluorescence loss in photobleaching (FLIP) [67][68]. In FRAP an area is completely bleached and the return of fluorescent molecules to the bleached area is observed. In FLIP the loss of fluorescent molecules from an area close to a repeatedly bleached region is monitored. Often the two techniques are used to complement each other, see for example [69], and can be used to find the stoichiometry in an area [70]. These techniques are more commonly applied as ensemble methods. A recent study using a technique the authors call single-molecule FRAP monitors single molecules returning to the bleached area [71] and localises them.

1.2.8 Reversible saturable optical linear fluorescence transitions

Reversible saturable optical linear fluorescence transitions (RESOLFT) microscopy [72][73] is a technique which works on the same principle as STED, but using an alternative method to deexcite the fluorescence emission outside the imaging area. In STED microscopy molecules are made dark by forcing them to their ground state which has a short lifetime before they can be excited again such that a large amount of laser power is required to continuously deexcite the molecules. In RESOLFT the molecules are made dark by forcing them to undergo a conformational change between cis- and trans- isomerisation states, which have much longer lifetimes. The longer lifetime means that less optical power needs to be pumped in to maintain the dark state, either allowing the use of less power, or the creation of an array of low power beams. An array of over one hundred thousand beams has been demonstrated [74]. As long as the individual beams are separated by more than the optical diffraction limit the area to be imaged can be scanned far faster than in STED, achieving similar localisation precision to STED, but, as in many of these technologies, localisation precision can be sacrificed to acquire images faster.

1.2.9 3D Imaging

All of the above techniques achieve sub-diffraction resolution in the lateral dimensions, and in their simplest forms do not resolve the third dimension. The response function is approximately two times larger in the axial direction

than in the lateral directions, so to better understand structure and dynamics real systems must be imaged in three dimensions.

Confocal microscopy is a scanning optical technique that uses a pinhole to reject out-of-focus light [75]. Confocal microscopy produces improvements in lateral and axial resolution [76], but in practice these are not as large as the other super-resolution techniques, and so it is not useful for specimens of only a few tens of nanometres in length that are the subject of this thesis. 4Pi confocal microscopy uses two objective lenses at 180 degrees to each other with a common focus in the sample and a common detection pinhole. Constructive interference at the common locations results in four times better axial resolution than is achieved in standard confocal microscopy (this is around one hundred nanometres but depends on the wavelength of illumination and the numerical aperture of the objective lenses) [77].

Astigmatism imaging [55] adds a cylindrical lens to a STORM microscopy setup, such that the response function becomes elliptically distorted when the molecule is out of focus. By comparison with a look-up table of set defocus distances an axial resolution of 50-60nm is achieved.

Another method to shape the response function is achieved using a phase mask in the Fourier plane of the imaging optics, and is again analysed by comparison to lookup tables. One example of this is the double helix point spread function [78][79] in which the illumination beam is split into two and the two lobes revolve around each other as the axial distance is varied, giving an axial localisation precision below thirty nanometres over a two micrometre range. Other shapes [80] have also been demonstrated which work over different axial length scales, such as the tetrapod point spread function which gives around seventy nanometre axial resolution over twenty micrometres, or twenty nanometre axial resolution over six micrometres [81]. It is of particular note that the lateral and axial resolution are comparable to each other when the tetrapod mask is used.

In light sheet microscopy the sample is illuminated orthogonal to the direction of observation for lower phototoxicity. The illumination beam is either thinned to a sheet using a cylindrical lens (this is also known as selective plane illumination microscopy, or SPIM) [82] or a thin beam is rapidly scanned across the sample [83]. The technique is particularly useful for thicker specimens, time lapse imaging, and for imaging thick, cleared samples [83][84][85][86][87]. There is an open-access platform for SPIM to help non-specialists use the technique [88][89]. Higher lateral resolution can be obtained using lattice light sheet microscopy, in which optical lattices are used to produce axially narrow illumination in an array of small spots separated by

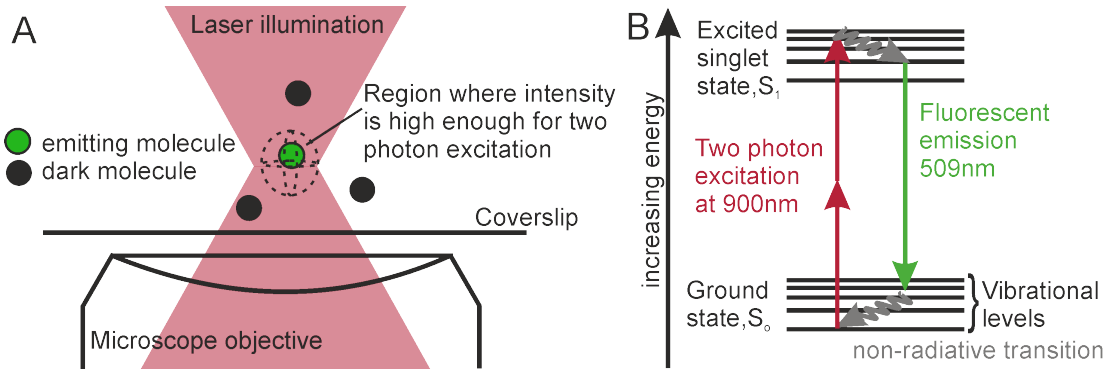

Figure 1.7: Two-photon imaging. (A) Schematic diagram showing the small excitation volume in two-photon imaging. (B) Jablonski diagram for two-photon imaging.

the diffraction limit [90].

Two-photon microscopy [91][92] uses light at half the wavelength of the desired electronic transition, such that electrons are only promoted when two photons arrive at the molecule at the same time: The probability of this happening depends on the light intensity which is highest in the focus of the beam (see figure 1.7). The light intensity drops below the level required for two photon excitation rapidly outside the focal volume, reducing background and improving axial resolution beyond the diffraction limit. Three-photon imaging has also been demonstrated [93], but has not been widely adopted due to concerns over the total phototoxicity.

1.2.10 Summary of super-resolution techniques

There are many techniques to achieve super-resolution fluorescence imaging. They all work by creating spatial or temporal separation of fluorophore emission, but vary in the method used to achieve this. There is no one best technique, rather the best technique for a specific application. The latest advances are in the realm of three dimensional and live cell imaging.

1.3 Biological Targets

Microscopy techniques are little more than an intellectual curiosity until they are successfully applied to a biological question. Fluorescence microscopy techniques can be applied to study anything that can be fluorescently labelled, such as proteins *in vitro* or *in vivo*, see for example [94], deoxyribonucleic acid (DNA) or lipids. The application of these methods is generally more challenging *in vivo* due to the autofluorescence of other cellular components,

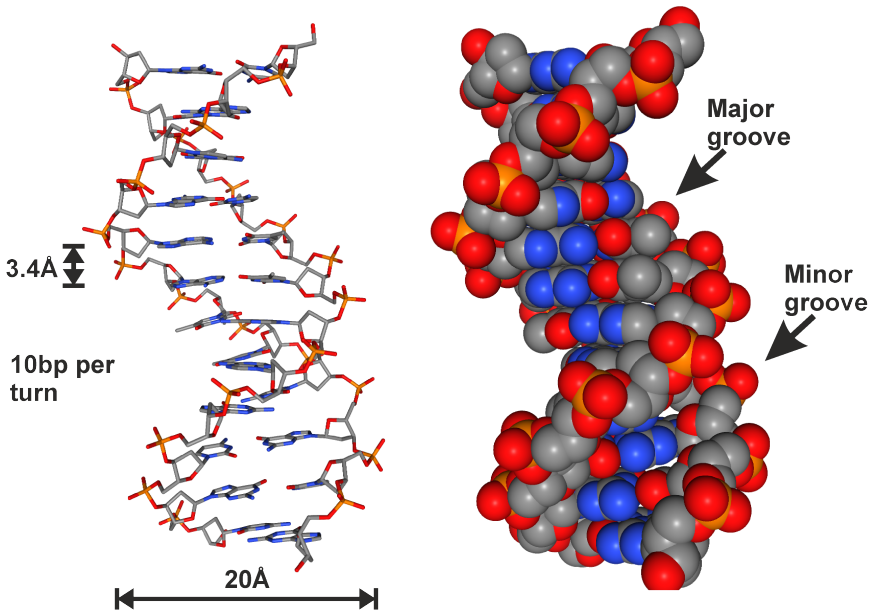

Figure 1.8: The structure of DNA. Wireframe (left) and spacefill (right) structure of B DNA dodecamer with dimensions annotated. Image created in NGL Viewer.

the 3D nature of the system and the inherent variation between different cells.

1.3.1 Deoxyribonucleic acid *in vitro*

Deoxyribonucleic acid (DNA) is the molecule responsible for coding genetic information. Each nucleotide is formed of a base, sugar and phosphate and there are four bases: Guanine, cytosine, adenosine and thymine. The bases form in two specific planar pairs, G-C and A-T such that two complementary strands form a double helical structure with the bases forming 'rungs' of a DNA ladder [95]. DNA can take on different structures dependent on the environment [96]. In cellular or physiological conditions DNA is usually found in the B form, in which the separation between base pairs is 3.4 Angstroms, the diameter of the helix is 20 Angstroms and there are 10 base pairs per turn of the helix [30][97]. These dimensions are shown on a B DNA dodecamer [30] in figure 1.8, which was created in NGL Viewer [98][99]. In the absence of water, for example in crystals, DNA adopts the A form which has a larger diameter and lower base pair separation [96]. Where DNA can be thought of as the master copy of genetic information, ribonucleic acid, (RNA), can be thought of as the working copy. RNA is a single stranded nucleic acid, made up of four bases; three of these are the same as in DNA, and uracil replaces thymine. The difference in oxygenation of ribose between DNA and RNA makes RNA more susceptible to hydrolysis [97].

In viruses the length of the genetic information falls approximately in the range 2 kilobases to 2 megabases; for example, lambda DNA is 48,502 bases [100]. In bacteria, DNA is stored in the cytoplasm, and is generally slightly longer than in viruses, with, for example, *Escherichia coli* having 4.6 megabases. In eukaryotes the genetic information is longer, at around 3.2 gigabases per haploid in humans [101], and stored in the cell nucleus. Eukaryotic DNA is packaged at multiple levels for tight compaction; the double helix is wound onto histones to give the "beads on a string" phase of chromatin. This is packaged into a chromatin fibre of nucleosomes which forms part of the extended or metaphase (higher compaction) chromosome [97].

The two copies of DNA in the double helix are antiparallel, and each strand is read from the 5′ end to the 3′ end; the presence of the second copy provides a mechanism for checking the sequence for errors [97]. The DNA in each cell of an organism (excluding the sex cells in eukaryotes) is a full copy of the genetic information of the organism. DNA encodes the amino acid sequences for proteins and the required control sequence. The four letters of the genetic code are read in groups of three units called codons, which encode the twenty naturally occurring amino acids and a 'STOP' for the end of a given gene sequence. The central dogma of molecular biology [102][103] states that DNA is transcribed to mRNA, which is then translated to protein. In prokaryotes these stages all occur in the cell cytoplasm, but in eukaryotes transcription occurs in the nucleus, and proteins are translated in the cytoplasm [104].

The structure of DNA is changed by the molecular machines that work on it, for example for replication or transcription. Any process which reads the genetic material must separate the strands and therefore causes winding or coiling of the DNA [105][106]. DNA becomes supercoiled in the cell as cellular machinery such as the replisome and RNA polymerases involved in replication and transcription cause additional winding during their function. The cell has molecular machinery for removing this, but it is not well understood.

Fluorescent dyes can bind to DNA in different modes: Intercalation, major groove binding, minor groove binding, external binding and bis-intercalation, as can be seen in figure 1.9. In both intercalation and bis-intercalation modes the dye molecules are almost planar and sit between the base pair rungs of the DNA ladder, whereas in the major and minor groove binding modes the dye the molecule aligns with the backbone. Some dyes are sequence specific, such as Hoechst 33258, which is accommodated by sequence specific changes in the width of the minor groove [107][108][109][110].

DNA is an attractive molecule for biophysical studies because of its well

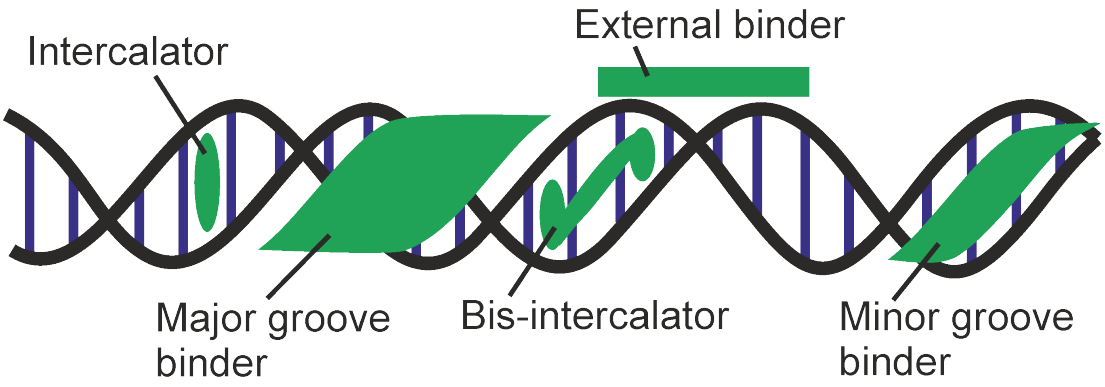

Figure 1.9: Schematic diagram of the five main DNA binding modes. Some DNA binding dyes show characteristics of more than one binding method.

defined structure (see figure 1.8) with high spatial periodicity. DNA has been the subject of many studies, from labelling with fluorescent dye, to measurement of force-extension curves, to DNA origami, amongst others [111][112][113]. The well defined structure with sequence variation also makes DNA popular for computational modelling [114][115][116].

1.3.2 Proteins

Proteins are chains of amino acid residues with sequences encoded by DNA. They are responsible for most cellular functions and often interact with other proteins in complex pathways to produce responses to stimuli. For protein localisation studies, genetic fusions to a fluorescent protein are often used (as in our work on EzrA in *Staphylococcus aureus*; a round, gram-positive bacteria [117]). Multi-colour super-resolution microscopy is often used to learn more about interactions between different proteins which are labelled with spectrally distinct fluorophores, for example to see which is recruited first or to study relative stoichiometries (see for example [24][70][118][119][120]).

1.3.3 Lipids

Lipid molecules form the majority of the phospholipid bilayer surrounding cells. When a cell is on a surface, this layer is two dimensional on the scale of the imaged area, and so has been studied extensively with two dimensional super-resolution techniques (see for example [81][121][122][123][124]). The membrane is also the point of entry into the cell, via channels or electroporation, and so many studies label proteins of interest diffusing in lipid membranes rather than lipids themselves (see for example [125][126][127][128]).

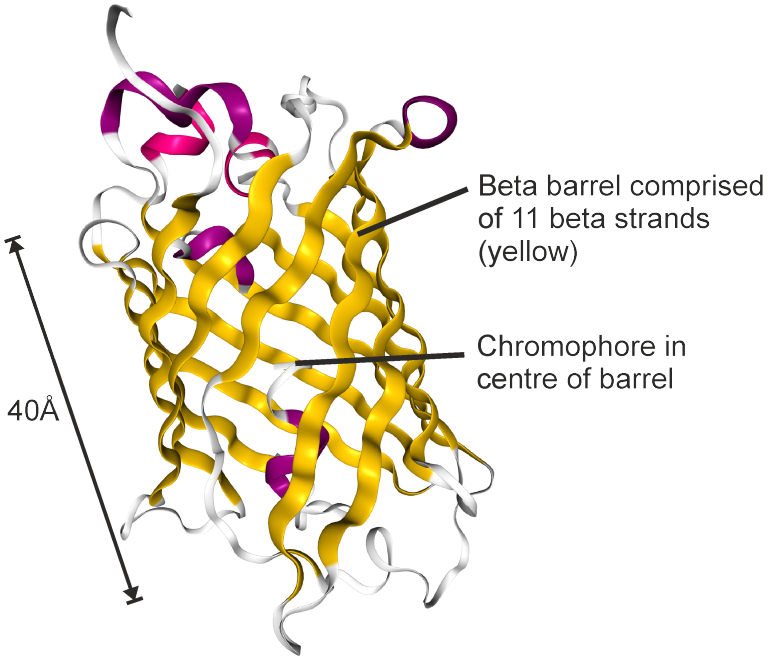

Figure 1.10: Secondary structure cartoon of a fluorescent protein (eYFP variant): The chromophore is inside an eleven beta sheet barrel (beta sheets shown in yellow). Image created in NGL Viewer.

1.4 Fluorescent Dyes

Fluorescent dyes are molecules that can be specifically attached to a molecule of interest or indicate certain conditions, and emit light after being excited. There are different classes of dye molecules that have different sizes, photophysical properties, and methods of attachment to biological targets [129].

1.4.1 Fluorescent proteins and genetic fusions

Fluorescent proteins are large proteins comprised of a chromophore surrounded by a barrel of eleven beta sheets, and are about 30 Angstroms in diameter by 40 Angstroms in length [130][131]. An eYFP variant [132] is shown in figure 1.10, created with NGL Viewer [98][99]. Green fluorescent protein (GFP) from the jellyfish *Aequorea victoria* was discovered by Shimomura [133] and isolated by Tsien and coworkers [20]. The main utility of fluorescent proteins is that they can be expressed conjugated to a target protein in different organisms, as shown by Chalfie [134]. Shimomura, Chalfie and Tsien shared the Nobel Prize in chemistry for these developments in 2008.

The ability to genetically encode the fluorescent tag attached to the protein of interest increases the population of singly-labelled proteins compared to

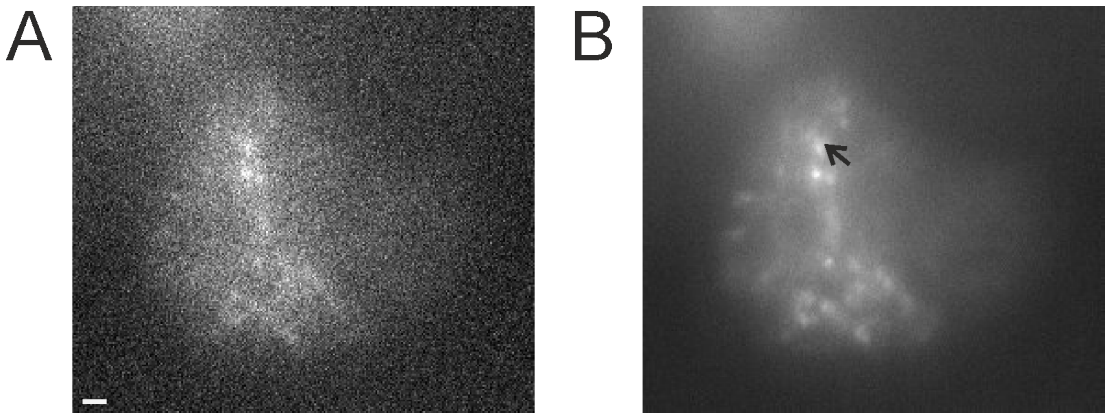

Figure 1.11: Fluorescence microscopy using fluorescent proteins. HEK293T cells with eYFP bound to E47, a nuclear transcription factor. (A) A single frame image at 40ms exposure. (B) Intensity average of 40 frames of the same cell. The black arrow indicates a cluster of eYFP. These cells were kindly donated by Karen Hogg and Peter O'Toole from the Technology facility at York. Scale bar 1µm.

post-translational labelling in which some molecules may not be labelled at all or some may be multiply labelled. Endogenous expression allows the researcher to follow proteins at their physiological expression level and without perturbing the cell when introducing a population of labelled molecules to an existing system. Genetic fusions can also be over-expressed (for example with Isopropyl β-D-1-thiogalactopyranoside (IPTG)) to achieve a large population of fluorescent proteins. There are now many variants of the various naturally occurring fluorescent proteins due to different modifications [135] which have been engineered for greater photostability and to cover the full visible spectrum (The properties and applications of the most common fluorescent proteins are concisely reviewed by Shaner *et al.*[136]).

The drawbacks of fluorescent proteins are their large size and limited photon budget compared to other fluorescent dyes. The large size of fluorescent proteins (GFP is 238 amino acids [20]) mean that they are unsuitable for labelling proteins of smaller or similar size as they hinder the native behaviour of the molecule. Additionally, the fluorescent protein may affect the folding state of the protein or its function, for example if it blocks a binding site, and control experiments must be carefully chosen to ensure the observed behaviour is the same as that of the unlabelled protein.

Enhanced yellow fluorescent protein (eYFP; a variant of GFP) is often used for blinking assisted localisation microscopy [63] because of its photoblinking nature. *In vivo* fluorescent imaging is challenging due to the three dimensional nature of the cell. In the single frame image of HEK293T cells with the nuclear transcription factor E47 labelled with eYFP (see figure 1.11), out of focus

fluorescence contributes to the overall intensity of the image as background noise (These cells were kindly donated by Karen Hogg and Peter O'Toole from the Technology facility at York). Fluorescent proteins have a shorter fluorescent lifetime than many other types of fluorescent dye. This means that on average they emit fewer photons before photobleaching than other fluorophores. This is challenging for single molecule tracking because high laser powers will produce high SNR images for just a few frames, and therefore precise localisations, but lower laser powers will allow longer tracks with lower SNR and lower localisation precision. As a result fluorescent proteins are more commonly used for structural studies than for tracking studies.

1.4.2 Quantum dots

Quantum dots are inorganic semiconductor nanocrystals with diameters of a few nanometres, which, after excitation, emit light at a wavelength dependent on their shape and diameter [137]. Quantum dots exhibit very high fluorescence stability compared to fluorescent proteins [138]. However, their size means they cannot enter cells through pores and so must be introduced by other means. To be compatible with biological samples the quantum dot must be coated to make it water soluble and to avoid fluorescence quenching in water, and must be functionalised for specific attachment to a protein of interest [139][140]. Quantum dots photoblink due to the excited electrons escaping to the surface of the semiconductor crystal; whilst this can be controlled in some cases (reviewed in [141]), generally the size and photoblinking properties of quantum dots make them unsuitable for single particle tracking of small biological molecules.

1.4.3 Organic dyes

Organic dyes are small fluorescent molecules with high photostability and long fluorescence lifetimes. Organic dyes are of lower molecular weight ($\sim 1000\,\mathrm{g/mol}$) than fluorescent proteins so are potentially less perturbative to the dynamics and function of the protein to be studied. Some organic dyes have to be conjugated to the biological target, such as xanthene dyes and the Alexa dyes, but others, such as a subset of cyanine dyes, can intercalate directly with DNA.

Cyanine dyes are molecules that contain a polymethine bridge with a delocalised charge between two nitrogen atoms. An example of this structural motif is seen in the centre of YOYO-1 (a homodimer of Oxazole Yellow) shown

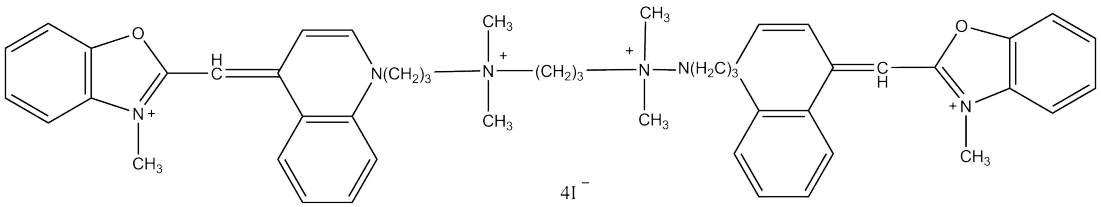

Figure 1.12: The chemical structure of YOYO-1 Iodide, an example of an organic cyanine dye.

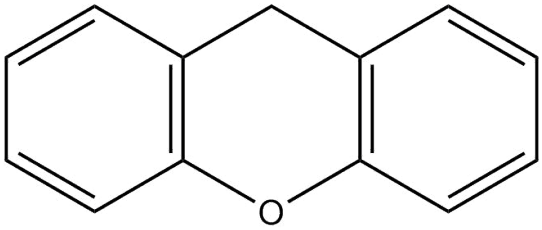

Figure 1.13: Xanthene structural motif.

in figure 1.12. The two most well-known cyanine dyes, Cy3 and Cy5, are highly water soluble because they contain an aryl sulfonate group [142] which makes them attractive for biological specimens.

There are a subset of cyanine dyes that bind directly to DNA, generally with a one hundred to one thousand fold increase in fluorescence on DNA binding [143]. These molecules are used as nucleic acid stains and include the bis-intercalating YOYO-1 and the minor-groove binding SYTO-13.

Xanthene dyes are characterised by the presence of a xanthene group (see figure 1.13). Examples include Fluorescein, Oregon green and Rhodamines. Fluorescein is one of the most commonly used fluorophores for labelling proteins because its excitation peak is close to the 448 nm argon-ion laser line. The xanthene dyes can be conjugated to a diverse range of biological targets via various chemical methods. For example amine chemistry can be used to attach the fluorescent dye to lysine residues (which are highly abundant) in the target protein (an amine is a functional group with a nitrogen with a lone pair of electrons). An alternative is thiol chemistry (sulphide bonds) to attach the dye to naturally less abundant cysteine residues in the target protein for a lower labelling density.

The family of Alexa Fluor dyes are created by sulfonation of existing fluorescent probes such as the cyanine dyes Cy3 and Cy5 and xanthene dyes [144][145]. That is, a hydrogen atom on an aromatic hydrocarbon is replaced with a sulfonic acid group. This modification provides the dye molecule with greater photostability, longer fluorescence lifetime, and higher tolerance to a range of pH conditions [144][145]. For example, Alexa 647 shows fluorescence

stability for pH 4-10 [145]. Like the xanthene dyes the Alexa dyes can be conjugated to targets by both thiol and amine chemistry.

1.5 Summary

The main forms of single-molecule super-resolution microscopy and the theory behind them have been introduced. The key classes of fluorescent molecules and biological targets have been summarised, and the following chapters will describe studies using a range of fluorescent molecules and imaging techniques to answer different biological questions.

Chapter 2

Materials and Methods

2.1 Materials

2.1.1 Buffers

Experiments were performed in phosphate-buffered saline (PBS): 10 mM phosphate buffer, 2.7 mM potassium chloride and 137 mM sodium chloride, pH 7.4 (P4417-100TAB, Sigma-Aldrich Co. LLC), at room temperature (20°C) unless otherwise stated. DNA ligation reactions were performed in T4 DNA ligase buffer: 50 mM Tris-HCl, 10 mM $MgCl_2$, 1 mM ATP, 10 mM DTT, pH 7.5 at 25°C (B0202S, New England Biolabs). Agarose gels were run in Tris-acetate-EDTA buffer (TAE): 40 mM Tris, 20 mM acetic acid, and 1 mM EDTA, pH 8.3 at 25°C (T9650-1L, Sigma-Aldrich Co. LLC).

2.1.2 Beads

Latex and fluorescent beads were used as fiducial markers for two colour image registration, brightfield surface localisation in sensitive fluorescence experiments, and for alignment procedures.

For alignment procedures a mixture of 0.3 µm carboxyl latex beads, 0.08 µm carboxyl latex beads, 0.2 µm 'red' fluorescent beads, 0.2 µm 'yellow-green' fluorescent beads and 0.024 µm 'Nile red' fluorescent beads (C37267, C37264, F8810, F8811, F8784, Thermo Fisher Scientific Inc.) were used. The larger carboxyl latex beads were used as fiducial markers as described in individual experiments.

For alignment of long wavelength laser beams in the chemokine project, 0.2 µm 'crimson' fluorescent beads (F8806, Thermo Fisher Scientific Inc.) were used. The DNA tethering project used 1 µm paramagnetic beads (Dynabeads® MyOne^{TM} Streptavidin C1, Life Technologies Ltd.), and 4.37 µm

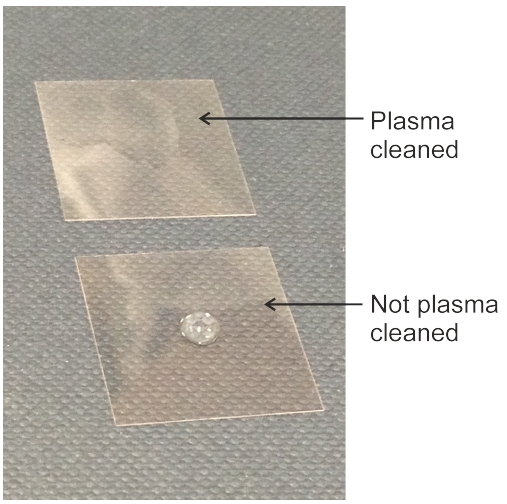

Figure 2.1: Photograph of the effect of plasma cleaning. Two 22 mm square coverslips, each with a 10µl drop of ultrapure water on, the top one has been plasma cleaned, and the water disperses, the bottom one has not, and the water remains as a droplet.

anti-digoxigenin coated polystyrene beads (AD01, Spherotech, Inc.).

2.1.3 Immersion oil

For all experiments Olympus type F immersion oil (MOIL-30, Thorlabs Inc.) was used. This is a low fluorescence immersion oil with refractive index 1.518 measured at 23°C.

2.2 Methods

2.2.1 Plasma cleaning

All coverslips (thickness 0.13-0.17 mm, MNJ-350-020H, Menzel Gläser) are cleaned in a Harrick PDC-32G plasma cleaner for 1 minute prior to use. Autofluorescent residues such as skin oils and manufacturing residues are removed by the breakdown of carbon-hydrogen bonds. The low molecular weight particles boil off the surface in the vacuum. Cleaned coverslips are placed onto samples with clean tweezers to avoid re-contamination.

Plasma cleaning also strips electrons from the top layer of glass; this effect relaxes exponentially with a time constant of around 4 hours [146], and can be visualised by placing a droplet of water on the coverslip; on an uncleaned or relaxed coverslip it remains as a well-rounded droplet, on a cleaned coverslip it spreads out. The difference between plasma cleaned and uncleaned coverslips is shown in figure 2.1 with a 10 µl drop of water.

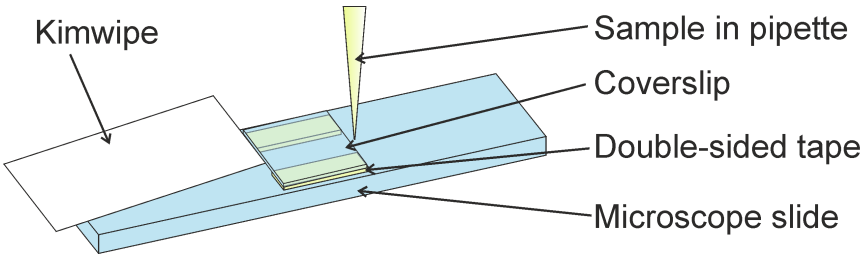

Figure 2.2: Schematic diagram of adding a sample to a tunnel slide.

2.2.2 Tunnel slides

Tunnel slides are prepared by laying down two lines of double sided tape on a standard sized microscope slide approximately 2-4mm apart. Scotch double sided tape in a dispenser (70071395118, 3M) was used to make tunnel slides of reproducible height. This particular tape was chosen as it does not have a fluorescent residue, which is common with other double-sided tapes, it is water resistant, and it does not stretch. To complete the tunnel a plasma cleaned coverslip is placed on top and gently tapped down with a pipette tip, avoiding the area to be imaged, before removing the excess tape (see figure 2.2).

Samples are added from a pipette via capillary action using a lint-free paper wipe (KimTech delicate task wipes, Kimberly-Clark Worldwide, Inc.) to wick the liquid through. To ensure the tunnel remains hydrated the tissue is removed before the last of the liquid is drawn through. Sequential flows of reagents and wash steps can be performed.

Before samples are introduced to the microscope test slides of the bead mixture described above are constructed from microscope slides and plasma cleaned coverslips. Poly-L-lysine is used to ensure that beads adhere to the surface. These slides are used as tests for illumination uniformity and optical aberrations.

2.2.3 Optical components

The optical components used were assembled on optical tables and boxed in using black hardboard (TB4, Thorlabs Inc.) to both eliminate stray light and increase safety by enclosing all beam paths. All lenses after the objective lens were achromatic to minimise spherical and chromatic aberration.

2.2.4 Removal of infrared radiation from laser beam

The supercontinuum lasers utilised in the microscopes used in this project generate wavelengths beyond the visible. Heating effects in the sample were minimised by safely dumping the infrared (IR) light using a dichroic mirror and beam dump, with slightly different specifications for the two different laser outputs. The laser used in the microscope designed in chapter 3 was previously used by another PhD student, Oliver Harriman, and his existing IR filter box was used [147]. This design was mimicked by for use on the supercontinuum laser used in the chemokines project.

2.2.5 Camera settings

All images for analysis were acquired on electron multiplying charged coupled device (emCCD) cameras cooled to -80 °C using Andor Solis software in frame transfer kinetic series mode. For brightfield imaging the electron multiplying gain was turned off, and fluorescence images were acquired at full electron multiplying gain of 300. Different cameras were used for each project. The chemokine imaging microscope utilised an Andor iXon^{EM}+ DU 860 camera (Andor Technology Ltd), operated with a vertical shift speed of 0.45 µs at 10 MHz pixel readout rate and maximum pre-amplifier gain of 4.6. The other setup used two Andor iXon 897 cameras (Andor Technology Ltd); when dual colour imaging was required the camera recording the red channel images was triggered by the software, and in turn used to trigger the green channel camera. Images were acquired with a vertical shift speed of 3.3 µs, pixel readout rate of 17 MHz and a pre-amplifier gain of 3, resulting in a total overall gain of ∼900. Some early alignment and characterisation images used for comparative purposes only were acquired on a Watec-902H (CCIR) controlled with custom written Labview software. All images were acquired as tagged image file format (.tiff) stacks, binned to include only the illuminated region or to increase the frame rate.

2.2.6 Laser power measurements

Laser power was measured using a power meter (PM130D, Thorlabs Inc.) with the sensor mounted perpendicular to the beam path before the objective lens in the illumination optics, such that the entire beam fell on the sensor. Each measurement was background corrected, repeated three times, and averaged.

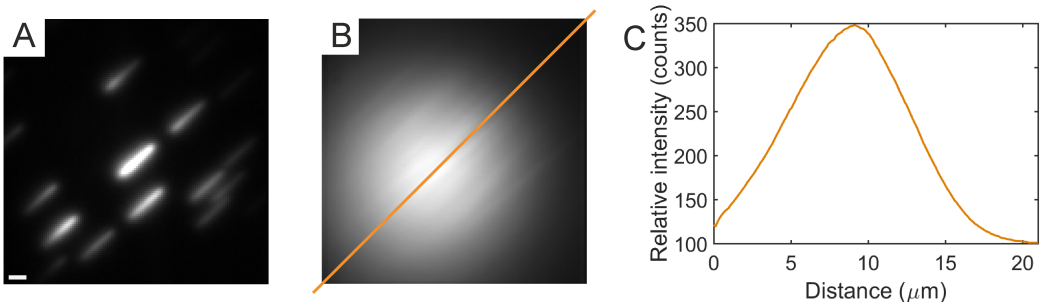

Figure 2.3: Finding a beam profile. A) Single frame from an image acquisition of rastered beads. B) Intensity average of the entire acquisition showing the direction of the line profile. C) Line profile through intensity average. Note image contrast levels have been adjusted for clarity. Scale bar 1 µm.

2.2.7 Spectral measurements

The spectrum of the excitation beam was measured using a CCD spectrometer (CCS200/M,Thorlabs Inc.) via a cosine corrector mounted to an optical fibre to enable free-space measurements (CCSA1, Thorlabs Inc.). The laser beam was attenuated one hundred times with a reflective neutral density filter with optical density 2 (ND520A, Thorlabs Inc.) to avoid detector saturation. The wavelength reading of the spectrometer was highly dependent on the angle light entered the cosine corrector, so the cosine corrector sensor was mounted perpendicular to the beam for all measurements.

2.2.8 Beam width measurements

The beam width at the sample was found by rastering a dense sample of immobilised fluorescent beads through the beam from a variety of directions at a constant speed whilst imaging at exposure times of around 50 ms. This produces a series of images of streaks from the moving fluorescent beads, which are not saturated. These images are then temporally averaged and show a disk within which the illumination intensity is high enough to excite the beads. An example 2D line profile is shown in figure 2.3. The average intensity from the rastered bead stack can be used without fitting for pixel-wise background correction. Alternatively, fitting the intensity values with a mesh plot allows the beam diameter to be found via the full width at half maximum (FWHM), and the power density can be found with the assumption of uniform power density in the excited area.

2.2.9 Gel electrophoresis

Agarose gel electrophoresis was performed in a horizontal gel tank (MSMIDI7, Scientific Laboratory Supplies Limited) to investigate various DNA samples. The distance a molecule migrates during gel electrophoresis depends on its charge and surface area, but for polymers such as DNA the surface area is usually assumed to be proportional to the molecular weight. 50ml gels at 0.75, 1 or 2% agarose (analytical grade, Promega) were run, depending on the mass of the DNA being analysed (lower percentage gels give higher resolution on high molecular weight DNA bands; higher percentage gels give higher resolution on low molecular weight DNA bands). All gels were run at 100 V (6.7 Vcm^{-1}) in TAE buffer, for times between 15 and 45 minutes, depending on the molecular weights of the samples. Gels were imaged on an automated gel imaging system (ChemiDoc MP Imaging System, Bio-Rad Laboratories).

DNA samples were prepared in 6 µl volumes with 0.6 µl of 10x running buffer, 0.75 µl 80% glycerol filtered with a 0.45 µm diameter pore syringe filter, and 1 µl of 6X purple loading dye (for pre stained gels) or 1 µl of ultrapure water (for post-stained gels). The rest of the sample volume comprised DNA diluted in ultrapure water to contain 50-100 ng of DNA.

For visualising dsDNA, 5 µl of 10,000x concentrated SYBR Safe (Invitrogen) was added to the agarose before casting and mixed with gentle swirling to ensure even staining. For acridine orange staining gels were run in TAE buffer without stain. The post-staining protocol was adapted from McMaster and Carmichael [148]; gels were post-stained with rocking incubation at 0.25 Hz for 30 minutes with 5 µl of 300 mg/ml acridine orange added to 50 ml of TAE, to completely submerse the gel. The buffer was exchanged for 1 hour destain in 50ml TAE, also under rocking incubation at 0.25 Hz.

2.2.10 ADEMS code

ADEMS (algorithm involving dilation/expansion in Matlab) code was written by Adam Wollman, and is used to track all fluorescent images in this thesis. There are several user-defined parameters that must be selected based on understanding of the workings of the code, so a description including the effects of these parameters is given here. ADEMS code uses morphological image processing including dilation and expansion to identify spots. This is followed by two stages of 2D Gaussian fitting; using two stages reduces the number of free parameters in each fit and increases the robustness of fitting at low signal to noise ratios compared to using a single 2D Gaussian fit [149]. Next, coincident spots are removed and the spots are linked into trajectories.

The code also incorporates a cursor mode which allows the user to identify spots which are then tracked to the end of the acquisition. A schematic diagram of the key steps of the fully automated version of ADEMS code is shown in figure 2.4.

ADEMS code has two inbuilt methods to identify candidate spots in an image. One is designed for identifying single molecules in cells and is based on finding the shape of the distribution of pixel intensity values in an image (based on the assumption of the presence of background in the image due to cell autofluorescence). The other method is based on removing noise from the image by morphological functions. Both methods use a structural element of a disk with a user-defined radius of 5 pixels for the application of morphological operations, unless otherwise specified: The size of the structural element is chosen to be larger than background pixel fluctuations and smaller than the fluorescent particles to be tracked. In the applications described in this thesis both methods to find spots are applied to increase the number of candidate spots found, because there is often background fluorescence in images acquired *in vitro* in non-TIRF modes, and high temporal resolution data have low SNR.

In the method designed for cells the original image is top-hat filtered to even out the background, and then low-pass Gaussian filtered to smooth the image. The original image intensities are put into a histogram to give a peaked distribution and the full width half maximum of this distribution is used to define a threshold at the modal (peak of histogram) intensity value plus 0.8 times the full width at half maximum of the intensity distribution. This threshold is applied to the low-pass Gaussian filtered image to convert it to a binary image.

In the second method, designed for *in vitro* studies, the original fluorescence image is morphologically opened with the structural element, using an erosion (makes elements smaller by retaining only the positions at which the structural element can be centred and still fit in the element) followed by a dilation (increases the size of an element by placing the centre of the structure element on each existing element edge pixel and including all the covered area). The effect of a morphological opening operation with a disk is to remove "corners" on any elements of an image. The morphologically opened image is then thresholded using Otsu's method [150] and converted to a binary image that can be used as a signal mask. Otsu's method separates data into a user-defined number of classes by minimising the intra-class variance; in this instance fluorescence images are segmented based on the pixel intensity as described in Wollman, Miller and Leake [117]. Other methods to separate

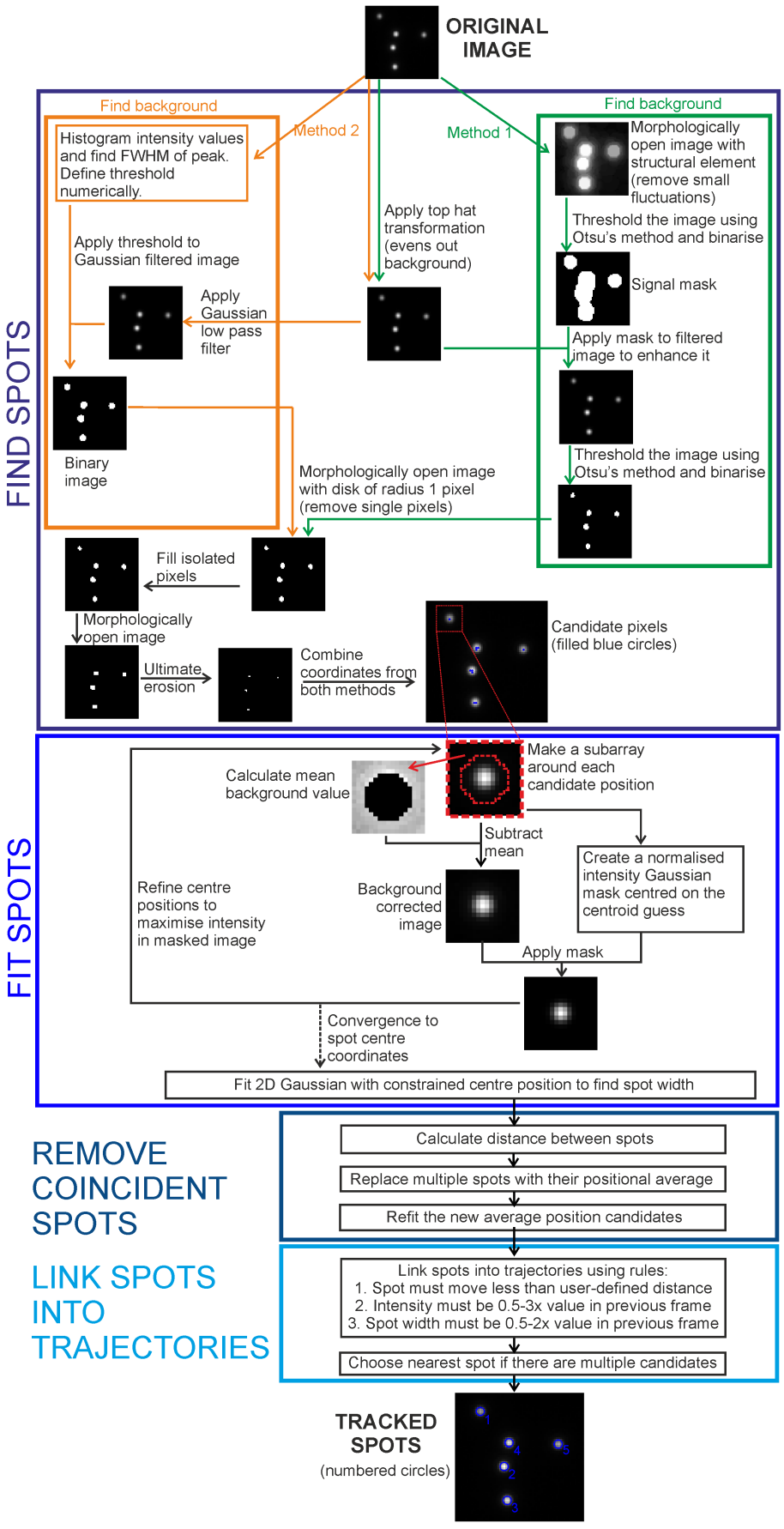

Figure 2.4: The steps taken in ADEMS code to get from an original image to a table of properties of tracked spots, illustrated with images of 0.2 µm 'crimson' fluorescent beads.

classes, such as valley sharpening [151] or fitting Gaussians [152] tend not to work well when there is no clear valley between the classes, as is often found in noisy fluorescence images. The signal mask is applied to the original image that has been top-hat filtered (as in the previous method) to enhance the image. The enhanced image can then be thresholded again using Otsu's method to convert it to a binary image.

The two methods then follow a common set of operations on the binary images of the spots. The binary images are morphologically opened with a disk of radius one pixel to remove single pixels, and then isolated pixels are filled with a disk of radius one pixel. This is followed by another morphological opening operation. In figure 2.4 this step is illustrated with the image from this stage in method two, and the spot in the top left corner is missing, this object is retained by method one, showing the importance of using both methods to extract candidates. An ultimate erosion (this finds the pixel(s) in an element that are furthest from the edges by looking at the eight-connected neighbourhood; an ultimate erosion of a dumbbell shaped element would likely produce a pixel at each end) is then performed to find candidates for spot centres. The list of candidates for the two methods are combined.

To fit spots the code takes each candidate position in turn. First a square sub array centred around the candidate is selected (this has a diameter of 16 pixels in the chemokine work where spots can be motion blurred, and 10 pixels in the origami work where the fluorescent molecules are stationary). If the candidate spot is close to the edge of the image the subregion is moved to be fully on the image, but the spot will likely "clip" the edge later in the tracking process, and if this happens it will be excluded from the final tracked data. An inner subregion with a user-defined radius is used to mask the fluorophore position and allows estimation of the mean of the local background. This radius was chosen as three pixels for both projects by preliminary analysis of spot size by examination of line profiles through spots. The mean background is removed from all pixel values in the subregion. A Gaussian mask is defined at the centroid estimate and is used on the background corrected image. The sum of the intensities from this image is stored and a revised centroid position is chosen by weighting the positions by intensity and normalising. The process is repeated until the centroid position converges. Once a spot that does not clip the edge of the image frame is found it is fitted with a 2D Gaussian with constrained centre position to find the spot width.

Coincident spots are removed by calculating the pairwise distance between each found spot and all the other spots; where spots are merged they are

replaced by a new candidate at the average of their positions, and the candidate is fitted as above. Spots are linked into trajectories based on three criteria: (1) There is an upper limit on how far a spot can move in one frame (5 pixels for the moving chemokines, 2 pixels for the stationary DNA origami). (2) The intensity has to be 0.5-3 $\times$ the value in the previous frame. (3) The spot width has to be 0.5-2 $\times$ the value in the previous frame. If there are multiple spots that could be the same molecule the spot that has moved the least distance is chosen. Tracking helps to eliminate noise as spots must be present in 5 consecutive images to be tracked.

Chapter 3

Design of a Single-molecule Microscope

3.1 Introduction

This chapter describes the range of bespoke optical microscopy methods implemented for use in several applications described in the following chapters of this thesis. It is important to consider the applications of a bespoke microscope during the design phase to ensure optimum performance is achieved from the available components, whilst ensuring flexibility is maintained to enable other experiments. In this chapter the design of a dual-colour fluorescence imaging microscope with single-molecule sensitivity is described. This microscope will be the fluorescence imaging aspect of a combined fluorescence and magneto-optical tweezers microscope, and has briefly been described in two papers from the Leake group [153][154].

3.1.1 Telescopes and the 4f system

There are two types of beam expander: Keplerian and Galilean (see figure 3.1). Galilean telescopes are composed of a planoconvex lens and a planoconcave lens, such that they have a virtual focus (shown as an unfilled circle with a solid line in figure 3.1). This is useful when there is little space available as the configuration requires only the focal length of the longer focal length lens, or when a very high laser power is used, as a local focus can produce a beam so intense that air is ionised. Keplerian beam expanders are composed of two planoconvex lenses, placed the sum of their focal lengths apart, with a focus between the lenses (filled black circle in figure 3.1). The presence of a focus can be used to apply beam shaping elements. The magnification of a beam expander is given by the ratio of the focal length of the downstream lens to

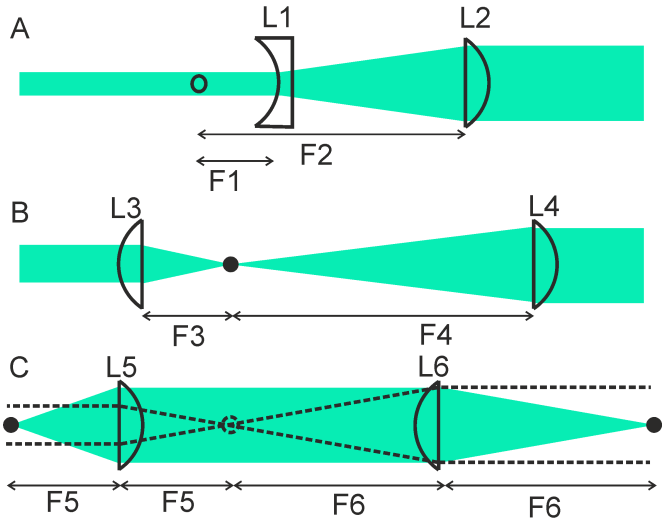

Figure 3.1: Beam expansion and the 4f system. (A) Galilean and (B) Keplerian beam expanders and (C) the 4f configuration: the dotted lines indicate the effect of the system on a collimated beam, whilst colour shows a focussed beam. Conjugate (back) focal planes are shown as (empty/)filled circles.

the focal length of the upstream lens. Whilst both a 75/150 and 150/300 beam expander will give 2 $\times$ magnification the 150/300 system would usually be chosen as small errors in lens positioning have a smaller cumulative effect.

A "4f system" where the total distance occupied by the system is double the sum of the focal lengths of the two lenses used allows access the conjugate back focal plane (indicated by the dotted circle in figure 3.1C). This is in effect a Fourier plane and the beam can be spectrally filtered here. The configuration is also useful when an image has been formed by scattering light from a collimated beam, such that the image and unscattered light propagate in opposite states of collimation and focussing.

3.1.2 Magnification

The magnification of the system affects the super-resolution localisation precision that can be achieved due to the pixelation of all electronic recording media. Scientific emCCD cameras generally have physical pixel sizes of 16-24µm square, and the highest numerical aperture objective lenses (required to increase the number of photons detected) are generally 100x magnifying when used with the manufacturer specific tube lens to forms a 4f system, for example when placed on a commercially available microscope from the same manufacturer. This gives an effective pixel size of 160-240 nm. Thompson *et al* [155] showed that the localisation uncertainty increases for both pixel sizes which are small compared to the imaged spot and for pixel sizes that

are large compared to the imaged spot, due to background and pixelation noise respectively. They showed that the optimal pixel size is the same as the imaged spot size, but the minimum in localisation precision is broad and ratios of pixel size to spot size in the range 0.6-1.4 do not suffer significant loss of localisation precision. For a diffraction limited spot of approximately 180 nm diameter this corresponds to an effective pixel size of 100-250 nm and so further magnification of 2-3 $\times$ is usually carried out before imaging.

3.1.3 Theory of TIRF microscopy

Key to many super-resolution optical techniques, in particular those studying the surface of cells, is total internal reflection fluorescence (TIRF) microscopy. This technique limits the axial length scale to be less than the optical diffraction limit by utilising the properties of evanescent field propagation when an inclined beam is internally reflected at an interface. Snells' law:

$$n_1 \sin\theta_1 = n_2 \sin\theta_2$$

describes the behaviour of light at the interface between two media of different refractive index. As light goes from the higher to the lower refractive index it is bent away from the normal, and above a certain, "critical", angle of incidence the ray is totally internally reflected. At a glass-air interface at total internal reflection (TIR) we have that:

$$\sin\theta_{air} = \frac{n_{glass}}{n_{air}} \sin\theta_{glass}$$

which is greater than one. The well-known trigonometric identity $\sin^2\theta + \cos^2\theta = 1$ can be rearranged using the above to give:

$$\cos\theta_{air} = \left(1 - \left(\frac{n_{glass}}{n_{air}}\right)^2 \sin^2\theta_{glass}\right)^{\frac{1}{2}} \tag{3.1}$$

$$= jb \tag{3.2}$$

where b is a real number and j is the square root of minus one. The equation describing the propagation of light (see for example [156]) is:

$$E = E_0 e^{j(\mathbf{k}.\mathbf{r}-\omega t)}$$

where $\mathbf{E}$ is the amplitude of the field, $\mathbf{E_0}$ is the amplitude of the original field and $\mathbf{k}$ is the wavevector. By substituting in our equation for $\cos\theta_{air}$ we

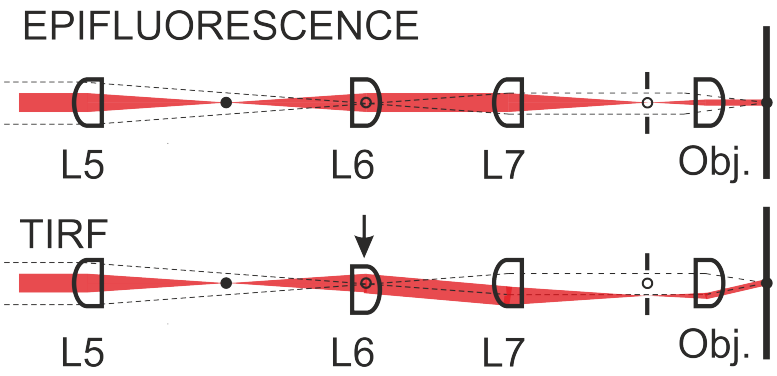

Figure 3.2: Lens positions in epifluorescence and TIRF imaging. L6 is translated from the epifluorescence position to achieve TIR. The beam is shown in red, black dashes are the back projection of the sample beam. Conjugate (back) focal planes are shown as (empty/)filled circles; the objective back aperture is shown at the back focal plane. Lenses are labelled for consistency with later diagrams.

come to:

$$E = E_0 e^{-k_{air} by} e^{j(k_{glass} x \sin\theta_{glass} - \omega t)} \tag{3.3}$$

This is a travelling wave along the interface which decays exponentially perpendicular to the boundary. The intensity of the evanescent wave is used to excite fluorophores within a limited depth of the coverslip, reducing background signal from out-of-focus molecules.

There are two main configurations for TIRF [157]; objective-type TIRF microscopy uses a beam incident through the objective at an angle to achieve TIR with the coverslip surface. To move from epifluorescence imaging to objective-type TIRF all that is required is to move one lens so that the beam does not pass through the centre (see figure 3.2). Alternatively, prism-type TIRF uses illumination from above the sample with an evanescent wave generated by TIR when a laser beam is incident on the prism face adjacent to the sample, but this method is technically more challenging to implement.

3.1.4 Statement of contributions

This chapter describes work preformed by myself to develop the fluorescence microscopy component of a dual purpose microscope to which another student is adding optical and magnetic tweezers. The IR filter box used was developed by a previous PhD student, Oliver Harriman. The two systems require different optical paths, but have a region of coaligned beam path directly before the commercial microscope body, containing only two shared optics.

3.2 Methods

All optics must be placed accurately to ensure good illumination of the sample and detection of the emitted light. Incorrect alignments can introduce aberrations and artefacts into images, or reduce the depth of field. Additionally, aligning components along perpendicular lines and using pinholes to define the beam path aids minor realignments of the beam as component positions inevitably drift over time, due to the need to use kinematic mounts.

3.2.1 Aligning components

The height of the laser beam on the optical bench is defined by the height of the laser aperture and the back aperture of the microscope. For safety the beam is kept at the lower height on the bench, and raised with a periscope (RS99,Thorlabs) immediately before the microscope body. Where possible the beam is aligned to run parallel to the lines of holes in the optical table which form a regular grid. This can aid correct alignment of components perpendicular to the beam.

Mirrors are used to define the light path before lenses are added. To be able to steer a beam through any given spot without the beam changing height requires control over two degrees of freedom; up and down, and left and right. Two steering mirrors must be used to achieve this and each mirror must have control over both degrees of freedom. For ease of further adjustments the mirrors should initially be in a neutral position at the centre of their range of movement, with the beam hitting them centrally.

To align a beam two pieces of card are used. The first is placed on a mount with the edge positioned to bisect the intended beam path, so a semicircle of light is seen on the card. The other is placed further downstream and the second semicircle falls here, with the desired beam position marked. The beam is walked into position by steering each mirror in turn to direct the beam towards the target positions on both cards until it is aligned with both.

Once the mirrors have been aligned the lenses can be placed. Before the lens is added a piece of paper should be placed in the beam path downstream of the lens position and the beam position marked. The lens can be added to the path, making sure the surface is perpendicular to the beam path. The beam should travel through the centre of the lens and fall in the same position on the sheet of paper as without the lens. If the lens is mounted in a screw mount it should be rotated slightly to check the beam passes through it centrally, and

that the beam is undeflected on the paper.

Once the beam is aligned pinholes can be added to define the beam position. As all optical components are adjustable they drift out of position slowly over time, and the pinholes aid the correction of this.

Care must be taken when adding components to the optical path to avoid placing them at focal planes or back focal planes unless that is the required position. This minimises the effect of dust and minute imperfections in the optical element on the beam and resulting images.

To change the size of the beam a beam expansion is required. In this project all beam expanders are Keplerian because the design allows spatial filtering of the beam profile at the focus if required. Unless otherwise mentioned, all beam expanders in this work use planoconvex lenses, with the flat side towards the focus.

3.2.2 TIRF alignment

From equations 3.2&3.3 we can see that the depth of penetration of the evanescent wave depends on the angle at which total internal reflection occurs. To determine the depth of evanescent wave penetration a prism was made by stacking ten glass slides (total thickness including immersion oil 11.34 mm) with immersion oil, and then placing a strip of graph paper on the top slide and adding an eleventh slide to keep the paper in place (as seen in figure 3.3A). By starting from a vertical beam position the angle of incidence can be calculated by geometry from the position of the beam centre, assuming a cone approximation to a Gaussian beam (see appendix C), as shown with fit equation in figure 3.3B. The TIRF prism is shown on the microscope with a range of incidence angles in figure 3.3C-F.

3.3 Microscope Design

The microscope design was completed sequentially, with the results of finalising one area of design influencing the next set of considerations, so the characterisation experiments are presented in chronological order.

3.3.1 First considerations

When building bespoke microscopes it is important to consider the layout of the components on the optical table to minimise the number of elements, but also to ensure there is enough control over the degrees of freedom of the

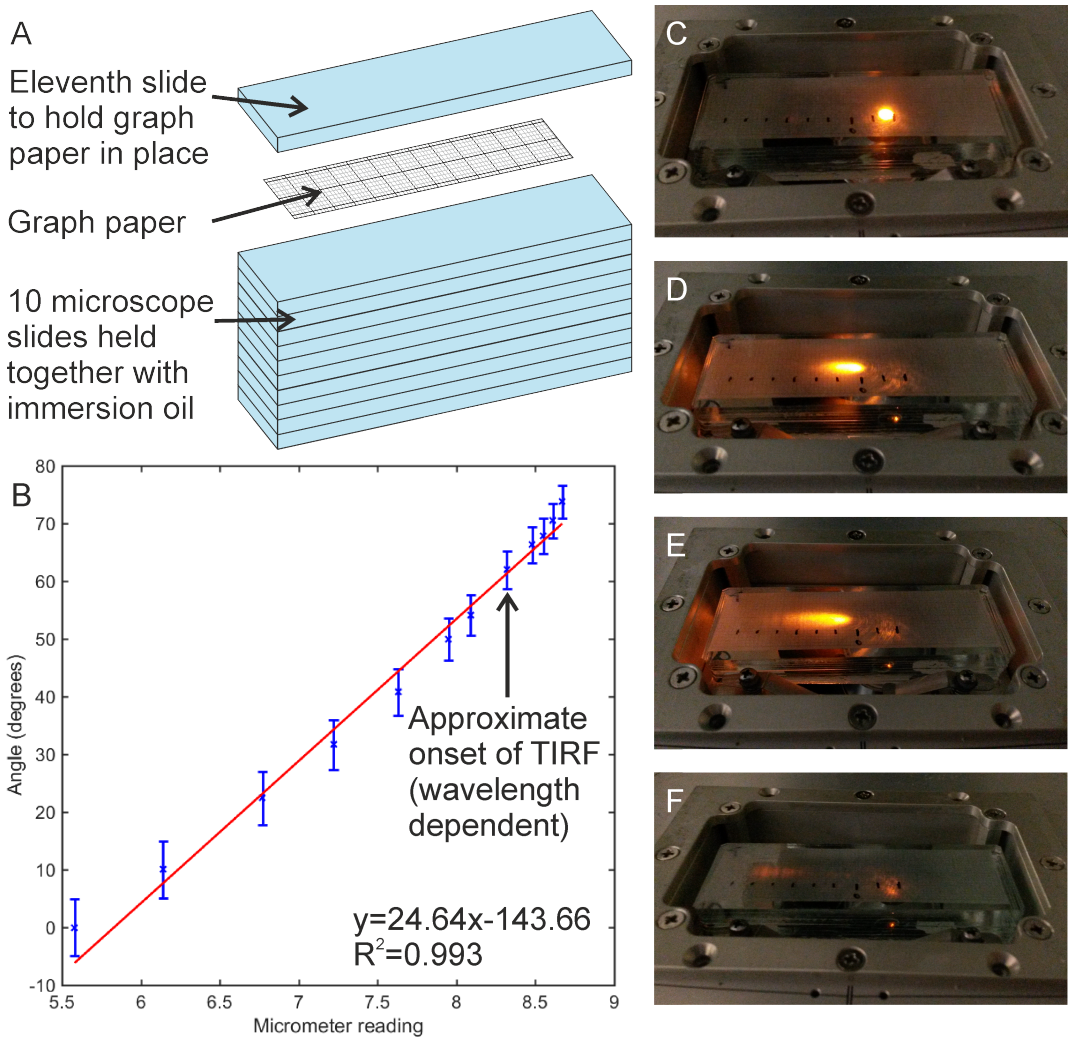

Figure 3.3: TIRF prism design and calibration (A) Schematic diagram of the construction of the prism. (B) Calibration curve for determining the beam angle from measured position on the graph paper with observational errors. (C-F) Show the beam incidence angle being driven from epifluorescence to TIRF imaging.

beam. Further, for configurations where there are two separate microscopy capabilities - such as infrared optical tweezers and fluorescence imaging care must be taken to choose the elements of the shared beam path to optimise both setups. For our experiments we are light limited in the fluorescence channel, and so the optic on the shared path was chosen for high visible transmission, with a loss expected in the infrared. Each system has its own periscope, so the only combined elements are a dichroic mirror cutting at 775 nm (FF775-Di01-25x35, Semrock Inc.), which is a mirror for the visible path, and the lens forming the 4f system with the microscope objective. The lens used was biconvex with f=300 mm and visible coating.

3.3.2 Illumination source

Lasers are the most commonly used light source in single molecule fluorescence microscopy because they offer high collimation, high coherence, narrow bandwidth, and high illumination intensity. A laser beam propagates with a Gaussian beam profile with low divergence, meaning that bespoke microscope systems can be designed with beam shaping elements before the objective lens, increasing the illumination path from around 50 cm to several metres, without significant adverse effects on the beam profile at the sample.

Light emitting diodes (LED's) [158] offer slightly larger bandwidth than lasers ($\sim$ few tens of nm) and high illumination intensity, without the coherence of a laser. When an LED is positioned directly at the epifluorescence port of a commercial microscope the power density of light over the sample is comparable to a laser expanded over the same area, but less input electricity is required to run the LED. Additionally, LED illumination is potentially less phototoxic than arc lamps that are conventionally used for brightfield illumination, as they do not produce additional wavelengths beyond the visible region that contribute heating, and LED illumination intensity does not decay over time. The use of LEDs has been demonstrated in video-enhanced differential interference contrast microscopy [159] and in inline holographic microscopy [160].

Collimating an LED beam poses a much more significant challenge than a laser beam. Whilst laser beams are emitted from a source that can be well approximated as a point, meaning the beam is well collimated and has a Gaussian profile which remains Gaussian as it propagates, by contrast, LEDs have an extended source, with a double peaked beam profile that is slightly different for each LED. Thus, to focus or collimate an LED beam, aspheric lenses must be used (rather than the planoconvex that can be used with a laser)

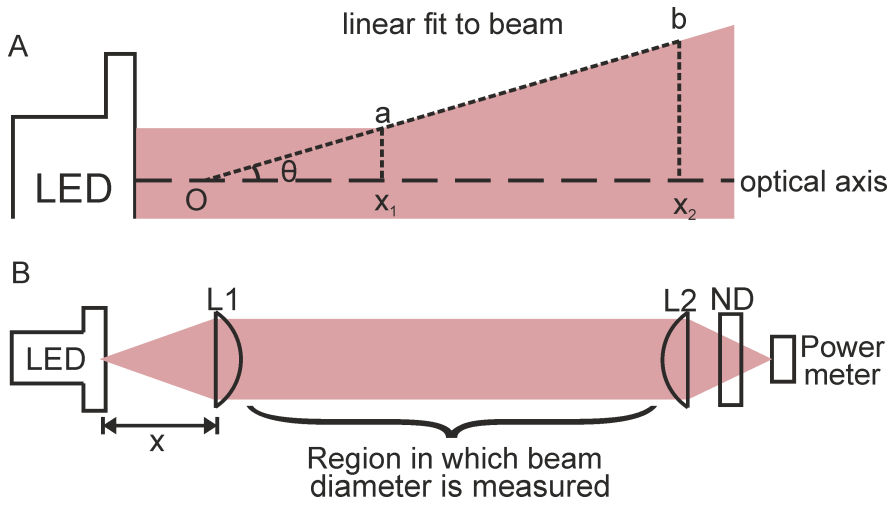

Figure 3.4: Schematic diagrams of the geometry and optical layouts used to measure beam divergence. (A) The geometry used to calculate the focal length of the lens required to collimate the beam. (B) Optical layout for measuring beam divergence with three different collimating lenses (L1). Light is focussed onto a power meter with a 1" aspheric lens with focal length 100mm.

[161]. It is impossible to perfectly collimate an LED beam, but approximately collimated beams can be created over short distances [162]. Higher power LED beams require larger light emitting elements, taking them further from the point source approximation and making them harder to collimate.

Initially it was hoped that an light emitting diode lightbox (Spectra X6 LCR SA, Lumencor) would be a suitable light source for the microscope. Initial images of 200 nm fluorescent beads with the LED source coupled directly to the epifluorescence port of the commercial microscope body showed good uniformity of illumination over the field of view. The beam diameter was assessed to determine the degree of collimation and suitability of an LED lightbox for bespoke single-molecule super-resolution fluorescence microscopy.

Beam diameter was measured by placing a board at defined distances from the source and marking the vertical and horizontal extremum of the beam profile on 1 mm graph paper. The distance between the two marks was measured using a ruler for each direction and the two measurements were averaged, and the standard deviation (s.d.) calculated. For these experiments the teal source on the lightbox was used - this is a 510/10 nm wavelength band with a maximum measured power of 14.6mW.

The focal length of the required collimating optic was found by fitting a linear relation to beam widths measured downstream of the LED fibre head. The geometry for this is shown in figure 3.4A, assuming that the beam expands following a linear relation, shown by the dashed line with small spacing. Using

similar triangles Oax_1 where the line ax_1 corresponds to the beam radius before divergence and Obx_2 where the line bx_2 corresponds to the beam radius at some further distance, given by the linear relation fitted to the beam profile, the distances from the LED source to the point O and the distance Ox_1 were calculated, as well as an estimate of the focal length of the lens to be used to collimate the beam. For these experiments the beam was attenuated 100 times with an ND2 filter.

Once suitable aspheric lenses were identified the beam diameter and power retained in the beam for each lens was measured as shown in figure 3.4B.

Light diverges from the LED, travelling to an aspheric lens (L1) one focal length (x) away from the source. Three different lenses are used as L1; 1″ f=100mm, 1″ f=500mm and 2″ f=200mm. A 1″ f=100mm lens is placed downstream to focus the beam onto a power meter. This lens was chosen to be 1″ in diameter to measure experimentally realisable power in the beam as the cost of switching all optical elements and mounts to 2″ diameter was deemed prohibitive.

The beam diameter in free space was measured and the diverging part was fitted with linear relation diameter=0.11(propagation distance from the LED fibre head)-5.3. This can be seen in figure 3.5A; the fit has a high R^2 value of 0.978, suggesting that the linear approximation is sufficient over this propagation distance. This corresponds to a distance Ox_1 of 110 mm, and a distance from the source to O of around 60mm. Using the radius of a standard one inch optic the ideal focal length to capture all of the beam would be 230 mm. Lenses come in stock focal lengths, and so the beam diameter achieved with a 1 inch 200mm focal length lens placed 270mm from the source (the additional 10 mm distance was added by observing the position of best collimation by eye, due to the breakdown of the linear approximation) is shown in 3.5B (which is shown on the same vertical scale as 3.5A). A much lower divergence is seen, and so the approximations used are empirically valid.

Three further different lenses were tested to choose the optimal beam collimation. These experiments were carried out without beam attenuation. The lenses used were a two inch f=200mm lens placed 270mm from the LED fibre head, a one inch diameter f=100mm lens placed 160 mm from the LED fibre head and a one inch f=500 mm lens placed 590 mm from the LED fibre head. The results of this are shown in figure 3.5C. The measured output powers (with observational errors) were 1.96 ± 0.005 mW, 0.80 ± 0.005 mW and 6.1 ± 0.05 mW; 13, 5 and 42 % of the maximum input power respectively.

The f=500 mm lens loses power as the beam is significantly wider than the

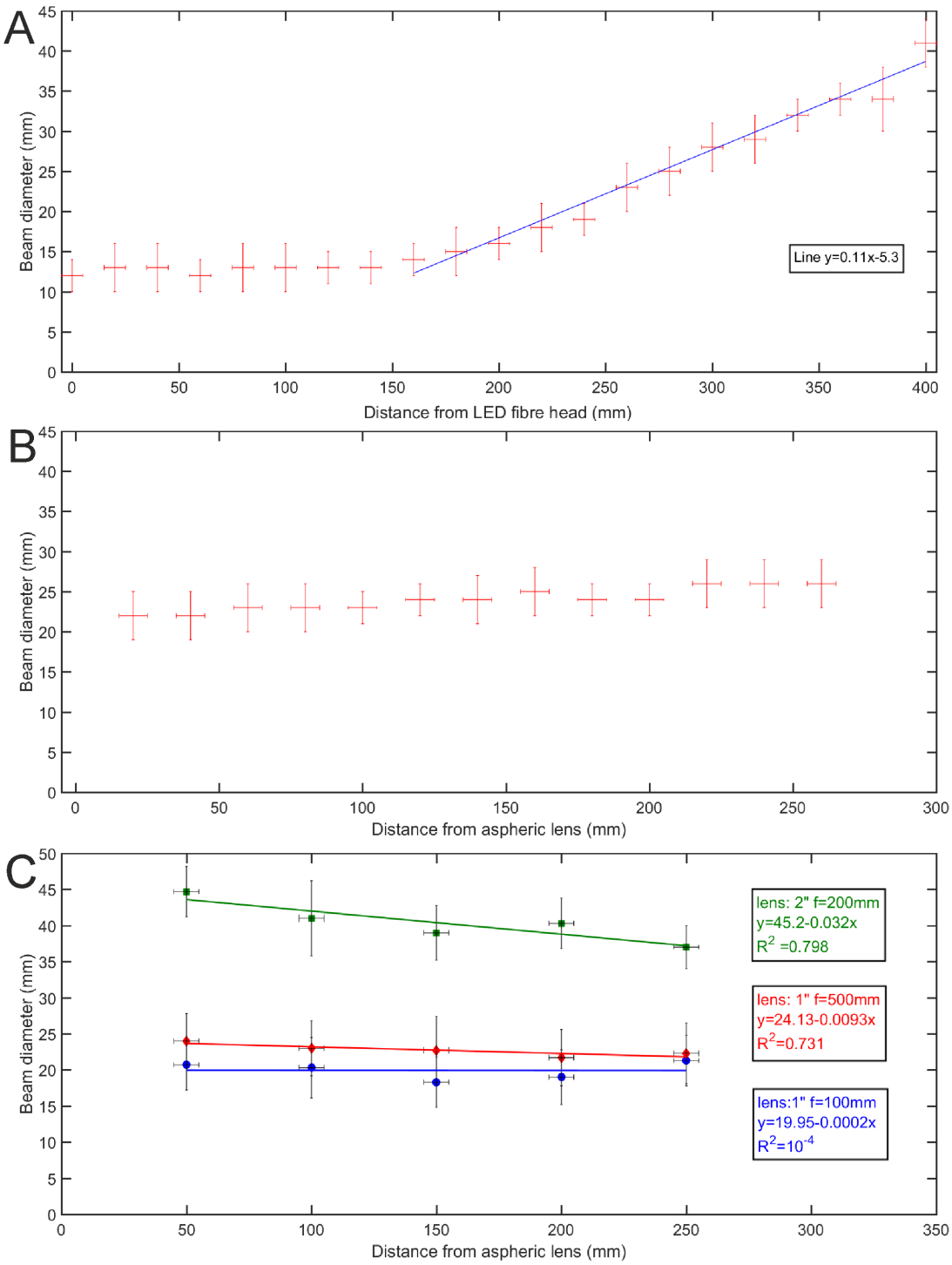

Figure 3.5: Beam diameters of the LED beam in free space. (A) Beam diameter as a function of propagation distance in free space with no additional optics. A linear fit to part of the data used to choose a collimating lens is shown. (B) Beam diameter as a function of propagation distance after a f=200mm aspheric lens. (C) Beam diameter as a function of propagation for three aspheric lenses. All beam diameter errors are the standard deviation of (A,B) 2 and (C) 3 measurements plus an observational error of 3 mm. All x-axis distance errors are observational errors.

lens when it has propagated 590 mm, so light passes around it and is lost from the beam. The f=100 mm beam diameter shows an extremely low gradient, implying good collimation, but the low R^2 value indicates that there is likely a local focus, which appears to be around 150mm from the aspheric lens based on a local minima in the points. The two inch f=200mm lens shows a wide beam diameter, larger than that seen in the earlier experiments, but this is explained by the lack of ND2 filter, allowing the lower power tails of the beam profile to be seen. This lens has not been placed correctly since the gradient is negative, but the larger size of the optic reduces losses and the power is higher than the other lens choices. However, the power would quickly drop below the $\sim$5 mW required for single molecule imaging at $\sim$20 ms exposures over a field of view of a few tens of μm^2, as propagation through further optical elements leads to further losses (even coated optics have approximately 1% reflectance losses).

To summarise: The beam diameter of the available LED was measured, and the focal length of the aspheric lens required to produce collimated light was calculated to be 200 mm (to the nearest stock size), this produces a large beam diameter greater than one inch after collimation. This has three very significant disadvantages: (1) the power of the LED was dispersed over a large area, meaning only a low power density could be achieved in the sample, (2) The beam was too wide to be accommodated with standard 1" optics, which would have added a large expense in acquiring new optics, or would have meant large power losses with the use of standard 1" optics and (3) further unavoidable power losses would reduce the total power below the required level for single-molecule imaging. It was decided that the supercontinuum laser used by a previous PhD student was the most suitable illumination source for this project.

3.3.3 Wavelength selection

The use of a white light fianium laser (SC400-4, Fianium Ltd.) means that colour filtering is necessary to limit the illumination power at the sample. The advantage of using a white light laser and filters over several co-aligned single line lasers is that the fluorescence excitation can be customised to the fluorophores being used in the application. This can help to reduce spectral overlap and bleedthrough between channels. Supercontinuum lasers remove the need to coalign many single laser lines, and with a set of filters any fluorophore can be used, rather than just ones excited by the specific laser lines chosen.

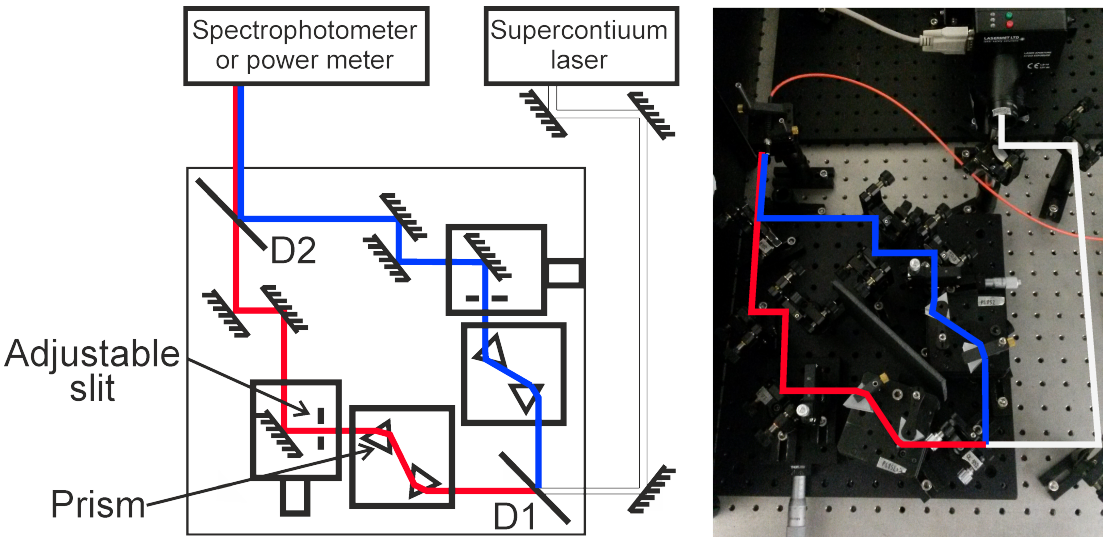

Figure 3.6: Schematic diagram and photograph of the prism filter module. The laser beam from the supercontinuum laser is shown in white, and the two colour channels are shown in red and blue.

"Off-the-shelf" filters do not cover a continuous range of wavelength specificity, and so for true flexibility in a system it is desirable to have a bespoke filtering system that can be tuned to the fluorophore in use. Such individual or multiband filters are available from manufacturers such as Semrock and Chroma. These filters are uniformly covered with the coatings required to achieve a certain transmission and reflection profile. For a truly versatile system it is desirable to have tunable filtering on a white light spectrum, such that the centre frequency and bandwidth can be optimised for the fluorophore in use. Acousto-optical deflectors (AODs) offer wavelength specificity but with narrow bandwidth. Two filtering methods were designed and tested; one using prisms to disperse the beam, and one using gradient linear filters.

The two designs for a dual band filter were developed and characterised on 30 cm square optical breadboards to be interchangeable; three magnetic mounts were arranged in a triangle under the breadboards for reproducibility of alignment when changing modules. Both designs must have the ability to steer the resultant beams, which requires two steering components. 552 nm dichroic mirrors (FF552-Di02-25x36, Semrock Inc.) were used to split and recombine the two colour channels in both modules.

The prism design uses two equilateral 25 mm dispersive prisms in each colour channel to disperse the beam and then prevent further divergence (see figure 3.6). An adjustable slit and mirror on a translation stage allow choice of the centre wavelength and band width for each channel. Following these components each channel contains two steering mirrors to control the path of the resulting beam.

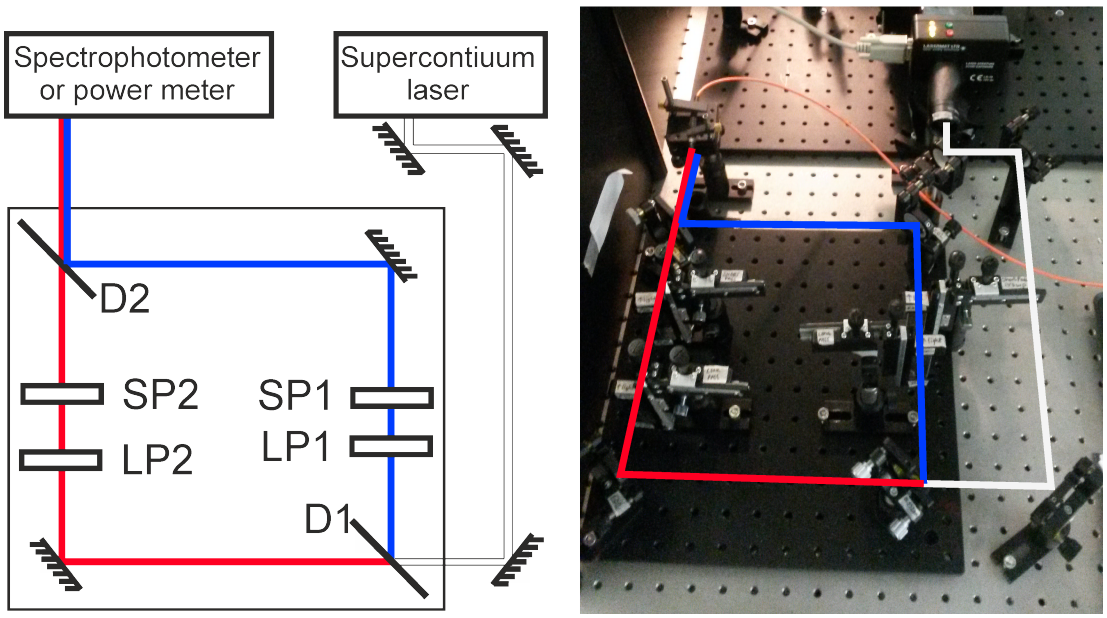

Figure 3.7: Schematic diagram and photograph of the gradient linear filter module. The laser beam from the supercontinuum laser is shown in white, and the two colour channels are shown in red and blue.

The second design (see figure 3.7) uses gradient linear filters. The beam is split by the dichroic, and each colour channel goes through a long pass gradient linear filter (1G LVLWP, Delta Optical Thin Film) and then a short pass gradient linear filter (2GV2 LVSWP, Delta Optical Thin Film), which are mounted in xy translation mounts for 1-3" optics (XYFM1/M, Thorlabs Inc.). In this design the longer wavelength colour channel has only one steering mirror unique to it, so the mirror before the filter module must be used to define the direction of the long wavelength channel, and the short wavelength channel must be coaligned with this using DC1 and the mirror in the short wavelength path.

To analyse the reproducibility of the setting of the desired wavelength band for each filter module, each unit was set to a pre-defined range of micrometer positions and slit widths, and the spectrum was measured (as described in the general Methods chapter). Each reading was taken 3 times using a ND 4 filter and the integration time was adjusted to avoid saturation of the spectrometer; the readings were averaged, and the standard deviation from the three spectra was used as the error for fitting.

The spectral data was analysed using custom written Matlab code. Analysis of spectral peak width is usually based on a FWHM criteria, however for certain peak shapes, this criteria can lead to large underestimation of the peak width. The Matlab code finds the gradient of the measured spectrum and outputs the cut wavelength as the position of maximum gradient; the user

must check the output and can reject the value if it is incorrect; the code will then give the next highest gradient.

In the prism filter module for each channel a micrometer on the adjustable slit controls the slit width, and this is mounted on a translation mount, which controls the centre wavelength. The reproducibility of each of these and the control over bandwidth and centre frequency respectively was characterised using spectra recorded keeping the other micrometer in a fixed position. Example spectra for each type of data are shown in figure 3.8(A,B).

The prism filter module short wavelength centre wavelength (figure 3.8C) shows good reproducibility with a high correlation ($R^2 = 0.9777$). The large gradient means that the centre wavelength can be set with high accuracy. One clearly anomalous value was excluded from the point at micrometer position 7 as the centre wavelength given was 450 nm. This was determined to be due to error during the Matlab processing of the spectrum. By contrast, the long wavelength centre wavelength (see figure 3.8E) shows lower reproducibility with a low correlation ($R^2 = 0.5697$). This may be affected by the large standard deviation of the values when the micrometer is set to 16 (as shown by the large error bar), but inspection of the data showed three values with large spread, rather than a single anomaly, which may be caused by fluctuation of the signal due to a low integration time in the spectral recording. Additionally, the gradient of the fit is much lower, giving lower accuracy. No error bar is shown on the first point as a clear peak was determined in only one of the three spectra.

For bandwidth the short wavelength channel gives a linear relation with $R^2 = 0.8413$, with a low gradient, ensuring the bandwidth can be tuned to a small tolerances (see figure 3.8D), however, less dispersion was achieved in the long wavelength channel with the components available. Whilst a linear relation with $R^2 = 0.8425$ was found for the initial part of the graph, the high gradient and large initial bandwidth of nearly 80 nm make selection of a narrow wavelength band impossible at long wavelengths (see figure 3.8F).

In the gradient linear filter module for each channel a micrometer controls the position at which the beam travels through the filter, and therefore the wavelengths that are allowed through. To investigate the reproducibility of these positions and the achievable bandwidths and centre frequencies, the effects of each micrometer were characterised separately with the other micrometer in a fixed position. Sample spectra for these measurements are shown in figure 3.9(A,B).

Each gradient linear filter is expected to show a linear relation between position and cut-off wavelength, with flat regions caused by other wavelength

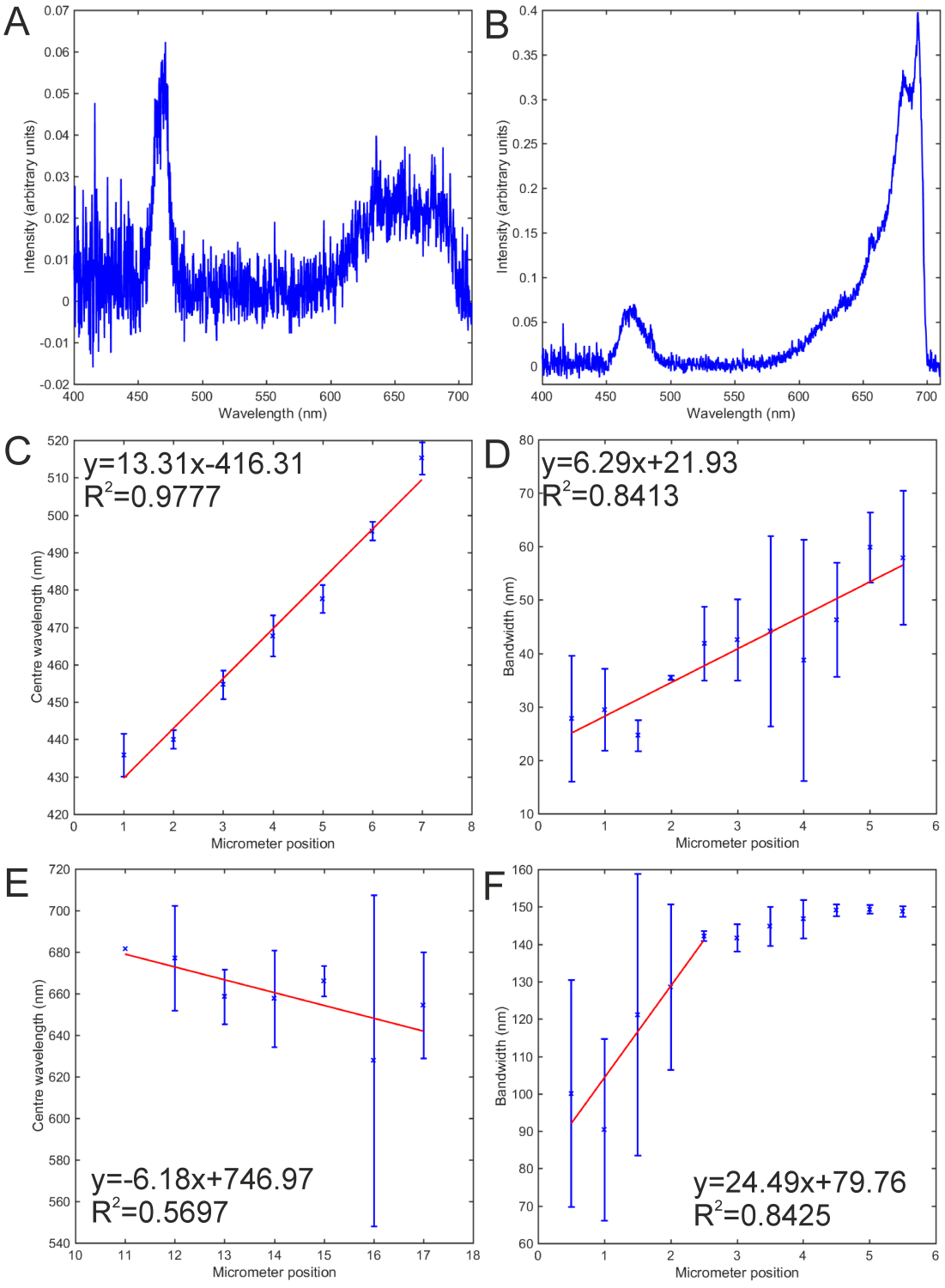

Figure 3.8: Calibration of the prism filter module. (A) and (B) example spectra for measuring the centre wavelength and bandwidth respectively. (C) and (D) Centre wavelength and bandwidth as functions of the position of the micrometers controlling slit translation and slit width respectively for the short wavelength channel. (E) and (F) Centre wavelength and bandwidth as functions of the position of the micrometers controlling slit translation and slit width respectively for the long wavelength channel. Error bars are the standard deviation from three repeat measurements.

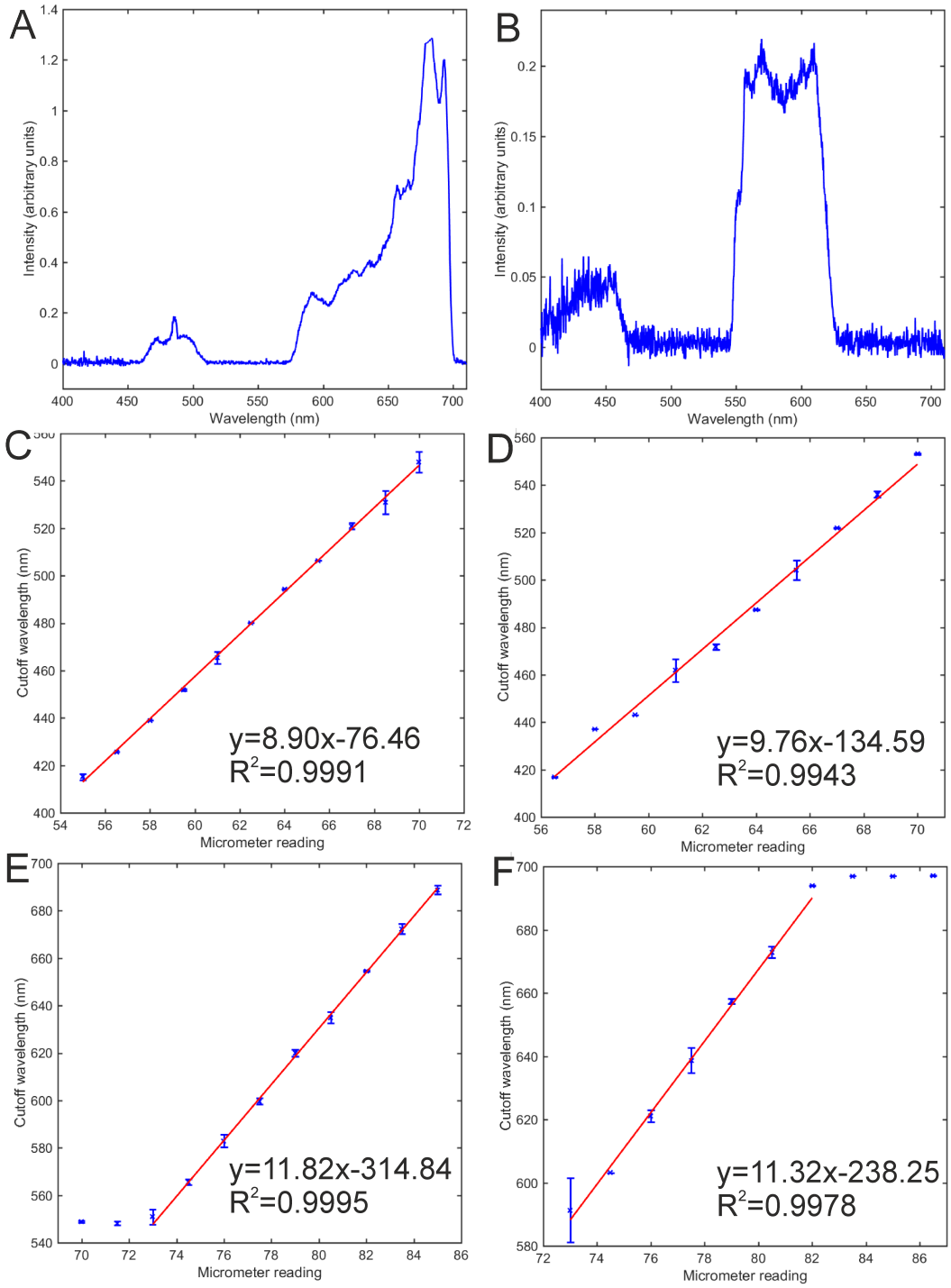

Figure 3.9: Calibration of the gradient linear filter module. (A) and (B) example spectra for measuring the long and short pass gradient linear filter cutoff wavelengths respectively. (C) and (D) Long and short pass gradient linear filter wavelength calibration for the short wavelength channel. (E) and (F) Long and short pass gradient linear filter wavelength calibration for the long wavelength channel. Error bars are the standard deviation from three repeat measurements.

filtrations applied to the beam, such as from the dichroic mirrors (at 552 nm) or the IR filter (∼700 nm). All graphs were fitted linearly, excluding points that were affected by these known wavelength constraints (see figures 3.9(C-F)). All 4 fits show very high ($\geq$ 0.99) values of R^2 and low standard deviations, implying high reproducibility, with gradients that enable high wavelength specificity.

By comparing the integration times without achieving saturation, it is also noted that that gradient linear filters retain more power than the prism filtration method for a given bandwidth setting.

Comparing the two methods, the dispersive prism method has an inherent difficulty in that for greater control over the bandwidth, more dispersion is desired, however, due to the wavelength- dependent nature of dispersion the resulting filtered beams' horizontal position is a function of its wavelength. This was overcome by placing a mirror on the same translation mount used to position the slit for selecting wavelength, but required an extremely precise alignment. By contrast, the linear filters allow high specificity without introducing dispersion to the beam.

Gradient linear filters were chosen as the preferred method of choosing two colour channels from the visible output of the supercontinuum laser. Compared to the prism filter scheme the gradient linear filters retained a higher proportion of the light, were simpler to align and had higher reproducibility. The biggest advantage is that the colours are not spectrally dispersed.

3.3.4 Illumination optics

The illumination optics were designed with two beam paths, split and recombined with 50:50 polarising beam cubes. One path can provide widefield illumination or can be used for fluorescence recovery after photobleaching (FRAP) experiments using a 125 mm focal length lens on a flip mount. The other beam path can be used for TIRF, narrowfield or widefield illumination depending on the lens configuration selected.

For TIRF imaging the laser beam must be incident above the critical angle. Most methods to achieve this result in the beam being displaced from the optical axis, and at high magnifications this means light no longer falls on the camera. The optics to avoid this are shown in figure 3.10: The lens L7 is placed its focal length away from L6, mounted on a translation stage to achieve the beam angle required for TIRF. This means the conjugate back focal plane falls in lens L6 and therefore the image plane is unaffected by the lens. The L7 in the

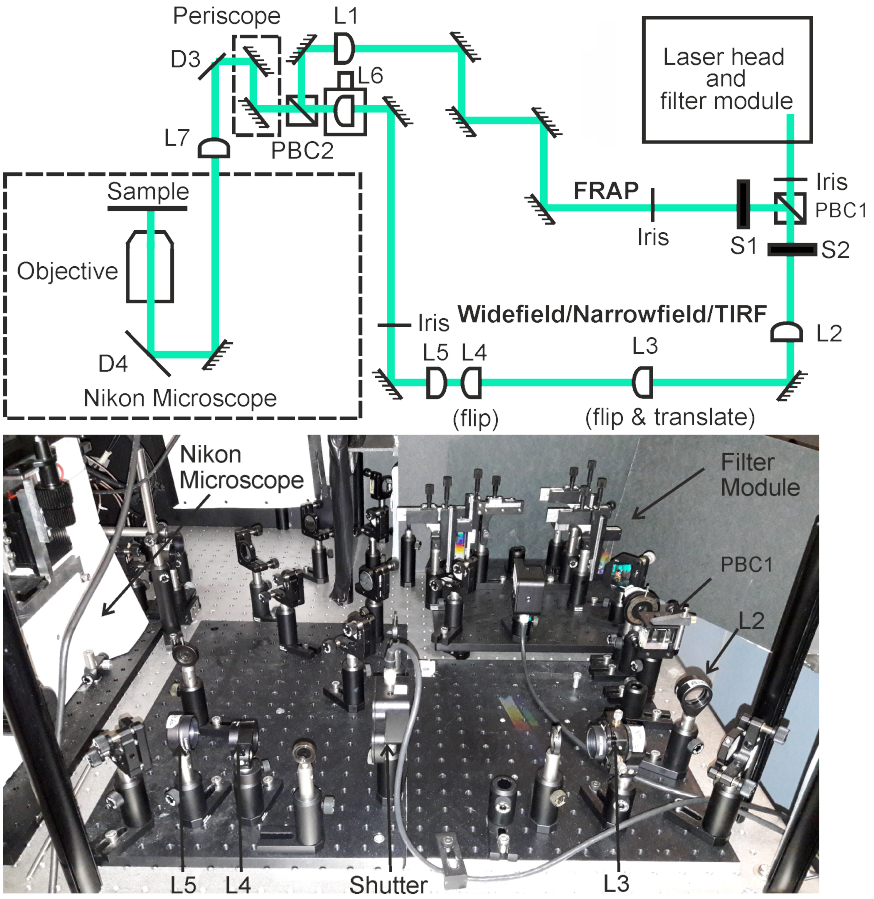

Figure 3.10: Schematic diagram and photograph of the illumination optics. The positions of the shutters and irises seen in the photograph have been modified by another student for a different experiment.

commercial microscope body would have required L6 inside the microscope body, so L7 was replaced with a longer focal length lens. This has the effect of deexpanding the beam between L7 and the objective relative to its previous size which is corrected upstream.

The choice of focal lengths for lenses L7, L6, L5 and the optics between them was influenced by a number of factors. Both infrared light for the magnetic tweezers and visible light for fluorescence imaging need to be coupled into the microscope so it is desirable to have the minimum number of common optics since the coatings cannot be optimised for both wavelength ranges. Since the visible laser is lower power than the infrared laser L7 was chosen to be anti-reflection coated in the visible. The height of the back port of the microscope requires a periscope to raise the beam height by around 100 mm. The periscope is common to both the FRAP and widefield paths, so the recombining beam cube must be placed upstream of the periscope. The minimum focal length of L7 that is available "Off the shelf" that allows all of these components to be placed in the correct position is 300 mm. L7 was chosen

to be bi-convex, focal length 300 mm; L6 planoconvex, focal length 300 mm; L5 planoconvex, focal length 300 mm. The Nikon lens that was replaced was measured to have a focal length of 135±1 mm (observational error), so this reduces beam diameter by a factor of 2.2 in the sample plane. An additional beam expander with two choices of second lens was added to this path to allow for compensation of the beam deexpansion if desired. The common lens, L2 was chosen to have a focal length of 125 mm, and L3 and L4 with focal lengths 75 and 400 nm were flip mounted for beam deexpansion by a factor of 0.6 or beam expansion by a factor of 3.2 respectively. Additionally lens L3 was mounted in a translation mount to aid repositioning as the flip mounts do not have perfectly reproducible positions.

Irises were placed to avoid conjugate focal and back focal planes, and are necessary to define the beam path to allow correction of the unavoidable drift of mechanical components over time. Shutters were placed for the experimental system being investigated, but can be moved for flexibility in illumination options. A commercial inverted microscope body (Nikon Eclipse Ti-S), was used to mount the samples and to allow for simple brightfield imaging. This provides a base with little mechanical noise, which is important for force transduction experiments which use back focal plane interferometry that will eventually be performed with fluorescence microscopy on this machine. Additionally, a commercial microscope can accept filter cubes, removing the difficulty that can be found in correctly aligning dichroic filters when switching between colours in bespoke machines.

3.3.5 Fluorescence detection

On leaving the commercial microscope body the beam was expanded by a factor of two using a 75/150 mm achromatic lens pair with visible anti-reflection coating to give 200 x magnification of 80 nmpixel^{-1} on the Andor cameras. The images recorded on the Watec camera were not further magnified.

An Andor TuCam was used to split the two colour channels into red and green on separate cameras; this is a commercial splitter module containing a dichroic (at 580 nm), a green bandpass filter (525/50 nm) and the red bandpass filter was replaced to be 640/20 nm. The TuCam contains 1:1 beam expanders that can be adjusted to ensure that both cameras acquire the same field of view.

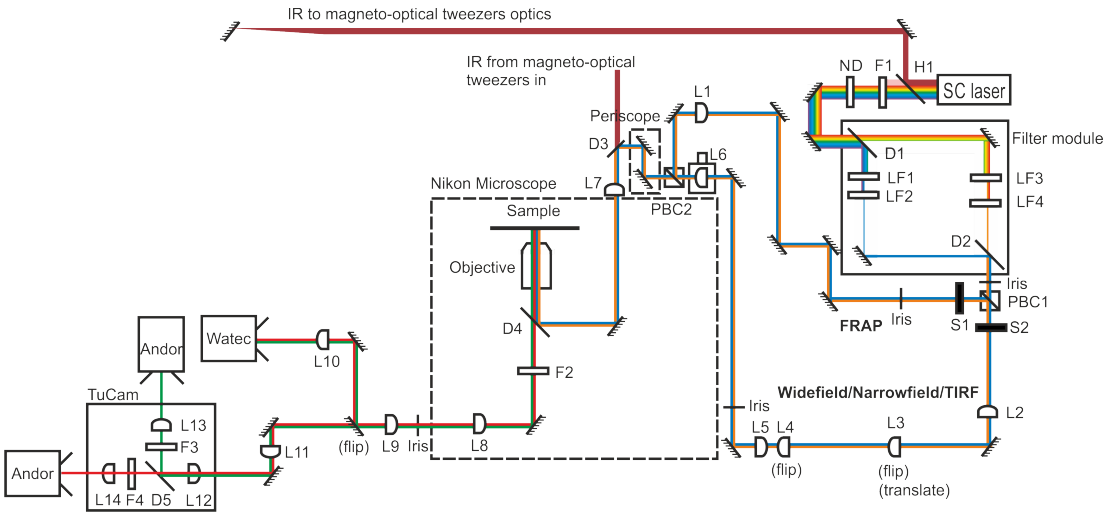

Figure 3.11: The final optical design as laid out on the optical table. Colours are shown spatially separated to show the filtering capability of each component, colours are not dispersed.

3.3.6 Synchronisation and control

To extract meaningful information from images recorded on multiple cameras they must be synchronised. It is also useful to trigger the opening of any laser shutters once the camera has started acquiring to ensure that the first "laser on" frames are captured, but that dark frames are minimised to save file space.

Andor cameras come with proprietary software (Andor Solis) which controls the camera, and can interface with the laser and shutters for precise timing control. This was set up so that triggering an image acquisition in the camera software would open the laser shutter. For two channel recording the red channel was chosen as the master, and triggering an image acquisition started the green channel camera and then opened the laser shutter. The Watec camera used on the combined fluorescence microscopy and magneto-optical tweezers set-up required custom software, which was written in LabVIEW to allow the user to view a live image feed and to record single images or kinetic series.

3.4 Final Optical Design

The complete optical design can be seen in figure 3.11, showing the layout of all the components on the optical table. A supercontinuum white light laser with tunable filtering using two channels of gradient linear filters was chosen for flexibility in illumination wavelength and power. The microscope design is very flexible to allow tuning to different biological applications;

giving one or two colour illumination via widefield or TIRF imaging with two beam diameters, and also enabling FRAP experiments. The compact design leaves space for the work of another student (Zhaokun Zhou) to add magneto-optical tweezers to the same microscope for combined fluorescence and force transduction experiments. In addition to the considerations detailed above, the infrared output of the laser was diverted in a tube system for use by two PhD students, Zhaokun Zhou and Jack Shepherd.

Chapter 4

Immobilising and Tethering DNA

4.1 Introduction

The aim of the work presented in this chapter was to develop assays for imaging single fluorescent dye molecules in two colours, to be combined at a later date with magneto-optical tweezers to investigate the interaction of DNA binding proteins with supercoiled DNA. This chapter will outline the design of the fluorescence assays for surface immobilised and tethered DNA, including the development of the DNA construct based on a DNA construct developed to study transcription bubbles by Tanner [163].

4.1.1 DNA and the molecules that act on it

As has been previously described (see section 1.3.1), DNA is an interesting molecule to study due to its highly periodic structure and biological importance. There are many proteins which act on DNA to maintain, transcribe, uncoil, unwind and repair it, amongst other functions. For example, DNA gyrase acts to remove strain created in DNA when it is unwound by helicase.

To study the mechanisms by which these proteins perform their functions DNA must be presented in a known configuration. *In vitro* under flow DNA is extended along the flow direction, and when tethered to the coverslip is extended in lines. This technique is elegantly used in DNA curtains, where many DNA strands are fixed to raised platforms in flow cells, aligning their start and end points and allowing the action of many fluorescently labelled proteins acting on DNA to be observed simultaneously in one field of view [164].

Whilst optical methods allow us to examine molecules without disturbing their state, for some molecules their function is directly related to movement

or how they respond to changes in their mechanical environment. To study the forces involved in these processes it is necessary to make single molecule measurements with instruments that can manipulate the system.

4.1.2 Force transduction techniques

Single-molecule force transduction measurements on filamentous molecules are often carried out by attaching a micron sized bead to a part of the molecule, with the other end attached to the microscope coverslip [165], or by attaching both ends of the molecule to beads [166][167]. This is similar to the fluorescence methods, but the addition of a bead, depending on its properties, allows manipulation with either optical [167] or magnetic [168] tweezers. Due to physical space constraints on standard inverted microscopes, magnetic tweezers are generally developed such that the bead can only be rotated in the plane of observation, so the DNA tether being manipulated is obscured from view by the bead [169]. Due to the geometry of the system changes of bead height within the assay due to shortening/lengthening of the DNA tether can be measured by back focal plane detection [167], but cannot be directly observed on the DNA itself.

4.1.3 Combined fluorescence and magneto-optical tweezers

Typically, experiments with magnetic tweezers have relied on visualising the probe particle, but combination with fluorescence would enable direct imaging of the molecule under study [153], and may lead to insight as to the location of an event; for example a protein binding event may be sequence specific which could not be determined via indirect methods.

The purpose of a combined magneto-optical and fluorescence tweezers microscope is to study the many proteins and molecular machines which act on DNA; previous studies have used either force transduction or fluorescence imaging to study them, but by combining the techniques both the spatial location of an interaction and the forces involved could be measured. For example, in [167] the DNA of the lambda phage (from here referred to as lambda DNA) is stretched by attaching latex beads to both ends, and one being held in an optical trap whilst the other is moved with a micropipette. Force was measured by recording the deflection of the trapping beam on a position sensitive detector. The researchers determined the forces involved in the transition between two stable forms of DNA, but witnessed hysteresis. They biochemically explored two possible mechanisms for the observed behaviour;

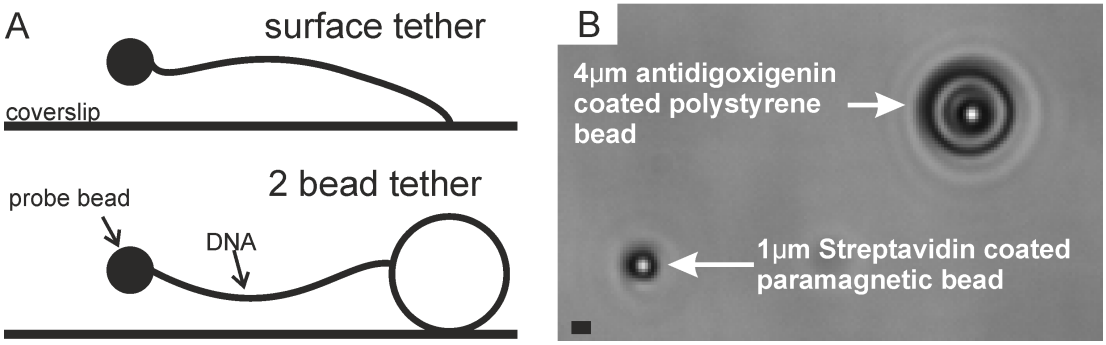

Figure 4.1: Assays for force transduction. (A) Schematic representation of: top; the assay performed using surface attachment, lower; the desired assay for combined magneto-optical tweezers and fluorescence microscopy using two beads. (B) Brightfield image of a streptavidin coated paramagnetic bead and an anti-digoxigenin coated polystyrene bead. Scale bar 1 μm.

unstacking of the helix to form a "ladder" with flat, parallel, intact bases, and melting and fraying of the two strands to single-stranded DNA. Through multiple experiments changing the sodium concentration and by cross-linking the DNA to prevent fraying, the researchers found that the hysteresis was eliminated when the DNA was crosslinked, suggesting that the DNA melted and frayed when extended. These two mechanisms could have been explored using a combined fluorescence assay with a single-stranded DNA binding dye and a spectrally distinct double-stranded DNA binding dye in a shorter series of experiments.

Zhaokun Zhou is developing a combined magneto-optical tweezer that allows manipulation of the bead in any direction, thus meaning the trapping geometry can be altered to allow transverse illumination of the DNA. This will combine the single molecule fluorescence imaging system developed in chapter 3 to permit combined fluorescence and force transduction experiments. For these assays it is necessary to constrain the fluorescently labelled DNA to a plane such that it can be imaged at high magnification where the depth of field is limited. The experiments below describe the development of a coverslip surface to paramagnetic bead DNA tether, but the final assay will require conjugation to another bead (these two situations are shown schematically with brightfield images of the two bead types in figures 4.1A,B).

4.1.4 Fluorescent dyes

There are multiple methods of dye binding to DNA, such as intercalators, which fit between the base pairs of the helical backbone, and minor groove binders, which lie along the narrow groove of the helical backbone. In this

project the intercalator YOYO-1 (491/508), minor groove binder SYTO-13 (488/506) and PicoGreen (502/522) which uses both DNA binding modes are initially investigated. These three DNA dyes have all been previously used for super-resolution microscopy (See for example: YOYO-1 [111][170]; SYTO-13 [170][171][172]; PicoGreen [173]). The effects of intercalating dyes have been well-studied [143], but the minor groove binders have not, and they may be less perturbative to the DNA structure [170].

YOYO-1 is a dimeric, unsymmetric cyanine dye which interacts with DNA primarily by intercalation, with no large preference for specific DNA sequences [174], especially at low salt concentrations [175]. The intensity of the dye increases approximately 1000-fold on binding to DNA, due to reduced flexibility of the linker in its bound conformation [176][143], making it highly suitable for detecting DNA *in vitro* due to the high fluorescence enhancement reducing background signal. At higher dye to base pair ratios an external, non-fluorescent groove binding mode is often observed [174][177][178], although this has recently been disputed [179]. Intercalating molecules in general are known to affect the mechanical properties of DNA [180][181][182]. In particular, upon intercalation YOYO-1 elongates and unwinds DNA without affecting the persistence length [183]. As tension in the DNA is increased YOYO-1 intercalation also increases [179], and dye unbinding rates are modified [179], which must be considered for studies of enzymatic action on YOYO-1 labelled DNA. The interaction of an oxidised guanine base from the DNA strand has been hypothesised as the mechanism of YOYO-1 quenching over time [178], and electron transfer reactions between intact guanine bases and the dye are proposed to cause the observed photoblinking behaviour [111].

The SYTO dyes are membrane permeant cyanine dyes often used to detect apoptosis [184][185]. The minor groove binding SYTO-17 has been shown to cause less disruption of nuclear architecture in cells compared to intercalating stains [186] and does not trigger the DNA damage response [187]. SYTO-13 is another minor groove binding member of the SYTO family, and may also be less damaging than intercalating dyes such as YOYO-1 [170]. SYTO-13 shows an approximately 40-fold increase in intensity on binding to DNA compared to being free in solution [184][170] usually attributed to an increased rigidity of the molecule on DNA binding [188], which increases the signal-to-noise ratio in fluorescence images.

PicoGreen binding shows characteristics of intercalation in FCS studies, and characteristics of minor groove binding in competition with the minor groove binder Hoechst [189]. It is thought that the quinolinium

group intercalates with no sequence dependence into the DNA backbone and the benzo-thiazol group sits rigidly on the DNA, with the two dimethylaminopropyl groups having backbones extended along the minor groove [189]. On binding to dsDNA PicoGreen exhibits a 1000-fold increase in intensity, and is non-sequence specific [190], making it suitable for DNA quantification assays. It also binds to RNA, but with a smaller fluorescence intensity increase.

4.1.5 Statement of contributions

The fluorescence microscope was built by myself, and after the DNA ordering (sequences designed by Adam Wollman) all the steps to create the DNA construct were performed by myself. Microscopy samples and data were prepared and imaged collaboratively with Zhaokun Zhou. This work was published in January 2015 [149]. Adam Wollman developed and utilised the ADEMS code for tracking the dye on the immobilised DNA tethers. Zhaokun Zhou produced simulations of the photoblinking behaviour of the dye. The analysis presented was performed by myself unless otherwise stated.

4.2 Methods

4.2.1 Optical design

The bespoke fluorescence and magnetic tweezers microscope is designed around a commercial Nikon Eclipse Ti-S inverted microscope body. The work in this chapter was conducted partway through the microscope design detailed in chapter 3. As such a dual-band bandpass filter was used to produce two colour channel excitation instead of the linear filter module, and the image after the commercial microscope body was not further magnified, resulting in a 100 x magnification of 160 nmpixel^{-1}.

Excitation illumination for fluorescence is from a white-light supercontinuum laser, with two channels centred on 479 nm and 585 nm generated with a dual-band bandpass excitation filter (Brightline 479-585, Semrock) placed directly after the filter for the infrared component of the laser emission (see laser transmission spectrum in figure 4.2A). The excitation field had 24 µm full width half maximum (FWHM) at the sample, and power density 1800 Wcm^{-2} (green), and 2900 Wcm^{-2} (red). Fluorescence emissions were captured on two EMCCD cameras cooled to -80°C. Two channel observation was enabled by the Andor TuCam colour splitter module

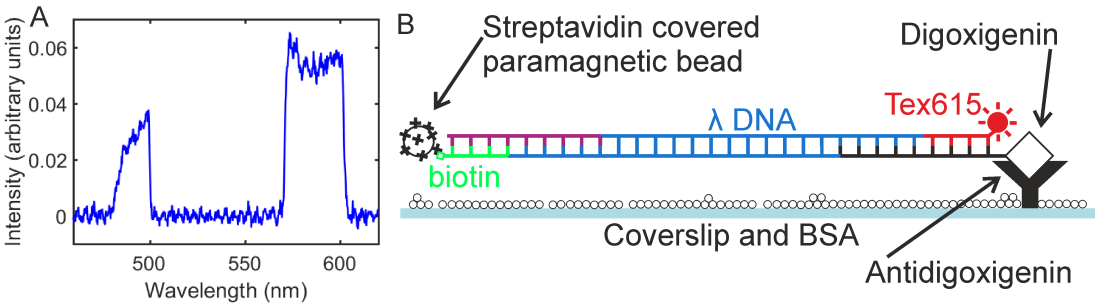

Figure 4.2: Methods: (A) Laser transmission spectrum used for two colour excitation. (B) Schematic diagram of the DNA construct used for the surface attachment assay.

which contains a dichroic mirror at 580 nm and bandpass filters 525/50 nm and 617/73 nm. The two colour channels were registered relative to each other with polystyrene beads which are visible in both channels. Images were acquired at video rate (40 ms per frame), typically for 1000 frames. Due to the low brightness of these dyes, images were acquired at full electron multiplying (EM) gain (300). For further details of the microscope design, see section 3.4.

The focus levels for fluorescence and brightfield are generally not coincident in microscopes with through-objective "standard" brightfield imaging and reflection "inverted" fluorescence imaging. To focus the sample in fluorescence without first imaging it, a sacrificial sample of fluorescently labelled DNA and latex beads was used to find the fluorescence focus, and then imaged in brightfield. The defocused image of the surface-immobilised beads was used to focus the other samples to the same level (see figure 4.1B).

4.2.2 DNA constructs

Lambda DNA is a 48,502 base pair (bp) long, double-stranded DNA molecule with two 12 bp single stranded 'sticky ends' which are complementary to each other. In solution, recircularisation is negligible since the molecules' long length means the ends are rarely close enough together to interact. The ends of the molecule were functionalised sequentially by the addition of one longer oligomer (12 bp of complementarity to lambda DNA, and then sequence complementary to the shorter oligomer) and one shorter oligomer. The oligomers were designed using NUPACK by Adam Wollman to avoid secondary structure. Oligomers 1 and 2 shown in table 4.1 enable surface attachment, and oligomers 3 and 4 allow conjugation of a paramagnetic bead to the DNA construct.

To produce the full DNA construct seen in figure 4.2B, oligomers 1 and 3

Oligomer number	Sequence
1	$5'-\mathrm{AGGTCGCCGCCCGTTCGTTGAGTCA}-\mathrm{digoxigenin}-3'$
2	$5'-\mathrm{Tex615}-\mathrm{GACTCAACGAAC}-3'$
3	$5'-\mathrm{GGGCGGCGACCTGGACAGCAAGTTGGACAA}-3'$
4	$5'-\mathrm{biotin}-\mathrm{TTGTCCAACTTGCTGTCC}-3'$

Table 4.1: Oligonucleotides used to extend and functionalise the DNA. 1 and 2 are used for surface attachment, 3 and 4 allow attachment of a paramagnetic bead.

were phosphorylated using 1 unit of T4 polynucleotide kinase in 1x T4 ligase buffer for 75 minutes at 37°C. Due to complementarity of oligomers 1 and 3 the two ends were annealed sequentially in excess over the lambda DNA substrate. Phosphorylated oligomer 1 and oligomer 2 at 20 nM concentration were annealed and ligated to 1.7 nM lambda DNA in 1x T4 DNA ligase buffer by heating to 65°C for 5 minutes, and cooling to room temperature in the heat block. 1 unit of T4 DNA ligase was added and incubated for 2 hours at room temperature before removal of excess DNA and enzyme with a QIAEX II gel extraction kit (QIAGEN) using the protocol "Desalting and Concentrating DNA Solutions". The bead attachment end was annealed, ligated and excess DNA and enzyme removed using approximately 1.2 nM (assumption of 100 % efficiency in all previous steps) of the first construct with 20 nM phosphorylated oligomer 3 and oligomer 4 using the same protocol described above. The final yield of 40 µl of 0.9 nM DNA construct was stored at 3-5°C. Due to the low concentration of DNA microscopy rather than gel electrophoresis was used to verify production of the DNA construct.

Unphosphorylated oligomers 1 and 2 were hybridised in 1x TBE buffer by heating to 90°C for 5 minutes, then cooled to room temperature over 20 minutes to produce 10mM DNA for experiments using only the Tex615 labelled "short end".

4.2.3 Sample preparation methods

Two techniques for sample preparation were developed. The first was a simple assay to produce surface immobilised DNA strands in a short preparation time. These samples were made by premixing the dye and DNA and then pipetting 5 µl onto a slide and placing the coverslip on top, such that DNA was confined to a narrow plane readily found during imaging; the second assay utilised tunnel slides (section 2.2.2) to produce tethered strands of DNA. For both experiments plasma cleaned coverslips were used (section 2.2.1), and

200 µl pipette tips were used for all steps involving lambda DNA to avoid shearing.

All experiments, and all dilutions of reagents were performed in 1x phosphate buffered saline (PBS; 10mM phosphate buffer, 2.7mM potassium chloride, 0.137mM sodium chloride, pH 7.4, Sigma Aldrich). YOYO-1 Iodide (1mM solution in Dimethyl sulfoxide (DMSO), Life Technologies Ltd.) and SYTO-13 (5mM solution in DMSO, Life Technologies, Ltd.), were used in both assays, whilst lambda DNA (500µg/ml, New England Biolabs) was used in the immobilised assay and bovine serum albumin (BSA; 0.1%, 1mg/ml, Sigma Aldrich), anti-digoxigenin (1µg/ml, Roche diagnostics), and the DNA construct were used only in the tethered DNA assay.

For immobilised DNA damage is not a problem because the DNA remains localised even if broken, but single strand breaks cause a problem for torsion or winding experiments because they allow DNA to rotate freely. Free rotation prevents supercoil formation and single strand breaks must be minimised with oxygen scavenging and repaired with ligase in the final combined magnetic tweezers and fluorescence assay if supercoils are to be studied.

For the immobilisation assay, 5µl of the diluted dye to be used and 5µl of the (unmodified) lambda DNA are premixed. A 5 µl droplet is placed on a microscope slide, and a standard 22 mm square, plasma cleaned coverslip is gently placed on top of this droplet, causing it to spread out under the full area to a thickness of about 10 µm. The fluorophore labelled DNA is constrained to a plane which is readily found during imaging. The samples were fully sealed with nail varnish before imaging to prevent evaporation and accidental shearing when adjusting the microscope stage.

The tethered DNA assay is to be developed for the combined fluorescence and magnetic tweezers study. Samples were prepared in tunnel slides (see section 2.2.2) using sequential wash steps. The first reagent added is 5 µl anti-digoxigenin, this is allowed 5 minutes to incubate inverted in a humidity chamber. This produces a surface covering of 5.5% (assuming a protein density of 1.37 g/cm^3 [191], spherical proteins and equal coverage of both tunnel surfaces); the rest of the surface is blocked with a 100 µl wash of BSA. The DNA construct (diluted to 0.1 nM) is then added to the tunnel, and again incubated for 5 minutes inverted in a humidity chamber. The tunnel is washed through with 100 µl PBS to remove any unbound DNA, and then 5 µl of the dye dilution (1:99 of the stock) is added and again incubated inverted for 5 minutes in a humidity chamber. A further wash of 100 µl PBS is performed to remove any excess dye. In some experiments a further wash of beads was performed and incubated for 5 minutes inverted in a humidity chamber before a final 100 µl

wash to aid focus. The type of beads used is detailed where applicable. This assay produces extended DNA constructs due to the capillary action drawing the liquid through the tunnel.

To conjugate a 1 µm paramagnetic bead (100 µg/ml, Dynabeads® MyOne™ Streptavidin C1, Life Technologies Ltd.) to the DNA construct 5 µl of 0.1 nM DNA construct was incubated with 5 µl of paramagnetic beads and 10 µl of the dye dilution for 30 minutes with manual agitation every 2.5 minutes to avoid sedimentation of the paramagnetic beads.

4.2.4 Super-resolution reconstruction- ADEMS code

Adam Wollman used three software packages including one custom written in Matlab (ADEMS code) to localise the dyes from the immobilised YOYO-1 and SYTO-13 labelled DNA. QuickPALM [192] runs as a plugin to ImageJ and finds bright spots in the image via the Högbom "CLEAN" method [193]. The rainSTORM software [194] segments the image via a $3\times$ 3 top hat filter, then finds the maxima above a user-defined threshold, the maxima are found by iterative Gaussian fitting, and candidates not meeting the Thompson precision [44] are rejected. ADEMs code is described in section (2.2.10) but has similar functionality to rainSTORM with added stages; it also uses a thresholded top hat function, but then also uses a dilation followed by an erosion on the found areas. The intensity centroid is found by iterative 2D Gaussian masking, and then 2D Gaussian fitting centred on the centroid position.

4.3 Results

4.3.1 Imaging the "short end"

To verify that single red molecules could be observed the "short end" was attached to the coverslip with anti-digoxigenin. The Tex615 fluorophore was seen to be at the surface by viewing the sample before and after washing with PBS; the depth of field and number of fluorophores was greatly reduced after washing (see figure 4.3). A kernel density plot, which is similar to a histogram but represents each point with a distribution with width proportional to the error instead of a box was used. From the peak of the kernel density plot the intensities of the found objects in the image show peaks at integer multiples of $\sim$17000 counts. This implies that at 40 ms exposure time the intensity of a single Tex615 fluorophore is 17000 counts, and the multiples are likely to be multiple fluorophores in the same diffraction limited volume. The intensity

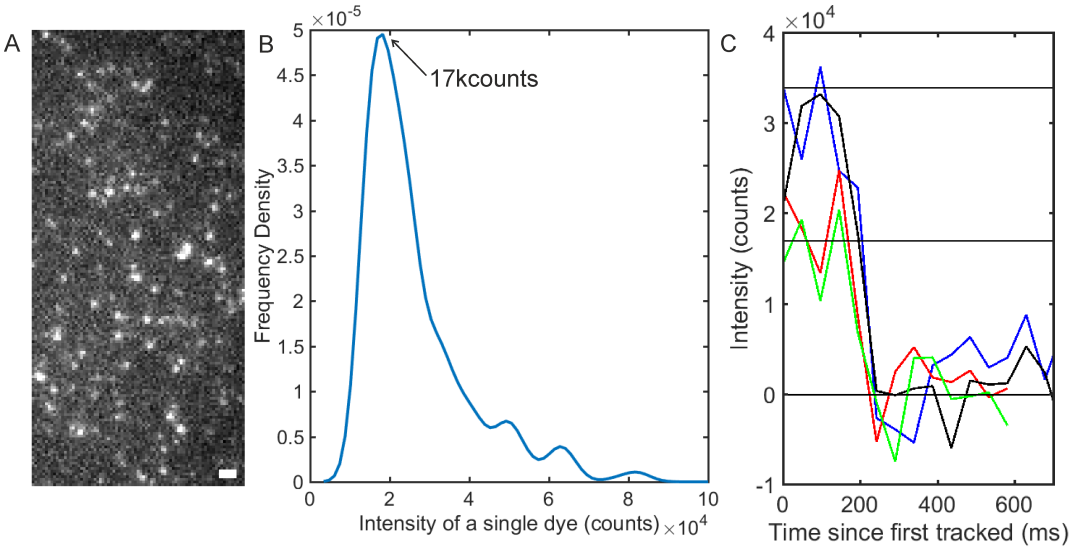

Figure 4.3: Analysis of Tex615. (A) Fluorescence image of surface immobilised "short end" (B) kernel density plot of the intensities of the identified bright spots in the fluorescence image, showing peaks at roughly 17000, 34000 and higher integer multiples of 17000 counts; (C) four example bleach traces from molecules in the fluorescence image, with horizontal lines at the peak values identified from the intensity analysis; stepwise bleaching behaviour can be seen. Scale bar 1 µm.

traces over time of the tracked particles support this; selected tracks are shown in figure 4.3 right with stepwise photobleaching seen.

It was determined by labelling DNA with both red and green fluorescent dyes that the green dye "bleeds through" into the red channel. Latex beads (Invitrogen FluoSpheres carboxylate modified microspheres, Thermo Fisher Scientific Inc.) were visible in both channels and were used as fiducial markers to register the red and green channel images against each other. Subtraction of the green image from the red image allowed red fluorophores to be observed.

4.3.2 Choosing the DNA dyes

PicoGreen, SYTO-13 and YOYO-1 were used to label DNA and imaged to look for tethered DNA particles, to decide which dyes were suitable under our illumination scheme for photoblinking experiments.

Samples were prepared in flow cells as follows: sequential incubations of the following were performed for 5 minutes each in a humidity chamber with 100 µl PBS wash steps between; anti-digoxigenin, DNA construct, fluorescent dye (YOYO-1 - 50 µM; SYTO-13 - 50 µM; PicoGreen - 0.2 units), 0.3 µm latex beads.

Images of extended DNA strands labelled with each of the three dyes,

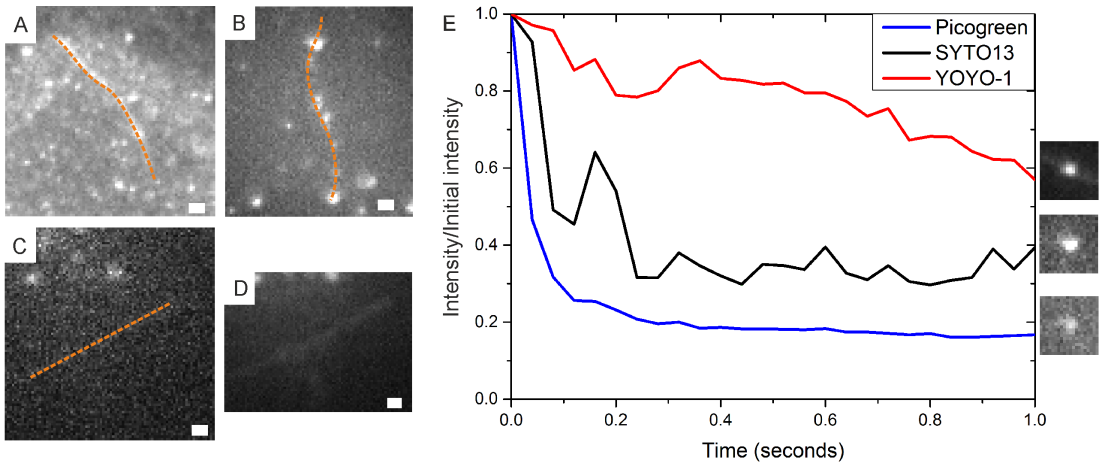

Figure 4.4: Extended and globular DNA constructs. (A-D) show fields of view with extended DNA constructs (orange dashed lines) labelled with (A) YOYO-1, 5 frame average (B) SYTO-13, 5 frame average (C) PicoGreen, 5 frame average, ND2. (D) is a 100 frame average of the same region as (C) for clarity. (E) The normalised decay of intensity for the three dye labelled globular DNA shown at the right of the figure. Scale bars 1 µm.

acquired at 40 ms exposure time are shown in figure 4.4, the largest, roundest objects are 1 µm latex (polystyrene) beads used to locate the surface. For PicoGreen the images were acquired using a neutral density filter as the intensity decayed quickly under these illumination conditions, in agreement with previously reported results [173] (see figure 4.4E). SYTO-13 and YOYO-1 were seen to exhibit photoblinking behaviour and so were chosen for further experiments.

4.3.3 Controls for fluorescence imaging experiments

To ensure the observed fluorescence was due to the increase in intensity of the dyes' fluorescence emission on binding to DNA rather than clumps of dye, a control was performed. The control sample was produced using sequential incubations of five minutes in a humidity chamber of anti-digoxigenin, 50 µM SYTO-13 and beads with 100 µl washes in between. This is the same assay as for examining the dyes, but without the DNA present. On average, one bright object was seen per two fields of view. The bright objects had an intensity consistent with the beads used for surface localisation in the full assay and were determined to also be beads. This suggests the fluorescence seen in the full assay is due to dye binding to DNA. The lower number of beads seen per field of view is likely due to a higher flow velocity on the last wash step.

Dye- bead interactions were minimised by using sequential washes of the dye and beads with excess dye washed out before beads were added.

Condition	Number of fields of view	Number of beads ($\pm$ s.d.)
Streptavidin coated paramagnetic beads, no blocking	10	24 ± 8
Anti-digoxigenin coated beads, no blocking	5	1.3 ± 0.7
Streptavidin coated paramagnetic beads, 10mg/ml PEG blocking	6	18 ± 4
Anti-digoxigenin coated beads, 0.1mg/ml PEG blocking	7	0.9 ± 0.8
Streptavidin coated paramagnetic beads, 1mg/ml BSA blocking	7	0.2 ± 0.2
Anti-digoxigenin coated beads, 1mg/ml BSA blocking	7	1.8 ± 0.6

Table 4.2: Number of beads seen per field of view under different blocking conditions. PEG blocking of anti-digoxigenin beads shown at 100$\times$ lower concentration than streptavidin as no beads were observed at 10 mg/ml.

4.3.4 Surface passivation

For the experiments described in this chapter the DNA is tethered to the surface by an anti-digoxigenin -digoxigenin linkage, however, for combined fluorescence and force transduction experiments it is crucial that the DNA is extended in a single focal plane, and the magnetic bead must be able to rotate freely without colliding with the coverslip surface. To extend the DNA in one focal plane, a 4 µm diameter anti-digoxigenin coated polystyrene bead will be used as a platform to raise the DNA attachment point above the surface (see figure 4.1A lower). Both 1 µm diameter streptavidin coated paramagnetic beads and 4 µm anti-digoxigenin coated beads adhere non-specifically to the coverslip so a blocking agent must be used that will block only the paramagnetic bead.

Relative to a control wash with PBS, a five minute incubation of one tunnel volume of 10 mg/ml (large excess over a monolayer) Polyethylene glycol N-succinimidyl propionate (PEG; 5,000 propionic acid; Sigma-Aldrich Co. LLC) was found to block $\sim 25\%$ of the magnetic streptavidin beads from the surface, but at this dilution the anti-digoxigenin beads were almost completely blocked from the surface compared to a control with no blocking agent. To control against human error a lower concentration of 0.01 mg/ml PEG was used and anti-digoxigenin coated bead binding was recovered. A tunnel volume of 1 mg/ml bovine serum albumin (BSA) incubated for 5 minutes was found to prevent paramagnetic bead attachment to the surface and seems to prevent the anti-digoxigenin coated beads from being washed out in the later

wash step, compared to the control. A summary of the number of beads observed per field of view is shown in table 4.2. Where images were taken on the 902h Watec CCD camera with a 768x576 pixel array the numbers have been adjusted for a 512x512 pixel area at 100x magnification such that all fields of view are the same size.

BSA at 1 mg/ml was chosen as the blocking agent to be used.

4.3.5 Prebleach regime of immobilised DNA

On initial illumination the sample is densely labelled, with strands of DNA seen as continuous filaments due to the fluorescing dyes being separated by less than the optical diffraction limit. A mixed population of DNA strands that have nonspecifically attached to the surface at one end and combed out under flow and globular clusters are seen.

In four fields of view of YOYO-1 labelled DNA, five strands of stretched lambda DNA were observed with a mean length 17.6±2.5 µm (± s.d.), this is consistent with the expected length of B-form lambda DNA of 16.5 µm with a base pair separation of 0.34 nm, given that we expect some stretching of the DNA under flow.

Globular DNA are approximately twice as common as stretched DNA strands in this assay. An average of five molecules from the same fields of view as the stretched DNA gives an average observed diameter of 1700±320 nm (± s.d.). The wormlike chain model (see for example [112]) predicts an end-to-end length (R^2) given by:

$$\langle R^2 \rangle = 2Pl\left[1 - \frac{P}{l}\left(1 - e^{-\frac{l}{P}}\right)\right] \tag{4.1}$$

where l is the length of lambda DNA and P is the persistence length, $\sim$50nm for B form DNA [167][180]. In this case the second term in equation 4.1 is negligible and the diameter of the DNA is expected to be of the order of 1.3 µm. When we consider the effect of the optical diffraction limit, this result is consistent with observation.

4.3.6 Postbleach regime of immobilised DNA

After the initial illumination many of the dyes have photobleached. In this regime photoblinking behaviour can be seen with separations between dyes that are greater than the optical diffraction limit. This means the dyes can be localised with super-resolution techniques for well separated fluorophores.

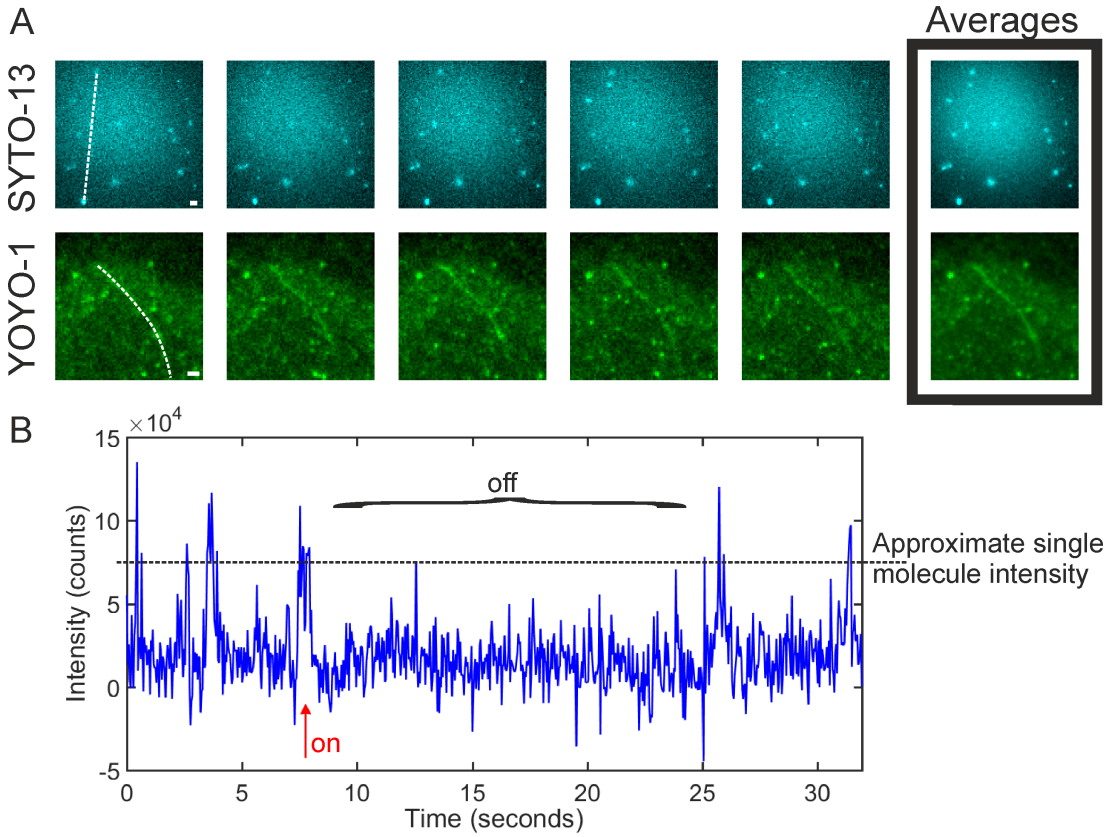

Figure 4.5: Single-molecule photoblinking events. (A) Upper: 5 consecutive frames of a lambda DNA strand labelled with SYTO-13 and their average. Lower: 5 consecutive frames of a lambda DNA strand labelled with YOYO-1 and their average. In the average frames (boxed) strands of lambda DNA can be seen vertically with SYTO-13, and diagonally from top left to bottom right in YOYO-1, these are indicated with white dashed lines in the first frame. (B) Example background corrected intensity vs time trace for a YOYO-1 molecule on lambda DNA. An "on" and "off" period are indicated. Scales bars 1 µm.

The photoblinking of SYTO-13 and YOYO-1 can be seen in the five consecutive frames and intensity vs. time trace shown in figure 4.5, but the overall structure of the lambda DNA can be seen in the average frames shown. In these two sets of images the volume and concentration of each dye added was the same.

Adam Wollman ran the spot data obtained in the post bleach regime through three localisation software packages, and generated simulations to compare them. Table 4.3 shows the percentage of candidates found from a simulation similar to the experimental data, showing that rainSTORM finds more simulated spots than the other methods. However, ADEMS code achieves higher localisation precision for the case of the lower intensity SYTO-13 data, by its method of looking at the standard deviation of the centroid position, compared to rainSTORM's use of the Thompson equation (QuickPALM does not output localisation precision information). Adam

Data	rainSTORM	ADEMS code	QuickPALM
Percentage of simulated spots found	78.3	67.3	48.5
Localisation precision (nearest nm) YOYO-1	35	40	N/A
Localisation precision (nearest nm) SYTO-13	67	62	N/A

Table 4.3: Summary of results of tracking simulated and immobile SYTO-13 and YOYO-1 data with three software packages.

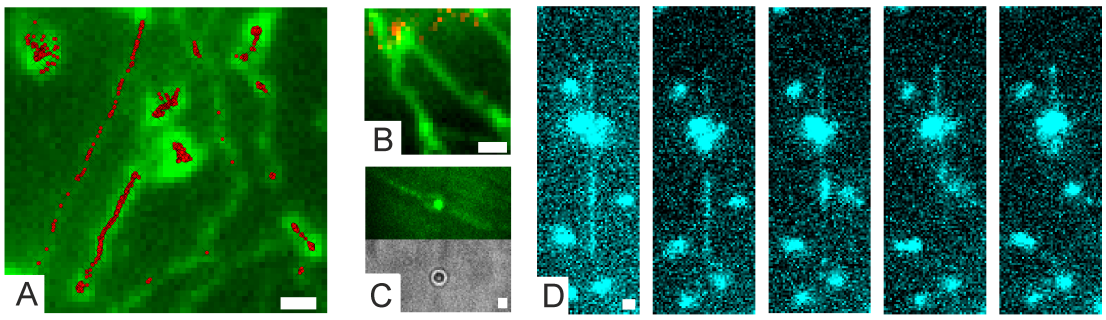

Figure 4.6: Imaging of immobilised and tethered DNA. Green images are of YOYO-1, and blue images are of SYTO-13 labelled DNA. (A) Found positions from blinking data produced from the simple assay, overlaid on the frame average. (B) Image showing two colour channel imaging capability with YOYO-1 labelled DNA (green) and Tex-615 (red) end label. (C) Fluorescence and brightfield images of a paramagnetic bead conjugated to two strands of DNA. (D) Sequential frames at 40 ms exposure showing snapping of a SYTO-13 labelled strand of lambda DNA. All scale bars 1 µm.

Wollman found that in the simple assay, using ADEMS software, YOYO-1 is localised to 40 nm precision, and SYTO-13 to 62 nm. Figure 4.6A shows an example of lambda DNA strands labelled with YOYO-1 and the dye localisations obtained.

4.3.7 Microscopy verification of short end conjugation to DNA tether

Via the dual colour imaging capability the Tex-615 (red) labelled end of the YOYO-1 labelled DNA construct is shown in figure 4.6B. The red fluorophore indicates the point of attachment, and since the contour length of the DNA is far greater than that of the short end (the image of which would be diffraction limited) it is verified that the short end is successfully conjugated to the lambda DNA.

4.3.8 Paramagnetic bead attachment to DNA tether

A paramagnetic bead has been conjugated to the end of the DNA construct; a paramagnetic bead attached to two strands of DNA is shown in figure 4.6C. Further work is required to achieve a one-to-one DNA tether to bead ratio, varying the relative concentrations of DNA tethers and beads. This verifies that the conjugation of the bead end to the lambda DNA has been successful.

4.3.9 Snapping of DNA tethers

Since this assay uses no oxygen scavenging system, free radical damage to the DNA is seen as double strand breaks, or snapping events (see figure 4.6D), similar to those witnessed by other researchers [195]. The tethers can be seen to snap after a few seconds of laser exposure, showing that they are not immobilised. However, often the tether does not snap into two globular DNA, with one usually remaining partly extended, implying that there is more than one non-specific attachment point. This should be reduced in the final assay, using the large anti-digoxigenin bead the DNA should not come into contact with the surface.

4.3.10 Modelling work

The experimental analysis was complemented by simulations performed by Zhaokun Zhou in Mathematica (Wolfram Research). The photoblinking behaviour seen could be explained either by binding of new dye or photoblinking of the already bound dye. To ensure the effects observed were not due to transient binding the rate constants for each possibility must be examined.

For binding, the rate of change of the number of dye-DNA complexes is proportional to two terms; one for the formation of new dye-DNA complexes which depends on the binding rate, number of free dye molecules and the number of available dye binding sites. The other terms depends on the rate of dissociation of the dye-DNA complex and the number of them. This equation can be solved at steady state using values for the binding constants reported in the literature to find that 0.0024-0.24 dyes bind to each lambda DNA molecule per second. This suggests that binding is not responsible for the observed photoblinking effect.

Zhaokun developed simulations of dye molecules on a line as 2D Gaussian intensity profiles with PSF from the experimental data. Each fluorophore underwent a number of on/off emission cycles before photobleaching, with

the parameters for this taken from tracking the experimental data. The simulations were pixelated to the size of the camera pixel array, and Gaussian white noise was added. In these simulations if the dye off time was modelled as an exponential decay the system showed almost no photoactivity beyond the first one hundred frames, incompatible with our observation. An off-rate whose distribution was not fitted by a simple single exponential function, but instead had an extended tail (created by adding a top hat function to the exponential) gives simulations compatible with our findings and previous work [111].

4.4 Conclusions and Future Directions

An assay using photoblinking to reconstruct images of fluorescently labelled DNA at sub-optical resolution has been developed for intercalating and minor groove binding dyes. The production of tethers with two end modifications for the combined fluorescence and magnetic tweezers assay has been shown via fluorescence microscopy, and simultaneous imaging of the Tex615 and YOYO-1 dyes suggests the future possibility of experiments looking at red-labelled DNA machinery acting on green-labelled DNA. The DNA tethers have some non-specific surface interactions which will need to be minimised, but this should be aided by the introduction of the anti-digoxigenin beads as a platform to raise the DNA attachment point above the coverslip.

The development of the magneto-optical tweezers is underway by Zhaokun Zhou [153], and the DNA construct design has been modified by Jack Shepherd and Zhaokun Zhou to produce three different length tethers from pET28a and pBluescript. The new tethers utilise modified bases to provide multiple attachment points to the DNA and thus torsionally constrain the surface and bead linkages. Jack Shepherd has developed an oxygen-scavenging system to extend the lifetime of the DNA tethers.

Chapter 5

Single-molecule Fluorescence Tracking of Chemokines

5.1 Introduction

Chemokines are small signalling molecules; in the lymph node they form gradients which direct lymphocyte migration, and their diffusion coefficients are known to be important for intercellular communication [196]. They are likely implicated in many immune disorders; for example, elevated levels of CXCL13 are known to be present in HIV patients [197]. This chapter describes experiments and analysis leading to single-molecule imaging and tracking of the fluorescently labelled chemokines CCL19 and CXCL13 at sub-millisecond timescales in collagen, and of CXCL13 at $\sim$2 millisecond timescales in lymph node tissue sections. To the author's knowledge the values of the diffusion coefficients of CXCL13 and CCL19 are determined in tissue-like environments for the first time. A comparative evaluation of fluorescence correlation spectroscopy, fluorescence recovery after photobleaching, and single-molecule tracking as used to measure diffusion coefficients is made on BSA labelled with AF647.

5.1.1 Chemokines

Chemokines are small ($\sim$10 kDa) cytokines that diffuse in lymph nodes to form concentration gradients that direct lymphocyte movement [198][199][200][201]. Chemokines are named according to their structural motifs: all chemokines have four cysteine residues which are connected by two disulphide bonds and the families of chemokines are denoted according to the motif containing the first two cysteine residues. The two most common families are the CC chemokines, which have two adjacent cysteine residues,

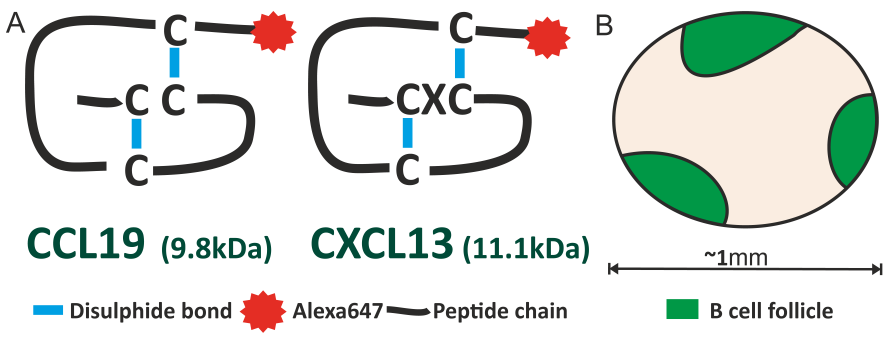

Figure 5.1: Schematic diagram of chemokine structure and B cell follicle location in the lymph node. (A) Schematic diagram of the structure of AF647 labelled CCL19 and CXCL13. (B) Schematic diagram showing the approximate locations of B cell follicles in a wild type murine lymph node, close to the subcapsular sinus (outer layer) of the lymph node.

and the CXC family, which have a different residue between the cysteines (see figure 5.1A). Chemokines bind with high specificity to the G-protein coupled receptors (GPCRs; 7 transmembrane helix proteins) on their target cell to initiate a cellular response [202].

B-Cell activation, regulated by chemokines, is a key part of the humoral immune response, triggering the secretion of antibodies. In particular, the chemokines studied in this project, CCL19 and CXCL13, are implicated in the humoral immune response thus: B cells search for antigen within B cell follicles of the lymph node (see figure 5.1B), directed by gradients of CXCL13; upon binding antigen the B cells move to the T cell regions under the influence of CCL19 to interact with T cells [203][204]. The dynamics of chemokine populations are governed by many factors: they are secreted in the highly heterogeneous extracellular matrix, and undergo interactions with both their cognate GPCRs and elements of the extracellular matrix, and can be scavenged by their receptors or enzymatically degraded [202][205]. The properties of the different chemokines are highly heterogeneous [204], and some chemokines can multimerise [206][207].

Most chemokines can bind to glycosaminoglycan (GAG) proteins, carbohydrate structures that are attached to proteins in the extracellular matrix or on cell surfaces [204]. Heparan sulfate is a polysaccharide that attaches to the extracellular matrix or cell surface proteins, and it is an example of a GAG protein, so it will bind to chemokines [208]. In this work, we use heparan sulfate to immobilise chemokines on the coverslip surface.

5.1.2 Fluorescently labelled chemokines

A range of chemokines labelled with Alexa Fluor 647 (AF647) are commercially available. As has previously been discussed in the introduction (section 1.4.3), Alexa Fluor dyes are created by sulfonating existing dyes to achieve higher photostability.

AF647 has excitation maximum 650 nm, and emission maximum 665 nm, similar to Cy5, but with higher photostability. AF647 is also insensitive to pH in the range 4-10; the excitation maximum and minimum of AF647 can vary by a few nanometres in solutions of different viscosity [209], but this will not stop detection due to the window of wavelengths collected in this work. AF647 is used extensively in STORM as it can be induced to photoblink under particular buffer conditions [56][210] but in PBS [211] lower levels of photoblinking are observed.

The high photostability combined with low photoblinking of AF647 in PBS buffer make it ideal for high-speed single particle tracking, as the molecules can be tracked through multiple frames without photoblinking behaviour which would cause missed localisations. Additionally, the long excitation wavelength is lower energy and therefore less phototoxic for cellular studies than most available dyes which fluoresce in the visible range, as well as allowing imaging deeper into the sample due to lower Rayleigh scattering.

5.1.3 Simulation of chemokines in the lymph node

In most previous work [212] the diffusion coefficients of the chemokines, D, have been approximated using the Stokes- Einstein relation for a spherical particle in water at low Reynolds number due to a lack of experimental measurements in tissue-like environments (the diffusion coefficient of CCL19 has been measured in buffer by nuclear magnetic resonance to be 142 $\mu m^2 s^{-1}$ [213]). The equation for the diffusion coefficient estimated by this method is [214]:

$$D = \frac{k_B T}{6\pi\eta r} \tag{5.1}$$

where k_B is the Boltzmann constant, T is the temperature, r is the radius and η is the dynamic viscosity of the fluid. This is likely to overestimate the diffusion coefficient in the highly complex environment of the lymph node where viscosity will not be constant. Additionally the viscosity is likely to be higher than water and the chemokines will not be spherical.

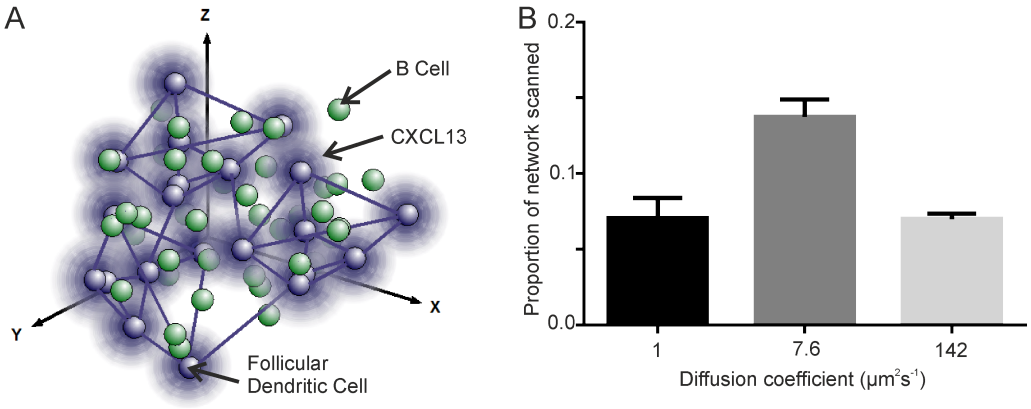

Figure 5.2: Agent-based simulation of CXCL13 in a lymph node B cell follicle. This work was performed by Jason Cosgrove. (A) Schematic diagram of the model network, showing follicular dendritic cells (purple) secreting CXCL13 and B Cells (green) migrating. (B) The effect of different CXCL13 diffusion coefficients on the proportion of the network scanned in 24 hours, average and standard deviation from 300 runs.

Jason Cosgrove produced agent-based models [215] of CXCL13 distribution in the B cell follicles of lymph nodes (Jason Cosgrove, unpublished). In this model the follicular dendritic cells are modelled as the nodes of a network, and the nodes secrete the chemokine CXCL13 which attracts B cells (see figure 5.2A). The model uses experimentally determined values for known parameters to enable assessment of which unmeasured parameters control the distribution of CXCL13 and have biological relevance for the dynamics of B cell scanning and perturbation.

The proportion of the network scanned by a B cell in one day was seen to change by a factor of two when varying the diffusion coefficient of CXCL13 from the theoretical maximum given by the assumption of a chemokine as a Stokes sphere in water down to the the value expected for a Stokes sphere in collagen (a key component of the extracellular matrix in which chemokines are present) (see figure 5.2B). This suggests that the diffusion coefficient of the chemokines is important in determining the rate at which B cells scan the network, and therefore in determining the efficacy of the immune response.

5.1.4 Methods to measure diffusion coefficients

Classically, the ensemble biophysics methods of fluorescence correlation spectroscopy (FCS) and fluorescence recovery after photobleaching (FRAP) are used to measure diffusion coefficients.

In FCS [216][217] a laser beam is focussed to a tight confocal volume of a few femtolitres in a sample [218], see figure 5.3A. The exact volume of the

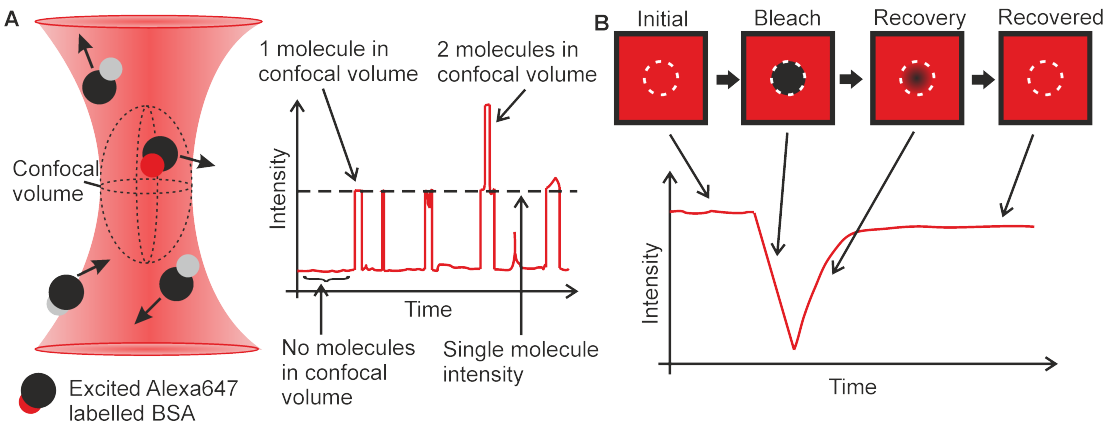

Figure 5.3: Schematic diagrams of FCS and FRAP microscopy. (A) Cartoon of FCS microscopy and intensity vs. time trace. The short dashed line indicates the confocal volume, in which fluorescent particles are detected. (B) Cartoon of FRAP microscopy and intensity vs. time trace showing the stages in an experiment.

confocal spot depends on the wavelength of light used as the the system is diffraction limited (so shorter wavelengths produce smaller volumes), and on the numerical aperture of the objective lens. Two-colour FCS with coaligned beams is technically challenging, requiring precise alignment and masks to limit the spot width. Nevertheless, two colour FCS has been demonstrated [219] and allows investigation of colocalisation of two differently labelled proteins by cross-correlating the intensity versus time traces in the two colour channels, but it can be achieved more elegantly using two- or three-photon microscopy [220]. Unfortunately, two-photon microscopy requires an extremely high laser intensity to achieve a high probability of two photons arriving at the same time which can be damaging to the sample.

In FCS the molecule under study is diluted to a concentration such that on average only one or two molecules are in the confocal volume at any time; this is a trade off between the best signals at one particle per volume and acquisition speed. The fluorescence intensity in the volume is recorded over time, with spikes occurring when a molecule is in the volume. The diffusion coefficient in two dimensions can be measured using the autocorrelation of the intensity versus time trace to find the time taken to transit the volume. FCS ideally uses fluorophores with high photostability, as a bleach event of a singly labelled molecule during transit of the confocal volume appears as a fast transit time and gives an artificially high value for the diffusion coefficient.

The theoretical basis for the technique is as follows [221]; we consider fluctuations in intensity, $\delta I(t)$, as the intensity value at that time, $I(t)$, minus the average intensity over the trace:

$$\delta I(t) = I(t) - \frac{1}{T}\int_0^T I(t)\,\mathrm{d}t$$

If fluctuations are only due to the number of molecules in the confocal volume then:

$$\delta I(t) = \kappa \int_V F_{ex}(\vec{r})S(\vec{r})\delta\big(\sigma q C(\vec{r},t)\big)\,\mathrm{d}V$$

Where κ is the detection efficiency and $\delta\big(\sigma q C(\vec{r},t)\big)$ describes fluctuations in the properties of each fluorescent particle, including the molecular absorption cross section, σ, the fluorescence quantum yield, q, and local concentration $C(\vec{r},t)$. The other two terms, $F_{ex}(\vec{r})$, and $S(\vec{r})$ are the excitation beam profile and the optical transfer function of the objective and pinhole system respectively. These two terms can be combined into the spatial distribution of light, $W(\vec{r})$:

$$W(\vec{r}) = \frac{F_{ex}(\vec{r})}{F_0}S(\vec{r})$$

Where F_0 is the maximum intensity of the excitation beam, and $W(\vec{r})$ can be modelled appropriately for the laser beam profile used. We can also define the photon counts per molecule per second, η_0 as:

$$\eta_0 = F_0\kappa\sigma q$$

such that the intensity fluctuation can be rewritten:

$$\delta I(t) = \int_V W(\vec{r})\delta\big(\eta_0 C(\vec{r},t)\big)\,\mathrm{d}V$$

The normalised autocorrelation, $G(\tau)$, where τ is the lag time is given by [222]:

$$G(\tau) = \frac{\langle \delta I(\tau)\delta I(t+\tau)\rangle}{\langle F(t)\rangle^2}$$

The form of the autocorrelation is greatly simplified if either the change in molecular properties, $\delta\eta$, or the change in concentration, $\delta C(\vec{r},t)$ is zero. Similarly, when the characteristic times of the two processes are vastly different, as here, between the lateral diffusion time (time to cross the confocal volume) and molecular fluctuations; the two solutions can be found separately and multiplied together. If we further define the lateral diffusion time, τ_D as:

$$\tau_D = \frac{r_0^2}{4D} \tag{5.2}$$

and the effective confocal volume, V_{eff}, as:

$$V_{eff} = \frac{\left(\int W(\vec{r})\,\mathrm{d}V\right)^2}{\int W^2(\vec{r})\,\mathrm{d}V}$$

Where r_0 is the radius of the confocal volume and D is the 3D diffusion coefficient we find that for fluctuations caused only by concentration fluctuations that the autocorrelation function is given by:

$$G_D(\tau) = \frac{1}{V_{eff}\langle C\rangle}\frac{1}{\left(1+\frac{\tau}{\tau_D}\right)}\frac{1}{\sqrt{1+\left(\frac{r_0}{z_0}\right)^2\frac{\tau}{\tau_D}}} \tag{5.3}$$

Where z_0 is the radius of the confocal volume in the axial direction and $\langle C\rangle$ is the average concentration. There are several terms that can contribute to the molecular properties of the fluorophore, but we shall consider only the largest of these, the contribution caused by photoblinking when a fluorescent molecule is shelved in a dark triplet state. The normalised autocorrelation term for this is:

$$G_T(\tau) = 1 + \frac{T\exp\left\{-\frac{\tau}{\tau_t}\right\}}{1-T} \tag{5.4}$$

where T is the triplet fraction and τ_t is the characteristic decay time of the triplet state. The total autocorrelation function for fluctuations, $G_\delta(\tau)$ is given by:

$$G_\delta(\tau) = G_D(\tau)G_T(\tau) \tag{5.5}$$

Over long time averages where there is no significant bleaching, this tends to:

$$G(\tau) = 1 + G_\delta(\tau) \tag{5.6}$$

Commercially available FCS is an excellent technique for determining the relative diffusion coefficients of populations containing high proportions of a single molecule weight. However, FCS that is able to discern populations with multiple molecular weight components is a highly specialised technique [223][224][225]. FCS measurements require the determination of the confocal volume by use of a protein with a known diffusion coefficient. Any error in this measurement will propagate into values calculated using the found confocal volume. As such, FCS is sometimes described as being only a relative measure of a diffusion coefficient, rather than an absolute [123].

Fluorescence recovery after photobleaching (FRAP) [64] [65] is a technique that can be applied in both ensemble and single-molecule modalities. In FRAP an area of the sample is bleached and the recovery of fluorescent molecules to the bleached area over time is monitored, with the time taken to reach a constant intensity after bleaching being related to the diffusion coefficient (see figure 5.3B). Other quantities which can be evaluated from a FRAP experiment include the relative proportions of the mobile and immobile populations, and in the single-molecule regime stoichiometries and area densities can be evaluated.

Fitting of the FRAP recovery curve is a non-trivial process, with various fitting equations accounting for bleaching with a uniform beam of circular [226][227] or square [228] areas, Gaussian profiles of the bleaching beam [229][230], and more besides. These equations can be extended to multiple diffusing species and photobleaching of the sample due to finite volumes. However, these different fit equations can produce large variation in the measure of a diffusion coefficient for a particular data set, and have sometimes been suggested as the source of inconsistency between FRAP and FCS measures of diffusion coefficients performed on the same area [231].

As ensemble methods, FCS and FRAP can be used to estimate diffusion coefficients at high chemokine concentrations which may not reflect the concentrations found in the native environment. However, the native environment of the lymph node is highly heterogeneous spatially and these methods give no spatial information. Single molecule tracking is ideally placed to probe heterogeneity on these scales.

In single particle tracking [46][125][127][232][233], molecules are identified in each frame of an image acquisition and the localisations from the different frames are linked temporally according to criteria set by the researcher, commonly based on proximity. When proximity criteria are used for linking trajectories, high frame rates must be employed to track fast moving particles. This technique allows investigation of the behaviour of a molecule on a step by step basis, rather than just measuring average behaviour. For example, tracks that are diffusive, static and contain both behaviours can be observed [120] to detect spatial variations in mobility on length scales that cannot be accessed by ensemble methods. If transient interactions occur it can be determined if they are randomly spatially distributed or localised to a specific site.

Whilst particles tracked for a long ($\sim$ seconds) time will tend to show a consensus value of the diffusion coefficient, over the short timescales accessible with probes that rapidly diffuse out of the focal volume diffusion coefficients are measured from short tracks and are known as “microdiffusion

coefficients". Microdiffusion coefficients form a gamma distribution which has a shape parameter determined by the number of steps used [127][234][235]. Commonly the first four steps of a track are used to determine the microdiffusion coefficient [236][237] by only counting tracks of at least four steps, and shortening longer tracks to include only four steps.

Whilst single-molecule tracking is well placed to study small scale heterogeneity, the tissue environment is highly complex and it experimentally practical to make initial measurements in a simplified system.

5.1.5 Collagen as an extracellular matrix mimic

Collagen is the main structural component of the extracellular matrix [238] and can be used as a simplified model system [239][240]. Collagen fibrils form elongated strands that combine in threes to form tropocollagen (∼280 nm long [241][242]) which has a well-defined triple-helical structure [243].

Collagen is an example of a hydrogel, and the mesh size is determined by the concentration of the gelling medium and the temperature at which it is gelled [244]. The mesh size determines the mobility of the molecules diffusing within the hydrogel [245], and there are many models for the mechanism of reduced diffusivity in the hydrogel, such as reducing the free volume for the diffusing molecule, increased hydrodynamic drag from the hydrogel network, and physical obstruction by the network [246]. Of these, obstruction is thought to be the dominant mechanism in collagen [247].

The correct formation of collagen into a noncentrosymmetric triple helical structure *in vitro* can be checked using second harmonic imaging microscopy (SHIM) [248][249] (also known as second harmonic generation; SHG). In SHIM light that has been frequency doubled by the optical properties of the material is collected: for example from infrared radiation at 900 nm to the visible at 450 nm. Second harmonic generation can occur when the second order non-linear susceptibility is non-zero. In general the total polarisation of a material, P, under high intensity incident light of frequency ω, $E(\omega)$, can be written [250][251]:

$$\vec{P} = \chi^{(1)}\vec{E}(\omega) + \chi^{(2)}\vec{E}(\omega)^2 + \chi^{(3)}\vec{E}(\omega)^3 + \dots \quad (5.7)$$

$$= \vec{P}^{(1)}(\omega) + \vec{P}^{(2)}(\omega) + \vec{P}^{(3)}(\omega) + \dots \quad (5.8)$$

Where χ are the susceptibilities. The main nonlinear effect comes from the second term, which can be expressed as:

$$\vec{P}_i^{(2)}(2\omega) = \chi_{ijk}^{(2)} \vec{E}_j(\omega)\vec{E}_k(\omega) \tag{5.9}$$

in the case where the two incident photons have the same energy, and this represents second harmonic generation. The second order non-linear susceptibility is zero in structures that have inversion symmetry, so they do not show second harmonic generation. Collagen is a strong upconverter of light by this effect and it can be used to produce diffraction limited images of the structure [252][253].

SHIM is a scattering process rather than a fluorescence process and so light is more readily detected in transmission than reflection, the process takes only femtoseconds and there are no losses in via non-radiative relaxation [33]. Similarly to two photon excitation, optical sectioning is achieved due to the low probability of a second order process occurring outside the laser focus.

Collagen is transparent in visible light and has a refractive index that is very similar to water [254] and so is difficult to visualise by conventional light microscopy. SHIM is the method of choice for visualising collagen structure and verifying its formation.

5.1.6 Statement of contributions

This work was performed in collaboration with Jason Cosgrove, who prepared the biological collagen and lymph node tissue samples. Microscopy was performed together, and I performed the analysis of microscopy data. Jason Cosgrove performed the agent-based modelling presented in the introduction. Adam Wollman performed the calculation of the intensities given by random particle overlap and provided the fluorescence data simulation code. Andrew Leech performed SEC-MALLS on the BSA-AF647 and analysed the results to determine the proportion of monomers to dimers.

5.2 Materials and Methods

All experiments are performed at room temperature (20 °C) unless otherwise stated.

5.2.1 Materials

The chemokines CCL19 and CXCL13 tagged with the far-red fluorescent tag Alexa Fluor 647 (AF647) (CAF-06 and CAF-12, Almac Group) were stored at 222 µg/ml in water. Type I collagen was extracted from rat tails [255].

Heparan sulfate (Sigma Aldrich Co Ltd.) was used at 50mg/ml in PBS. The test probe, bovine serum albumin (BSA) labelled with AF647 (Thermo Fisher Scientific Inc.), was used at 10 nM concentration in SMT and FCS, and at 100 nM concentration in FRAP. 0.1 g Ficoll 400 (Sigma-Aldrich Co Ltd.) was added to 1 ml PBS to give a 10% Ficoll solution (called 10% Ficoll 400).

5.2.2 Collagen matrix

Samples for fluorescence microscopy were prepared in tunnel slides (as described in section 2.2.2) by Jason Cosgrove. Fluorescently labelled chemokines were added to collagen (3.3 mg/ml - concentration chosen by Jason Cosgrove based on previous studies such as [244]) to achieve a final chemokine concentration of 111 ng/ml, and set to pH7 with NaOH. To aid correct formation of the collagen network, tunnel slides were cooled to 4°C before addition of collagen and fluorescently labelled chemokines and incubated at 15°C for 30 minutes. This was followed by a 30 minute incubation at 37°C; all incubation steps were performed in the dark to avoid photodamage to the fluorophores.

5.2.3 Heparan sulphate immobilisation

Plasma-cleaned coverslips were coated in heparan sulfate (50mg/ml, Sigma Aldrich Co Ltd.) in PBS for 30 minutes. The heparan sulfate was washed off with PBS, and the coverslips were air dried for 30 minutes at room temperature prior to tunnel slide assembly. After assembly, 10 nM fluorescently labelled chemokine solution in PBS was introduced to the tunnel slide and incubated inverted in the dark in a humidity chamber for 15 minutes at 20°C. Excess unbound chemokine was removed with a PBS wash before fluorescence imaging.

5.2.4 SHIM imaging

Second harmonic imaging was performed on a Zeiss LSM 780 Multi-Photon attached to a Zeiss invert microscope using a plan-apochromat 63x oil objective lens with numerical aperture 1.4. Laser excitation at 900 nm (Coherent Ultra Laser) was used for illumination and detected light was filtered with a 485 nm short pass filter to remove autofluorescence before collection on a non-descanned detector.

5.2.5 Lymph node tissue sections

Acquisition of mouse tissue and preparation of lymph node tissue sections as described in this section was performed by Jason Cosgrove and Anne Thuery.

Six to eight week old wild type mice (C57BL/6) were housed in the Biological Services Facility at the University of York. All experiments conformed to the ethical principles and guidelines approved by the University of York Institutional and Animal Care Use Committee. Popliteal lymph nodes were removed from the mice and excess fat or connective tissue was removed with forceps. Samples were transferred to optimal cutting temperature medium (OCT, Tissue-Tek, Sakura Finetek) and snap frozen on dry ice prior to sample sectioning using a cryostat. 10 µm thick sections were cut and collected onto poly-L-Lysine coated microscope slides (6 per slide), dried overnight in the dark, and then stored at -20°C.

Before use, the lymph node sections were incubated at room temperature for 30 minutes. Following this, sections were hydrated in PBS for 5 minutes and then air dried. To aid liquid retention during staining a wax ImmEdge pen (Vector Laboratories) was used to draw a circle around each lymph node section. To determine the location of B-cells in the tissue a FITC (Fluorescein derivative with excitation/emission maxima at 495/519 nm [256]) labelled antibody for B220 was used, which is a protein expressed on all murine B cells. This antibody can also be bound non-specifically by Fc receptors and so these receptors must be blocked before the antibody (eBioscience) is added. Blocking of the Fc receptors was performed by a 60 minute incubation in a blocking buffer of PBS 5% goat serum (Sigma-Aldrich Co. LLC) at room temperature. Following blocking the sections were incubated with the antibody (diluted 1:200 in blocking buffer) for 60 minutes at room temperature. Samples were washed for 5 minutes with PBS three times and then 1 µM of CXCL13-AF647 was added to the slides and incubated overnight at 4°C. Before use slides were washed in PBS for 30 seconds. A plasma cleaned coverslip was mounted on top and the slide was sealed with nail varnish and imaged.

5.2.6 The microscope and imaging parameters

Illumination is provided from a supercontinuum laser (Fianium SC-400-6, Fianium Ltd.), controlled with an acousto-optical tunable filter (AOTF). For this project two illumination settings were used: The first is for Alexa Fluor 647 imaging, and uses settings of 612.5 nm at 60%, 621.5 nm at 75%, and 625 nm at 60%, giving a spectral profile that is centred on 619 nm and an output power of 2.6 mW. For excitation of the B220 stain which exhibits green fluorescence,

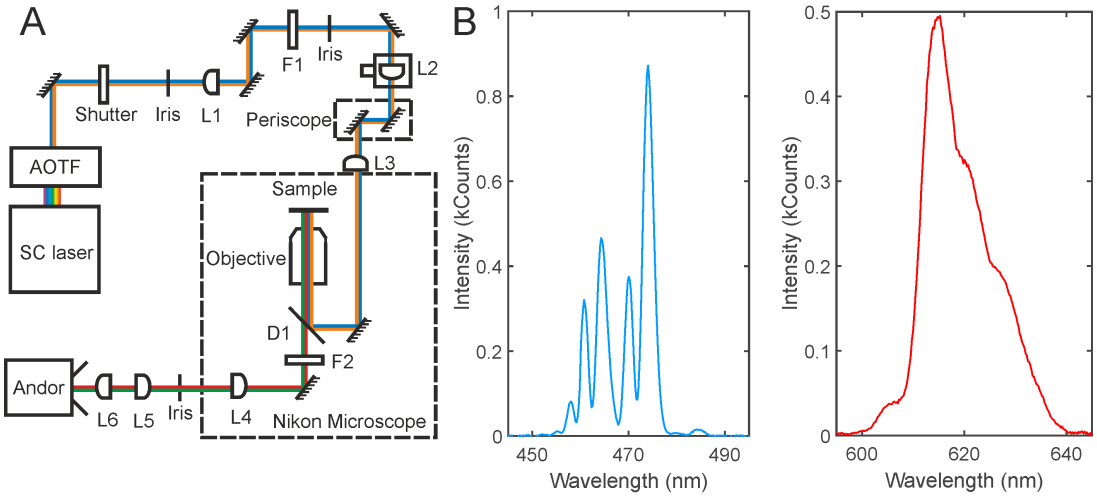

Figure 5.4: Optical design of the microscope used for sub-millisecond imaging. (A) Schematic diagram of the optical path, component labels are explained in the main text. (B) Laser transmission spectra for excitation centred on 470 nm (blue) and 619 nm (red).

465 nm and 475 nm both at 60% power are used which gives a measured power of 0.99 mW (measured at 470 nm). The spectral profile of these settings can be seen in figure 5.4B; the relative heights are a function of integration time (100 ms and 20 ms for blue and red respectively) which was chosen to avoid saturation of the detector.

The optical path (seen in figure 5.4A) contains a shutter which is opened by triggering image acquisition, and due to the method of operation of an AOTF, an iris is required to restrict the beam profile emanating from the AOTF to achieve an approximately Gaussian distribution. A bandpass filter (F1) is required to remove the "leak" wavelength from the AOTF at ~590 nm if it falls outside of the desired illumination bandwidth. The beam path contains steering mirrors for alignment purposes plus an additional two mirrors due to physical space limitations. Lenses L1 and L2 form a 1:1 beam expander, both with focal length 300 mm; lens L2 is placed the focal length of L3 (300 mm) from L3 and mounted on a translation mount, so that its configuration in the beam expander allows it to be translated to controllably move from epifluorescence illumination to TIRF microscopy, as previously described in chapter 3. Lens L3 forms a beam deexpander with the microscope objective lens and in this case replaces the lens in a commercially available inverted microscope body (Nikon Eclipse Ti-S) to physically allow the placement of L2 at the correct distance.

For stability during imaging and ease of brightfield image acquisition samples were mounted on a commercially available inverted microscope body with two objective lenses: a 100x NA 1.49 Nikon oil immersion lens and a 10x

NA 0.22 Zeiss air lens. Zeiss and Nikon use different standard tube lenses to give the rated magnification of an objective, and so the 10x Zeiss objective gives 12.1x magnification when mounted on a Nikon microscope. Imaging with the 100x objective lens produces an excitation field of 12 µm FWHM. For red fluorescence imaging a 633 nm dichroic mirror and 647 nm long pass emission filter were installed in a filter cube beneath the objective turret. For green fluorescence imaging a 515 nm dichroic mirror and a 535/15 nm bandpass emission filter were used. The power density at the sample in narrowfield excitation was 2300 $\mathrm{Wcm^{-2}}$ in the red and 875 $\mathrm{Wcm^{-2}}$ in the blue (for green fluorescence imaging).

Images are magnified by a factor of two by the lens pair L5/L6 with focal lengths 50 mm and 100 mm to give a final magnification of 200 times for the high magnification objective lens, corresponding to 120 $\mathrm{nmpixel^{-1}}$ when recorded on a back-illuminated emCCD camera (860 iXon+, Andor Technology Ltd). All images were acquired at an emCCD temperature of -80°C. 128x128 pixel images using the entire sensor were acquired at the minimum exposure time of 1.98 ms (2.04 ms cycle time). For sub-millisecond imaging the camera was sub-arrayed in one direction, with 128 x 29 pixel image strips allowing 0.59 ms exposure times (0.65 ms cycle time). All images were acquired for 1000 frames at the full EM and pre-amplifier gains of 300 and 4.6 respectively.

When imaging in lymph node tissue sections it was necessary to switch from the low magnification objective lens (992 nm/pixel) with blue illumination to a high magnification objective lens (120 nm/pixel) with red illumination without moving the sample. The target area of the tissue was identified by fluorescence of the B220 antibody under blue illumination with the low magnification objective and green fluorescence cube, using a 475/50 nm bandpass filter as F1. Illumination light, filter cube, and the objective lens were switched for high magnification red imaging, with immersion oil added to the sample avoiding movement of the microscope stage, and filter F1 was switched to 617/73 nm bandpass to allow through only the desired excitation.

5.2.7 FCS and FRAP microscopy

The diffusion coefficient of the well-characterised protein bovine serum albumin (BSA) labelled with AF647 was carried out by FRAP, FCS and single particle tracking in a solution of 10% Ficoll 400 to assess agreement between the three methods. FCS and FRAP experiments were performed on a Zeiss LSM 880 (Zeiss) using a GaAsP detector. 10 nM (FCS) and 100 nM (FRAP) solutions

of the fluorescently labelled proteins were placed in MatTek glass-bottom microwell dishes (1.5 coverglass, P35G-1.5-20-C, MatTek corporation) and imaged with 633 nm illumination, with a 63X 1.2 C-Apo water immersion objective, using distilled water as the immersion medium.

To obtain diffusion coefficients from FCS the confocal volume must be measured by using a protein of known diffusion coefficient, in effect the structural parameter must be experimentally determined. We used BSA-AF647 in PBS buffer for this purpose, which has a diffusion coefficient of 59 $\mu m^2 s^{-1}$ [257]. For the samples with diffusion coefficients to be measured three repeats of ten experiments were conducted. Traces were excluded when the intensity counts spiked over a threshold which indicated multimeric clumps (700 counts for BSA, 400 counts for chemokines), or where there was visible bleaching in the trace baseline, indicating proximity to the surface. In our system the bleaching can be considered negligible due to this manual filtering and as the total volume of liquid is very much larger than the confocal volume, such that bleaching does not decrease the overall average fluorescence signal. This allows use of the fitting function for the autocorrelation trace found by substituting equations 5.3, 5.4 and 5.5 into equation 5.6 to give:

$$G(\tau) = 1 + \left(1 + \frac{T \exp\left\{\left(-\frac{\tau}{\tau_t}\right)\right\}}{1-T}\right)\left(\frac{1}{V_{eff}\langle C\rangle}\frac{1}{\left(1+\frac{\tau}{\tau_D}\right)}\frac{1}{\sqrt{1+\left(\frac{1}{s}\right)^2\frac{\tau}{\tau_D}}}\right)$$

Where the structural parameter, s has been defined as:

$$s = \frac{z_0}{r_0} \tag{5.10}$$

The diffusion coefficient was found from the mean of the fitted values of τ_D using equation 5.2, where the axial radius of the confocal volume, r_0, was 0.322 µm.

For FRAP microscopy an area is bleached and the recovery of the fluorescence is monitored. The radius of the bleached area, ω, must be measured to allow calculation of the diffusion coefficient from the characteristic diffusion time, τ_2, using an equation of the same form as for FCS (equation 5.2):

$$D = \frac{\omega^2}{8\tau_2} \tag{5.11}$$

The size of the bleached area was measured with a sample of immobile CXCL13-AF647, non-specifically adhered to the glass coverslip. To measure

diffusion coefficients thirty intensity versus time recovery traces were acquired and fitted using Zeiss Zen Black software with a single exponential fit of the form:

$$I = I_0 - I_1 e^{-\frac{t}{\tau_2}} \tag{5.12}$$

Where the characteristic diffusion time, unbleached intensity, I_0, and the initial drop in intensity, I_1, were experimentally fitted. A single exponential fit was used (as opposed to a bi-exponential fit) as was expected to correspond to the physical situation.

5.2.8 Intensity analysis

The intensity of each tracked spot was given by ADEMS code, based on the total number of counts in the identified spot (see section 2.2.10). The intensity of a track was given by the intercept of a linear fit applied to the intensity versus time graph of the first three localisations in a track.

Photobleaching traces were found by tracking the last spot location of a track for ten frames after the end of a track and plotting the measured intensity in each frame.

5.2.9 Fitting diffusion coefficients in single molecule imaging

Data was collected in .tiff (Tag Image File Format) files and analysed in Matlab. Single molecules were tracked using ADEMS code written by Adam Wollman (see section 2.2.10). Code written by Adam Wollman was modified to calculate the microdiffusion coefficients from the data. Gamma distributions were fitted to the microdiffusion coefficient data using custom written Matlab code.

Microdiffusion coefficients are values of the diffusion coefficient calculated from tracks that are all truncated to the same number of steps, in this case, 4 [236][237]. Single molecule tracks of four steps (5 localisations) or more were used for the diffusion coefficient analysis, longer tracks were shortened to four steps to ensure high numbers of measurements were used at each timepoint [236][258]. The microdiffusion coefficient for each track was found by fitting a linear relation to the mean square displacement (MSD) versus time graph for the track, where the gradient is the microdiffusion coefficient. The microdiffusion coefficients were histogrammed with a bin width given by the localisation precision found when the same type of molecules were surface immobilised with heparan sulfate. The localisation precision was found from the offset of the linear fit to the MSD versus time graph for immobile samples.

To ensure a high probability of all histogram bins used for the fitting containing counts, microdiffusion coefficients up to 49.6 $\mu m^2 s^{-1}$ were used in collagen, and up to 19.6 $\mu m^2 s^{-1}$ were used in the lymph node tissue sections. The distributions generated by this method composed two fractions: a highly mobile population diffusing in the sample, and a population of molecules that had non-specifically adhered to the surface.

The microdiffusion coefficient distribution for a single diffusive species over a number of independent steps, N, is given by a gamma distribution [127][234][258]:

$$F(x; D, N) = \frac{(\frac{N}{D})^N x^{N-1} e^{-\frac{Nx}{D}}}{(N-1)!} \tag{5.13}$$

Where D is the true diffusion coefficient. In all fits the area of the fit was constrained to be the same as the area of the distribution. Using a fitting function comprised of two gamma distributions of the above form yielded initial estimates for the diffusion coefficients, but the fits were sensitive to the initial conditions. Simulations of the data were performed and fitted with the same constraints as the actual data to refine the fitting parameters. Iterations between fitting the data and the simulations were used to converge on a robust fitting procedure where the simulated diffusion coefficients were returned from a fit to the simulation data.

In the final 2 gamma fit used, the N value for immobile spots was constrained to be less than one and the diffusion coefficient of the immobile fraction was constrained to fall in the first bin of the histogram, implying the spots are not independent, as would be expected if they were truly immobile and apparent motion was due to the localisation precision of tracking. For highly mobile spots the N value was also reduced from its maximum value of four, as even for a moving particle the localisation error in each postion measurement means two consecutive steps are not independent. N was fixed at two, as there are two steps with no common localisations when the first four steps are used.

5.2.10 Simulations of fluorescence data

Image data was simulated and fitted in Matlab using simulation code written by Adam Wollman. In these simulations fluorescent spots were simulated at the same density as they were observed in a real data set. The spot and background intensities for a given simulated spot were taken randomly from an experimental data set, and placed at randomly chosen locations in the image

frame.

The code allowed one or two different diffusion coefficients to be modelled in a single distribution and allowed control of the relative proportion of the number of molecules with each diffusion coefficient. The distance travelled by a fluorescence spot between frames was randomly chosen from a Gaussian distribution centred on the spot location in the previous frame. The Gaussian distribution used for this had a width given by the mean square displacement of a particle diffusing with the simulated diffusion coefficient.

In real data fluorescent spot trajectories can cross each other, fluorophores can move out of the focal volume, and fluorophores can undergo photophysical changes such as photobleaching or photoblinking causing a permanent or temporary dark state. All of these effects cause fluorescent tracking data to become truncated, and this is accounted for in the code by randomly reassigning trajectories to a new location 10% of the time, which also accounts for new particles diffusing into the focal volume.

This information is classed as a "no noise" data set in this work as it does not account for readout noise introduced in the detector. "Noisy" simulations included zero mean Gaussian white noise with intensity proportional to the local intensity of the image. Both no noise and noisy data sets could be recorded from the same simulated data for comparison.

5.2.11 Bootstrapping

Standard errors on the fitted values of the diffusion coefficients found by FRAP, FCS and single molecule tracking for all samples were found by a method known as bootstrapping [259][260]. The measured value is found by fitting all of the experimental data. Then, the error on this value is found by taking randomly chosen subsets of 80% of the experimental data, and fitting each of these with the same fitting constraints (except that the total number of observations is reduced to 80% in the fitting of the diffusion coefficient distribution). This process is repeated ten times and the standard deviation from the ten repeats is taken as the standard error on the fitted parameter.

5.2.12 Segmentation of tissue images

Images acquired in tissue sections contain stroma, which is autofluorescent. Stroma consists of the components of a tissue that are not related to its function, such as blood vessels and connective tissue. The stromal region was segmented out by assuming the intensity was proportional to the density. The

intensity average of an image stack was top hat filtered using a disk of radius 4 pixels as the structuring element to even out the background. The image was then thresholded using Otsu's method and a binary mask was created. The binary mask was used on the original image to enhance it, and then it was eroded and dilated using a disk of radius 2 pixels as the structuring element to remove small holes in the identified stromal area.

5.2.13 SEC-MALLS on BSA-AF647

Size Exclusion Chromatography - Multi-Angle Laser Light Scattering (SEC-MALLS) was performed on BSA-AF647 by Andrew Leech in the Bioscience Technology Facility at the University of York. Unlabelled BSA is a common control sample for SEC-MALLS, and was used as the control sample in these experiments.

The experimental system comprised a Wyatt HELEOS-II multi-angle light scattering detector and a Wyatt rEX refractive index detector attached to a Shimadzu HPLC system (SPD-20A UV detector, LC20-AD isocratic pump system, DGU-20A3 degasser and SIL-20A autosampler). Superdex S200 columns (G.E. Healthcare) were run for 60 minutes at 0.5 ml/minute flow rate using PBS as the running buffer, and BSA-AF647 (100 µM stock, diluted to ∼2.5 mg/ml) was also in PBS. The column was equilibrated with BSA (filtered with 0.2 µm filter before use, and the system contains a second, 0.1 µm filter) and the 100 µL samples were run at room temperature (20 °C). Data were analysed using Astra V software using the Zimm fit method with degree 1; a value of 0.183 was used for protein refractive index increment (dn/dc). To calculate the amount of material in a peak the refractive index signal is integrated over the entire peak: errors in defining the peak will produce errors in the measured mass.

5.3 Results and Discussion

5.3.1 SHIM imaging of collagen

2D and 3D SHIM imaging performed on rat tail collagen (see figure 5.5) showed the presence of extended collagen fibres, with the 2D image similar to those shown in figure 1a of Chen *et al.* [253] (a self-assembled collagen gel). Our images show collagen fibres of diameter ∼750 nm (30 pixels), whereas Chen *et al.* show fibrils which can be seen to be around 1.5 µm (4 pixels) in diameter. Their data is acquired at a lower magnification and lower resolution,

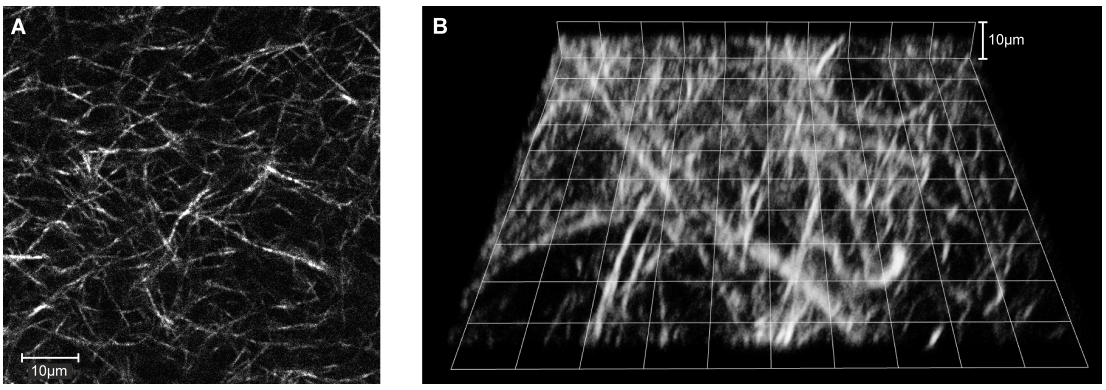

Figure 5.5: SHIM images of collagen network. (A) 2D and (B) 3D images of the structure of an 10 µm square grid. Scale bars 10 µm.

which may explain the discrepancy. Both values are consistent with previously reported collagen fibre diameters of 500 nm up to a few microns [261].

As a control a rat tail collagen sample prepared by adding collagen to a tunnel slide at room temperature and incubating at 37°C was also investigated with SHIM imaging. This sample showed regions of structure similar in appearance to figure 5.5, but these regions had limited spatial extent (~ 80 µm) and were surrounded by regions which gave no SHIM signal. This suggested collagen formed in the single step protocol did not contain extended regions of triple-helical collagen, and confirmed that the observed signal with the two stage collagen setting protocol was due to the presence of correctly formed collagen.

5.3.2 Fluorescence Correlation Spectroscopy of BSA-AF647

Initially BSA-AF647 in PBS buffer was used to calculate the structure parameter of the confocal volume, by assuming that the diffusion coefficient of this molecule is the same as the diffusion coefficient of BSA in water (59 $\mu m^2 s^{-1}$ [257]).

Intensity versus time traces were used (n=10), with none excluded for containing large multimers or for being close to the surface, three examples are shown in figure 5.6. The large fluctuations in autocorrelation at small lag times were excluded from the fitting procedure, which was applied between 1 µs and 3.35 s with a fixed diffusion coefficient of 59 $\mu m^2 s^{-1}$. This gave a mean structural parameter of 6.6.

To measure the diffusion coefficient of BSA-AF647 in 10% Ficoll 400, thirty intensity versus time traces were collected, three example autocorrelation functions and fits are shown in figure 5.7. Three traces were excluded due to the presence of an obvious large multimer/aggregate in the confocal volume.

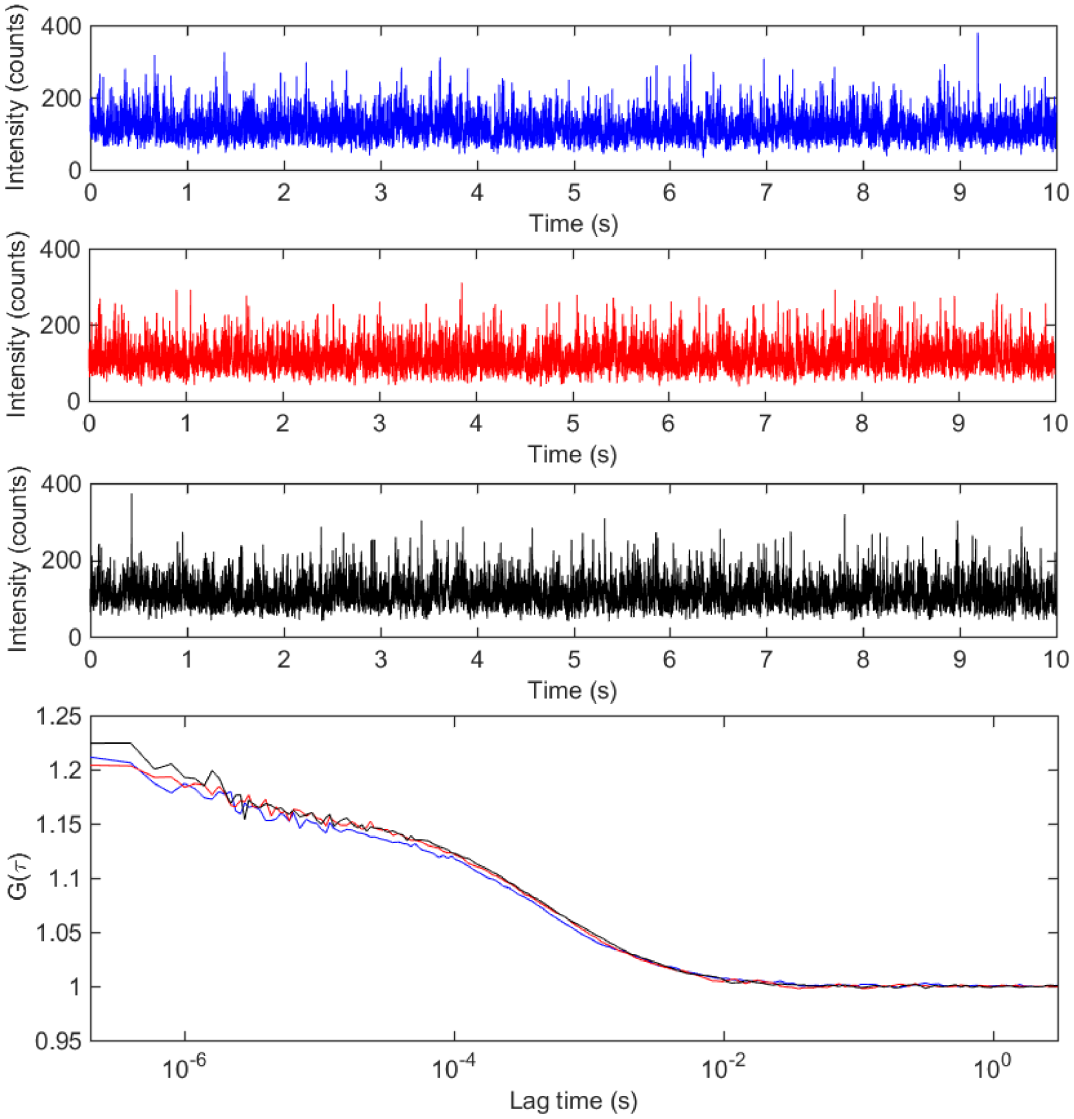

Figure 5.6: Results of FCS on BSA-AF647 in PBS buffer. Three example intensity versus time traces are shown, the three autocorrelation traces for these three traces are shown in the bottom panel in corresponding colours.

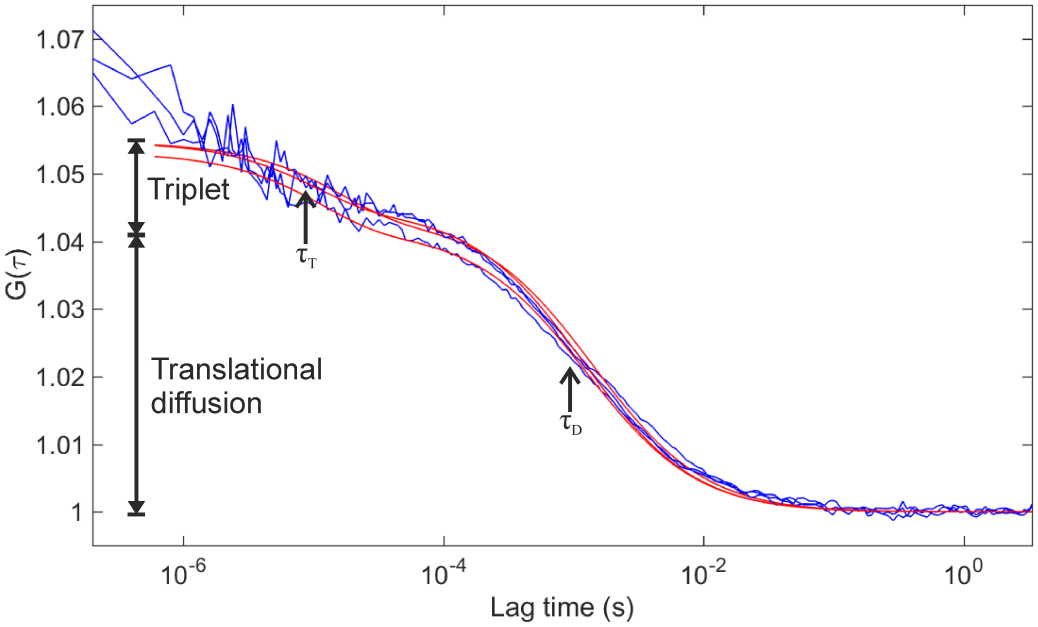

Figure 5.7: Three example FCS autocorrelation traces from BSA-AF647 in 10% Ficoll 400. The components due to the triplet and translational diffusion terms are shown. Data shown in blue, fits shown in red.

The diffusion coefficient was found to be $18.8 \pm 0.3\,\mu m^2 s^{-1}$ from the mean of the characteristic diffusion times. The error was found by bootstrapping the same values.

Several sources of error in this value must be considered: All diffusion coefficient values evaluated in non-scanning FCS setups are always calculated with respect to a reference value, and so can be argued to only ever be relative measures [262]. As the chemokines were labelled with AF647 it was necessary to use a reference with the same excitation wavelength, as the confocal volume is wavelength limited. Rhodamine 6G [263] is often used as a standard reference in FCS, but this has green fluorescence. We used BSA-AF647 in PBS buffer to measure the confocal volume, assuming that the label did not affect the diffusion coefficient. Whilst the AF647 tag has a small mass compared to BSA its attachment is likely to affect the hydrodynamic radius of the molecule. Without data from the manufacturer as to where the dye is attached it is hard to estimate how it will affect the shape and therefore diffusion coefficient of the molecule, but this is likely to be a small correction. Any error arising from a difference in diffusion coefficient between BSA and BSA-AF647 will be carried through to all other values of diffusion coefficients calculated using the structural parameter determined from this measurement.

Additionally, the error calculated by bootstrapping includes errors only

due to statistical fluctuation. The use of a theoretical value for the axial radius of the confocal volume is likely to be a slight underestimate as optics cannot be perfect; this would lead to an increase in value of the measured diffusion coefficient, however the theoretical value is unlikely to be more than a few nanometres too small.

Further, the model used for fitting the autocorrelation contained only translational diffusion and a triplet state for one molecular species. BSA is known to dimerise [264], but the proportion should be low and no clear evidence (a second step in the autocorrelation trace) of a dimeric population was seen in the FCS data. Due to this a single species fit was used to reduce the number of free parameters in the fit. Photobleaching of the molecule in the confocal volume is a likely cause of an overestimate of the diffusion coefficient, as it leads to a an apparent faster diffusion time.

5.3.3 Fluorescence Recovery After Photobleaching microscopy of BSA-AF647

FRAP, like FCS, requires knowledge of the size of the probed area to calculate diffusion coefficients from intensity versus time traces. In FRAP the size of the 2D area bleached must be found. A 4x4 pixel area (1 pixel = 1.1 µm) was defined on the FRAP software, but the laser bleaches a larger area than this. The size of the bleach area was found from the average of the first post-bleach image of ten repeats of FRAP on an immobile sample of CXCL13-A647 (see figure 5.8), by taking the average intensity profile horizontally through the four pixels that were defined as the bleach area. The average profile was fitted with a Gaussian distribution, assuming a round, rather than square bleaching area (see figure 5.8), so the profile has a flatter top than the fitting function. The halfwidth of the spot found from the FWHM is 4.9 ± 0.1 µm.

Using a circular rather than square bleaching region in the fitting model simplifies the function used to fit the exponential recovery. However, the fact that the TIRF spot is square rather than circular will mean that the value of the halfwidth used is an underestimate, and so D will be slightly underestimated.

Thirty FRAP traces for BSA-AF647 in 10% Ficoll 400 were collected and the characteristic decay constants fitted with a single exponential fit (see equation 5.12 and figure 5.9). The diffusion coefficient corresponding to the average of these values was found to be $7.1 \pm 0.3\,\mu m^2 s^{-1}$, with error found by bootstrapping. The example fit shown in figure 5.9 is illustrative of a single exponential fit to the experimental data, with the single exponential fit chosen for expected correspondence to the physical situation. For the first 3 seconds

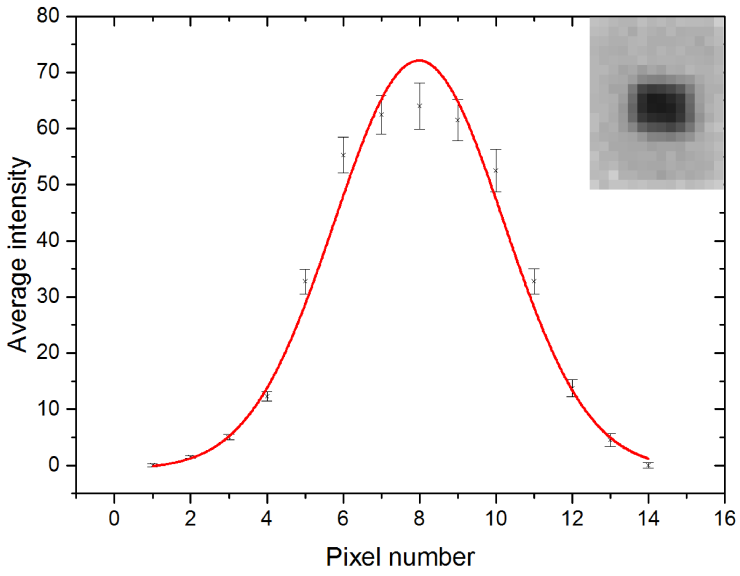

Figure 5.8: Finding the width of the FRAP spot. Fitted profile of the FRAP spot with average image of the bleach spot used for analysis shown inset. Error bars ± standard error (s.e.).

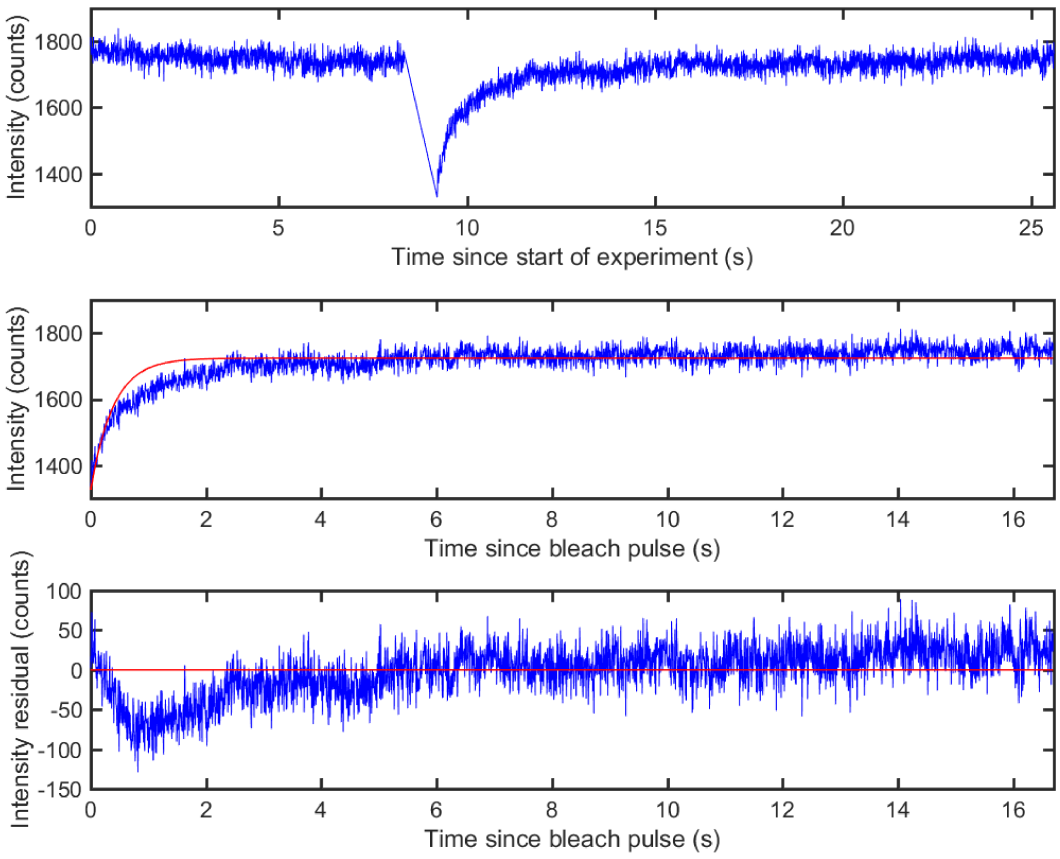

Figure 5.9: Example FRAP intensity recovery trace for BSA-AF647 in 10% Ficoll 400. The top trace shows the entire intensity versus time trace, the middle trace shows the post-bleach recovery with single exponential fit, and the lower trace shows the fitting residuals.

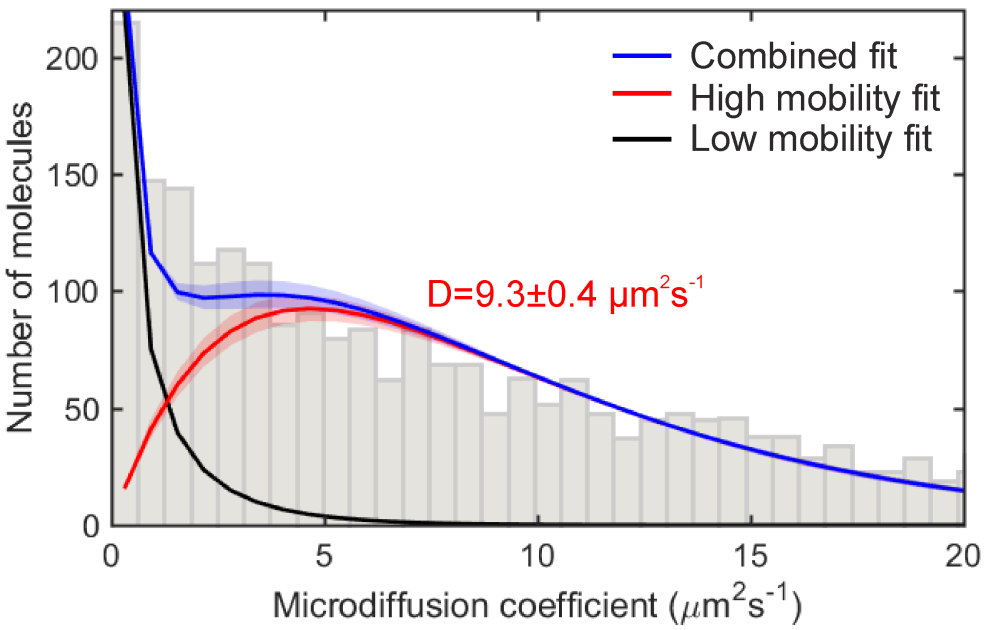

Figure 5.10: Two gamma distribution fit to the microdiffusion coefficient distribution of BSA-AF647 in 10% Ficoll 400. The distribution of microdiffusion coefficient values is shown in the histogram and the fitted gamma distributions for the high mobility (red), low mobility (black) and summation of the the two fits (blue) are shown. Errors on the fits generated by bootstrapping are shown as shaded areas of the same colour as the fit. The diffusion coefficient of the mobile fraction is shown.

the residual is strongly negative, suggesting the fit overestimates the rate of recovery, and that the characteristic decay time fitted is too short, and the diffusion coefficient is correspondingly too high. Bleaching of an immobile fraction can have this effect as the immobile fraction cannot recover, however, this would also cause an exponential decay in the pre-bleach region of the intensity versus time curve, which is not observed.

5.3.4 Single molecule tracking of BSA-AF647

A histogram of the microdiffusion coefficients with bin width of $0.62\,\mu m^2 s^{-1}$ was created. Histogram bins used in fitting must have a high chance of containing tracked molecules as zero values can cause convergence of a fit to a non-optimal solution; as such values between 0 and $49.6\,\mu m^2 s^{-1}$ were used for analysis, comprising 2608 tracked molecules. Part of this distribution can be seen in figure 5.10. The fitting procedure found highly mobile molecules had a diffusion coefficient of $9.3 \pm 0.4\,\mu m^2 s^{-1}$, and the overall combined fit had an R^2 of 0.927, close to 1, indicating a good fit. The fitted value of the shape parameter for the immobile fraction was 0.27 ± 0.03.

Method	Diffusion coefficient (μm^{2}s^{-1})
Theoretical (monomer)	12.3 ±0.1
Theoretical (15:2 monomer:dimer)	11.6 ±0.1
Theoretical (Faxén's law)	9.4 ±0.1
FCS	18.8 ± 0.3
Single Molecule	9.3±0.4
FRAP	7.1 ±0.3

Table 5.1: Diffusion coefficients (μm^{2}s^{-1}) of BSA-AF647 in 10% Ficoll 400 measured by different methods. There are systematic errors present which are not included in the quoted errors, and errors for the theoretical values allow for temperature fluctuations of $\pm 2^{\circ}C$.

There is a population of low mobility molecules present in this sample which has not previously been reported with BSA measurements. This could be caused by the addition of the negative charge (-3) of the AF647 molecule [265], as this would tend to be attracted to glass which often acquires a positive charge, especially after plasma cleaning, which we applied to all of our coverslips. As these molecules are putatively immobile their diffusion coefficient should be affected only by the localisation precision of the tracking code [266], which is around 40 nm under these imaging conditions.

5.3.5 Comparison of the 3 methods of calculating the diffusion coefficient of BSA-AF647 in 10% Ficoll 400

Three commonly used methods (FCS, FRAP and single molecule tracking) were used to evaluate the diffusion coefficient of BSA-AF647 in a solution of 10% Ficoll 400 and the results of each method have been analysed in detail above. Here, these three values are compared to each other and the theoretical expectation of the diffusion coefficient with an error estimate to account for fluctuations in room temperature of $\pm 2^{\circ}C$. The theoretical value of the diffusion coefficient was calculated using equation 5.1 assuming a dynamic viscosity of 0.005 Pas [267] for 10% Ficoll 400 and a Stokes radius of 3.48 nm [268][269] for monomeric BSA, and found to be 12.3 ±0.1 μm^{2}s^{-1}. These results are summarised in table 5.1.

FCS may give a larger value (18.8 ±0.3 μm^{2}s^{-1}) than SMT (9.3 ±0.4 μm^{2}s^{-1}) and FRAP (7.1 ±0.3 μm^{2}s^{-1}) for the diffusion coefficient if there is bleaching present in the sample during acquisition, as this leads to apparent faster transit times as the molecule goes dark before leaving the confocal volume. FRAP values may be lower than FCS and SMT due to the fitting procedure

underestimating the recovery times if other photophysical processes, such as photoblinking, are present. Whilst photoblinking may be present in all methods it would likely affect the FCS data the most, as it raises the diffusion coefficient for a track, whereas in SMT the trajectory is simply truncated. In FRAP it would contribute to the noise on the track, rather than explicitly raising the diffusion coefficient.

For this data, single molecule tracking gives a value of the diffusion coefficient closest to the theoretical expectation (see table 5.1), whilst FRAP underestimates the value by a factor of 1.7 and FCS overestimates it by a factor of 1.5. Whilst there are many reviews comparing the three techniques (see for example [270] or [271]) there are far fewer papers comparing data on the three techniques. FCS and FRAP have often been compared to each other; in live cells FCS has been shown to regularly produce values of the diffusion coefficient an order of magnitude higher than FRAP [272][273], however, Macháň *et al.* find that on supported lipid bilayers FRAP gives values of the diffusion coefficient 1.2-2.8 times higher than FCS, but in cells FCS gives values 1.4 times higher than FRAP [231]. Results where FCS gives lower values than FRAP are in the minority, and the difference in non-cellular systems is usually a factor around 1.5-3 [123], in agreement with our results. Guo *et al.* measure diffusion coefficients by SMT, FRAP and FCS, finding the value from FRAP to be the lowest and SMT to be the highest, with a difference of 2.3x between them, whilst Lagerholm *et al.* [274] compare STED-FCS (a slightly different method) and SMT in live cells and find STED-FCS values that are higher than SPT values, but that agree when all appropriate corrections are applied to SMT. In all of these works different microscopy methods, assumptions and fitting procedures are followed, but discrepancies are attributed to the inherent differences in techniques. The relative magnitudes of the values found are in agreement with the general trend that $D_{FRAP} < D_{SMT} < D_{FCS}$ and ranges of values 3x higher than found here have been successfully attributed to discrepancies in fitting, assumptions, and methods by other authors, differences that also occur in the methods applied here.

Both FCS and FRAP give a diffusion coefficient that is an average value for the distribution, and cannot, without far higher statistics and higher quality data account for more than one population of molecules, however we can incorporate these effects into our calculation of the theoretical value of the diffusion coefficient.

SEC-MALLS on BSA-AF647 (performed and analysed by Andew Leech) showed a mixed population of monomeric, dimeric and multimeric BSA in the stock solution used for the comparative experiments (see figure 5.11). Data

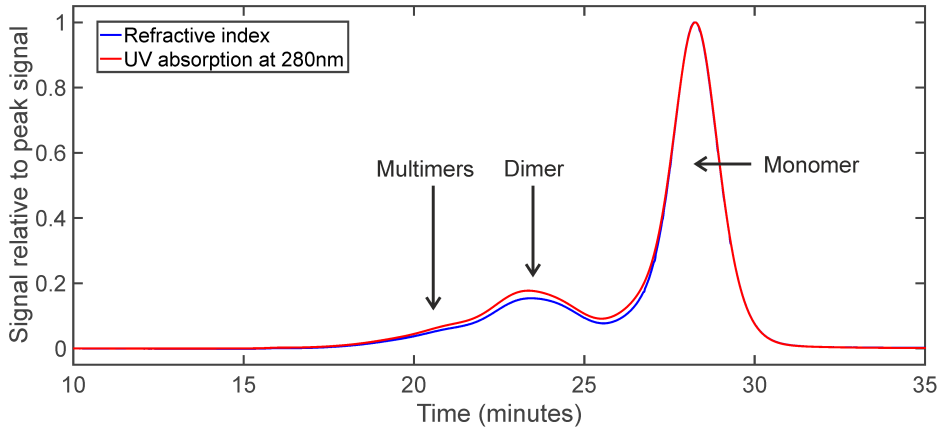

Figure 5.11: Results of SEC-MALLS measurements on BSA-AF647. Refractive index measurements shown in blue, UV absorption at 280 nm shown in red. Both traces have been scaled to the maximum height of the monomer peak, to allow visual comparison of the relative size of the monomer, dimer, multimer fractions.

Component	Elution time (minutes)	Mass (µg)	Percentage (%)
Monomer	26.02-31.00	189.7	74
Dimer	22.02-25.98	48.5	19
Multimers	18.00-21.98	16.5	6
Total mass	17.50-32.00	256.4	100

Table 5.2: Mass fractions found from refractive index measurements during SEC-MALLS of BSA-AF647.

from UV absorption at 280 nm and refractive index were collected, however, due to the the presence of the AF647 fluorescent tag, the complementary techniques of light scattering and quasi-elastic light scattering (QELS) could not be applied. Peak analysis on the refractive index data gives the mass of the monomer as 189.7 µg and the dimer as 48.5 µg (see table 5.2).

This gives a total recovered mass of 256.4 µg, in good agreement with the expected value of 250 µg. The mass fractions give a ratio of around 15:2 monomers to dimers from the refractive index data. The height of the dimer peak relative to the monomer is higher for the UV absorbance at 280 nm than it is for the refractive index, which would suggest a slightly higher dimeric and oligomeric population. This population ratio supports the decision to account for only a monomeric population in the FCS, FRAP and single molecule tracking fitting procedures. Large oligomers, likely caused by incomplete mixing of the BSA-AF647 powder into the buffer were occasionally ($\sim$1 in 100 fields of view) observed in FCS, FRAP and single molecule imaging as a large, often saturating, spike in intensity. When this occurred the fluorescence

images were checked to verify this cause, and the data was excluded from the analysis. Additionally, it was noted that the BSA-AF647 eluted from the column faster than unlabelled BSA, indicating an increased radius compared to the unlabelled BSA. This would usually be checked using light scattering, but the fluorescence of the label makes this impossible.

Assuming the sample to be a 15:2 mixture of monomer and dimer and further assuming that the maximum Stokes radius of the dimer will be 6.96 nm, double the single molecule radius for unlabelled BSA, we find an expected diffusion coefficient of the dimer of 6.2 $\mu m^2 s^{-1}$. Performing a weighted average of the diffusion coefficients according to the relative numbers of the monomer and dimer gives an average diffusion coefficient of 11.6 $\mu m^2 s^{-1}$.

We can further consider the effects of Faxén's law [275][276] which accounts for the increase in viscosity a particle moving close to a surface experiences due to a non-slip boundary. Whilst imaging was performed a few micrometres from the coverslip, the use of epifluorescence imaging meant coverslip immobilised particles were still visible. At a distance of 10 nm from the surface Faxén's law causes an increase in viscosity by a factor of 1.24 and would lower the diffusion coefficient for the monomer-dimer mixture to 9.4 $\mu m^2 s^{-1}$.

This value is in agreement with the measured value by single particle tracking whilst the value for FCS is a factor of two higher and the FRAP value is a factor of 1.3 lower. Whilst it is unlikely that the native dimer of BSA has a Stokes radius of double the monomer, the structure of the AF647 labelled dimer is not known and, being a larger particle, may have a larger Stokes radius. For example the dimer may take the form of two monomers bound side-to-side rather than a sphere of double the radius. The single molecule measurements contained an immobile fraction expected to be non-specifically bound to the coverglass, and whilst the excitation volume is far deeper than 10 nm, some molecules will be this close to the surface, and this will reduce the effective diffusion coefficient, likely not as far as this, but certainly below the theoretical value of solution far from boundaries.

Overall, single molecule tracking gives a diffusion coefficient of BSA-AF647 closest to the expected value. This is likely due to single molecule tracking being able to investigate heterogeneity at low concentration levels whilst FCS and FRAP can give only an average value.

5.3.6 FCS and FRAP of chemokines

If we model chemokines as uniform spheres of density 1.35 gcm^{-3} we expect diffusion coefficients of 146 $\mu m^2 s^{-1}$ for CXCL13 and 149 $\mu m^2 s^{-1}$ for CCL19 in

water. The value of 1.35 gcm^{-3} is based on measurements from hydrodynamic and adiabatic compressibility experiments, but other methods such as Voronoi modelling or looking at buried residues can give values of the same order of magnitude, but slightly lower or higher than this [277]. The value of 1.35 gcm^{-3} was chosen as there is no current consensus and this value is the most commonly used [278].

This led to investigating the possibility of measuring the diffusion coefficients of the chemokines with FCS and FRAP. Large numbers of molecules tended to localise on the coverglass surface and required us to focus deeper into the sample to avoid the signal from the immobile population. This may again be caused by the negative charge on the AF647 tag.

FCS on CCL19-AF647 and CXCL13-AF647 in 10% Ficoll 400 produced autocorrelation curves with similar initial amplitude to those observed with BSA-AF647, but showed high variation in the relative sizes and characteristic decay times of the triplet and translational diffusion populations (see figure 5.12A). This produced huge variation in the measured diffusion coefficient that did not produce a consensus value.

The presence of the large multimer of CXCL13 in the recovery of the FRAP trace in 10% Ficoll 400 (see figure 5.12B) is seen not to affect the fit to the data (shown in figure 5.12C) by the fact the trace is exactly replicated in the residual plot (see figure 5.12D), but this would cause a large effect if present around the bleach pulse and so results of using this method are not reliable.

FCS and FRAP are not suitable in the author's hands for measuring the diffusion coefficients of chemokines at these concentrations, as the results show large variation.

5.3.7 Single-molecule tracking of heparan sulfate immobilised chemokines

AF647 labelled chemokines were immobilised with heparan sulfate on the coverslip, imaged in fluorescence and tracked. Heparan sulfate was used to increase the fraction of immobilised chemokines to estimate the localisation precision from the immobile fraction. Linear relations were fitted to the mean square displacement versus time graph for each track, with the intercept taken as an estimate of the localisation precision. Immobile molecules must be used for this estimate as otherwise Brownian diffusion is assumed, which might be incorrect. Plotting heat maps of the localisation precision versus the microdiffusion coefficient allows estimation of the localisation precision of the immobile fraction when more than one component is present, by looking

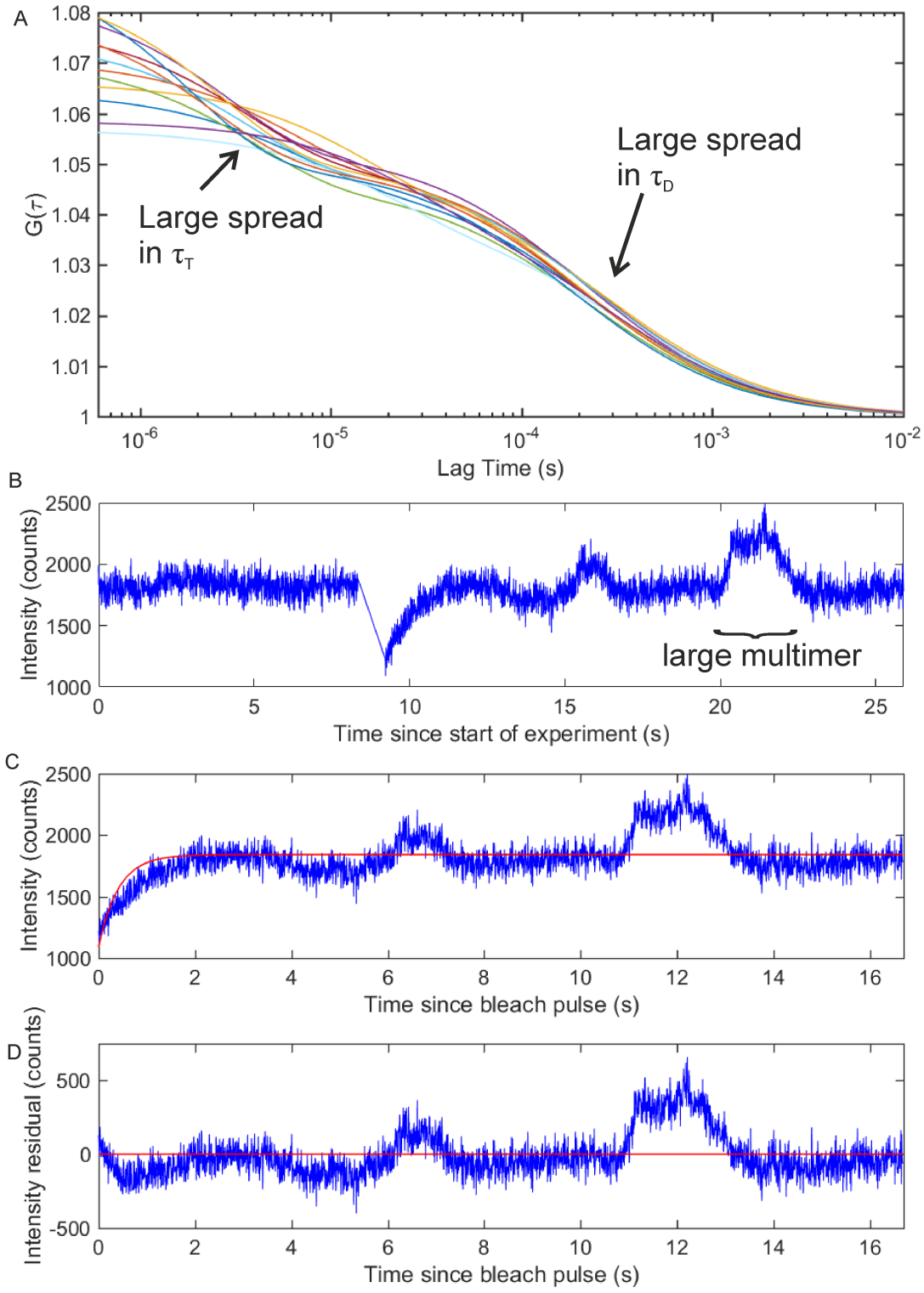

Figure 5.12: Example FCS and FRAP data of chemokine diffusion coefficients in 10% Ficoll 400. (A) 12 fits to the autocorrelation of FCS data for CCL19 showing large variation. (B) Example FRAP trace of CXCL3 showing a large multimer diffusing into the measurement region during recovery. (C) & (D) Fit to the FRAP trace and residuals.

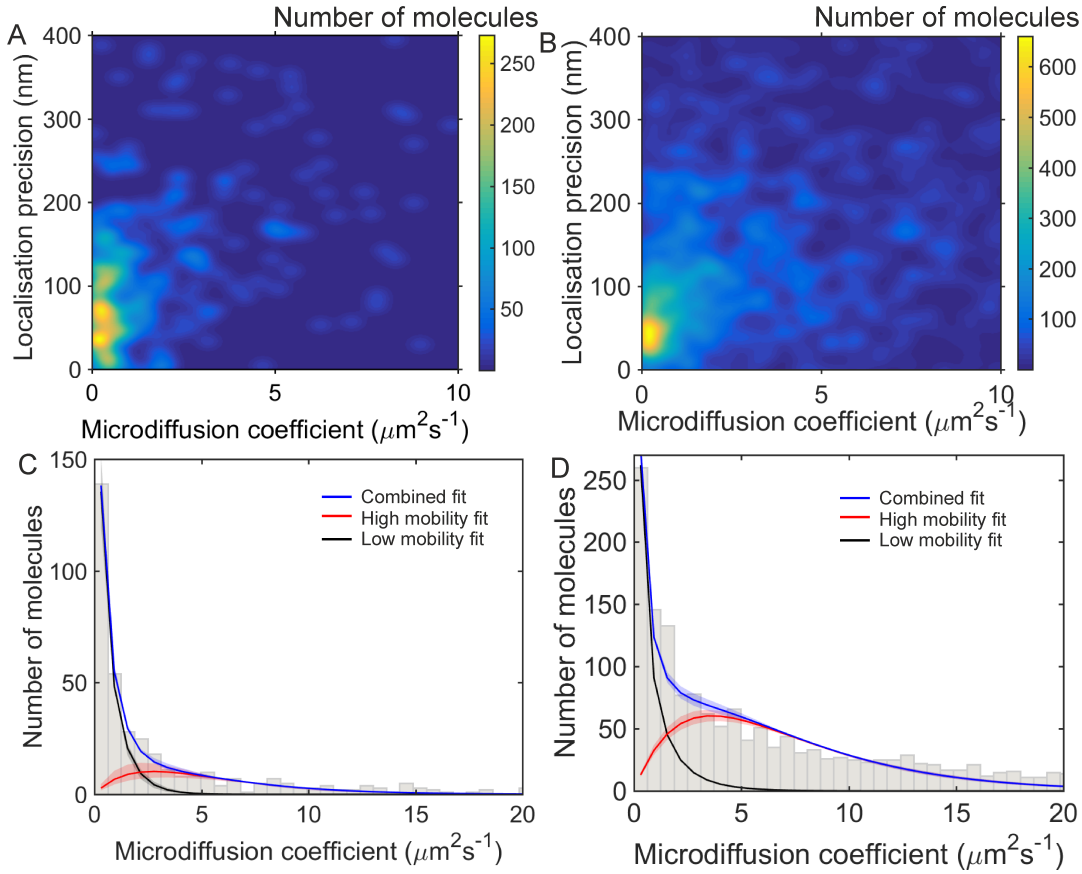

Figure 5.13: Localisation precision and microdiffusion coefficient distributions for heparan sulfate immobilised chemokines. (A) and (B) heat map of localisation precision versus microdiffusion coefficient for CCL19 and CXCL13, colour coded as to number of localisations (see scale bars to right of each figure). (C,D) Distribution of microdiffusion coefficients for heparan sulfate immobilised CCL19-AF647 and CXCL13-AF647.

for the peak in localisation precision closest to D=0 µm^{2}s^{-1}. This is preferable to simply defining a cut-off microdiffusion coefficient for the measurement as microdiffusion coefficients have a characteristic distribution.

Figure 5.13(A,B) show sections of these heat maps for CCL19 and CXCL13. CCL19-AF647 has peaks at around 35 and 70 nm, whilst CXCL13-AF647 shows a peak at around 40-45 nm. The localisation precision is converted to a diffusion coefficient and used as the bin width to histogram the microdiffusion coefficient data for fitting. Approximately four times more tracks were gathered for CXCL13 than for CCL19 which showed higher localisation precisions. The localisation precision was estimated to be 40 nm.

From this, the microdiffusion coefficient data was binned into histograms and fitted. The fits for the CCL19-AF647 (384 tracks) and CXCL13-AF647 (1648 tracks) data are shown in figure 5.13C,D, and are well fitted (CCL19 $R^2 = 0.992$, CXCL13 $R^2 = 0.954$) with a high fraction of immobile tracks, justifying the use

of this data to estimate the localisation precision.

5.3.8 Single-molecule tracking of chemokines in collagen

AF647 labelled chemokines were tracked in the collagen matrix (sample images are seen in figure 5.14C). As observed with the BSA, a fraction of the molecules are immobile on the surface. To allow imaging of chemokines diffusing in the collagen, rather than just at the edges, a widefield epifluorescence mode was used, instead of TIRF which has a limited axial depth of a few hundred nanometres. Consequently, when focussed in the sample the surface immobilised molecules were still seen. Multiple image acquisitions were performed in the same location to bleach the surface immobilised molecules and allow us to image particles diffusing into the imaging region from elsewhere. As a result of this, the analysis cannot make any claims about relative populations of mobile and immobile states.

The diffusion coefficient of the highly mobile population of CCL19-AF647 was found to be $8.4 \pm 0.2\,\mu m^2 s^{-1}$ from 8023 tracks fitted with a two gamma distribution model. This fit had an R^2 value of 0.985. The diffusion coefficient for the highly mobile population of CXCL13-AF647 was found to be $6.2 \pm 0.3\,\mu m^2 s^{-1}$ from 3569 tracks with an R^2 value of 0.980. This gives a faster diffusion coefficient for the lower molecular weight chemokine, in line with expectations from hydrodynamic theory. The individual fits to the data showing the high and low mobility fits and the combined fit are shown in figure 5.14A,B and the distributions of the highly mobile component are shown normalised by the number of tracks comprising the data set in figure 5.14D.

Fitting a three component gamma distribution model to these data (perhaps to account for immobile, monomeric and dimeric diffusing populations) is possible, however, the number of free parameters would be increased by 2. As the observed microdiffusion coefficient populations do not show a clear second peak, adding this population would result in an improvement in the R^2 value due to the increased number of parameters, but the fit cannot be justified by the presence of clear peaks in the data and simulations.

Imaging unconfined diffusion at the sub-millisecond level as achieved here is challenging due to practical constraints. To achieve such short exposure times the camera sensor must be sub-arrayed in one direction, resulting in a field of view 29 pixels in height for an exposure times of 0.59 ms and a cycle time of 0.65 ms. The tracking software will reject spots that are too close to the edges of the image, as it cannot compare the intensity levels that are not recorded (this can be seen as the missing of the localisations closest to the

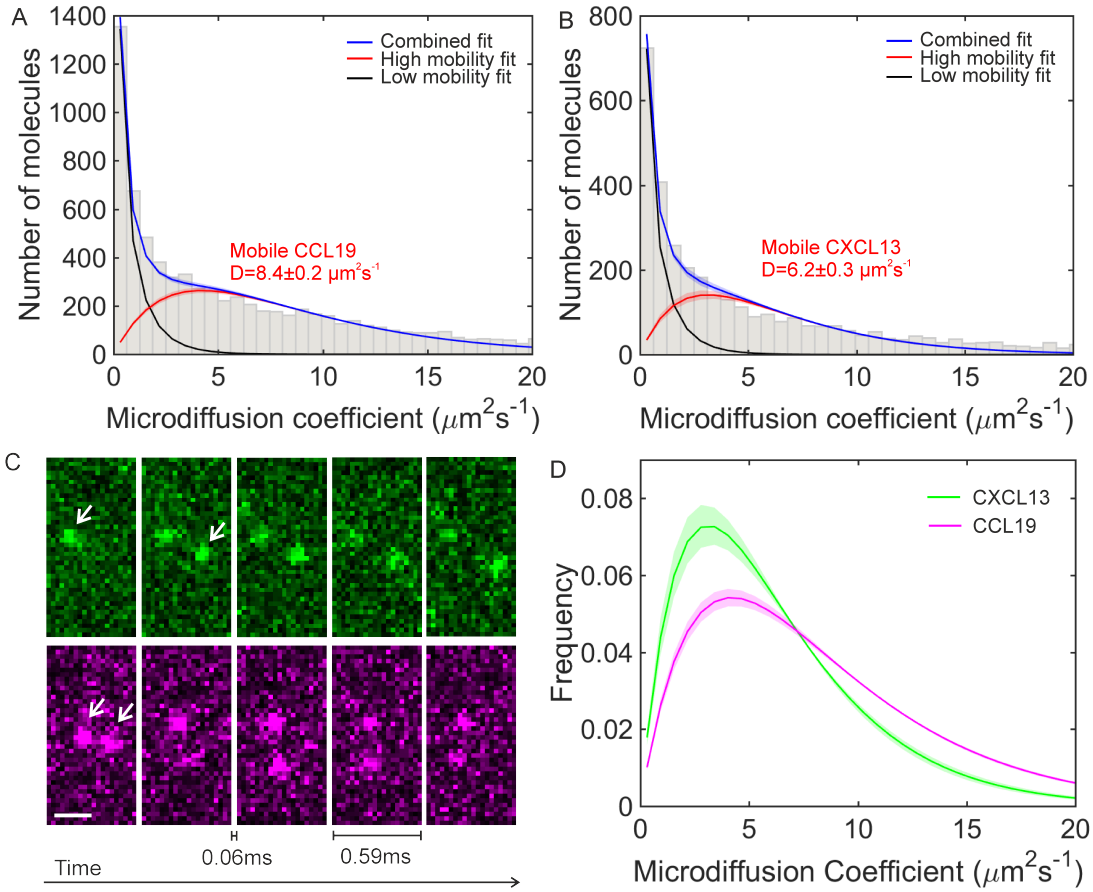

Figure 5.14: Tracking of chemokines in a collagen matrix. (A,B) Distribution of diffusion coefficients of CCL19 and CXCL13 in collagen. (C) Example sequential fluorescence images of diffusing CXCL13 (green) and CCL19 (magenta) in collagen; two proteins are seen in each set of images; the first occurrence of each is marked with a white arrow. (D) Area normalised fits of the microdiffusion coefficient distributions of CXCL13 (green) and CCL19 (magenta) showing faster diffusion for CCL19.

corners in figure 1.6), further reducing the effective area in which the centre of the object must remain to be tracked to around 19 pixels, or 2.3 µm. In the collagen samples this is not likely to cause a problem as the structure should be similar in all directions, such that no direction of diffusion should be preferred, however imaging such a small area in tissue sections might lead to bias in the results based on local conditions. Despite the drawbacks of imaging at this speed, it is required to track molecules with high diffusion coefficients to ensure successive localisations are close enough together to be linked into a trajectory, and has here, for the first time, to the author's knowledge, enabled the measurement of the diffusion coefficients of CXCL13 and CCL19 in tissue-like conditions.

5.3.9 Intensity analysis of AF647 labelled molecules

The kernel density estimates of the intensity found from the intercept of a line to the first three intensity measurements of a track (see figure 5.15A) were plotted. These were similar (in the range 2000-3000 counts) for all conditions except the CCL19-AF647 heparan sulfate immobilised data. This was determined to be due to an imaging anomaly as a repeat showed intensity values consistent with the 2000-3000 count range. The values of the intensity of a single dye molecule are expected to vary for each sample, due to the different positions of AF647 on each molecule allowing different orientations and flexibility in the linker. Further, the observed small variation in peak intensity for heparan sulfate immobilised CXCL13-AF647 and CXCL13-AF647 in collagen is expected as the viscosity of the medium is known to affect the emission profile of AF647 [209].

Normalising the data to the peak intensity and likelihood allows comparison of the data (see figure 5.15B,C). The absence of distinct peaks at multiples of the intensity indicates the chemokines are primarily monomeric in our experiments. Adam Wollman calculated that the slight peaks at multiples of the initial peak were consistent with random overlap of diffraction limited spots, based on their width in the acquired images. Chemokines are known to dimerise [207], but the lack of dimers detected suggests that the AF647 tag may block the binding site. The BSA-AF647 sample is known to contain dimers at a ratio of monomer:dimer of 15:2, so the chemokine samples, being similar in appearance to the BSA-AF647 data may contain some dimers also at this level, but, like the BSA-AF647, this will not affect the fitting procedure.

The intensity of the BSA-AF647 was expected to be higher than the intensity of CXCL13-AF647 or CCL19-AF647 as the manufacturers analysis suggests the

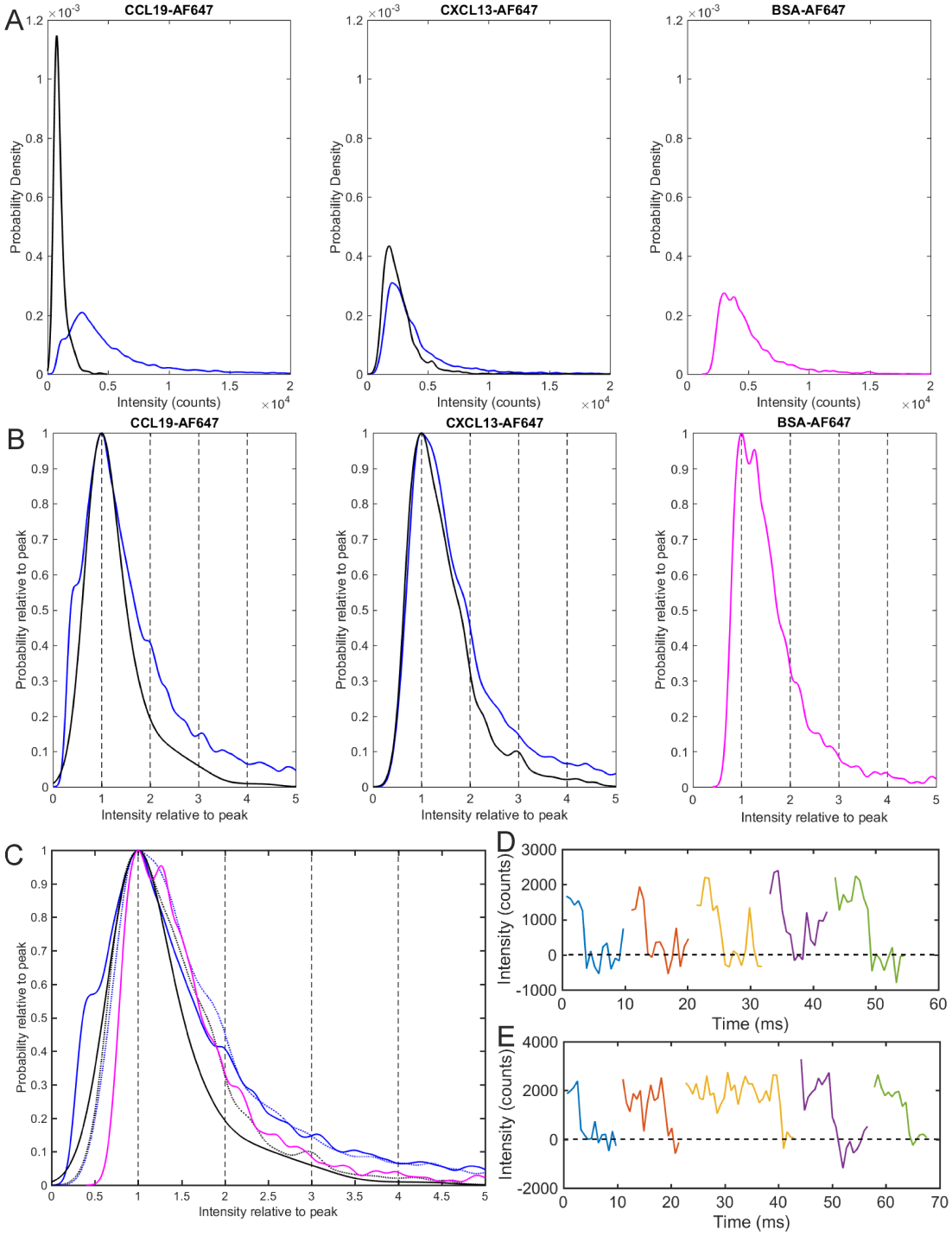

Figure 5.15: Intensity analysis of tracked AF647 labelled molecules. (A) Kernel density estimates of intensity for CCL19-AF647, CXCL13-AF647 and BSA-AF647, in collagen (blue), under heparan sulfate immobilisation (black) and in 10% Ficoll 400 (magenta). All are shown on the same axes. (B) The same figures in (A) normalised to the highest peak along both axes, these are shown on one axis in (C) where dotted lines indicate CXCL13-AF647 and solid lines indicate CCL19-AF647. (D)&(E) 5 sample photobleach traces in collagen for CXCL13-AF647 and CCL19-AF647 respectively.

BSA should be labelled with 3-6 fluorescent labels rather than a single label per molecule on the chemokines. Multiple labelling on the BSA is consistent with the SEC-MALLS result which suggested that the labelled BSA eluted faster than the unlabelled BSA - an effect we would not expect to see for a single labelling increasing the mass by less than 2%.

It is surprising that the observed intensity of single BSA molecules is similar to single chemokine molecules if the former is labelled with three fluorophores and the latter with only one. To investigate whether the chemokine molecules were actually dimers photobleaching traces were examined for CCL19-AF647 and CXCL13-AF647 (shown in figure 5.15D,E). Five example bleach traces are shown for each, showing the step-like bleach signature of a single molecule with heights of $\sim$2000 counts for CXCL13-AF647 and $\sim$2800 counts for CCL19-AF647, in agreement with the intensity distributions.

In ADEMS code a condition for the acceptance of a spot is that the intensity in a second frame must be 0.5-3$\times$ the intensity in the previous frame. This makes it 50% likely that a dimer undergoing a first stepwise bleach would cease to be tracked. This is useful in ensuring that a dimeric molecule will not be tracked at a single molecule intensity, although AF647 is unlikely to bleach in the 3.25 ms required for a track to be used in the analysis. If dimeric molecules were present, they would have been found in the photobleaching analysis that extended the tracking on each tracked spot by a further 10 frames. The fact that such molecules were not found suggests that the fluorescently labelled chemokine molecules tracked are indeed single molecules.

The method of labelling the BSA is not known from the manufacturers specifications, although it seems likely, as is often the case, that lysine is the target. It may be that in some positions the fluorophore is non-fluorescent and we see fluorescence from only one fluorophore, to give intensities similar to those seen with the chemokines, or that the chemical environment the fluorophores are in is very different, perhaps affecting their rotation or charge, and this could cause the discrepancy.

5.3.10 Modelling of collagen results

To determine the fitting function and initial fitting conditions required to produce robust fits to the experimentally measured distributions, simulations were performed.

Initially, to determine the number of gamma distributions to use for fitting, two 10,000 frame data sets were simulated, both with Gaussian white noise; one had only a single component: 1.6 $\mu m^2 s^{-1}$, and the other a 50:50

$\mathbf{D}_{sim}$	Fit model	$\mathbf{D}_1$	%	$\mathbf{D}_2$	%	$\mathbf{D}_3$	%	$\mathbf{R}^2$	χ^2
1.6	1 gamma fit	3.9	100	-	-	-	-	0.7839	14.73
	2 gamma fit	3.1	63.1	11.6	36.9	-	-	0.9865	21.3
	3 gamma fit	0.6	2.6	3.2	63.1	11.7	34.4	0.9940	24.7
1.6&10	1 gamma fit	8.7	100	-	-	-	-	0.2208	7.42
	2 gamma fit	3.6	40.5	14.7	59.5	-	-	0.9606	5.24
	3 gamma fit	3.6	38.7	13.8	53.7	57.5	7.6	0.9654	5.25

Table 5.3: Results of fitting three functions to the noisy simulated data showing the fitted values of the diffusion coefficients (μm^{2}s^{-1}) and the percentage of the simulated data at them, also the R^2 and χ^2 values for each fit. 95% confidence bounds for each fitted parameter are given in table D.1 in appendix D.

mixture of 1.6 μm^{2}s^{-1} and 10 μm^{2}s^{-1}. These data were plotted using kernel density estimation to smooth the distributions, and fitted with one, two and three gamma distributions assuming that all steps were independent (N=4 in equation 5.13 above). For the single gamma distribution the fitting equation was:

$$F(x; D_1) = \frac{(\frac{4}{D_1})^4 x^3 e^{-\frac{4x}{D_1}}}{3!} \tag{5.14}$$

For the two gamma distribution the fitting equation was:

$$F(x; A, D_1, D_2) = A\frac{(\frac{4}{D_1})^4 x^3 e^{-\frac{4x}{D_1}}}{3!} + (1-A)\frac{(\frac{4}{D_2})^4 x^3 e^{-\frac{4x}{D_2}}}{3!} \tag{5.15}$$

For the three gamma distribution the fitting equation was:

$$\begin{aligned} F(x; A, B, D_1, D_2, D_3) =& A\frac{(\frac{4}{D_1})^4 x^3 e^{-\frac{4x}{D_1}}}{3!} + B\frac{(\frac{4}{D_2})^4 x^3 e^{-\frac{4x}{D_2}}}{3!} \\ &+ (1-(A+B))\frac{(\frac{4}{D_3})^4 x^3 e^{-\frac{4x}{D_3}}}{3!} \end{aligned} \tag{5.16}$$

The prefactors, A, B, are fractions to conserve the unity area of the KDE plot, and χ^2 and R^2 goodness-of-fit values were calculated for each fit. Initially the only bound set was that all parameters must have positive values. The results of fitting the three functions above to the simulated data are shown in table 5.3. χ^2 is a measure of the goodness of fit that considers the number of free parameters fitted, with the lowest value being the best fit. The lowest χ^2 for the simulation of one diffusion coefficient is obtained using a single gamma fit, and for the simulation of the two diffusion coefficients using a two gamma fit.

By fitting the experimental data with the same three distributions we can

Simulated condition	Tracks	D	N	R^2
1.6 $\mu m^2 s^{-1}$, no noise	1579	1.7 (1.68, 1.76)	2.2 (2.15, 2.33)	0.9892
1.6 $\mu m^2 s^{-1}$, noise	401	2.2 (2.12, 2.25)	1.8 (1.67, 1.83)	0.9777
10 $\mu m^2 s^{-1}$, no noise	1519	10.2 (9.77, 10.6)	2.3 (2.08, 2.45)	0.9343
10 $\mu m^2 s^{-1}$, noise	463	10.0 (9.53, 10.54)	2.8 (2.47, 3.08)	0.8968

Table 5.4: One gamma fitting to simulated single diffusion coefficient distributions, with 95% confidence bounds indicated.

determine the number of diffusion coefficients present. With the exception of the CCL19 heparan sulfate data (which has a very low population of mobile tracks) the lowest χ^2 values were found with a two gamma distribution. It is noted that already, for each fitting method run on the experimental data, the fitted diffusion coefficient of CXCL13 is lower than the fitted diffusion coefficient of CCL19. Two gamma distributions will be used for all further fitting to the experimental data.

In the initial fits the number of independent steps was assumed to be four, but in reality the imperfect localisation precision will mean that consecutive steps using the same localisation as their end and start points will not truly be independent. A diffusion coefficient of 1.6 $\mu m^2 s^{-1}$ was simulated with and without Gaussian white noise added, and the same for 10 $\mu m^2 s^{-1}$ (examples of simulated images are shown in figure 5.16A). This time, the distributions were plotted as histograms and so fitted with equation 5.13 multiplied by the total area, with free parameters D the diffusion coefficient and N the number of independent steps. The results are shown in table 5.4.

These fits suggest the number of independent steps, N, is around 2 for mobile populations, in agreement with the simple argument that in four consecutive steps there are two which contain no common localisations. The fits in general show a good agreement with the simulated values of D, and indicate that the number of molecules missed is due to the presence of the Gaussian noise, rather than motion blur dependent on the diffusion coefficient.

From this result the mixture of 1.6 $\mu m^2 s^{-1}$ and 10 $\mu m^2 s^{-1}$ was simulated again, with and without noise, and fitted with a two gamma distribution with the same parameter N in both distributions, that is, the fitting equation:

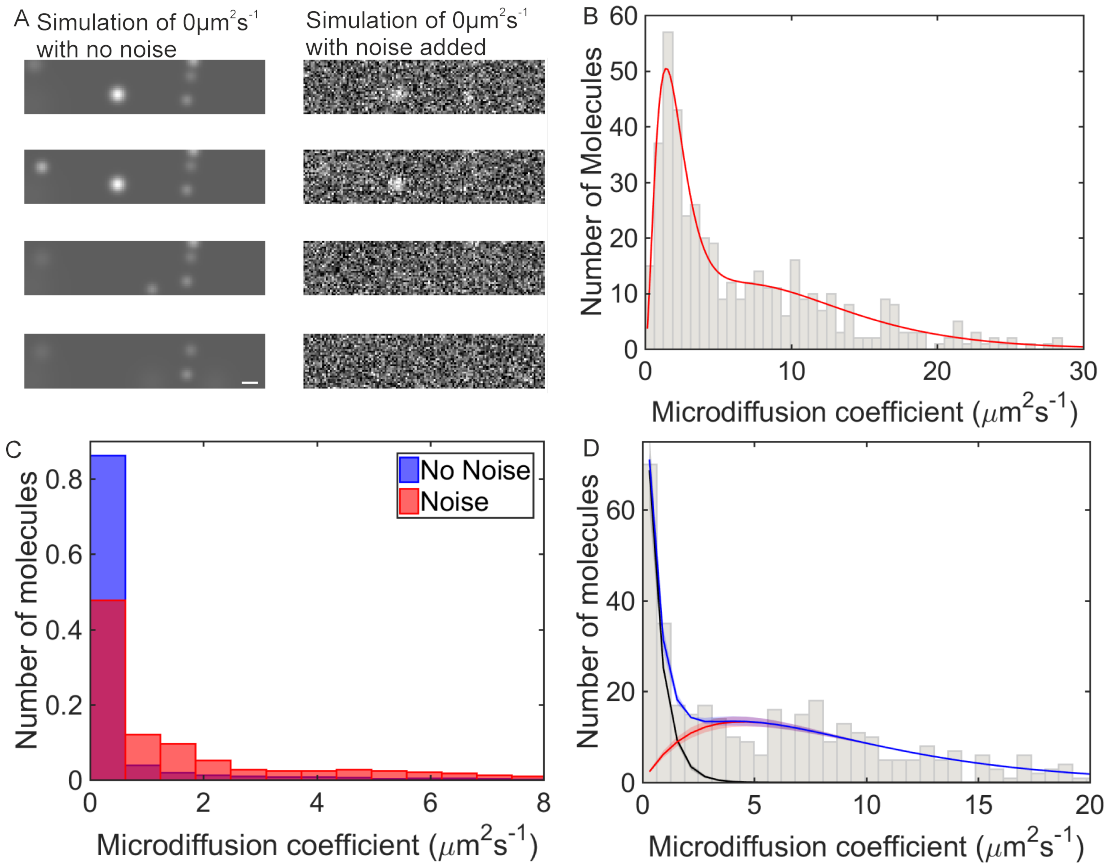

Figure 5.16: Results of simulation of fluorescence data. (A) Sample simulation images of $0\,\mu m^2 s^{-1}$; the same images are shown with and without Gaussian white noise added. (B) Two gamma distribution fit (red) to microdiffusion coefficients found from a simulation of $1.6\,\mu m^2 s^{-1}$ and $10\,\mu m^2 s^{-1}$ data with Gaussian white noise. (C) Area normalised microdiffusion coefficient distributions of $0\,\mu m^2 s^{-1}$ data with Gaussian white noise (red) and without (blue). (D) Microdiffusion coefficient distribution found from a simulation of $0\,\mu m^2 s^{-1}$ and $9\,\mu m^2 s^{-1}$ data with Gaussian white noise. Scale bar 1 μm.

Simulated condition	Tracks	A	D_1	D_2	N	R^2
1.6 & 10 µm^{2}s^{-1}, no noise	1511	461	1.62	9.82	2.17	0.9837
1.6 & 10 µm^{2}s^{-1}, noise	450	125	2.10	10.89	2.98	0.9476

Table 5.5: Two gamma fitting with one fixed number of independent steps to simulated mixed diffusion coefficient distributions. 95% confidence bounds for each fitted parameter are given in table D.2 in appendix D.

$$F(x; A, N, D_1, D_2) = A\frac{(\frac{N}{D_1})^N x^{N-1} e^{-\frac{Nx}{D_1}}}{(N-1)!} + (Area - A)\frac{(\frac{N}{D_2})^N x^{N-1} e^{-\frac{Nx}{D_2}}}{(N-1)!} \quad (5.17)$$

Where $Area$ is a constant calculated by the bin width multiplied by the number of tracks. The results of the two fits are given in table 5.5. Comparing the microdiffusion coefficient distributions of the data sets with and without Gaussian white noise the appearance of highly diffusive molecules is an artefact of the noise. The distribution of the simulated data including white noise is shown in figure 5.16B with the fit. The shape of the distribution is not the same as the experimental data. In histograms of the experimental data with this bin size the highest number of counts is in the first bin, whereas here it is in the third bin. This implies that the experimental data has a diffusion coefficient lower than 1.6 µm^{2}s^{-1}. Compared to the fits to the simulations of the two diffusion coefficients separately the fit has not found the simulated diffusion coefficients with as high accuracy in the combined simulation, implying that the N values should be different for the two components.

Immobile data with and without Gaussian white noise was simulated to see if the histogram of the distribution would have a peak in the first bin. The normalised distributions are shown in figure 5.16C, and do show a peak in the first bin. These distributions were fitted with a single gamma fit with only the area constrained. In the following, 95% confidence bounds are given in brackets. Without Gaussian white noise N=1.41 (1.36, 1.47) and D=0.25 µm^{2}s^{-1} (0.24, 0.26), but with the noise was added N=0.07 (0.07, 0.07) and D=0.4 µm^{2}s^{-1} (0.29, 0.49), giving a gamma distribution without a peak. As the bin width was chosen to be the localisation precision it would agree with expectation to find that the peak of an immobile data set would fall within the first bin, and because the fitting algorithm does not have access to information below the bin width, it will fit a gamma distribution without a peak. This simulation looks like the first bins of the experimental data, and so 0 µm^{2}s^{-1} and 9 µm^{2}s^{-1} data with Gaussian white noise was simulated. This simulation is similar to the

experimental data in that it has a peak in the first bin and then an extended tail with no clear peak. Based on the previous results this distribution was fitted with the equation:

$$F(x; A, N, D_1, D_2) = A\frac{(\frac{N}{D_1})^N x^{N-1} e^{-\frac{Nx}{D_1}}}{(N-1)!} + (Area - A)(\frac{2}{D_2})^2 x e^{-\frac{2x}{D_2}} \qquad (5.18)$$

with the immobile peak constrained to fall in the first bin and have $N < 1$. The distribution and fit are shown in figure 5.16D. This gave D_2=8.9±0.4 µm^{2}s^{-1} with $R^2 = 0.9618$. The fitted mobile diffusion coefficient agrees within error with the simulated value, despite the small number of tracks fitted (374). For the experimental data to be fitted the number of tracks is in the thousands. Therefore this model, with the constraints that the diffusion coefficient of the less mobile population had to fall in the first bin, and therefore $N < 1$, was used to fit the experimental data.

In these simulations the tracks were randomly reassigned 10% of the time. This may be an overestimate for the effects of photobleaching, diffusion out of the volume and overlap with another particle that cause truncation of the trajectory, and so the noise level may be higher than that in the original data. However, the simulated and real images appear to contain similar noise levels. The Gaussian white noise is modelled as being proportional to the intensity in the image, and since electron multiplying gain is applied to the experimental data on chip, this is likely to be true.

5.3.11 Identification of B cell follicles in tissue

FITC-antibody staining for the B cell surface protein B220 was used to determine the locations of the B cell follicles in the lymph node. A marked increase in fluorescence intensity was seen in some regions compared to others (see figure 5.17). The regions with increased intensity were determined to be B cell follicles. The location of these areas was seen to be close to the lymph node capsule (outer, fibrous layer of the lymph node), in agreement with previous studies [279].

A control sample prepared with staining for B220 but with PBS added instead of fluorescently labelled CXCL13 also contained regions with high and low green fluorescence intensity, consistent with the AF647 labelled chemokine stained B cell follicles. This suggests bleed through from the chemokine was not responsible for the green fluorescence signal used to detect the B cell regions.

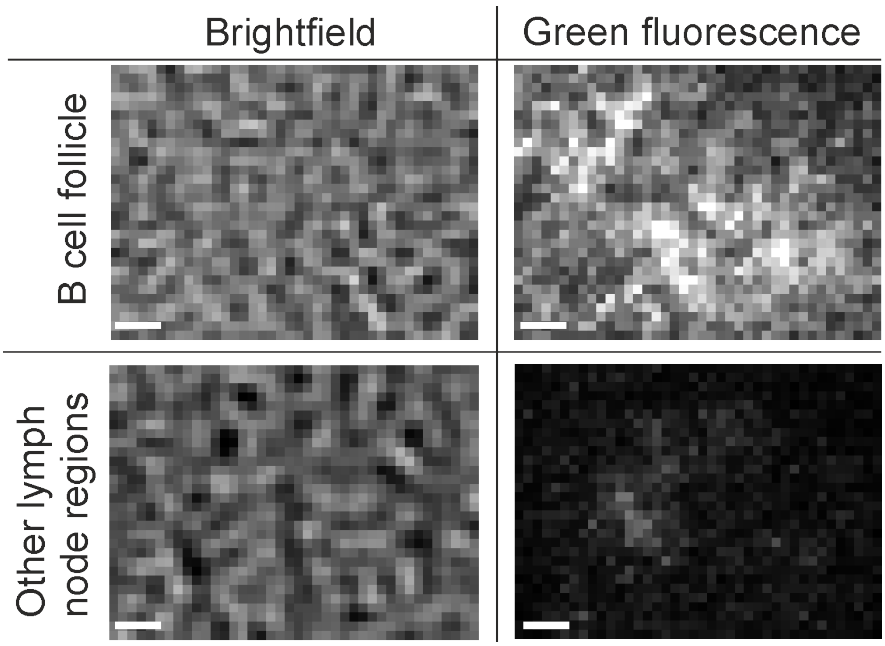

Figure 5.17: Brightfield and green fluorescence images of lymph node stained with FITC conjugated to the antibody for the B cell surface marker B220. The two green fluorescence images are displayed at the same contrast levels. B cell follicle locations can be determined by the presence of green staining. Scale bars 5 µm.

5.3.12 Tracking CXCL13 in B cell follicles

CXCL13-AF647 was tracked in red fluorescence in lymph node tissue sections in regions identified as B cell follicles. In these images bright regions that do not bleach over the timescales observed with the laser power used are seen, and these are consistent with autofluorescence. To ensure the signal tracked as chemokine was not due to the B220 stain a control experiment was performed. The control sample was prepared with staining for B220 but with PBS added instead of fluorescently labelled CXCL13. When B cell follicle regions of this slide were imaged in red fluorescence no mobile fluorescent spots of the type observed in the collagen and CXCL13 containing slides were observed but static non-bleaching fluorescence was seen. This is strong evidence that the mobile fluorescence signal observed in non-control data sets is from CXCL13-AF647 and not mobile B220 antibody labelled with FITC bleeding through into the red channel, and that the autofluorescence is not an artefact of the presence of labelled chemokines.

Stroma was segmented by first smoothing the image with a Gaussian top hat filter, and then applying an erosion followed by a dilation to remove small isolated areas and fill in small gaps in the identified regions. The areas identified in this process can be seen in figure 5.18, for both the sample and the

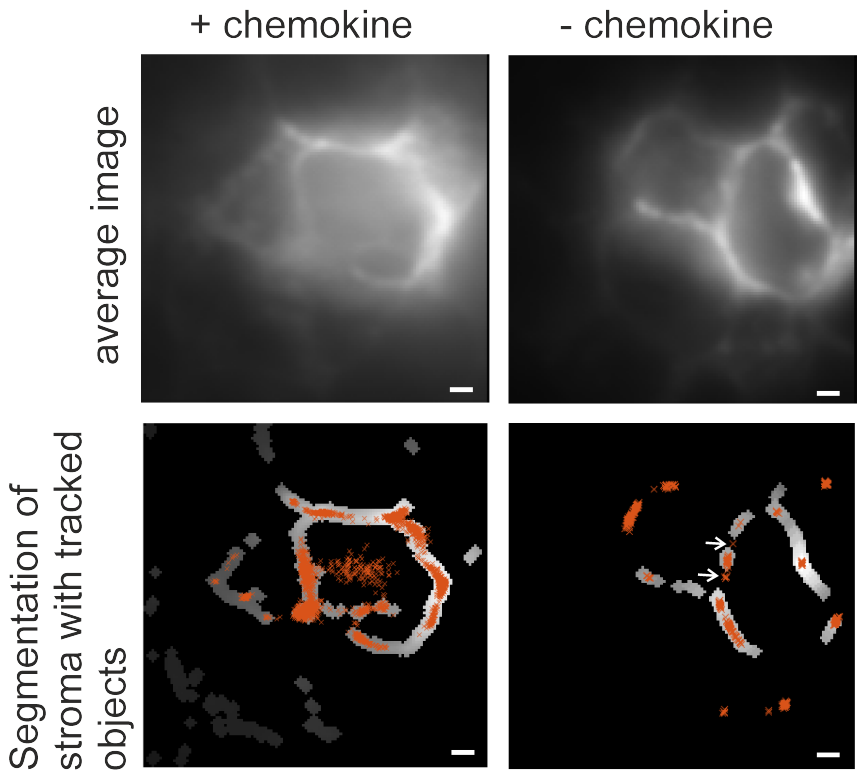

Figure 5.18: Segmentation of stroma by intensity. The tissue section with CXCL13-AF647 is shown left and the no chemokine control shown right, displayed at the same contrast levels. Top row: unsegmented intensity average images of image stacks. Bottom row: Regions of the image segmented as stroma, with localisations from tracking data overlaid as orange crosses. Scale bars 1 µm.

control with no fluorescently labelled chemokine present. These images show the full extent of the camera sensor, and it can be seen that the signal does not fill the full sensor due to the narrowfield excitation. In the image of the control it is clear that regions of stroma further from the centre of the excitation are not identified by this segmentation algorithm, and also regions where the intensity of the stroma is lower (indicated by white arrows) are missed, but the second of these could be where the stroma is out of focus and at another axial level, and so the localisations at a location such as this in the slide containing chemokine may include mobile tracks. In the image where CXCL13-AF647 is present there is a clear population of mobile tracks in the region at the centre of the stromal "web", which is not present in the control and represents the majority of the tracks identified as chemokine.

The area normalised distributions of the microdiffusion coefficients in the two regions identified by segmentation are shown in figure 5.19A (the locations of the localisations are shown colour coded inset). The stromal distribution is similar in having a very low diffusion coefficient to the distributions seen in the simulation of the immobile fluorophores and the immobile population seen in the collagen data, reinforcing that it is indeed likely to be a part of the tissue structure. The population identified as not being part of the stroma by contrast has a distribution similar in shape to the mobile components of the distributions found in collagen, which is fitted in figure 5.19B. The bin width in the histogram used for fitting the data was chosen so that in fitting microdiffusion coefficients up to $\sim 20\,\mu m^2 s^{-1}$ only around 5% of the bins were empty, as narrow bins give more accurate fits, but empty bins can cause fitting procedures to converge on a false optimum. The bin width was chosen as $0.52\,\mu m^2 s^{-1}$ for this reason, and 192 tracks were included in the fitting to 38 bins.

The fitted diffusion coefficient for CXCL13-AF647 in B cell follicles was found to be $6.6 \pm 0.4\,\mu m^2 s^{-1}$, with an R^2 value of 0.7297. This agrees within error to the value found in collagen, as would be expected for a molecule chosen as an extracellular matrix mimic. As the value was found by segmenting out the stroma transient interactions with the stroma may be present but not observed in this analysis. The value of diffusion coefficient found lies in the range identified by agent-based simulation as being where the efficacy of B cell scanning depends the most sensitively on the diffusion coefficient. This implies that the diffusion coefficient values may have a large effect on the efficacy of the humoral immune response to the presence of antigen.

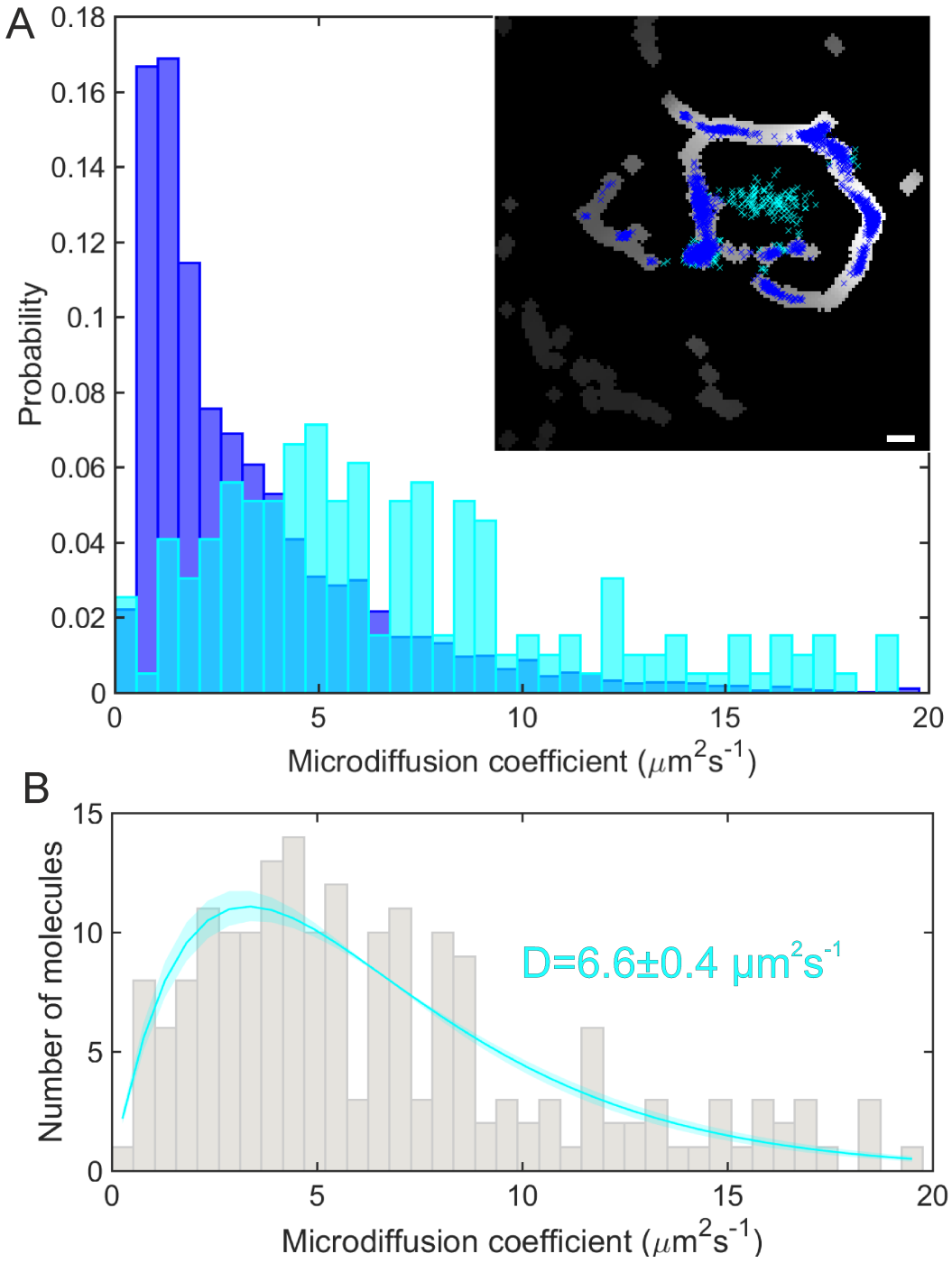

Figure 5.19: Results of tracking CXCL13-AF647 in a tissue section. (A) The area normalised distribution of microdiffusion coefficients in the tissue section in areas segmented as stroma (blue) or freely diffusing (cyan). The inset shows the position of the first localisation in each track colour coded as to whether it lies on stroma (blue) or is freely moving (cyan). (B) Single gamma distribution fit to the microdiffusion coefficients of freely moving CXCL13-AF647 in the lymph node. Scale bar 1 µm.

5.4 Conclusions and Future Directions

The work in this chapter has shown that single molecule tracking can be used to analyse the diffusion coefficients of proteins such as chemokines at endogenous concentrations, with the potential to differentiate between monomers and dimers. Single molecule tracking also has the ability to spatially interrogate the occurrence of events, looking for binding hotspots, although this has not been applied in this work.

Fluorescence correlation spectroscopy, fluorescence recovery after photobleaching and single particle tracking have been compared on the same model system (BSA-AF647 in 10% Ficoll 400) and show similar values, within the range expected by the literature, but single particle tracking was the best suited to extracting the diffusion coefficient from a mixed population at the low concentrations used. This is important both to ensure the molecular properties (such as the dimeric fraction) are not affected by a non-physiological concentration, and practically, because fluorescently labelled chemokines are currently very expensive. Improving on ensemble methods, single-molecule tracking is the best tool to date to elucidate information at biological concentrations where ensemble techniques such as FCS and FRAP do not achieve the required count rates.

Various forms of sub-millisecond super-resolution microscopy have been previously reported, including the use of large fluorescent bead probes [280], tracking single molecules one at a time [281] and the use of TIRF and highly inclined and laminated optical sheet (HILO) microscopy [282]. Sub-millisecond super-resolution localisation microscopy of single fluorescently labelled cholesterol molecules has been reported previously in plasma membranes [283]. However, the work reported here is the first time, to the author's knowledge, that sub-millisecond nanoscale precise particle tracking has been performed using nanoscale single-molecule fluorescent probes in an intracellular tissue-like environment whose viscosity, comparable to that found physiologically in the vicinity of B cells in lymph nodes, is less than that in a lipid bilayer by 2-3 orders of magnitude.

The ability to image at sub-millisecond timescales has enabled, to the author's knowledge, the first measurement of the diffusion coefficients of chemokines in a tissue-like environment: Fluorescently labelled CCL19 and CXCL13 have been tracked at the single molecule level at 1500 Hz in a collagen matrix. Diffusion coefficients of $6.2 \pm 0.3\,\mu m^2 s^{-1}$ for CXCL13-AF647 and $8.4 \pm 0.2\,\mu m^2 s^{-1}$ for CCL19-AF647 were found, with the higher molecular mass protein having the lower diffusion coefficient, as expected.

Further, CXCL13-AF647 was tracked in B cell follicles of *ex vivo* lymph node tissue sections at $\sim$500 Hz, giving a diffusion coefficient of $6.6 \pm 0.4\,\mu m^2 s^{-1}$. This value will be used by Jason Cosgrove in simulations of B cell follicles, which will be used for *in silico* experimentation, in a project which aims to reduce the number of animal experiments conducted in research laboratories.

CCL19 localises to a different area of the lymph node to CXCL13, and so to image it a different stain would have to be used for that region. This would be interesting further work to see if the diffusion coefficient of CCL19 in the tissue agreed with the value for collagen, as was the case for CXCL13, or if the molecular environment was different in the areas where CCL19 localises. However, the two chemokines can not be compared in the same region of tissue as it would be non-physiological.

AF647 is known to be negatively charged, and this would explain the non-specific adhesion to glass that observed, as well as suggesting a possible cause for the lack of observed dimeric chemokines, although this may simply be due to a lower population of dimers than monomers that cannot be discerned, or dimers may not be doubly labelled.

Chapter 6

Low Temperature Plasma Damage of DNA Origami

6.1 Introduction

In this chapter experiments to qualitatively and quantitatively assess damage caused to DNA origami by low temperature plasma are described. Gel electrophoresis, fluorescence microscopy and AFM imaging are used to develop a model of the method of damage to DNA origami.

6.1.1 DNA origami

The DNA in a human cell is folded and compacted for storage by proteins and mechanisms that are incompletely understood; without these processes the DNA in one human cell would be around two metres in length. *In vitro*, we can fold smaller lengths of DNA into 2D or 3D DNA origami by careful design of specific binding sites.

Seeman was the first to suggest the possibility of designing DNA structures [284] and to experimentally prove it was possible [285], however the method was extremely dependent on having 1:1 stoichiometry between the strands to be hybridised, and small deviations caused low yield. The DNA tetrahedron [286] uses strands of similar lengths, which therefore have similar melt temperatures, to achieve almost 100% yield. Any stoichiometry other than 1:1 will still produce a large number of misfolded patterns. In 2006 Rothemund [113] developed DNA origami; this technique uses Watson-Crick base pairing such that two complementary DNA strands of sufficient length will bind together with high specificity. By taking a single-stranded bacterial plasmid and short single stranded 'staples' which are complementary to two separated regions of the plasmid template, the plasmid can be folded into a well-defined

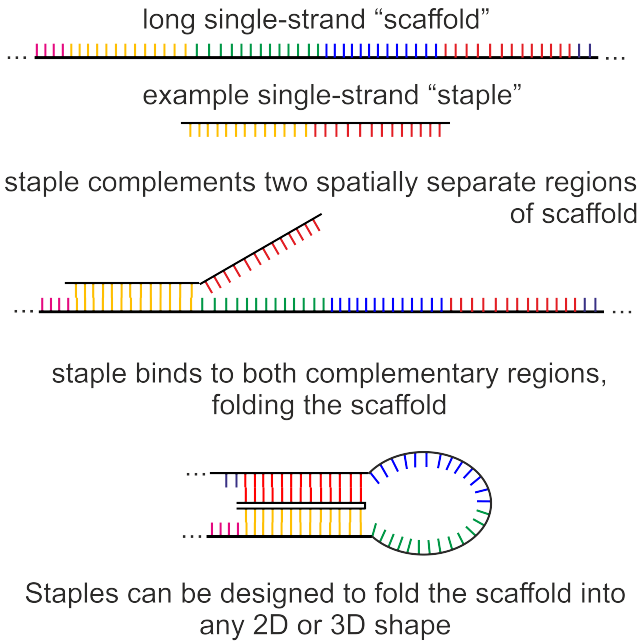

Figure 6.1: The formation of DNA origami. A simplified example of single-stranded DNA staples folding a single-stranded DNA scaffold into DNA origami. The colours indicate regions which are complementary.

shape (see figure 6.1). High temperatures are required to hybridise the strands - heating to $\sim 95\,^{\circ}\mathrm{C}$ is commonly used to remove secondary structure (interactions between short regions of complementary sequence of ssDNA with other regions of the same strand) to allow the desired interactions to take place. DNA origami has revolutionised the field due to having a higher tolerance for stoichiometric imbalance than previous methods.

The DNA origami design used in this work is a modification of the rectangular tile designed by Paul Rothemund [113]. The original tile uses the viral ssDNA of m13mp18ss as a template and 216 32-mer staple strands to fold it into a rectangle approximately 70x100 nm in size with a central seam. Katherine Dunn has modified the design by adding poly-T loops to 24 of the staples to inhibit edge stacking that was seen in the original study (poly-T loops were suggested as a means to combat the stacking [113]). 4 strands have had biotin added at the 5′ end, such that these will all protrude on the same side of the tile and enable surface attachment, and 3 original staples have been replaced with 4 alternative staples, one of which is extended to allowed attachment of a fluorophore in the future if desired (The full details of the modified staples are given in appendix E). This structure can be seen in the AFM images taken by Sonia Antoranz Contera in figure 6.2.

An exciting recent development is protein folded origami [287]. This removes the high temperature annealing step required in forming origami

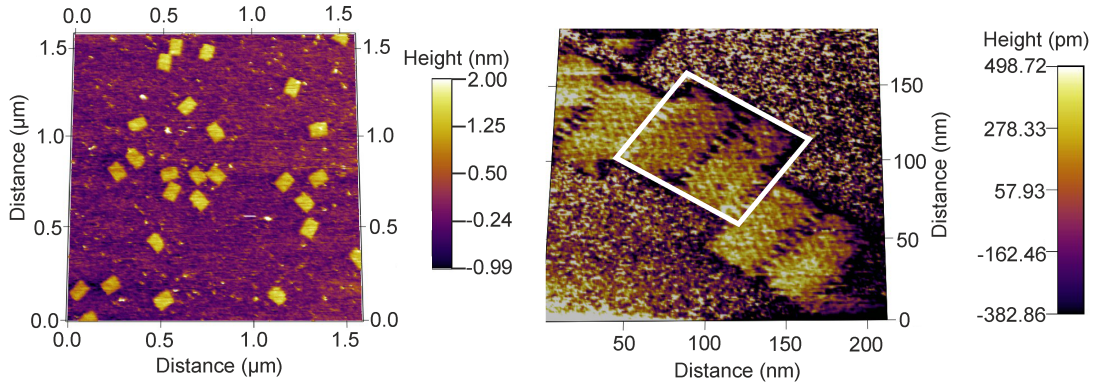

Figure 6.2: Sonia Antoranz-Contera's AFM images of the intact DNA origami used in this project, taken in tapping mode in fluid. Left: multiple undamaged tiles. Right: High magnification image of 3 undamaged tiles. The white box indicates a single tile and the central seam can be seen.

from two single strands, by using proteins to bind to DNA and fold it into shape. It remains to be seen whether this will work *in vivo*, where there will be competition for DNA binding sites.

6.1.2 Low temperature plasma

Plasma is an overall electrically neutral state of matter created by passing an electromagnetic field through a gas; it breaks bonds and forms positive, negative, and neutral species, along with gamma rays. Low temperature plasma (LTP) is currently being developed as a novel prostate cancer treatment which acts to induce necrosis in the tumour cells via DNA damage [288]. The plasma source used in this work is shown in figure 6.3A. LTP may provide considerable advantages over existing treatments for prostate cancer as plasma can be guided down a needle to allow treatment in the patient without highly invasive surgery.

Previous work to quantify DNA damage by low temperature plasma has used coiled plasmids to investigate the conversion from coiled to nicked to linear DNA according to single or double strand break by gel electrophoresis [289]. At high levels of damage an initially coiled plasmid may be broken into several pieces which become spatially separated. In gel electrophoresis, the current workhorse method to evaluate DNA damage at the ensemble level, many molecules must be run together for a signal to be detected. This means that only average behaviours can be seen, and it cannot be determined if any given molecule suffered single or multiple double strand breaks. DNA origami is an intriguing prospect for damage assays because the structure, with multiple staples connecting different regions, will putatively allow parts

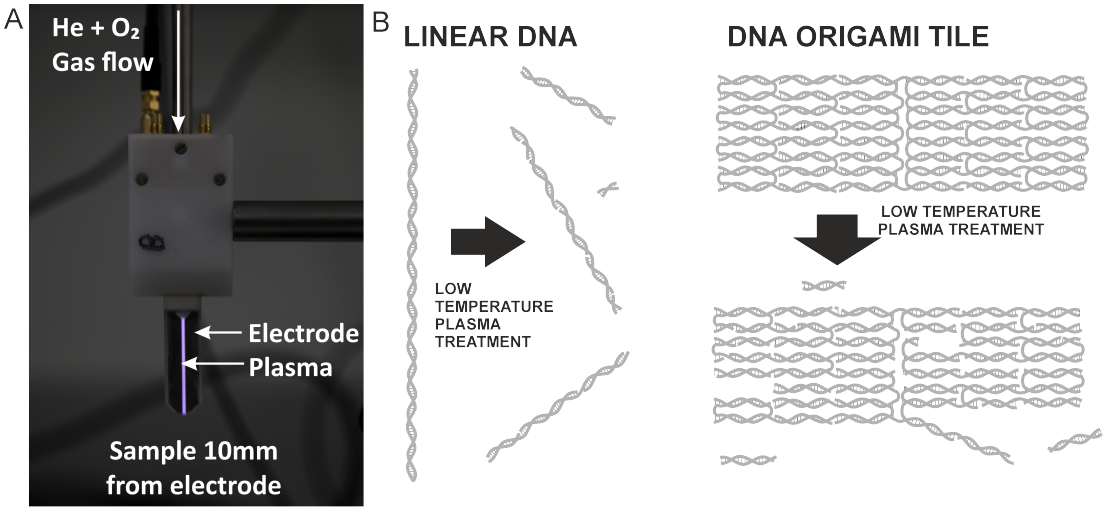

Figure 6.3: Low temperature plasma damage of DNA. (A) The low temperature plasma source used. (B) Putative method of DNA damage to linear DNA and DNA origami.

of the tile affected by double strand break to remain tethered to the backbone, potentially allowing investigation of each DNA tile at the single molecule level (see figure 6.3B).

6.1.3 Quantifying DNA damage

Gel electrophoresis is commonly used to determine the presence of DNA damage outside of a cell. In a buffer, an agarose gel is placed under a electric field, and charged molecules added to the gel will migrate through it, with distance travelled depending on their charge and cross-sectional area. For many polymers such as DNA mass is proportional to cross-sectional area, and the two terms are often used synonymously. Generally lower mass molecules travel further from their starting point. If all the molecules have similar mass, they will form a distinct band when the gel is stained and imaged. A continuous range of masses will tend to produce a continuous signal with no vertical edge definition. Usually the gel is stained with a dye that is excited by UV radiation, such as ethidium bromide or the less harmful SYBR safe. Acridine orange is a dye which fluoresces red when bound to single stranded DNA and green when bound to double stranded DNA [148]. Potentially this may offer insight into the mechanism of DNA damage if there is a change in the red/green ratio as tiles are damaged.

The comet assay [290][291] is essentially gel electrophoresis in cells and is often used for quantifying DNA damage. In this method entire cells are embedded in agarose, cast onto microscope slides, lysed to allow the DNA

to migrate, electrophoresed and stained. The distance the DNA travels from its starting point depends on its configuration (e.g. supercoiled or linear) and its molecular weight, again with smaller fragments travelling further from the source. This results in characteristic shapes which give the technique its name, with the large DNA migrating only a short distance and the shorter DNA forming the long tail of the comet. Unlike gel electrophoresis where the DNA begins in a narrow well, here the DNA source is extended, and the comets can overlap at high densities; this can make it difficult to determine the starting location of DNA and makes analysis somewhat subjective, although there is now open-source software which aims to standardise the analysis (OpenComet [292]).

Immunofluorescence labelling [293][294] is a single cell technique used to qualitatively estimate DNA damage in cells. DNA is labelled via fluorescent antibodies which bind to antigens *in situ*, giving more spatial information than the comet assay, but the use of conventional imaging means only one plane can be imaged at a time. This has been used to show that low temperature plasma causes double strand DNA break in primary epithelial cells cultured from a human prostate tumour [295]. Tunel staining [296] is another single cell fluorescence technique, often used to identify programmed cell death by fluorescently labelling the 3' OH of damaged DNA, but this chemical group is not present in drug induced DNA damage and cannot be used in this work.

DNA damage *in vivo* and *in vitro* are different; the cellular environment is far more complex than that of buffer, and cellular components and machines may help to prevent or accelerate DNA damage compared to DNA in buffer. However, it has been shown that for low temperature plasma, dose times for low to high levels of damage are in the range of seconds to $\sim$10 minutes *in vivo* and *in vitro* [288][289].

6.1.4 Atomic force microscopy

Atomic force microscopy (AFM) is the tool of choice for atomic level resolution imaging of single molecules, which is beyond the level attainable by super-resolution fluorescence microscopy. Here, a very thin, sometimes atomically thin cantilever is in contact with the sample. A laser is deflected from the back of the cantilever, and the deflection of the reflected beam as the cantilever is scanned over the sample is used to generate a readout of the height of the sample [297]. Angstrom level imaging is readily achievable with this method, and as DNA origami has only a thin depth, is well suited to investigation by AFM. AFM can be a slow technique, and so is best suited

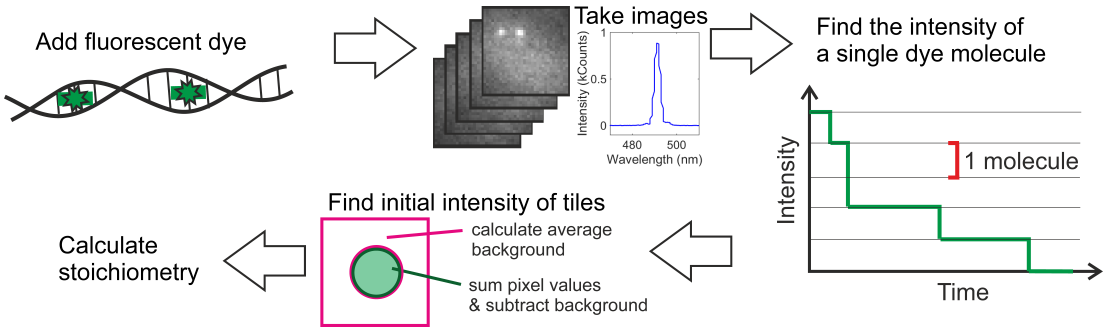

Figure 6.4: Schematic diagram of the method to find the stoichiometry of a tile, including the laser transmission spectrum used in the quantitative part of this work.

to non-dynamic processes. A problem that is sometimes observed in AFM is damage to the sample due to mechanical perturbation with the tip, but AFM has previously been successfully used to assess damage to DNA strands extended from DNA origami [298], so this should not be a problem.

6.1.5 Fluorescence microscopy to determine stoichiometry

Fluorescence microscopy is commonly used to investigate the copy numbers and relative stoichiometries of proteins (see for example [69]). Fluorescent probes have a characteristic intensity under illumination that can be found by looking for stepwise photobleaching traces of molecules. For stoichiometries up to around 6 molecules, the total number of molecules is often determined by counting the number of individual steps in many bleaching traces. For higher numbers of molecules, the stoichiometry can be found by dividing the total intensity of the complex at first illumination by the intensity for a single dye molecule [299]. The application of this to DNA origami is shown in figure 6.4.

Chung-Kennedy filters [43] are an important tool for finding the presence of steps in noisy data, such as single molecule bleach events. These filters preserve edges in the data, by comparing a window of data preceding (causal) and following (anti-causal) the point, and choosing the one with the lowest variance. The length of this window can be adjusted to look for effects on different timescales, and multiple length windows can be combined. The result from the window with the lowest variance is taken, to account for the presence of effects occurring on multiple timescales within the data.

In theory as DNA is damaged the number of intact base pairs should decrease, and it is desirable to use an intercalating dye, which will bind when DNA is intact, but should not be able to bind to damaged DNA. An intercalating dye, YOYO-1 was used previously in the DNA tethering project,

and will be used again here. The total fluorescence intensity of a maximally labelled DNA origami tile at high damage levels is expected to be lower than that of the undamaged tile.

6.1.6 Statement of contributions

In this project all experimental work was carried out and analysed by myself, except the following specific contributions: Sonia Antoranz Contera performed the AFM imaging shown and produced the AFM images. Katherine Dunn designed the modifications to the DNA origami tile. Adam Hirst and Sandra Schröter set up and ran the plasma when inflicting the DNA damage. Steve Johnson suggested the biotin-avidin surface immobilisation protocol used for microscopy of the DNA origami, which he had previously developed.

6.2 Materials and Methods

6.2.1 Buffers

Phosphate buffer (PB) at pH 7 was made in 50 ml volumes by mixing 19.5 ml 0.2 M monobasic sodium phosphate monohydrate and 30.5 ml of 0.2 M anhydrous dibasic sodium phosphate. Purification buffer was 10 mM Tris, 1mM EDTA, 50mM NaCl and 10mM $MgCl_2$, that is TE buffer with added sodium and magnesium chloride. Synthesis buffer was 1xTAE (40 mM Tris-acetate and 1 mM EDTA, pH 8.3) with 12.5mM magnesium acetate.

6.2.2 DNA

The DNA origami tile uses the 7249 bp m13mp18 single stranded circular DNA as a scaffold (N4040S, New England Biolabs), and linearised lambda DNA (N3011S, New England Biolabs) was used in some control DNA damage experiments. Oligonucleotide sequences (Integrated DNA Technologies, Inc.) used as controls in the acridine orange gel staining experiments are given in the table 6.1. The staples and their complements were annealed to form a 10 µM solution of DNA in synthesis buffer by heating to 95°C, and cooling at 1°C per minute.

6.2.3 Plasma damage

Adam Hirst or Sandra Schröter operated the LTP plasma source. The 13.56 MHz source utilised a peak to peak output voltage of 450-500 V with

Oligomer name	Sequence
r3t10f	$5'-\mathrm{ATTATTTAACCCAGCTACAATTTTCAAGAACG}-3'$
r3t10f complement	$5'-\mathrm{CGTTCTTGAAAATTGTAGCTGGGTTAAATAAT}-3'$
r3t22f	$5'-\mathrm{AGGCGGTCATTAGTCTTTAATGCGCAATATTA}-3'$
r3t22f complement	$5'-\mathrm{TAATATTGCGCATTAAAGACTAATGACCGCCT}-3'$

Table 6.1: Oligonucleotides used in gel electrophoresis.

1 standard litre per minute (slm) helium and a 5 % admixture of oxygen. Samples were treated in 20 µl volumes (unless otherwise stated) in the lids of 500 ml Eppendorf tubes without the tube attached, at a distance of 10 mm from the plasma source and treated for up to two minutes.

6.2.4 Making origami

DNA origami was formed by annealing ∼10 nM m13mp18ss scaffold with a ∼100 times excess of the non-biotinylated strands in synthesis buffer at 95°C, and cooling at 1°C per minute, to remove any secondary structure. Once cooled to room temperature, the biotinylated strands were added at ∼100x excess in synthesis buffer, and left to hybridise at room temperature overnight.

6.2.5 Purifying origami

To remove the excess staples from synthesis, DNA origami was purified using high resolution Sephacryl S-300 media (GE Healthcare), following the method of Dunn [300] who adapted it from Wickham [301]. Sephacryl media is packed into filtration columns. When the DNA origami is added to the packed columns, the small staple strands enter the gel media and are trapped, whilst the larger DNA origami molecules move through the matrix and are eluted. Full details of the preparation of the filtration media and packing of the spin columns are given in appendix E.

6.2.6 Preparation of functionalised coverslips

The surface immobilisation protocol involves coverslip functionalisation. In all steps care is taken to ensure the cleaned side is maintained. Batches of coverslips can be prepared and used as needed. First the coverslips are plasma

cleaned for 5 minutes to remove organic residues. The coverslips are then soaked in BSA-biotin (0.5 mg/ml in PB) for 1 hour (150-200 µl of liquid is pipetted onto each coverslip), then rinsed twice with phosphate buffer (PB) and air dried. At this point the coverslips can be stored at room temperature in petri dishes sealed with Parafilm M (Bemis Company, Inc.).

6.2.7 Origami immobilisation protocol

Functionalised coverslips are used to create tunnel slides. 20 µl PB is flowed in to hydrate the tunnel. 10 µl avidin (1 mg/ml, pH 7) is flowed in and incubated for 1 hour in a humidity chamber. The tunnel is washed with 20 µl purification buffer and then 7.5 µl of purified biotinylated origami diluted in purification buffer (approximately 0.78 nM, concentration not checked after purification). This is incubated for 5 minutes and washed with 20 µl of purification buffer. Next the dye is flowed in: 10 µl of YOYO-1 diluted 1:199 in purification buffer and incubated for 5 minutes. In the last step the sample is washed with 100 µl purification buffer, and then imaged.

6.2.8 Fluorescence microscopy

Both fluorescence microscopes previously described in this thesis were used to acquire images. Images of lambda DNA labelled with YOYO-1 at various concentrations (diluted in PBS) were acquired on the fluorescence microscope described in chapter 3. Lambda DNA samples were prepared and imaged using the immobilised DNA assay as described in sections 4.2.3 and 4.2.1 under identical illumination and image acquisition settings. The recovery experiments of YOYO-1 blinking on DNA origami were performed on this microscope in TIRF at an angle of incidence of $65 \pm 1.5^{\circ}$.

Images of DNA origami used for the analysis of stoichiometry were collected using the microscope described in section 5.2.6, with an excitation field at the sample of FWHM 12 µm. Images were collected using the 100 x objective. Laser illumination at 491 nm was used, with an AOTF setting of 45 %, corresponding to a power density at the sample of 775Wcm^{-2}. The laser transmission spectrum is shown in figure 6.4. The filter cube beneath the objective contained a 515 nm dichroic mirror and a 535/15 bandpass emission filter. 128x128 images were acquired at 10 ms exposure time (10.06 ms cycle time) at the full EM and pre-amplifier gains of 300 and 4.6 respectively.

6.2.9 Gel electrophoresis

Gel electrophoresis was performed as described previously in section 2.2.9. Post treatment, the DNA is run in 1% agarose gels either pre-stained with SYBR safe or post-stained with acridine orange. Images were analysed using ImageJ (NIH, USA, https://imagej.nih.gov/ij/). To quantify the red/green ratio of bands in the acridine orange stained gel a box of 42x4 pixels was used to measure the intensity in the band in each colour channel, and the mean value was used. Errors on red/green ratios were calculated by displacing the 42x4 box by one pixel to account for band edges not aligning with pixel edges.

6.2.10 Atomic force microscopy

Atomic force microscopy was performed by Sonia Antoranz Contera in Oxford with a MFP-3D BIO^{TM} (OXFORD Instruments Co., Ltd, UK) with silicon nitride RC800 cantilever tips (Olympus) with spring constant $0.4\,\mathrm{Nm}^{-1}$. 5 µl of DNA origami tiles were incubated in purification buffer on freshly cleaved mica for 15 minutes. Images were taken in purification buffer at room temperature at a scan speed of 1 Hz.

6.2.11 Tracking and analysis

ADEMS code, written by Adam Wollman, (see section 2.2.10) was used to track the fluorescence intensity of the tiles over time. As the DNA origami tiles are stationary due to the biotin immobilisation the found spots were linked into trajectories based on location rather than the usual criteria in ADEMs code on the intensity and distance travelled in consecutive frames. The usual criteria are ideal for tracking diffusing particles, but here surface immobilisation means that localisations separated by skipped frames can still be linked with confidence, to produce longer tracks.

Images were tracked in this manner and corrected for non-uniform illumination using an image created by raster scanning fluorescent beads through the focal volume. The intensity, *I(t)* of objects found within a 40 pixel radius of the beam centre containing at least 20 localisations within the first 100 frames were fitted. The fitting function was an exponential of the form:

$$I(t) = I_0 e^{-Bt} + C \tag{6.1}$$

Where *C* is an offset to account for the presence of photoblinking behaviour which is seen after the initial illumination. As the tracked spots are being fitted,

in the ideal case C is the characteristic intensity of a single dye. I_0 is the height of the photobleaching exponential above the photoblinking behaviour, and B is the characteristic photobleaching time. The initial intensity was taken as $C+I_0$. Images showing intensity saturation in initial frames had the frames containingg saturation excluded from the analysis, and an exponential was fitted to the remaining data.

6.2.12 Finding fluorescence stoichiometries

Mean stoichiometries were found from kernel density estimates of the intensity distribution of single tiles divided by the characteristic intensity of a YOYO-1 molecule. The location and full width half maximum (FWHM) of the first peak in the kernel density estimate were used to define a sub region around the peak. If a second peak was identified by the Matlab "findpeaks" function within the FWHM of the first peak the data was truncated to include only the first peak. The sub region around the peak was then fitted with a Gaussian distribution, with the mean value taken as the mean stoichiometry, and the sigma width as the error on the mean stoichiometry.

6.3 Results and Discussion

6.3.1 Seeing damage by gel electrophoresis

Agarose gels are stained with DNA dyes that require UV illumination to fluoresce. In the raw images background is black and high fluorescence regions corresponding to the presence of DNA are white. It is convention to invert the colours for publication, resulting in the apparently decreasing axes on the line profiles presented here.

Firstly, dose times to measurably damage the DNA whilst still maintaining some structure had to be found. Previous work [289][288] has shown that small levels of DNA damage are typically inflicted in the range of a few seconds to a few minutes. Two forms of DNA were tested; linear DNA, similar to previous experiments, and the DNA origami tile, which has a more compact structure. For both DNA forms low levels of damage were seen after 15 seconds of treatment, whilst at 2 minutes considerable damage was seen, in the form of a smear beneath the band for intact DNA in gel electrophoresis (see figure 6.5).

It is interesting that both the linear lambda DNA and the compact form of DNA origami show damage over the same timescales, implying that the folded structure does not protect the DNA from damage. However, as this technique

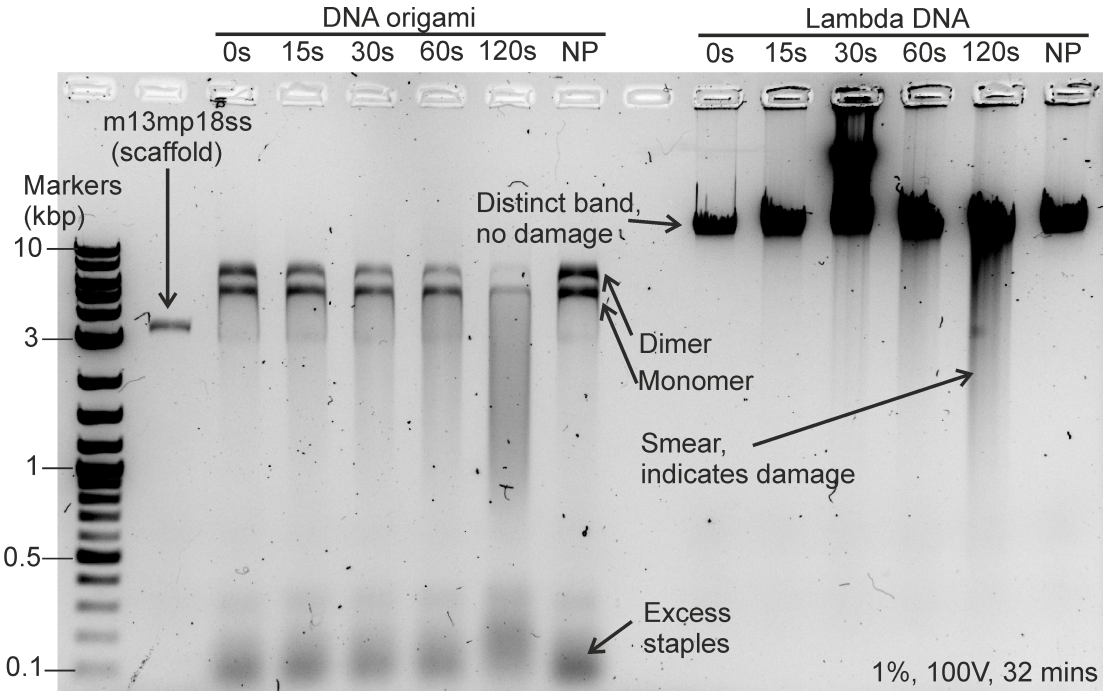

Figure 6.5: Gel electrophoresis of DNA origami and lambda DNA under LTP treatment times of 0-120s. NP indicates control samples where the plasma was not ignited.

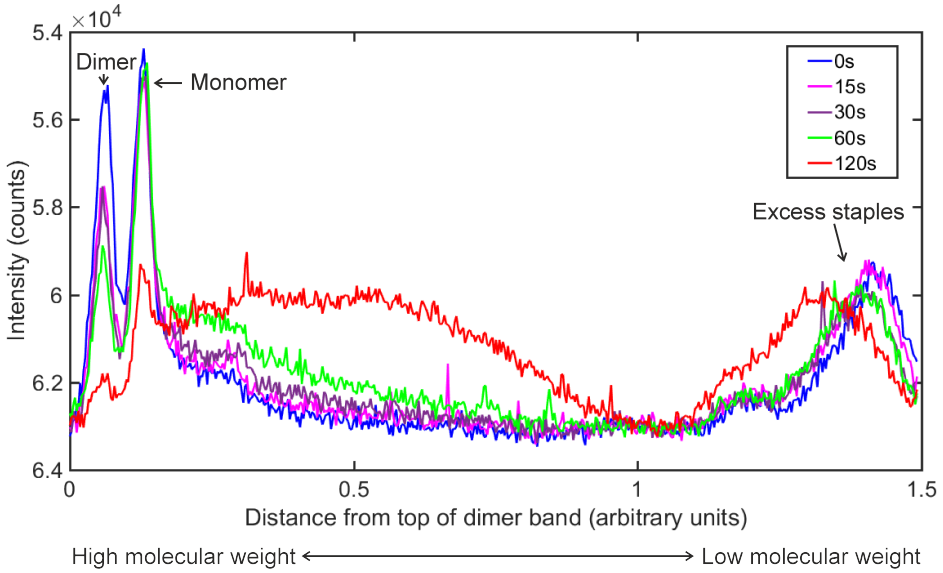

Figure 6.6: Line profiles of the intensity of the DNA origami damage shown in figure 6.5 at different treatment times.

Sample	Volume recovered (µl) ± 0.05
Control (nothing to prevent evaporation)	8.65
Parafilm M	10
Humid environment	8.65

Table 6.2: Recovered volumes of solution (and measurement errors) when a 10 µl droplet of lambda DNA in buffer is plasma treated for 30 seconds.

is not quantitative there may be real differences. It can be seen that in the samples where the plasma was not ignited but the gas flow was on (marked with NP in the figure) that damage has not been inflicted, ruling out shearing due to air flow as the cause of the damage.

In line profiles taken vertically through the DNA origami damage samples (see figure 6.6) the change from sharp band to extended smear is clearly visible. The intensity of the dimer band drops quickly as the damage level is increased, indicating a drop in the molecular mass of DNA present in the band. However, the monomer band stays at relatively similar intensity until 120s of damage. This suggests that the dimers are broken into monomers, maintaining the monomer population. Between the bands formed by the monomer and the staples there is a clear increase in intensity as treatment times are increased, showing the increase in DNA damage.

At the other end of the gel the staples can be seen to run less distance from the well as the dose is increased. This is likely due to the increased salt concentration as the buffer is evaporated during treatment (after two minutes of treatment, 10µl of buffer is reduced to 8.65µl). High sodium chloride concentrations can reduce the distance travelled by staples due to electrostatic screening effects [302]). Whole tiles are not affected as distance travelled in gel electrophoresis is not linearly dependent on mass, and higher molecular weight molecules will not exhibit a noticeable shift (the staples are mostly 32 bp, whilst the DNA origami scaffold is 7249 bp).

As mentioned above, the plasma jet evaporates the solution containing the DNA. Two methods to prevent evaporation were tested: maintaining the sample in a humid environment by keeping a wet paper towel close to the sample during treatment, and covering the sample with Parafilm M. 10 µl of sample were treated, and the recovered volumes are given in table 6.2. The humid environment did not reduce the evaporation, but the Parafilm M did.

Unfortunately, on running an electrophoretic gel it is clear that whilst the Parafilm M prevents evaporation, it also prevents the DNA from being damaged by the LTP (see figure 6.7). The line profiles shown on the right of this figure shown very similar traces for the control and the humid environment,

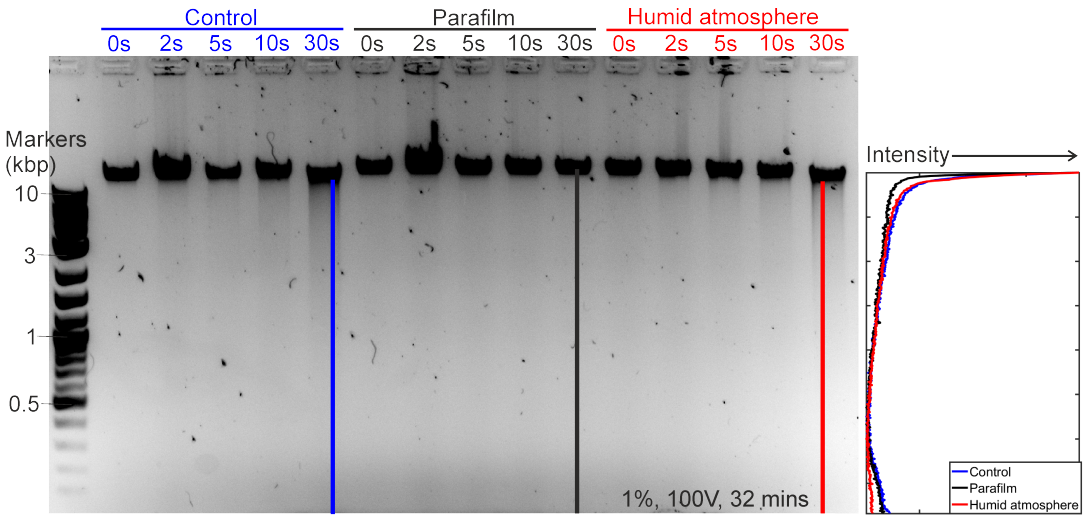

Figure 6.7: LTP damage to lambda DNA testing two methods to prevent evaporation. Gel electrophoresis for the 5 LTP treatment times is shown for both evaporation prevention methods and the control. Line profiles from the 30 s treatment are shown right, control in blue, Parafilm M in black and the humid environment in red. NP indicates the samples where the plasma was not ignited.

but the intensity of the Parafilm M sample drops to the background level almost immediately after the band for intact origami, indicating the presence of very much less damage than the other two conditions. Neither of the tested methods prevented evaporation whilst allowing DNA damage, and the remaining experiments were performed with evaporation allowed to occur.

Microscopy experiments on DNA origami require that once the sample has been damaged it does not disintegrate before imaging. There are two likely causes of the DNA disintegrating further after damage: 1) Reactive species produced by the plasma continue to exist in the buffer and cause further damage 2) the origami disintegrates due to thermal forces producing the energy to remove staples from the structure.

Tris is known to be a radical scavenger [303], and so synthesis buffer, which contains Tris, should act as a radical scavenger. To test this the DNA was treated indirectly; the buffer was treated with plasma, and then treated buffer was added to DNA immediately post treatment. Figure 6.8A shows a gel comparing direct treatments (where the DNA is in the buffer under the LTP) and indirect treatments. Whilst damage can be seen for the direct treatments, there is less smearing present under the gel bands for the indirect treatments than for even 15 s of direct treatment, and the small smudges seen might be artefacts of the gel as they do not cover the full width of the gel lane.

The experiment was repeated with larger dose times for the indirect treatments, up to 300 s. In the gel run immediately after treatment the band

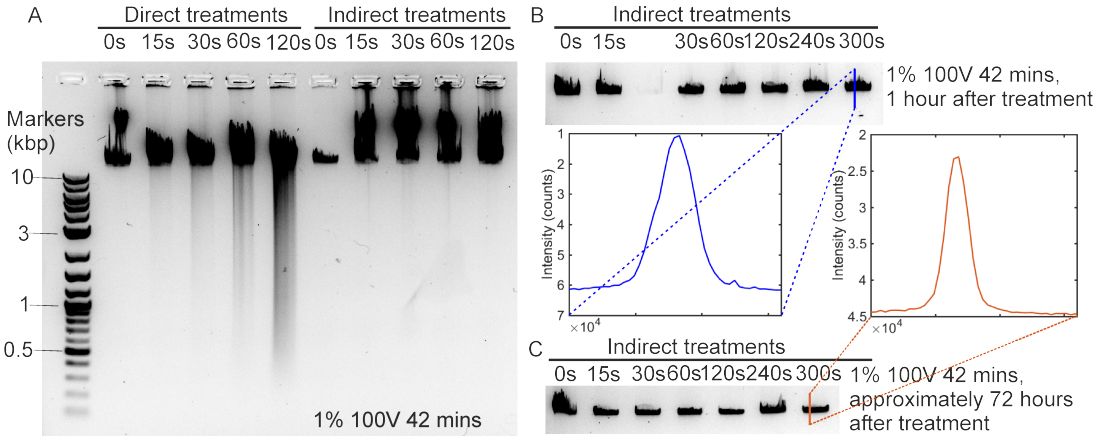

Figure 6.8: Direct and indirect damage to lambda DNA. (A) Gel electrophoresis comparing direct and indirect treatments of lambda DNA. (B) Indirect treatments of lambda DNA with line profile of damage at 300 s treatment of the buffer. (C) The same samples as in (B) after 72 hours, with line profile of band after 300 s of buffer treatment.

for the lambda DNA added to the buffer treated for 300 s shows no smudge indicating damage. Further, a line profile through the band is symmetric with no tail on the lower molecular weight side to indicate damage (see figure 6.8B). The indirectly treated samples were kept at 4°C for 72 hours, and a new gel was run (see figure 6.8C). Again, no smudge to indicate damage was seen and a line profile through the 300 s of indirect treatment band was symmetric with no extended tail to indicate damage.

Taken together, these results indicate that no further damage occurs to the DNA due to the presence of radicals in the buffer after treatment, however, the possibility that DNA origami may disintegrate due to random separation of the staples from the scaffold must also be investigated.

It has previously been observed via AFM that purified DNA origami begins to dissociate after 2-3 days [301]. Wickham achieved this result using the unmodified version of the DNA origami tile used in this work, but without deliberately inflicting damage. Gel electrophoresis is not as sensitive as AFM, but it can indicate whether or not we see large scale degradation.

In figure 6.9A three damage levels are compared between experiments performed 24 hours apart. There is no visible difference between the samples in this time. Figure 6.9B shows the sample run after 24 hours in 6.9A after less than one hour, showing that DNA damage is caused. Unfortunately, due to small differences in the constituency of the agarose gel it is impossible to quantitatively compare samples run in different gels. The samples which are shown immediately after damage in figure 6.9A are shown after a further 5 days (120 hours) of storage at 4°C in figure 6.9C. Qualitatively these gels all

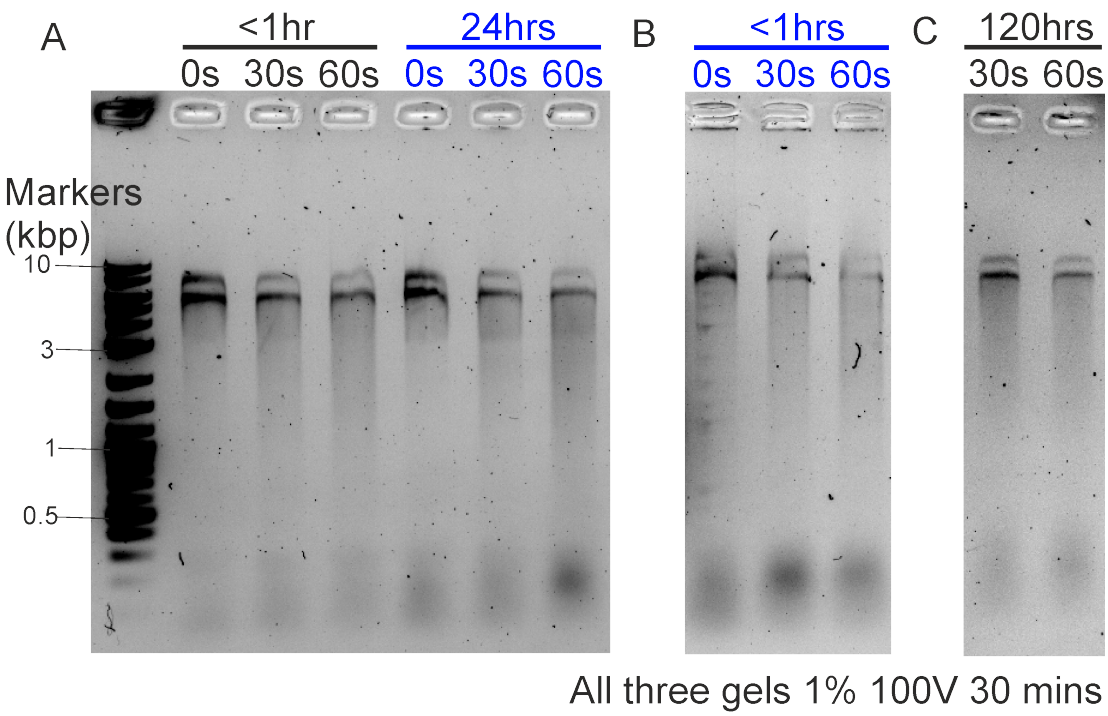

Figure 6.9: Gel electrophoresis of damaged DNA origami after different time intervals. (A) DNA origami that has been treated with LTP less than an hour previously (black), and 24 hours previously (blue). (B) The DNA origami shown after 24 hours in (A), less than an hour after initial damage. (C) DNA origami samples shown after less than an hour in (A), run in another gel after 120 hours.

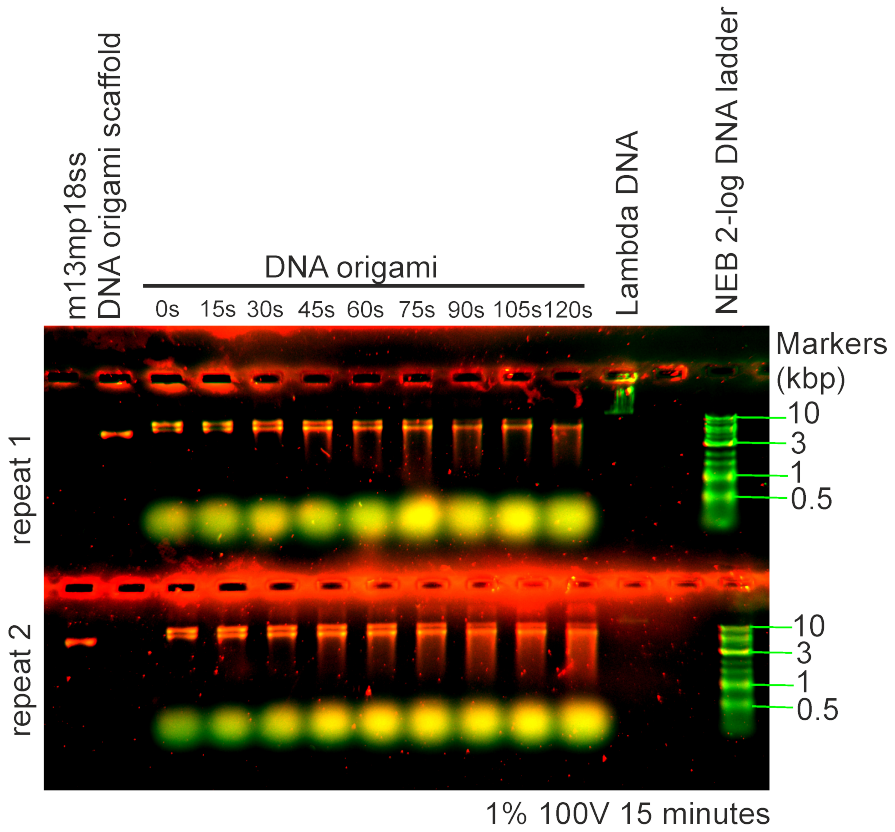

Figure 6.10: Acridine orange stained 1% agarose gel of DNA origami treated with LTP for different treatment lengths with two rows of DNA samples. The gel was run at 100V for 15 minutes and post-stained with acridine orange.

look similar apart from small differences that are likely due to differences in the composition of the gel. Whilst disintegration of the DNA origami tiles over these timescales is not observed, all DNA origami experiments were performed within 24 hours of the purification which removes the excess staples.

6.3.2 Acridine orange staining of agarose gels

Acridine orange fluoresces red when bound to single stranded DNA and green when bound to double stranded DNA. It is therefore expected that if the DNA origami is correctly formed it will fluoresce green when stained with acridine orange.

DNA origami was damaged for treatment times between zero seconds and 2 minutes in 15 second intervals. Two samples of each damage condition, the double stranded ladder and the DNA origami scaffold were run in the same agarose gel (see figure 6.10). In this image the contrast levels of the red and green overlaid images of the gels have been adjusted for clarity, and show that the origami are stained more red than the double stranded DNA ladder

and lambda DNA. In fact, the DNA origami are closer in colour to the images of the single-stranded scaffold, which is red. Quantitatively, the ratio of the intensities in the red and green images gives more insight, although it can only be compared within gels, as post staining with acridine orange can achieve different levels of dye uptake and using the same exposure times for images of different gels is not feasible.

Gel electrophoresis is often affected by small imperfections or contaminants in the gel, which can be seen as small flecks or fibres when imaged, but cannot be removed. Their small size compared to the bands makes them distinguishable from the DNA signal, but they are difficult to correct for, and so technical repeats are often performed, as in the two rows of samples in this gel. The bands of the DNA origami monomer contain less contaminants in the lower repeat (repeat 2). Due to the pixelated nature of the gel images, the gel bands not being perpendicular to the image orientation, the presence of contaminants in the gel and non-uniform background the ratios of the red/green intensity ratio have large errors, but the general trends can tell us something. The single-stranded scaffold has a red/green ratio of 1.35 ± 0.09, whilst the purportedly double-stranded bands of the ladder give values in the range 0.59-0.84 (± 0.09), unfortunately the lambda DNA was contaminated. Applying the same red/green ratio measure to the monomer band of the DNA origami gave values with a range of 1.17-1.25 (± 0.09) and mean of 1.22. The values of the red/green ratio for the double and single stranded DNA do not overlap and the DNA origami has a ratio that falls between the values, closer to the values for single stranded DNA. This suggests that the acridine orange binds to the DNA origami as if it is single stranded.

The results of acridine orange staining the gel containing origami are unexpected, as we expect the DNA origami to be mostly double stranded, at least for undamaged origami. Several single stranded and double stranded DNA samples were chosen as controls. In particular two staples that were predicted to have low or high secondary structure by NUPACK [304] were investigated. Staples with high secondary structure have self complementarity and are expected to appear double stranded and therefore green, whereas staples with low secondary structure have low self-complementarity and are expected to appear as single stranded, red molecules. Whilst Rothemund [113] did minimise the secondary structure of the staples, some remains. The staple r3t10f is predicted to have low secondary structure and r3t22f is expected to have high secondary structure.

The stained and fluorescently imaged agarose gel is shown in figure 6.11. The red to green ratios for this gel cannot be compared to the previous gel,

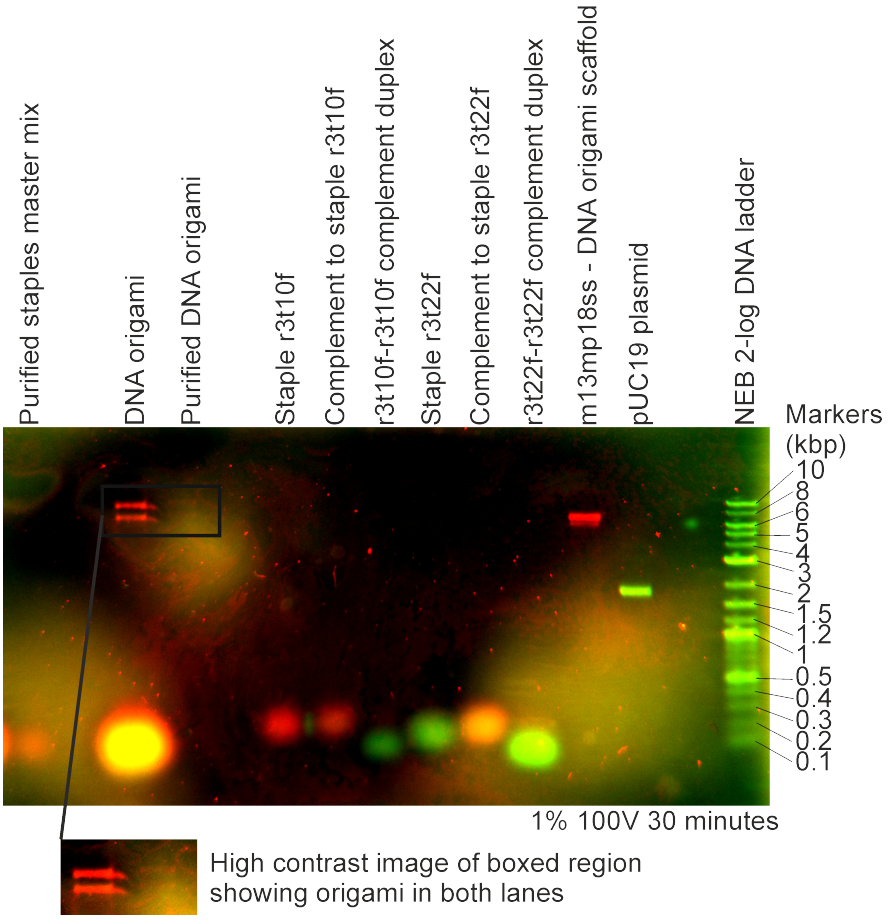

Figure 6.11: Controls for acridine orange staining of agarose gels. With the exception of the DNA origami, the samples are all known to be single stranded (red) or double stranded (green).

but can be compared with each other. The samples expected to be double stranded have red/green ratios in the range 0.61-0.78 ($\pm$0.08), whilst the scaffold and r3t10f staple have ratios of 2.05 and 1.41 ($\pm$0.08) respectively. The samples expected to have components of both single and double stranded behaviour have ratios of 1.33 for the monomer origami band, 1.22 for the r3t10f complement and 1.12 for the r3t22f complement (all $\pm$0.08). The ratios are again non-overlapping for the single and double stranded cases. The samples expected to exhibit intermediate behaviours lie between the two.

Staple r3t10f stains as red (R/G = 1.41 ± 0.08), as expected due to the predicted low secondary structure, and the complement also stains as single-stranded (R/G = 1.22 ± 0.08). Due to the low molecular weight of the staples they can diffuse into the agarose separating the lanes, and the hybridisation between the two single stranded staples is seen in the area of green fluorescence between the bands. Staple r3t22f, expected to have high self complementarity, stains green (R/G = 0.75 ± 0.08), as expected and its complement stains red (R/G = 1.12 ± 0.08). These strands do not hybridise in

the area between the lanes as the high self-complementarity of r3t22f prevents this. The annealed staples and complements both stain green, as expected (0.75 and 0.85 ± 0.08 for the r3t10f and r3t22f duplexes respectively). The duplexes run further from the well than the single strands. This is likely because duplex DNA tends to have a more rigid structure than single stranded DNA for a given number of base pairs which facilitates its migration through the agarose matrix.

The two plasmids that are available commercially stain as expected, with m13mp18ss staining red and running to around the expected molecular weight of 7249 bp (R/G = 2.05 ± 0.08). The plasmid PUC19 stains green (R/G = 0.71 ± 0.08), as expected for a double stranded DNA, but, due to being circular, it runs further from the well than linear DNA of the same length (the PUC19 plasmid is 2686 bp). The ladder is double stranded, staining green (R/G range for the ladder bands 0.61-0.72 $\pm$ 0.08), and gives molecular weights for dsDNA without secondary structure.

As in the previous gel the origami staining showed intermediate character between single and double stranded behaviour, and so this is not experimental error. There are several possible reasons for this: the tightly packed DNA origami structure may prevent the green fluorescence intercalation mode seen in double stranded DNA [305], thereby causing electrostatic binding to the phosphate groups of the DNA, as is seen in the red fluorescence mode usually associated with single stranded DNA [148]. Concentration-dependent effects in the binding of acridine orange to DNA have recently been shown [306] but would not show appreciable differences for the concentration ranges used in the agarose gel, and so cannot be the cause of this result. We know the origami are well formed from the AFM images of intact origami, so it is not single stranded, though it is possible that the dye binds to the gaps between staples or to the region of scaffold that is unused (although this is unused because it contains secondary structure, so it should also show green fluorescence). However the spaces between staples are not really single stranded; whilst the DNA is not ligated, there are no unpaired bases. The tightly packed nature of the origami preventing intercalation and instead allowing phosphate binding is the favoured explanation.

This suggests two potential models for DNA intercalator binding to DNA origami. One is that all YOYO-1 binding sites through the DNA origami tile can be filled. Each DNA origami tile contains 6480 spaces between base pairs. Due to the origami not being ligated there are gaps between staples, so there is an important distinction between the number of base pairs (6912) and the number of spaces between base pairs. Assuming the reported maximum

labelling of 1 YOYO every 8 base pairs [178][307][308] there are 810 dye binding sites. Assuming instead that only the outermost helices of the DNA origami tile can be filled the maximum stoichiometry is 67 dye molecules.

6.3.3 Fluorescence microscopy: The intensity of a single YOYO-1 molecule

To calculate the number of fluorescent molecules attached to a substrate the initial intensity of the labelled substrate and the intensity of a single fluorescent molecule must be known. This number will vary depending on factors such as exposure time and illumination intensity and must therefore be measured under the conditions the microscopy is to be performed at.

To find the characteristic intensity of a single YOYO-1 molecule fluorescence microscopy images of DNA origami with sparse YOYO-1 labelling were used. Using a low labelling density increases the proportion of tracked molecules that have low stoichiometry, and using frames after a period of initial illumination reduces the observed stoichiometry further due to photobleaching. In figure 6.12A a histogram of such molecules has a peak at around 380 counts, giving an initial estimate for the single molecule intensity.

To corroborate this value the pairwise distance (in intensity units) can be calculated between the found spot intensities, and the histogram plotted. Whilst it is expected that there will be a peak at the single molecule intensity, at low signal to noise ratios the noise can obscure the single molecule peak, although higher multiples of the single molecule intensity can be seen. The noise peak can be created when two localisations contain the same number of fluorophores but differ in intensity by noise values. Here, the situation is further complicated by the known photoblinking behaviour of YOYO-1. In figure 6.12 the pairwise distance distribution shows a peak at around 730 counts, and also a wide peak around 220 counts. These are likely the two molecule peak and the noise level. Taking the fast Fourier transform of this distribution gives the common step sizes - in figure 6.12C these are around 360 and 750 counts, in agreement with the value found from the histogram in figure 6.12A. However, care must be taken as the fast Fourier transform evaluates only a predefined set of intensity values, rather than a continuous range, and so these values should be treated as ballpark figures.

Comparing the values from the three methods suggests a single YOYO-1 fluorophore intensity of $\sim$370 counts. A raw intensity against time trace is shown in figure 6.12D; single molecule photobleaching steps can be discerned at approximate multiples of 370. To preserve steps in the intensity traces whilst

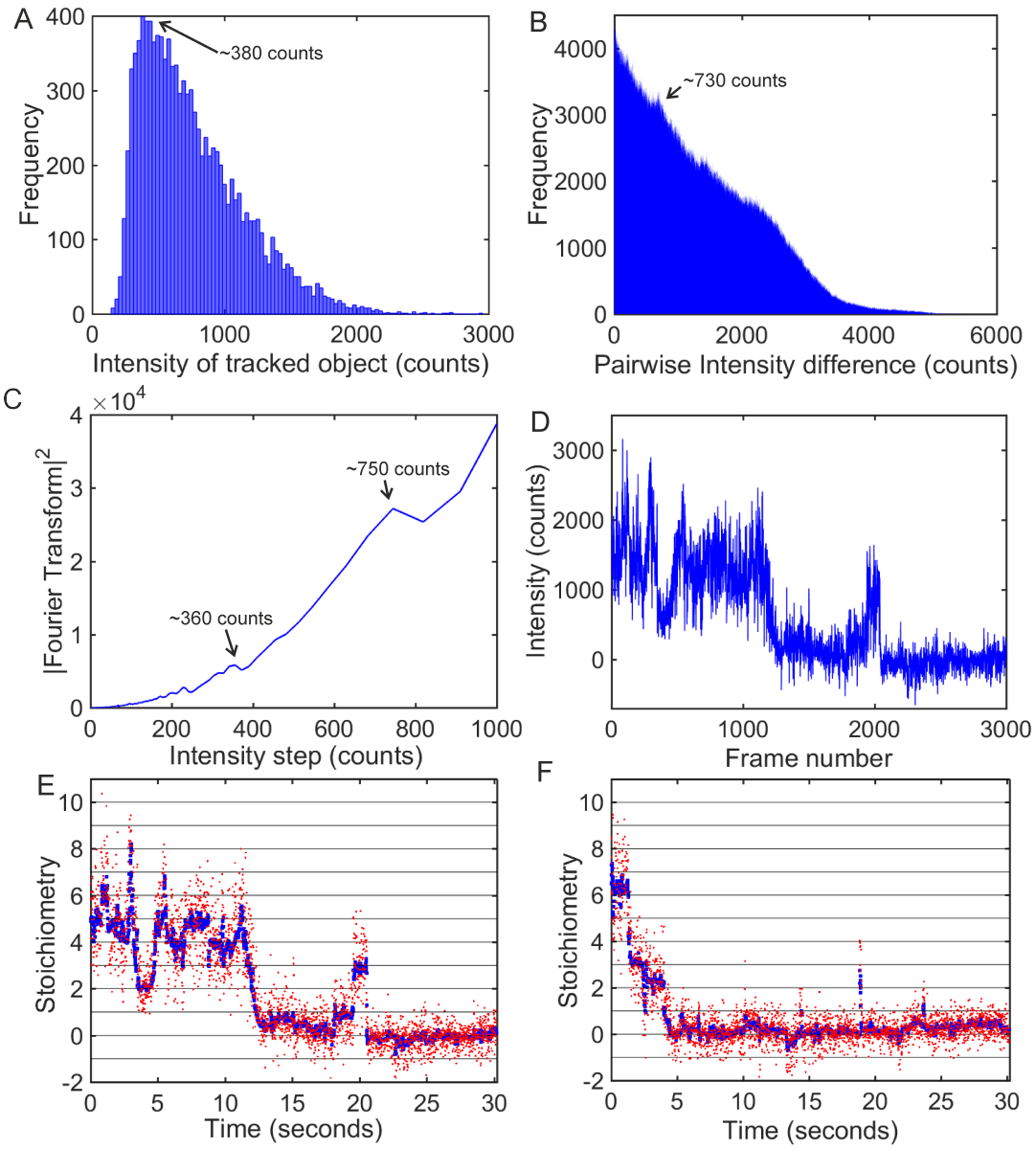

Figure 6.12: Finding the intensity of a single YOYO-1 fluorophore. (A) Histogram and (B) pairwise distribution of fluorescence intensities of a sparsely labelled DNA origami tile. Arrows indicate peaks in the distribution. (C) Fourier transform of pairwise intensity distribution shown in (B). (D) Intensity against time trace for a sparsely labelled DNA origami tile; (E) and (F) data (orange) and Chung-Kennedy filtering (blue) of data in (D) and a second trace showing stepwise bleaching events.

filtering to remove noise, raw intensity traces were Chung-Kennedy filtered [43] using a two window filter, with windows of length 50 and 10 frames to account for photoblinking and photobleaching behaviours. These values were chosen from preliminary exponential fitting to the entire bleach trace, and were chosen to pick out the broad photobleaching behaviour, and photoblinking events lasting more than a few frames. The results of applying this filter to two intensity traces are shown in figure 6.12E,F.

The Chung-Kennedy filter is seen to produce steps which lie at multiples of 370 counts, in agreement with the values found from multiple traces. Also seen are departures between two defined intensity levels. These are likely due to fluorophores photoblinking on a timescale shorter than the ten frame window. These occurrences are seen more frequently at the beginning of the trace than at the end, suggesting they are removed by photobleaching. The intensity of a single YOYO-1 fluorophore was taken to be 370 counts (range of values 356-383).

To acquire a large number of images, fluorescence microscopy data of different LTP damage conditions was acquired over several microscopy sessions. The correction for uneven illumination, and the characteristic intensity of YOYO-1 were evaluated each time. The ratio between the noise levels with and without the laser on should also be the same as the ratio of the characteristic intensities.

The noise levels can be evaluated by examining unilluminated regions of the field of view, with the dark current (signal due to residual current when no illumination is present) subtracted. Noise was measured in 8x8 regions 2 pixels in from the edge in each corner of a typical image. The very edge pixels were excluded as there are often dead pixels in the outermost rows. The measured mean intensity values and standard deviations are given in table 6.3. Assuming that the standard deviation of each dye molecule is the same and that difference in illumination is due to a constant factor, α, more photons being collected from each molecule, the variance in the noise should increase by a factor proportional to $\alpha^{\frac{1}{2}}$, which should be the same as the ratio of characteristic intensities. For two sessions of experiments described here this ratio is found to be 2.9$\pm$0.2 ($\pm$ standard error (s.e.)), corresponding to a characteristic intensity in the range 1000-1150 counts for the second session, compared to the 370 counts found in session one.

This was verified by applying the same Chung-Kennedy filter parameters used above to long (100 second) acquisitions from the second session. The pairwise intensities of the filtered trace were calculated, showing a plateau at 1000, and a rise in the associated fast Fourier transform also at this

Damage time (s)	Noise with laser off (counts per pixel, ±s.d.)	Noise with laser on (counts per pixel, ±s.d.)
0, 60	98.6 (±4.5)	149.3 (±8.7)
15, 30	97.6 (±2.1)	514.1 (±68.8)

Table 6.3: Average noise and dark current values for two days of data collection.

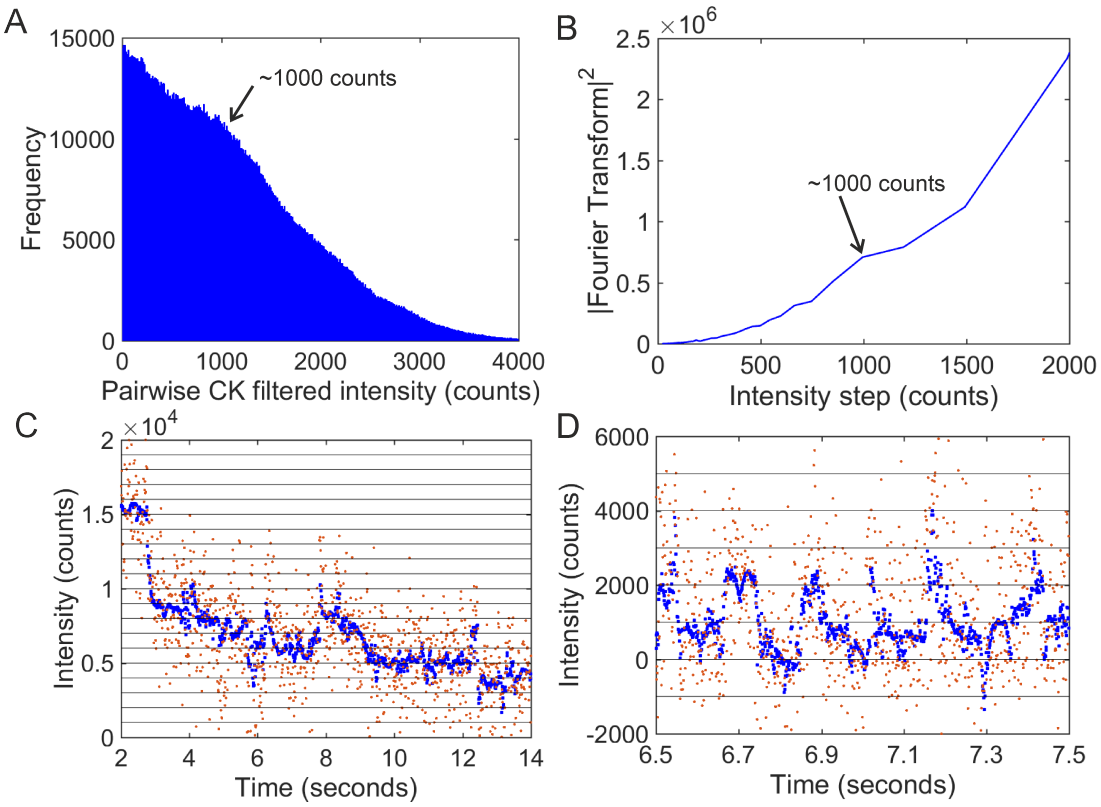

Figure 6.13: Characteristic intensity of YOYO-1 labelled DNA origami treated with LTP for 15 or 30s. (A) Pairwise distance distribution of intensity steps in the Chung-Kennedy filtered intensity trace and (B) associated fast Fourier transform. (C) and (D) show Chung-Kennedy filtered (blue) data traces (orange) at 30 and 15s with steps at multiples of 1000 counts.

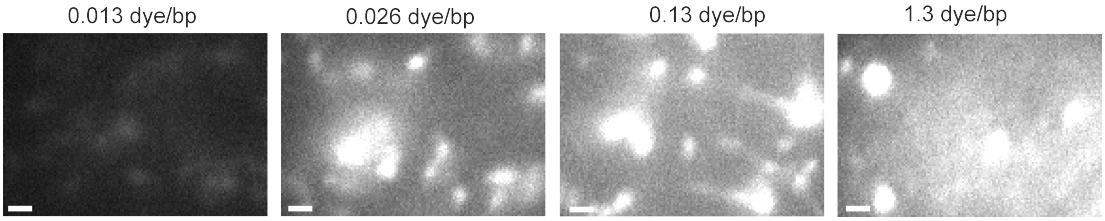

Figure 6.14: Lambda DNA with different dye/bp ratios. All images are displayed with the same contrast levels and scale bars are 1 µm.

intensity (see figure 6.13A,B). The signal is expected to be more noisy for this measurement than for the previous one as this was performed at 100x higher dye concentration meaning that there is a higher intensity contribution from the photoblinking of YOYO-1. Chung-Kennedy filtered traces acquired at 15s and 30s also show steps at multiples of 1000 counts (see figure 6.13C,D).

6.3.4 Fluorescence microscopy at different YOYO-1 concentrations

DNA can be labelled with different densities of dye. To determine the change in fluorescence signal caused by damage, each available dye binding site must be occupied. The most commonly reported maximum dye loading of YOYO-1 onto DNA is one YOYO-1 every eight base pairs [178][307][308]. The value found for the related dye TOTO of one every six base pairs is sometimes quoted from Spielmann [309], and a small value of one YOYO-1 every four base pairs has been reported on very short DNA [310].

To determine the required concentration of dye, experiments were performed with lambda DNA and DNA origami tiles. Figure 6.14 shows the first full illumination image of lambda DNA labelled with different dye/bp ratios of YOYO-1, imaged on the microscope designed in chapter 3 at 10 ms exposure times. Qualitatively, there is little difference between the images of 1.3 dye/bp and 0.13 dye/bp, suggesting that a maximum labelling density may have been reached. At 0.013 dye/bp the labelling density is low and the DNA appears blurry, whilst at 0.0013 dye/bp only sparse fluorescent signals were seen, which were not visible at the contrast level chosen for the figure (and are not shown). The apparent saturation at high dye loading suggests, in line with the literature, that one YOYO-1 requires around eight base pairs to bind on linear DNA.

Linear DNA such as lambda can be sheared during the preparation of these samples, and so to quantify the level of DNA labelling it is more instructive to examine undamaged DNA origami than linear DNA. The DNA tethering

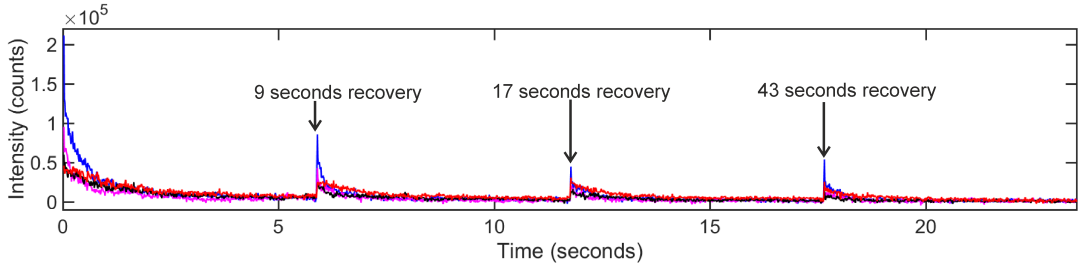

Figure 6.15: Intensity recovery trace for 4 DNA origami tiles labelled with YOYO-1 at 2 dye per base pair. Four 500 frame acquisitions with variable (indicated) recovery times are shown for the same four tiles.

project utilised the photoblinking behaviour of YOYO-1, and it must be seen whether this occurs here. In the DNA tethering project the time for a dye to unbind from DNA was found to be of the order 10^6 seconds; if this is the case, the intensity of a labelled DNA origami tile should recover after short ($\sim$seconds) periods of illumination followed by darkness. To test this, four acquisitions of 500 frames at 10 ms exposure times (11.755 ms cycle time) of DNA origami and YOYO-1 at $\sim$ 2 dye per base pair were acquired in TIRF microscopy at an angle of incidence of $65\pm1.5°$. The acquisitions were of the same region of view with varying recovery intervals, as seen in figure 6.15.

The fluorescence intensity does indeed recover between acquisitions, as indicated by the presence of 3 peaks after the initial fluorescence decay. As these experiments were performed in TIRF microscopy the illumination intensity is not uniform across the field of view and so the intensity of the different tiles and their bleaching rates cannot be meaningfully compared.

To find the YOYO-1 concentration required for maximum dye labelling images of DNA origami tiles incubated with concentrations of YOYO-1 in the range 0.05-5 µM were acquired. These images were tracked as described in the methods section above. The mean and standard error on the intensity for all tracked molecules at each concentration was found, as given in table 6.4. The largest value of the standard error (1894) was used as a kernel width to produce a kernel density plot of the dye stoichiometry (see figure 6.16A), and the stoichiometry was found by Gaussian fitting to the first peak, as detailed in section 6.2.12 above (see table 6.5). This method assumes that the first peak in the distribution corresponds to the single tile peak, based on the AFM result that undamaged tiles are well-folded. Values higher than the stoichiometry of a single tile can be caused by multiple tiles being within the same diffraction limited spot.

The initial intensity of single tiles as a function of concentration is shown in figure 6.16B. The intensity of the tiles shows a steep rise with concentration

Concentration	Mean intensity (counts)	Standard error (counts)	Number of tracks, n
5µM	32,500	762	452
1µM	49,200	1894	326
500nM	7,900	746	67
50nM	13,000	1746	169

Table 6.4: Initial intensity statistics for YOYO-1 concentrations in the range 0.05-5 µM.

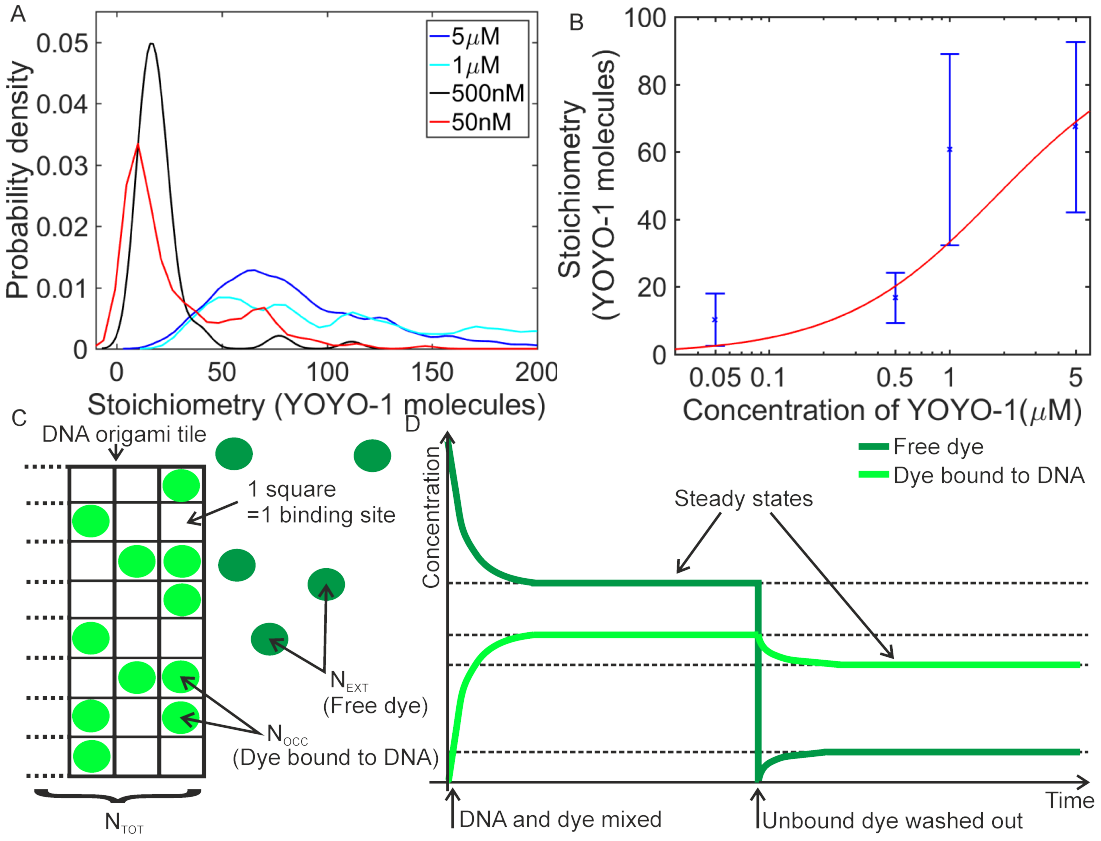

Figure 6.16: Labelling of DNA origami with YOYO-1 at 0.05-5 µM concentrations. (A) Kernel density estimate of the stoichiometry of dye labelling on DNA origami tiles. (B) Analysis of single tile stoichiometry at four concentrations (error bars ± standard deviation of fitted Gaussian), with a fit from the simple model shown schematically in (C). (D) Schematic diagram showing the behaviour of the dye concentrations of the free and DNA bound states during microscopy sample preparation.

Concentration	Peak stoichiometry (YOYO-1 molecules)	Error (s.d. of fitted Gaussian) (YOYO-1 molecules)
5µM	67.4	25.2
1µM	60.8	28.3
500nM	16.8	7.4
50nM	10.3	7.7

Table 6.5: Stoichiometry of YOYO-1 molecules for dye concentrations in the range 0.05-5 µM with standard deviations from a Gaussian fit to the first peak of the kernel density estimate.

before reaching a saturating intensity. This behaviour can be simply modelled [311] by considering the system shown in figure 6.16C: Here the conversion between free and bound dye ($[N_{EXT}]$ and $[N_{OCC}]$) over time, t, is modelled by the equations:

$$\frac{\mathrm{d}[N_{OCC}]}{\mathrm{d}t} = k_{bind}[N_{EXT}]\big([N_{TOT}] - [N_{OCC}]\big) - k_{unbind}[N_{OCC}] \tag{6.2}$$

$$\frac{\mathrm{d}[N_{EXT}]}{\mathrm{d}t} = -\frac{\mathrm{d}[N_{OCC}]}{\mathrm{d}t} \tag{6.3}$$

where k_{unbind} and k_{bind} are the unbinding and binding constants, and $[N_{TOT}]$ is the total number of dye binding sites. These equations can be solved and produce single exponentials (see appendix F). When a steady state is reached the number of binding sites that are occupied is:

$$[N_{OCC}] = \frac{[N_{EXT}][N_{TOT}]}{\frac{k_{unbind}}{k_{bind}} + [N_{EXT}]} \tag{6.4}$$

Fitting this model to the data in 6.16B gives a value of the dissociation constant of 1.83 µM (range 0-3.71 µM), and a maximum dye labelling of 94 (range 36-152) YOYO-1 per DNA origami tile, although the intrinsically high spread of the stoichiometry values resulted in a relatively low goodness-of-fit statistic (R^2=0.6940). A dissociation constant of 1.83 µM is higher than that found by Reuter *et al.* (12.1 nM) [308] on stretched lambda DNA, but lower than that found for a completely relaxed molecule in 1M NaCl (35.7 µM) by Biebricher *et al.* [179]. Biebricher *et al.* found that under tension more YOYO-1 molecules can intercalate into DNA and their lifetime bound to the DNA is increased. The bound state lifetime is k_{unbind}^{-1} so the off rate decreases as the bound lifetime increases. In a DNA origami tile the structure introduces more tension than is present in simple native DNA, and additionally some scaffold crossovers (where a staple changes between helices, effectively changing rows)

are under tension. The fitted value found here for the unbinding coefficient, for DNA under light tension, lies between the values found for stretched lambda DNA and relaxed DNA, but the errors on the fitted value are large.

The situation in this experiment is not as simple as this model. Free dye is flowed into the chamber containing immobilised DNA origami tiles, incubated for 5 minutes and then washed out. This results in a bound dye concentration over time as shown in figure 6.16D. For the simple model to be valid either the unbinding constant needs to be small such that the concentration of occupied states has made little progress towards the new steady state when it is imaged, or the new steady state needs to vary very little from the previous steady state.

If we assume that a steady state is reached during the initial dye incubation period; which it should be based on reported values of the binding coefficient [149], we can call the time the wash is performed t=0. If we further assume that all of the free dye is washed out then $[N_{OCC}]_0 = [N_{OCC}] + [N_{EXT}]$, where $[N_{OCC}]_0$ is the steady state value reached during the incubation of dye (see equation 6.4). Equations 6.2 and 6.3 hold true at all times, and so the steady state concentration of occupied dye binding sites after the dye has been washed out is found to be (taking the physical solution to the quadratic equation):

$$[N_{OCC}] = \frac{b - \sqrt{b^2 - 4[N_{OCC}]_0[N_{TOT}]}}{2} \tag{6.5}$$

where;

$$b = \frac{k_{unbind}}{k_{bind}} + [N_{OCC}]_0 + [N_{TOT}] \tag{6.6}$$

Where a subscript $_0$ indicates the value of the quantity before the excess dye was washed out. Values of the dye concentration during incubation, $[N_{EXT}]_0$ as 5µM and a reported dissociation constant for stretched DNA, $\frac{k_{unbind}}{k_{bind}}$ as 12.1 nM [308] can be substituted in. The concentration of available dye binding sites can be estimated (assuming one dye molecule every eight base pairs) as the concentration of the DNA origami tiles, multiplied by the number of base pairs per tile and divided by eight. From this, the change in $[N_{OCC}]$ between the two steady state values is found to vary by 18%. Whilst this is a large change the model is overly simple for the situation, as the DNA origami tile has many more constraints on its structure than a free strand of DNA, and tension has been shown to increase the bound state lifetime [179]. Increasing the bound state lifetime would decrease the fractional difference between the states.

The measured value for the maximum stoichiometry of a tile (67.4±25.2) is consistent with the model where only the outermost helices of the DNA

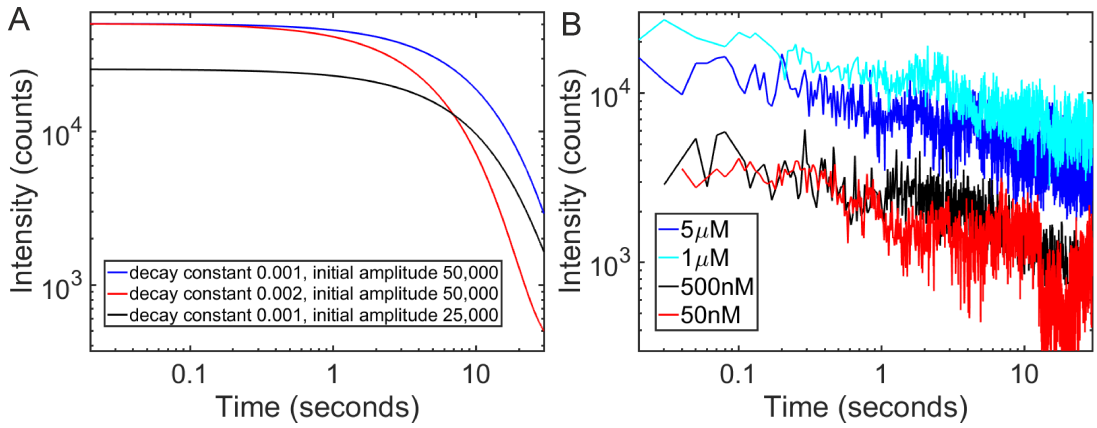

Figure 6.17: Intensity vs time traces for long acquisitions. (A) Theoretical examples of exponential decays with varying decay constants and initial amplitudes. (B) Sample intensity against time traces until bleaching of YOYO-1 labelled DNA origami with dye concentrations 0.05-5 µM, showing gradients at long times that are insensitive to concentration.

origami tile are accessible to intercalating dye (67 dye molecules). The structure of DNA origami is quite tightly packed, with this particular design having measured helix separations of 0.9-1.2 nm [113]. The size of TOTO (a bis-intercalating dye very closely related to YOYO-1) is larger than this gap, at around 2 nm [309]. It is plausible that the inner helices of the origami structure are not accessible to YOYO-1. If only the outermost helices of the DNA origami tile are accessible to YOYO-1 then inflicting damage will open up the structure and the fluorescence intensity will increase. However, if the dye can bind to the entire undamaged tile, we expect a decrease in the fluorescence intensity as the base pairs are damaged and less YOYO-1 can bind.

Another explanation for the low observed stoichiometry could be self-quenching, caused when two molecules are so close together they can exchange energy non-radiatively. This occurs on similar length scales to FRET, that is a few nm [312]. One obvious sign of quenching would be a peak in the intensity versus dye concentration graph, which is not observed here. Additionally, if quenching was occurring, the intensity would not simply decay exponentially, as once a certain bleaching level had been obtained, corresponding to an effective rise in dye separation, the intensity would increase, changing the decay constant. To investigate this long (>30 second) image stacks were acquired at different concentrations (sample traces are shown in figure 6.17).

These traces have a low decay constant, and are displayed on log-log plots to emphasize the early time points before single molecule bleaching statistics cause deviations from the exponential. This way of displaying exponential

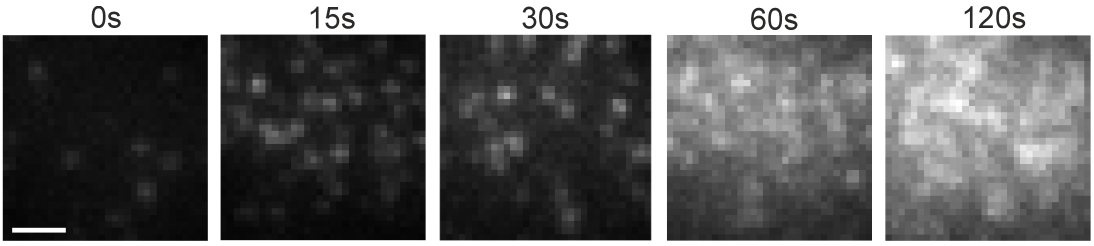

Figure 6.18: Fluorescence microscopy images of YOYO-1 labelled DNA origami after LTP treatments of 0-120 s displayed at the same contrast levels. Scale bar 1 µm.

data is not easy to interpret intuitively. In figure 6.17A example traces are shown for exponential decays with different starting intensities and the same decay constant (blue and black) and the same starting intensity and a larger decay constant (red and black). The traces where the decay constant is the same show the same shape, with a 'shoulder' occurring at the same time point, and noticeably, the decays are almost linear at later times, converging to the same point. The theoretical trace with double the decay constant has a very different gradient in the linear region compared to the other graphs. The four example traces from the real data (see figure 6.17B) all show a similar gradient in the linear part, indicating they have similar decay constants and providing further evidence that quenching is not present in these experiments.

6.3.5 Fluorescence microscopy of damaged DNA origami

Preliminary fluorescence microscopy data of DNA origami damaged with LTP for a range of treatments 0s-120s was collected (see figure 6.18). Compared to the experimental procedure detailed above both the DNA origami and YOYO-1 were washed through the tunnel slide at double the concentrations above (giving the same dye:bp ratio, but a more dense sample), and the final wash step before imaging was only 20 µl of purification buffer. Other than this, all steps were as detailed above.

Qualitatively, an increase in fluorescence of individual tiles is seen as the level of damage is increased. This suggests that LTP treatment increases the number of dye binding sites, favouring the model with only the outermost helices available for YOYO-1 binding.

The stoichiometries of YOYO-1 labelled DNA origami tiles can be evaluated using a kernel density estimate, once again using the largest standard error on the mean dye labelling across the conditions as a kernel. The kernel used here is 4.77 dye, from the standard error on the 60 s data. The stoichiometries and errors are again calculated by fitting a Gaussian to the first

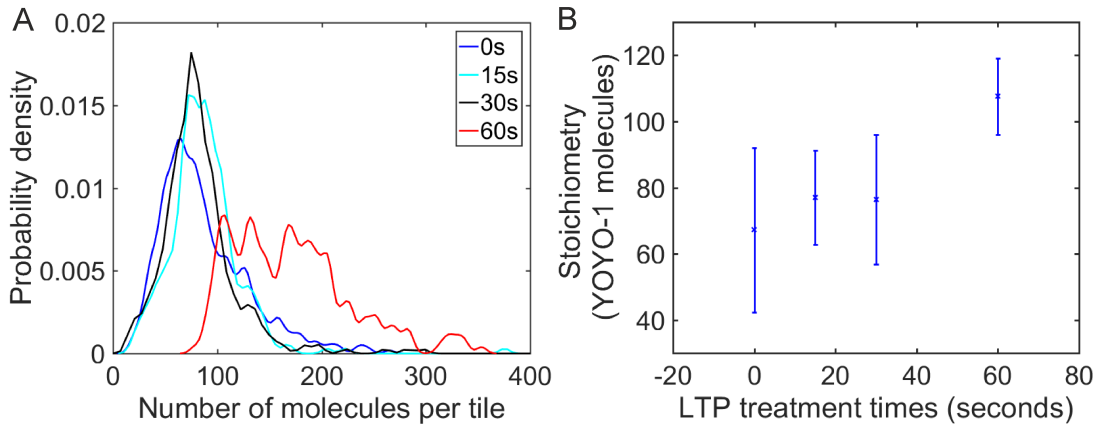

Figure 6.19: Stoichiometry of damaged DNA origami tiles after LTP treatment for 0-60s. (A) Kernel density plot of stoichiometry at varying LTP doses and (B) Stoichiometry as a function of LTP damage, error bars are ±1 s.d. of the Gaussian fitted to the first peak of the kernel density plot.

Damage time (s)	**Stoichiometry (YOYO-1 molecules ± s.d. of fitted Gaussian)**	**Number of tracks**
0	67.2 (±24.8)	452
15	77.1 (±14.2)	281
30	76.4 (±19.6)	319
60	107.6 (±11.5)	224

Table 6.6: Stoichiometry of LTP treated DNA origami labelled with YOYO-1.

peak (see section 6.2.12). As can be seen in figure 6.19A, the stoichiometry of the YOYO-1 labelled DNA origami tile increases as the LTP damage level is increased.

Qualitatively, the data for 0, 15 and 30 s all show a prominent peak, in contrast to the 60 s data which has multiple peaks. This suggests that tiles are mostly intact as one molecule up to 30 s but the plasma damage allows more YOYO-1 to intercalate. Figure 6.19B plots the stoichiometry of YOYO-1 molecules as a function of LTP treatment time. The values are also given in table 6.6. The number of dye binding sites increases as the DNA origami tile becomes damaged, suggesting that as the tile is treated with LTP the structure is opened up and allows YOYO-1 to intercalate, supporting the model of dye binding to only the outermost helices of the undamaged tile. After 60 s of LTP treatment the number of intercalated dye has approximately doubled from the initial values, suggesting that twice as much DNA helix is accessible for YOYO-1 binding. It is possible that the origami has cleaved into two along the long axis, which would expose double the number of DNA helices.

It is worth noting that Cosa *et al* [313] have shown that YOYO-1 is not

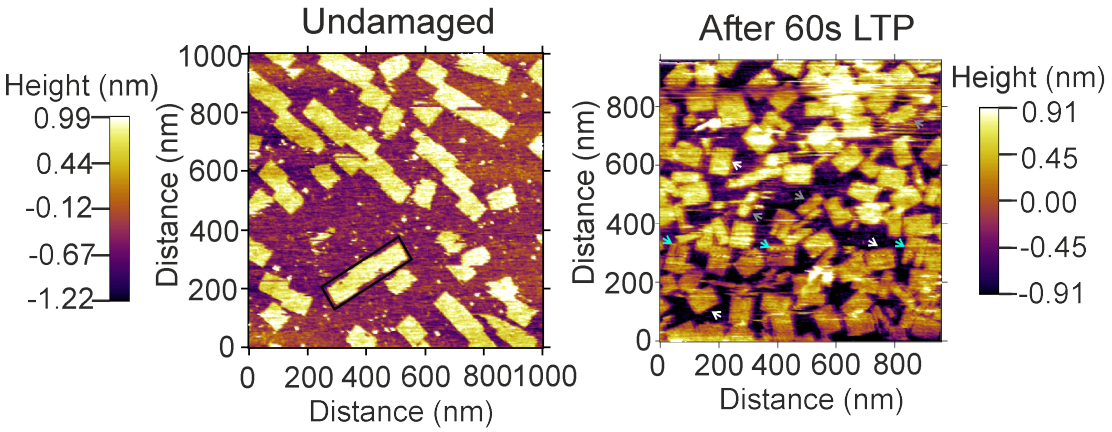

Figure 6.20: AFM images of DNA origami tiles undamaged and after 60s of plasma treatment. The black box indicates three tiles stacked end-to-end. In the 60s treated sample the white arrows indicate intact tiles, the grey arrows indicate broken tiles and the cyan arrows indicate fractured tiles.

suitable for fluorescence lifetime imaging microscopy (FLIM) to assess DNA damage. This is due to biexponential decays of fluorescence intensity when bound to dsDNA, probably due to cooperative binding effects between the two linked chromophores. If this had an effect in the first second after illumination it would serve to systematically alter the initial stoichiometries found in this work, however, it would not alter the trend showing an increase of intensity with an increase in damage.

6.3.6 Atomic force microscopy

Sonia Contera performed AFM on DNA origami tiles that were undamaged, and also on tiles that had been damaged with LTP for 60 seconds, see figure 6.20. Qualitatively several observations can be made: compared to the undamaged DNA origami tiles which tend to end-stack to form ribbon shapes, the damaged tiles are usually singular and separated, consistent with the observation of the decreasing intensity in the dimer band seen in gel electrophoresis. Many damaged DNA origami tiles were seen to be incomplete, but often two apparently complementary parts of a tile can be seen in close proximity. It appears that the tiles tend to break along the long axis, as many fragments appear to be of the same length as the long axis of the tile. Very few holes in the DNA origami are seen, implying that single staples are not removed during damage, as omission of single staples has previously been shown to produce small holes in the DNA tiles [113].

This suggests that DNA origami tiles fracture along the long axis after 60 s; this would give a doubling of the fluorescence intensity at this time, as

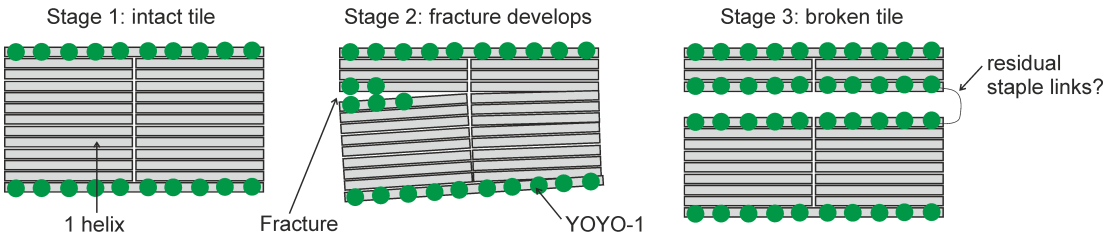

Figure 6.21: Schematic diagram of proposed model for the method of damage to a DNA origami tile with potential accessible YOYO-1 binding sites indicated. For clarity only half the real number of helices are shown, YOYO-1 is shown schematically rather than at real concentration and individual staples between helices are omitted.

is observed. The following model of the damage to DNA origami by LTP is proposed: LTP causes damage to the DNA origami structure producing a nick in one of the helices which becomes a target for further damage, propagating the fracture. This is shown in figure 6.21. This would allow the YOYO-1 stoichiometry of the DNA origami tile to increase as damage was applied, with a doubling in value when the two pieces of tile become separate, at around 60 s.

6.4 Conclusions and Future Directions

DNA origami tiles have been damaged with LTP. Gel electrophoresis reveals that the dimer portion of tiles is decreased as the LTP treatment time is increased, in agreement with AFM imaging which shows the number of dimers to be reduced by LTP damage.

Acridine orange staining of DNA origami in agarose gels gives a surprising result - that the DNA origami stains as if it is single stranded, possibly suggesting that the inner helices of the tile are not accessible to intercalating dye due to their tight packing. Fluorescence microscopy of YOYO-1 labelled DNA revealed a low stoichiometry, consistent with only the outermost helices of the DNA origami tile being accessible to the dye (at the reported maximum packing ratio of one YOYO-1 per eight base pairs). These two results taken together suggest that only the outermost helices of the DNA origami tile are accessible to intercalative dye binding. As the LTP dose was increased the number of YOYO-1 bound to the origami in fluorescence microscopy was seen to increase, reaching approximately double the initial value after 60s. AFM imaging of DNA origami treated for 60s shows the presence of closely spaced objects with the same long axis length as the full DNA origami tile.

YOYO-1 perturbs the DNA environment around it, with each bisintercalation causing unwinding of the helix by 106° [307] and extension of

0.68 ± 0.04 nm [179]. If the dye binds only to the external helices it will cause distortion of the DNA origami tile, which may be a source of damage in the fluorescence imaging.

Future work should quantify the qualitative observations made on the AFM images to refine the model of the method of damage to DNA origami tiles, and a Gaussian mixture model could be used to fit the fluorescence stoichiometry data as an alternative to the analysis presented here. Further ahead, it would be interesting to examine other DNA binding dyes, both intercalators and minor groove binders, and to change the length of the helices on the edges of the DNA origami tile.

Chapter 7

Summary and Future Directions

7.1 Summary of Findings

This thesis has developed and optimised single-molecule imaging for applications covering several themes in biophysics. Instruments and assays have been produced that will become part of machines capable of correlative microscopy; in this case combining both fluorescence microscopy and magneto-optical tweezers. High speed single-molecule imaging was compared against FCS and FRAP; three different biophysical techniques for measuring diffusion coefficients of small molecules in aqueous environments. This highlighted the advantages of single-molecule imaging over ensemble methods. Single-molecule tracking was then used to measure a parameter of biological importance, the diffusion coefficient of the chemokine CXCL13, in an *ex vivo* tissue section at extremely high temporal resolution. Finally single-molecule tracking was applied to the high stoichiometry case of DNA origami labelled with the intercalating dye YOYO-1. Imaging DNA origami after varying durations of LTP treatment lead to the proposal of a model for the method of DNA damage to DNA origami.

7.1.1 Fluorescence microscope design

A bespoke microscope for single-molecule imaging was developed and applied to a range of biological questions. In chapter 3 an LED lightbox with monochromatic power outputs in the tens of milliwatt range was tested against a supercontinuum white light laser for application to single-molecule microscopy. LED light sources of this type are relatively new to the market. When directly coupled to the epifluorescence port of the microscope excellent uniformity of illumination was achieved. However, LEDs have an extended source and cannot be collimated. Despite compensation, power losses from

the diverging LED beam made it unsuitable for propagation through the beam shaping optics required in bespoke applications.

To use the supercontinuum laser as a light source for a bespoke microscope it must be filtered. Incident radiation causes photodamage of the sample, and so should be limited to the required excitation wavelengths. Two filtration methods were tested; gradient linear filters were found to be the most suitable technique as they did not introduce dispersion and could be positioned in a highly reproducible manner compared to the prism filter method.

7.1.2 DNA immobilisation and tethering

The dual colour imaging capability was applied in work towards creating a correlative fluorescence and magneto-optical tweezers microscope. It is becoming increasingly common to use two biophysical techniques simultaneously on the same sample to record complementary information. Examples include AFM and fluorescence microscopy [314][315][316][317][318][319], correlative light and electron microscopy (CLEM) [320][321], and combined fluorescence microscopy and optical tweezers [322].

Surface passivation and conjugation of a paramagnetic bead to a DNA tether were demonstrated. The dynamics of DNA tethered to a coverslip at one end were seen, with tethering verified by two colour microscopy. This work shows promise for a combined fluorescence and magneto-optical tweezers microscope to monitor dynamic DNA processes *in vitro* in real time.

A simple assay for immobilising DNA was developed and used to localise single molecules of the photoblinking intercalating DNA stain YOYO-1 *in vitro* to a sub-diffraction limit localisation precision of 40 nm at video rate sampling. Under the same conditions SYTO-13, a minor groove binding dye with a lower single molecule intensity, was found with a localisation precision of 62 nm, still far below the diffraction limit. This data was used to test the ADEMS tracking code used in all further work.

7.1.3 Comparison of SMT, FCS and FRAP

There are three commonly used techniques to determine diffusion coefficients of fluorescently labelled molecules; single molecule tracking, FRAP and FCS. Whilst there exist many reviews comparing all three techniques (two examples are [270] and [271]), experimental data is much rarer (see for example [123]). The three techniques were compared on the test molecule of BSA-AF647 in

10% Ficoll 400, as BSA is a well known standard.

It was found that $D_{FRAP} < D_{SMT} < D_{FCS}$, in general agreement with other studies [272][273][231]. The value obtained by SMT ($9.3 \pm 0.4\,\mu m^2 s^{-1}$), was the closest to the theoretical value ($12.3 \pm 0.1\,\mu m^2 s^{-1}$), with the value found by FRAP ($7.1 \pm 0.3\,\mu m^2 s^{-1}$) slightly lower, and the value for FCS slightly higher ($18.8 \pm 0.3\,\mu m^2 s^{-1}$), but all 3 results varied by less than an order of magnitude.

The advantage of SMT over FCS and FRAP, apart from giving a value of the diffusion coefficient closest to the theoretical expectation, is that it can be performed at very low physiological concentrations, where the influence of noise drowns the ensemble measures. Additionally, although not applied here, SMT can be used to investigate spatial inhomogeneity in a medium or tissue - for example hotspots for transient binding.

7.1.4 Single-molecule fluorescence tracking of chemokines

The experiments with BSA-AF647 showed single-molecule tracking to be the technique best suited to measuring diffusion coefficients at low concentrations, so the diffusion coefficients of two chemokines in the extracellular matrix mimic of collagen were measured using single-molecule tracking. To the author's knowledge, this is the first application of sub-millisecond nanoscale precise tracking of single biological molecules labelled with nanoscale fluorescence probes in a tissue-like environment whose viscosity is less than that of a lipid bilayer by 2-3 orders of magnitude. Imaging with a cycle time of 0.65 ms the diffusion coefficients of CXCL13-AF647 and CCL19-AF647 were found to be $6.2 \pm 0.3\,\mu m^2 s^{-1}$ and $8.4 \pm 0.2\,\mu m^2 s^{-1}$ respectively. To the author's knowledge, this is the first measurement of the diffusion coefficients of these molecules in a physiologically relevant medium, and this was enabled by the high imaging speed.

Further, the diffusion coefficient of CXCL13-AF647 was measured at $\sim$500 Hz in B cell regions of *ex vivo* lymph node sections and found to be $6.6 \pm 0.4\,\mu m^2 s^{-1}$, in agreement with the value found in collagen. This parameter will be incorporated into an *in silico* model of the lymph node which is being developed with the aim of reducing the number of animal experiments by allowing optimisation stages of experiments to be performed *in silico*. Eventually the model will be applied to medical questions of disorders affecting the lymph node.

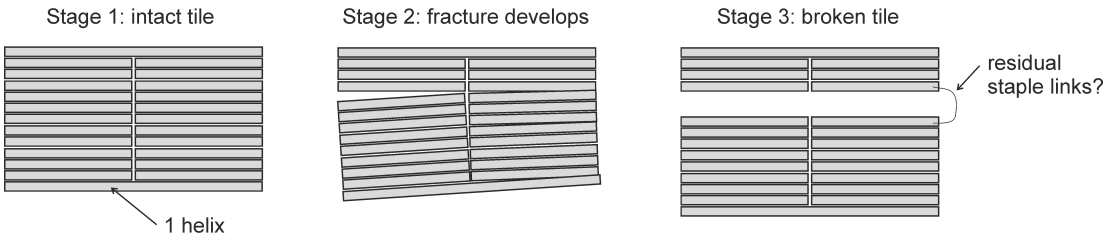

Figure 7.1: Proposed model for the method of damage to a DNA origami tile. For clarity only half the real number of helices are shown, and individual staples between helices are omitted.

7.1.5 Low temperature plasma damage of DNA origami

To extend the ability to investigate the stoichiometry of fluorescently labelled objects LTP damage of DNA origami was investigated with fluorescence microscopy, as well as agarose gel electrophoresis and AFM imaging. DNA origami tiles contain many dye binding sites in an area far smaller than the diffraction limit, and so offer the opportunity to measure high stoichiometries of dyes. As the LTP dose is increased, damage to the DNA origami can be seen via agarose gel electrophoresis, where it no longer forms a well-defined band. Additionally the dimer band contains less mass, suggesting that damage prevents end-stacking of the DNA origami tiles. The DNA origami also stains as if it is single-stranded when bound to acridine orange, suggesting the inner regions of the DNA origami tile are not accessible to the intercalating moieties.

Fluorescence microscopy reveals that before damage 67.4±25.2 YOYO molecules can bind to each DNA origami tile. This is consistent with a model where 1 dye binds every 8 base pairs along the outermost helices of DNA origami. As the damage is increased the stoichiometry of the DNA origami tile increases, suggesting that the damage allows more dye molecules to bind to the structure. After 60 s of treatment the DNA origami has approximately double the intensity of the undamaged DNA origami. AFM imaging before damage shows many well-formed tiles which end stack. After 60 s of damage the damaged tiles do not end stack and fragments of DNA origami tile which appear to have the same length long axis as the undamaged tile can be seen. This suggests that the DNA origami tile cleaves along the long axis of the tile, which would be consistent with a doubling of fluorescence intensity over the 60 s timescale.

A model in which a nick between two helices of the DNA origami tile propagates into a crack and eventually breaks the tile was proposed based on the observations (see figure 7.1).

7.2 Future Directions

The results presented in this thesis develop single-molecule fluorescence microscopy in several directions - multiplexing with other techniques, extremely high temporal resolution *in vitro* and in *ex vivo* tissue slices, and investigating high fluorescence stoichiometries. Single-molecule biophysics is a fast-moving field and below are described possible future developments from the work presented in this thesis that incorporate developments from other research groups.

7.2.1 Development of bespoke microscopes

The microscopes built in this thesis are all limited to two-dimensional microscopy. Whilst this has been the workhorse of single molecule tracking up to this point the field is moving towards three-dimensional tracking to follow single-molecules *in vivo*. There are several methods available to achieve three-dimensional tracking. Of these the highest temporal resolution is gained with techniques which modify the point spread function (PSF) in the acquired images, making the PSF larger than the diffraction limited PSF. The acquired images are then compared to a lookup table to determine the distance of the molecule from the imaging plane. The drawback of this class of techniques is that a large separation between individual molecules is required to ensure that the PSFs of different molecules do not overlap.

Whilst astigmatic imaging using a cylindrical lens to distort the PSF to an ellipse along the x- or y-axis (depending on its position relative to focus) is one of the simplest of these methods to implement, it is not suitable for measuring dynamics at speeds at which motion blur of the particle can occur, as the two effects have similar appearance. For imaging fast-moving particles such as chemokines in 3D a two-lobed PSF such as the double helix point spread function [323] would be extremely attractive, and these have recently been extended to multiple colours [324] making them suitable for studying the interaction of multiple labelled proteins.

7.2.2 Combining fluorescence microscopy and magneto-optical tweezers

The combination of fluorescence imaging and magneto-optical tweezers using the fluorescence microscope developed in this thesis is now being pursued by my colleagues from the Leake group, Zhaokun Zhou and Jack Shepherd.

They have developed and characterised the magneto-optical tweezers, and have designed multiple DNA tethers to which they have added torsional constraints. They are in the process of optimising the conjugation of DNA constructs to beads.

Since our work was published it has been shown that tension affects the binding of intercalating dyes to DNA [179]. In particular it has been shown that overstretching of YOYO-1 labelled DNA does not cause unbinding of the dye, and that very similar results are found for other intercalating dyes [179]. The results of these researchers suggest that YOYO-1 stabilises the DNA against unwinding a melting- a result that will affect studies of enzymatic DNA on YOYO-1 labelled DNA.

A member of the family of minor groove binding SYTO dyes has been shown to be less perturbative to nuclear structure *in vivo* than intercalating dyes [186]. The effect of minor groove binding dyes on DNA under tension should be characterised using the combined fluorescence and magneto-optical tweezers microscope. If minor-groove binding dyes are found not to stabilise the DNA they would be suitable for studying the interaction of molecules of interest, such as gyrase, on fluorescently labelled DNA.

7.2.3 Tracking CCL19 in lymph node tissue slices

The microscopy and data analysis techniques applied in the measurement of the diffusion coefficient of CXCL13 in the B cell follicle of the lymph node can be extended not only to the measurement of diffusion coefficients of other chemokines, but to other molecules of similar size, in the same or different tissues. The obvious route is to measure the values of the diffusion coefficients of other chemokines, comparing their relative values. With this approach there is scope to find out something more fundamental about the humoral immune response, giving the opportunity to progress medical science and do good. The most obvious targets continuing from this point would be to measure the diffusion coefficient of CCL19 in T cell regions of the lymph node, and to achieve this with sub-millisecond imaging. A second route would be to investigate other small complex molecules, perhaps that exhibit transient binding to their environment, and to investigate the spatial heterogeneity.

7.2.4 Further testing of the DNA origami damage model

There are two courses of action for the DNA origami damage project: looking at how DNA origami are damaged, or characterising properties such as the

'kill radius' of the LTP jet. The proposed method of damage to DNA origami could be tested by changing the length of the outer helices on the DNA origami tile or by changing the dye. Inflicting LTP damage on DNA origami tiles with changes of helix direction, such as the triangle in Rothemund's original work, would show whether damage does indeed propagate between helices.

To move towards characterising the DNA damage caused by the plasma source it is important to know if densely or loosely packed DNA is affected differently by the plasma, and this can be investigated using different, possibly 3D DNA origami shapes. To test the "kill radius" of the jet, DNA origami would have to be patterned onto a coverslip and damaged *in situ*.

Further work with the existing data should analyse the AFM images to determine which origami shapes are present after damage. For the fluorescence data, the existing method to calculate the intensity of a single tile and the associated error may be improved by utilising a Gaussian mixture model to fit the populations of different tile geometries.

Appendix A

Foldscope

Highly specialised microscopes, such as those built during this work are inherently fixed to the optical benches they are built upon. The Prakash lab at Stanford have developed the Foldscope [325], a paper based, portable microscope that costs less than $1 to manufacture and uses a microlens (a lens less than 1 mm in diameter that can be manufactured to high optical quality for low cost, due to its size). Additionally, the foldscope has low weight, takes standard microscopy slides, and fits into a pocket.

The Leake group received two Foldscopes and assembled them each in about 15 minutes. A completed foldscope can be seen in figures A.1A,B. The images in figure A.1C,D,E,F were acquired with a smartphone directed through the eyepiece. As can be seen in figure A.1C the microscope can allow a high level of resolution, but this is not uniform across the entire field of view. This is likely due to the small size of the lens and the flexibility of the paper sample stage. However, in the centre of the field of view the resolution is high, and this could be useful for teaching purposes or for medical applications such as the diagnosis of malaria [326] in remote areas, or where more expensive equipment is not available. The images captured with the foldscope also convey the difficulty in recording images through the microlens, whilst the low cost of the microlens has enabled this low-cost microscopy technology, it also has limitations in quality. Whilst useful for a person making a diagnosis, it is more difficult to capture an image that might need to be sent for analysis by a medical expert elsewhere.

The design of the microscope, with eyepiece directly in front of the light source makes it incompatible with laser illumination, as this would damage the eyes of the user. However, LED illumination, as explored in this thesis, would provide a low cost route to combining the foldscope technology with diagnostic stains used to identify proteins associated with specific conditions.

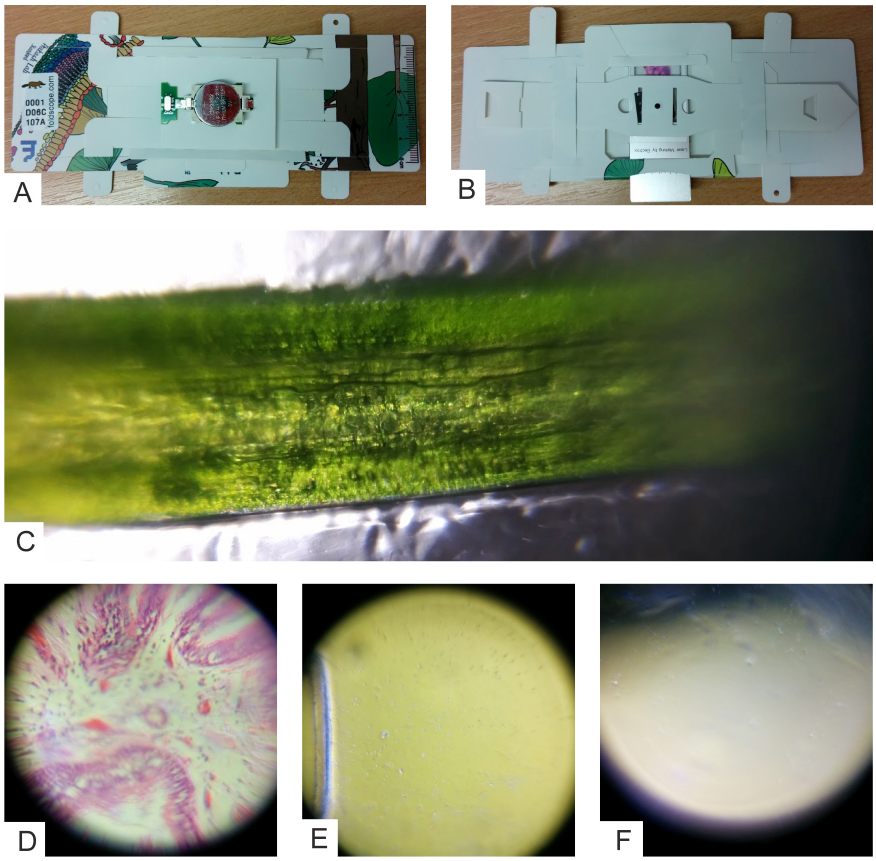

Figure A.1: Foldscope structure and sample images (A) Foldscope from light source side. (B) Foldscope showing sample stage and imaging lens. Images taken with the foldscope: (C) blade of grass (D) stained tissue section (E) fluorescent beads (F) yeast (Image of yeast by Adam Wollman and Erik Hedlund). Scale bars are not given as the pixel size in the camera phones used to acquire the images was unknown.

Appendix B

pH microscope

The emission spectrum of fluorescent probes is dependent on their local environment. Many engineered fluorescent proteins have been developed to have a very large tolerance to environmental changes to allow their use in physiological conditions different to their native ones (see for example [327]). However, in wild-type GFP (and in mutants over larger ranges) changes to the pH can change the shape and peak wavelength of the emission. This is usually examined in bulk using a fluorimeter, whereas in single cells only fluorescence intensity is monitored [328][329]. Probes that are highly sensitive to changes in conditions can be used to monitor them, for example to look for changes in pH during imaging caused by free radicals which may indicate the end of physiological conditions.

The emission spectrum of single particles can be monitored by using a diffraction grating to turn the image of point-shaped fluorophore into an emission spectrum. Two images must be recorded; one of the fluorophore as a point, and one of the emission spectrum. The change in emission spectrum can be calculated relative to a chosen reference spectrum. This was implemented with Adam Wollman on one of the existing Leake group microscopes.

To operate this on the microscope used for chemokine imaging, a second Andor camera (Andor iXon emCCD+ 897, Andor Technology Ltd.) with a larger pixel array (512×512) was added to the imaging path via a mirror mounted on a flip mount. The image beam was restricted to a slit measuring approximately 256×512 using an adjustable slit to enable the 0^{th} and 1^{st} order images formed by a 300 grooves/mm diffraction grating placed after the slit to be recorded side-by-side on the camera. A focal length 50/100 mm lens pair gives a total magnification of $200\times$ and an effective pixel size of 80 nm. An exposure time of 50.28 ms was used at full electron multiplying gain of 300. This is shown schematically in figure B.1A.

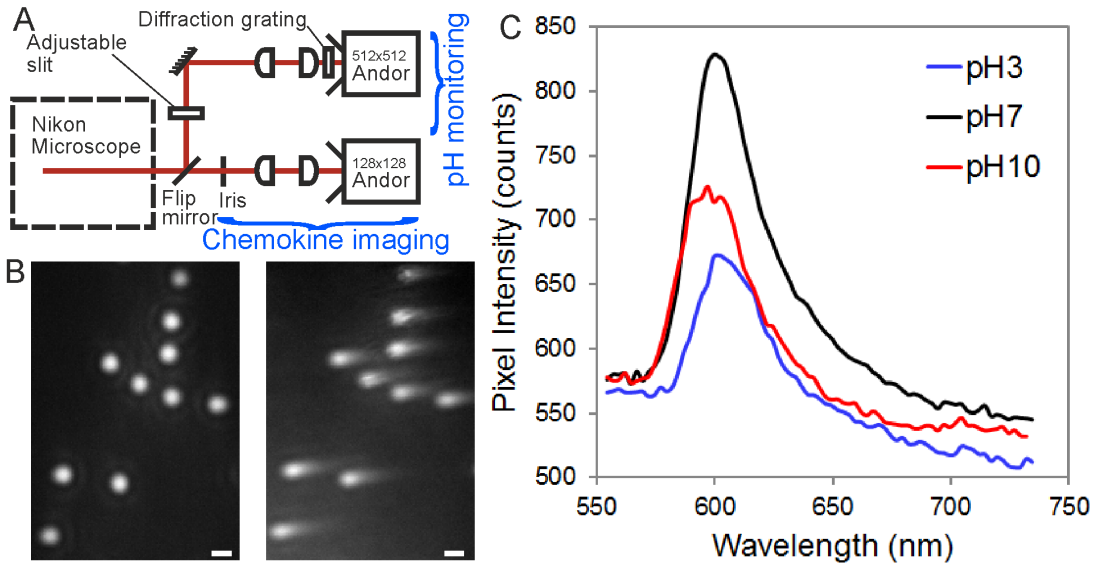

Figure B.1: pH sensitive microscope. (A) Schematic diagram of imaging optics (B) 100 frame averages of red beads at pH 7.1 showing zeroth and first order images. (C) Spectra of first order images under three pH conditions.

The spectra of 200 nm red beads (580/605 nm excitation/emission) in PBS buffer at pH 3.0, 7.1 and 10.0 were compared under illumination at 600 nm, with pH 7.1 used as the reference. Tunnel slides were prepared with a 0.002% solids concentration of beads diluted in each buffer to give sparse coverage. Beads were flowed into the tunnel slide and incubated inverted for five minutes in a humidity chamber to allow the beads to non-specifically adhere to the surface before imaging.

Adam Wollman performed the image analysis (sample images can be seen in figure B.1B) to extract the profiles, shown in figure B.1C. A change in shape and shift in peak pixel position is seen, so the microscope can be used to detect changes in the pH. For greater sensitivity a smaller grating spacing (more grooves per mm) would give a larger spectral shift.

Appendix C

TIRF prism

A prism made from microscope slides and immersion oil was used to calculate the beam angle to ensure TIRF was achieved or to estimate the angle of incidence. When the beam is incident at no angle the centre can be simply determined by the highest intensity in the centre of the beam, which is narrow. However, as the angle is increased projection effects of the collimated Gaussian beam make the beam extended and the centre can no longer be unambiguously determined.

When in a neutral, zero angle position the beam has a diameter of 4 mm on the graph paper in the TIRF prism. The thickness of the prism at this point is measured to be 11.34 mm. By modelling the beam as a cone from the incidence position at the bottom of the prism and having a diameter of 4 mm at 11.34 mm from the incidence position the expected locations of the outer edges of the beam for a given angle can be calculated by geometry, and measured to find the corresponding lens position, as was shown in 3.2.2. This is shown schematically in figure C.1.

In theory, the beam should be perfectly collimated, but real beams cannot be perfectly collimated and the beam was observed to have diverged when projected onto the gantry above the optical table. The beam was also modelled as perfectly collimated, but this gave a worse fit (R^2=0.98257) compared to the cone approximation (R^2=0.98993). A Gaussian beam propagation profile can be considered, but no local focus was observed to justify this. However, over the distances considered here the Gaussian beam profile would be well approximated by a cone. The beam output from the laser fibre head is 2 mm in diameter and undergoes two successive de-expansions to give a radius of 4 µm. The beam is however broadened by the linear filters and is around 14 µm at the sample. The Rayleigh range, z_R, of a Gaussian beam is given by:

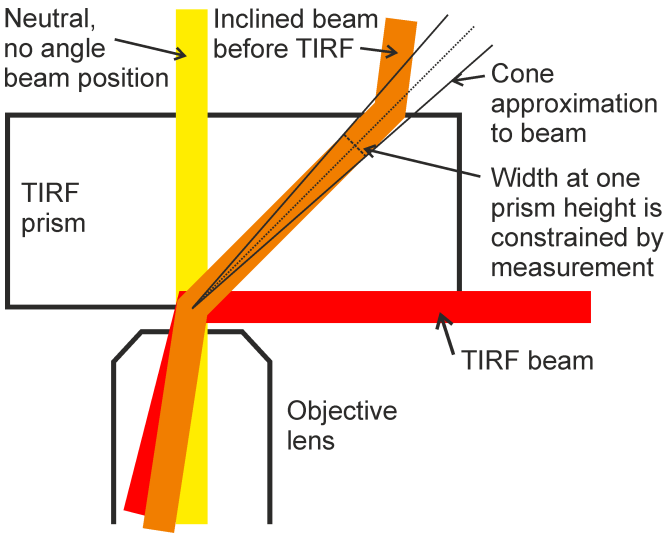

Figure C.1: Schematic diagram showing the approximation used to calculate the TIRF angle.

$$z_R = \frac{\pi \omega_0^2}{\lambda} \tag{C.1}$$

Where ω_0 is the beam radius at the focus and λ is the wavelength of the laser beam. The Rayleigh range can be calculated from this to be around 90 µm, depending on the wavelength used, and when the distance from a focus is much greater than the Rayleigh range the beam radius is well approximated as being linear with relation to distance from the source. The height of the stack of slides is several orders of magnitude higher than this, so even assuming the worst case of a focussed laser beam the cone approximation would hold.

Appendix D

Fit data tables for chemokine fluorescence microscopy data

Simulations of the chemokine fluorescence data were presented in the main text in section 5.3.10. The tables of the results in the main text do not contain error values due to space limitations. The following tables are the same data, but with 95% confidence intervals included.

Table D.1 is the full version of 5.3.

Table D.2 is the full version of 5.5.

$\mathbf{D}_{sim}$	**Fit model**	$\mathbf{D}_1$	%	$\mathbf{D}_2$	%	$\mathbf{D}_3$	%	$\mathbf{R}^2$	χ^2
1.6	1 gamma fit	3.9 (3.94, 3.95)	100 -	- -	- -	- -	- -	0.7839	14.73
	2 gamma fit	3.1 (3.12, 3.13)	63.1 (63.09, 63.21)	11.6 (11.57, 11.61)	36.9 (36.79, 36.91)	- -	- -	0.9865	21.3
	3 gamma fit	0.6 (0.63, 0.64)	2.6 (2.54, 2.57)	3.2 (3.20, 3.20)	63.1 (63.04,63.16)	11.7 (11.69, 11.72)	34.4 (34.30, 34.39)	0.9940	24.7
1.6&10	1 gamma fit	8.7 (8.63, 8.67)	100 -	- -	- -	- -	- -	0.2208	7.42
	2 gamma fit	3.6 (3.60, 3.61)	40.5 (40.42, 40.55)	14.7 (14.66, 14.71)	59.5 (59.45, 59.58)	- -	- -	0.9606	5.24
	3 gamma fit	3.6 (3.55, 3.56)	38.7 (38.65, 38.79)	13.8 (13.77, 13.82)	53.7 (53.50, 54.00)	57.5 (56.00, 59.10)	7.6 (7.40, 7.70)	0.9654	5.25

Table D.1: Results of fitting three functions to the noisy simulated data showing the fitted values of the diffusion coefficients (μm^{2}s^{-1}) and the percentage of the simulated data at them, and also the R^2 and χ^2 values for each fit. 95% confidence bounds are indicated in brackets.

Simulated condition	Tracks	A	D_1	D_2	N	R^2
1.6 & 10µm^{2}s^{-1}, no noise	1511	461 (440, 483)	1.6 (1.55, 1.70)	9.8 (8.99, 10.65)	2.2 (2.05, 2.29)	0.9837
1.6 & 10µm^{2}s^{-1}, noise	450	125 (116, 135)	2.1 (1.96, 2.24)	10.9 (9.77, 12.00)	3.0 (2.64, 3.33)	0.9476

Table D.2: Two gamma fitting with one fixed number of independent steps to simulated mixed diffusion coefficient distributions with 95% confidence bounds for each fitted parameter.

Appendix E

Additional DNA Origami materials and methods

E.1 Staple modifications

The sequences of the staples that have been adapted by Katherine Dunn to include a poly-T loop from Rothemund's original design are given in table E.1, with the name of the staple that has been replaced. The sequences of the four strands modified to include biotin are included in table E.2. The sequences of the four strands which replace the three strands r-5t2f,r-5t4f and r-5t6f from Rothemund's original design are given in table E.3.

E.2 Preparation of Sephacryl media

Sephacryl S-300 High-Resolution media is shipped in ethanol and must ideally be transferred to the same buffer as the samples that will be purified in it to avoid electrostatic effects. This protocol was developed by Wickham [301], and refined by Dunn [300].

Equal volumes of S-300 and pure water were mixed, and then centrifuged at 1000 g for 1 minute. Three times, the supernatant was removed, replaced with pure water, resuspended and respun at 1000 g for 1 minute. This was then repeated a further 5 times with the buffer to be used; purification buffer.

E.3 Packing spin columns

Sephacryl media was used to purify the excess staples out of the DNA origami solution before use in experiments. This protocol was developed by Dunn [300].

For each sample to be purified 3 spin columns were prepared. 500 ml of S-300 in purification buffer was added to each column, and spun for 3 minutes at 3.8 krpm in 1.5 ml eppendorf tubes. The flow through was discarded and the columns were spun again for 1 minute to remove any excess buffer. A further 500 ml of S-300 in purification buffer was added to each column, and spun for 3 minutes at 3.8 krpm, elutant was discarded, and then re-spun for a further minute. After this, the columns were transferred to clean 1.5 ml eppendorf tubes and the DNA origami sample was added to the first column, and spun at 3.8 krpm for 4 minutes. The elutant was transferred to the second column, and again spun at 3.8 krpm for 4 minutes. The elutant was added to the final column, spun for 4 minutes at 3.8 krpm and the final elutant was kept for experiments. Generally, the final eluted volume of DNA was a few percent higher than the initial volume of DNA added, hence the need to ensure that the sample and filtration media were in the same buffer.

Original staple name	Modified staple name	Modified staple sequence (5′ to 3′)
r9t0f	r9t0fTloop	TTTTTATAAGTATAGCCCGGCCGTCGAG
r9t10f	r9t10fTloop	GCGCATTATTTTGCTTATCCGGTATTCTAAATCAGA
r9t12f	r9t12fTloop	TATAGAAGTTTTCGACAAAAGGTAAAGTAGAGAATA
r9t14f	r9t14fTloop	TAAAGTACTTTTCGCGAGAAAACTTTTTATCGCAAG
r9t16f	r9t16fTloop	ACAAAGAATTTTATTAATTACATTTAACACATCAAG
r9t18f	r9t18fTloop	AAAACAAATTTTTTCATCAATATAATCCTATCAGAT
r9t20f	r9t20fTloop	GATGGCAATTTTAATCAATATCTGGTCACAAATATC
r9t22j	r9t22jTloop	AAACCCTCTTTTACCAGTAATAAAAGGGATTCACCAGTCACACGTTTT
r9t2f	r9t2fTloop	AGGGTTGATTTTATAAATCCTCATTAAATGATATTC
r9t4f	r9t4fTloop	ACAAACAATTTTAATCAGTAGCGACAGATCGATAGC
r9t6f	r9t6fTloop	AGCACCGTTTTTTAAAGGTGGCAACATAGTAGAAAA
r9t8f	r9t8fTloop	TACATACATTTTGACGGGAGAATTAACTACAGGGAA
r-9t10e	r-9t10eTloop	ATATAATGTTTTCATTGAATCCCCCTCAAATCGTCA
r-9t12e	r-9t12eTloop	GCTAAATCTTTTCTGTAGCTCAACATGTATTGCTGA
r-9t14e	r-9t14eTloop	AGAGAATCTTTTGGTTGTACCAAAAACAAGCATAAA
r-9t16e	r-9t16eTloop	GATTGACCTTTTGATGAACGGTAATCGTAGCAAACA
r-9t18e	r-9t18eTloop	CACGACGTTTTTGTAATGGGATAGGTCAAAACGGCG
r-9t20e	r-9t20eTloop	GGGAGAGGTTTTTGTAAAACGACGGCCATTCCCAGT
r-9t22e	r-9t22eTloop	TATCAGGGTTTTCGGTTTGCGTATTGGGAACGCGCG
r-9t24e	r-9t24eTloop	TTTTCGATGGCCCACTACGTAAACCGTC
r-9t2i	r-9t2iTloop	CAGCGAAATTTTAACTTTCAACAGTTTCTGGGATTTTGCTAAACTTTT
r-9t4e	r-9t4eTloop	ACGGTCAATTTTGACAGCATCGGAACGAACCCTCAG
r-9t6e	r-9t6eTloop	GGACGTTGTTTTTCATAAGGGAACCGAAAGGCGCAG
r-9t8e	r-9t8eTloop	TAAATATTTTTTGGAAGAAAAATCTACGACCAGTCA

Table E.1: Staples modified to include a T- loop to prevent edge stacking.

Original staple name	Modified staple name	Modified staple sequence
r-7t4e	r-7t4eBIOTIN	$5'-\text{biotin}-\text{TTTTGCTCCATGAGAGGCTTTGAGGACTAGGGAGTT}-3'$
r7t4e	r7t4eBIOTIN	$5'-\text{biotin}-\text{TTTTTGCCTTTAGTCAGACGATTGGCCTGCCAGAAT}-3'$
r-7t20e	r-7t20eBIOTIN	$5'-\text{biotin}-\text{TTTTGCCAGCTGCCTGCAGGTCGACTCTGCAAGGCG}-3'$
r7t20e	r7t20eBIOTIN	$5'-\text{biotin}-\text{TTTTATCAACAGTCATCATATTCCTGATTGATTGTT}-3'$

Table E.2: Staples that have been modified to include biotin for surface attachment.

Staple name	Staple sequence (5′ to 3′)
r-5talt1	AATAATAAGGTCGCTGAGGCTTGC
r-5talt3	TCGAAATCTGTACAGACCAGGCGC
r-5talt4	TTAATCATTGTGAATTACAGGTAG
r-5talt2ext	AAAGACTTTTTCATGAAAATTGTGGGATACACGCATACACCCAT

Table E.3: Staples which replace the three strands r-5t2f,r-5t4f and r-5t6f from Rothemund's original design.

Appendix F

Modelling YOYO-1 binding to DNA

The binding of YOYO-1 to DNA can be modelled simply by considering the rates of the different reactions, as described in the main text and in Alon [311]. There are only two states available to the dye in this situation: free in solution and bound to the DNA. The two equations that describe the conversion between free and bound dye ($[N_{EXT}]$ and $[N_{OCC}]$) over time, t, are reproduced here:

$$\frac{\mathrm{d}[N_{OCC}]}{\mathrm{d}t} = k_{bind}[N_{EXT}]\big([N_{TOT}] - [N_{OCC}]\big) - k_{unbind}[N_{OCC}] \tag{F.1}$$

$$\frac{\mathrm{d}[N_{EXT}]}{\mathrm{d}t} = -\frac{\mathrm{d}[N_{OCC}]}{\mathrm{d}t} \tag{F.2}$$

where k_{unbind} and k_{bind} are the unbinding and binding constants, and $[N_{TOT}]$ is the total number of dye binding sites. The first term in equation F comes from free dye molecules binding to DNA, which is governed by their binding rate, the concentration of free dye molecules and the concentration of available dye binding sites, which is the concentration of the total number of binding sites minus the number that are already filled. The second term in the equation arises from unbinding of the dye from the DNA, which is governed by an unbinding rate and the concentration of existing bound dye molecules. Equation F.2 arises because this is a simple system in which the dye can only exist in two states.

To solve equation F we must first rearrange it to give:

$$\frac{\mathrm{d}[N_{OCC}]}{\mathrm{d}t} = k_{bind}[N_{EXT}][N_{TOT}] - \big(k_{bind}[N_{EXT}] + k_{unbind}\big)[N_{OCC}] \tag{F.3}$$

which we see can be solved with an exponential trial function, Y, of the form:

$$Y = A + Be^{-(k_{bind}[N_{EXT}]+k_{unbind})t} \tag{F.4}$$

The values of the constants A, B can found from the initial conditions. For the initial part of the experiment where dye is binding to DNA $[N_{OCC}]$=0, and rises to a steady state value before the dye is washed out. This steady state value is found when $\frac{\mathrm{d}[N_{OCC}]}{\mathrm{d}t}$ =0 in equation above. This gives:

$$[N_{OCC}] = \frac{[N_{EXT}][N_{TOT}]}{\frac{k_{unbind}}{k_{bind}} + [N_{EXT}]} \tag{F.5}$$

This steady state value (referred to as $[N_{OCC}]_0$) reached in the dye-DNA incubation stage of the experiment is the initial value of $[N_{OCC}]$ when the unbound dye is flowed out. Additionally at this point $[N_{OCC}]_0 = [N_{EXT}] + [N_{OCC}]$, as all unbound dye is assumed to be washed out. Substituting this into equation F.5 gives a quadratic equation for $[N_{OCC}]$ after the excess dye has been washed out. The solution of this equation is the steady state value of the concentration of the number of occupied dye binding sites after excess dye has been washed out.

List of abbreviations

AF647	Alexa Fluor 647
AFM	Atomic Force Microscopy
bp	base pair
BSA	Bovine serum albumin
CCD	Charge-coupled device
DNA	Deoxyribonucleic acid
ds	Double-stranded (in particular dsDNA)
emCCD	electron multiplying charge-coupled device
FCS	Fluorescence correlation spectroscopy
FLIP	Fluorescence loss in photobleaching
FRAP	Fluorescence recovery after photobleaching
FRET	Förster resonance energy transfer
FWHM	Full width half maximum
HWHM	Half width half maximum
IR	Infrared
kDa	kiloDalton; 10^3 atomic mass units
LED	Light emitting diode
LTP	Low temperature plasma
ms	millisecond
ND	Neutral density
ns	nanosecond
nm	nanometre
PALM	photoactivated localisation microscopy
PBS	Phosphate-buffered saline
PSF	Point spread function
s.e.	Standard error
s.d.	Standard deviation
SHIM	Second harmonic imaging microscopy
SMT	Single molecule tracking
SNR	Signal-to-noise ratio
SPT	Single particle tracking
ss	Single-stranded (in particular ssDNA)
STED	Stimulated emission depletion
STORM	stochastic optical reconstruction microscopy
TIRF	Total internal reflection fluorescence
µm	micrometre

References

[1] Chiu, S.-W. and Leake, M. C.: Functioning nanomachines seen in real-time in living bacteria using single-molecule and super-resolution fluorescence imaging. *International journal of molecular sciences* 12, 2518–42 (2011)

[2] Hess, S. T., Girirajan, T. P. K., and Mason, M. D.: Ultra-high resolution imaging by fluorescence photoactivation localization microscopy. *Biophysical journal* 91, 4258–72 (2006)

[3] Betzig, E., Patterson, G. H., Sougrat, R., Lindwasser, O. W., Olenych, S., et al.: Imaging intracellular fluorescent proteins at nanometer resolution. *Science (New York, NY)* 313, 1642–5 (2006)

[4] Rust, M. J., Bates, M., and Zhuang, X.: Sub-diffraction-limit imaging by stochastic optical reconstruction microscopy (STORM). *Nature* 3, 793–795 (2006)

[5] Betzig, E.: Single Molecules, Cells, and Super-Resolution Optics (Nobel Lecture). *Angewandte Chemie International Edition* 54, 8034–8053 (2015)

[6] Hell, S. W.: Nanoscopy with Focused Light (Nobel Lecture). *Angewandte Chemie International Edition* 54, 8054–8066 (2015)

[7] Moerner, W. E.: Single-Molecule Spectroscopy, Imaging, and Photocontrol: Foundations for Super-Resolution Microscopy (Nobel Lecture). *Angewandte Chemie International Edition* 54, 8067–8093 (2015)

[8] Hall, C. E.: Method for the observation of macromolecules with the electron microscope illustrated with micrographs of DNA. *The Journal of biophysical and biochemical cytology* 2, 625–8 (1956)

[9] Watson, M. L.: Staining of tissue sections for electron microscopy with heavy metals. *The Journal of biophysical and biochemical cytology* 4, 475–8 (1958)

[10] Moerner, W. E. and Kador, L.: Optical detection and spectroscopy of single molecules in a solid. *Physical Review Letters* 62, 2535–2538 (1989)

[11] Hirschfeld, T.: Optical microscopic observation of single small molecules. *Applied Optics* 15, 2965 (1976)

[12] Orrit, M. and Bernard, J.: Single pentacene molecules detected by fluorescence excitation in a p -terphenyl crystal. *Physical Review Letters* 65, 2716–2719 (1990)

[13] Rotman, B.: Measurement of activity of single molecules of beta-D-galactosidase. *Proceedings of the National Academy of Sciences of the United States of America* 47, 1981–91 (1961)

[14] Ambrose, W. P. and Moerner, W. E.: Fluorescence spectroscopy and spectral diffusion of single impurity molecules in a crystal. *Nature* 349, 225–227 (1991)

[15] Ash, E. A. and Nicholls, G.: Super-resolution Aperture Scanning Microscope. *Nature* 237, 510–512 (1972)

[16] Betzig, E. and Trautman, J. K.: Near-Field Optics: Microscopy, Spectroscopy, and Surface Modification Beyond the Diffraction Limit. *Science* 257 (1992)

[17] Betzig, E., Chichester, R. J., Lanni, F., and Taylor, D. L.: Near-field fluorescence imaging of cytoskeletal actin. *Bioimaging* 1, 129–135 (1993)

[18] Betzig, E. and Chichester, R. J.: Single molecules observed by near-field scanning optical microscopy. *Science (New York, NY)* 262, 1422–5 (1993)

[19] Gelles, J., Schnapp, B. J., and Sheetz, M. P.: Tracking kinesin-driven movements with nanometre-scale precision. *Nature* 331, 450–453 (1988)

[20] Heim, R., Prasher, D. C., and Tsien, R. Y.: Wavelength mutations and posttranslational autoxidation of green fluorescent protein. *Proceedings of the National Academy of Sciences* 91, 12501–12504 (1994)

[21] Patterson, G. H. and Lippincott-Schwartz, J.: A Photoactivatable GFP for Selective Photolabeling of Proteins and Cells. *Science* 297 (2002)

[22] Ptacin, J. L., Lee, S. F., Garner, E. C., Toro, E., Eckart, M., et al.: A spindle-like apparatus guides bacterial chromosome segregation. *Nature Cell Biology* 12, 791–798 (2010)

[23] Lee, S. F., Thompson, M. a., Schwartz, M. a., Shapiro, L., and Moerner, W. E.: Super-resolution imaging of the nucleoid-associated protein HU in Caulobacter crescentus. *Biophysical journal* 100, L31–3 (2011)

[24] Shroff, H., Galbraith, C. G., Galbraith, J. A., White, H., Gillette, J., et al.: Dual-color superresolution imaging of genetically expressed probes within individual adhesion complexes. *Proceedings of the National Academy of Sciences* 104, 20308–20313 (2007)

[25] Greenfield, D., McEvoy, A. L., Shroff, H., Crooks, G. E., Wingreen, N. S., et al.: Self-Organization of the Escherichia coli Chemotaxis Network Imaged with Super-Resolution Light Microscopy. *PLoS Biology* 7, e1000137 (2009)

[26] Schawlow, A. L. and Townes, C. H.: Infrared and Optical Masers. *Physical Review* 112, 1940–1949 (1958)

[27] Klar, T. A., Jakobs, S., Dyba, M., Egner, A., and Hell, S. W.: Fluorescence microscopy with diffraction resolution barrier broken by stimulated emission. *Proceedings of the National Academy of Sciences of the United States of America* 97, 8206–10 (2000)

[28] Hecht, E.: *Optics*. Addison Wesley, fourth edn. (2002). ISBN 0-321-18878-0

[29] Spencer, M.: *Fundamentals of light microscopy*. Cambridge University Press (1982). ISBN 0521247942

[30] Drew, H. R., Wing, R. M., Takano, T., Broka, C., Tanaka, S., et al.: Structure of a B-DNA dodecamer: conformation and dynamics. *Proceedings of the National Academy of Sciences of the United States of America* 78, 2179 (1981)

[31] Hirons, G. T., Fawcett, J. J., and Crissman, H. A.: TOTO and YOYO: New very bright fluorochromes for DNA content analyses by flow cytometry. *Cytometry* 15, 129–140 (1994)

[32] Foot, C.: *Atomic Physics*. Oxford University Press, first edn. (2005). ISBN 978 0 19 850696 6

[33] Mertz, J.: *Introduction to Optical Microscopy*. Roberts and Company Publishers, first edit edn. (2010)

[34] Eggeling, C., Widengren, J., Rigler, R., and Seidel, C. A. M.: Photobleaching of Fluorescent Dyes under Conditions Used for Single-Molecule Detection: Evidence of Two-Step Photolysis. *Anal Chem* 70, 2651–265 (1998)

[35] Ha, T. and Tinnefeld, P.: Photophysics of fluorescent probes for single-molecule biophysics and super-resolution imaging. *Annual review of physical chemistry* 63, 595–617 (2012)

[36] Hübner, C. G., Renn, A., Renge, I., and Wild, U. P.: Direct observation of the triplet lifetime quenching of single dye molecules by molecular oxygen. *The Journal of Chemical Physics* 115, 9619–9622 (2001)

[37] Tinnefeld, P., Buschmann, V., Weston, K., and Sauer, M.: Direct Observation of Collective Blinking and Energy Transfer in a Bichromophoric System. *J Phys Chem A* 107, 323–327 (2003)

[38] Renn, A., Seelig, J., and Sandoghdar, V.: Oxygen-dependent photochemistry of fluorescent dyes studied at the single molecule level. *Molecular Physics* 104, 409–414 (2006)

[39] Aitken, C. E., Marshall, R. A., and Puglisi, J. D.: An oxygen scavenging system for improvement of dye stability in single-molecule fluorescence experiments. *Biophysical journal* 94, 1826–35 (2008)

[40] Dave, R., Terry, D. S., Munro, J. B., and Blanchard, S. C.: Mitigating unwanted photophysical processes for improved single-molecule fluorescence imaging. *Biophysical journal* 96, 2371–81 (2009)

[41] Vogelsang, J., Kasper, R., Steinhauer, C., Person, B., Heilemann, M., et al.: A reducing and oxidizing system minimizes photobleaching and blinking of fluorescent dyes. *Angewandte Chemie (International ed in English)* 47, 5465–9 (2008)

[42] Glembockyte, V., Lin, J., and Cosa, G.: Improving the Photostability of Red- and Green-Emissive Single-Molecule Fluorophores via Ni 2+ Mediated Excited Triplet-State Quenching. *The Journal of Physical Chemistry B* 120, 11923–11929 (2016)

[43] Chung, S. H. and Kennedy, R. A.: Forward-backward non-linear filtering technique for extracting small biological signals from noise. *Journal of Neuroscience Methods* 40, 71–86 (1991)

[44] Thompson, R. E., Larson, D. R., and Webb, W. W.: Precise nanometer localization analysis for individual fluorescent probes. *Biophysical journal* 82, 2775–83 (2002)

[45] Deschout, H., Neyts, K., and Braeckmans, K.: The influence of movement on the localization precision of sub-resolution particles in fluorescence microscopy. *Journal of Biophotonics* 5, 97–109 (2012)

[46] Michalet, X. and Berglund, A. J.: Optimal diffusion coefficient estimation in single-particle tracking. *Physical Review E* 85, 061916 (2012)

[47] Andor Technology Ltd (Andor): Comparing sCMOS

[48] Huang, Z.-L., Zhu, H., Long, F., Ma, H., Qin, L., et al.: Localization-based super-resolution microscopy with an sCMOS camera. *Optics Express* 19, 19156 (2011)

[49] Long, F., Zeng, S., and Huang, Z.-L.: Localization-based super-resolution microscopy with an sCMOS camera Part II: Experimental methodology for comparing sCMOS with EMCCD cameras. *Optics Express* 20, 17741 (2012)

[50] Singh, A. P., Krieger, J. W., Buchholz, J., Charbon, E., Langowski, J., and Wohland, T.: The performance of 2D array detectors for light sheet based fluorescence correlation spectroscopy. *Optics Express* 21, 8652 (2013)

[51] Davidson, M. W. and Campbell, R. E.: Engineered fluorescent proteins: innovations and applications. *Nature Methods* 6, 713–717 (2009)

[52] Cranfill, P. J., Sell, B. R., Baird, M. A., Allen, J. R., Lavagnino, Z., et al.: Quantitative assessment of fluorescent proteins. *Nature Methods* 13, 557–562 (2016)

[53] Fernández-Suárez, M. and Ting, A. Y.: Fluorescent probes for super-resolution imaging in living cells. *Nature Reviews Molecular Cell Biology* 9, 929–943 (2008)

[54] Terai, T. and Nagano, T.: Small-molecule fluorophores and fluorescent probes for bioimaging. *Pflügers Archiv - European Journal of Physiology* 465, 347–359 (2013)

[55] Huang, B., Wang, W., Bates, M., and Zhuang, X.: Three-dimensional super-resolution imaging by stochastic optical reconstruction microscopy. *Science (New York, NY)* 319, 810–3 (2008)

[56] Heilemann, M., van de Linde, S., Schüttpelz, M., Kasper, R., Seefeldt, B., et al.: Subdiffraction-resolution fluorescence imaging with conventional fluorescent probes. *Angewandte Chemie (International ed in English)* 47, 6172–6 (2008)

[57] Heilemann, M., van de Linde, S., Mukherjee, A., and Sauer, M.: Super-Resolution Imaging with Small Organic Fluorophores. *Angewandte Chemie International Edition* 48, 6903–6908 (2009)

[58] van de Linde, S., Löschberger, A., Klein, T., Heidbreder, M., Wolter, S., et al.: Direct stochastic optical reconstruction microscopy with standard fluorescent probes. *Nature protocols* 6, 991–1009 (2011)

[59] Hell, S. W. and Wichmann, J.: Breaking the diffraction resolution limit by stimulated emission: stimulated-emission-depletion fluorescence microscopy. *Optics letters* 19, 780–2 (1994)

[60] Ha, T., Enderle, T., Ogletree, D. F., Chemla, D. S., Selvin, P. R., and Weiss, S.: Probing the interaction between two single molecules: fluorescence resonance energy transfer between a single donor and a single acceptor. *Proceedings of the National Academy of Sciences of the United States of America* 93, 6264–8 (1996)

[61] Kapanidis, A. N., Laurence, T. A., Lee, N. K., Margeat, E., Kong, X., and Weiss, S.: Alternating-Laser Excitation of Single Molecules Climbing the Ladder of Complexity. *Acc Chem Res* 38, 523–533 (2005)

[62] Lee, N. K., Kapanidis, A. N., Wang, Y., Michalet, X., Mukhopadhyay, J., et al.: Accurate FRET measurements within single diffusing biomolecules using alternating-laser excitation. *Biophysical journal* 88, 2939–53 (2005)

[63] Burnette, D. T., Sengupta, P., Dai, Y., Lippincott-Schwartz, J., and Kachar, B.: Bleaching/blinking assisted localization microscopy for superresolution imaging using standard fluorescent molecules. *Proceedings of the National Academy of Sciences of the United States of America* 108, 21081–6 (2011)

[64] Edidin, M., Zagyansky, Y., and Lardner, T.: Measurement of membrane protein lateral diffusion in single cells. *Science* 191 (1976)

[65] Axelrod, D., Ravdin, P., Koppel, D. E., Schlessinger, J., Webb, W. W., et al.: Lateral motion of fluorescently labeled acetylcholine receptors

in membranes of developing muscle fibers. *Proceedings of the National Academy of Sciences of the United States of America* 73, 4594–8 (1976)

[66] Reits, E. A. and Neefjes, J. J.: From fixed to FRAP: measuring protein mobility and activity in living cells. *Nature Cell Biology* 3, E145–E147 (2001)

[67] Cole, N. B., Smith, C. L., Sciaky, N., Terasaki, M., Edidin, M., and Lippincott-Schwartz, J.: Diffusional Mobility of Golgi Proteins in Membranes of Living Cells. *Science* 273 (1996)

[68] Ellenberg, J., Siggia, E. D., Moreira, J. E., Smith, C. L., Presley, J. F., et al.: Nuclear Membrane Dynamics and Reassembly in Living Cells: Targeting of an Inner Nuclear Membrane Protein in Interphase and Mitosis. *The Journal of Cell Biology* 138 (1997)

[69] Badrinarayanan, A., Reyes-Lamothe, R., Uphoff, S., Leake, M. C., and Sherratt, D. J.: In vivo architecture and action of bacterial structural maintenance of chromosome proteins. *Science (New York, NY)* 338, 528–31 (2012)

[70] Leake, M. C., Chandler, J. H., Wadhams, G. H., Bai, F., Berry, R. M., and Armitage, J. P.: Stoichiometry and turnover in single, functioning membrane protein complexes. *Nature* 443, 355–358 (2006)

[71] Mudumbi, K. C., Schirmer, E. C., and Yang, W.: Single-point single-molecule FRAP distinguishes inner and outer nuclear membrane protein distribution. *Nature Communications* 7, 12562 (2016)

[72] Hell, S. W., Dyba, M., and Jakobs, S.: Concepts for nanoscale resolution in fluorescence microscopy. *Current Opinion in Neurobiology* 14, 599–609 (2004)

[73] Hofmann, M., Eggeling, C., Jakobs, S., and Hell, S. W.: Breaking the diffraction barrier in fluorescence microscopy at low light intensities by using reversibly photoswitchable proteins. *Proceedings of the National Academy of Sciences of the United States of America* 102, 17565–9 (2005)

[74] Chmyrov, A., Keller, J., Grotjohann, T., Ratz, M., D'Este, E., et al.: Nanoscopy with more than 100,000 'doughnuts'. *Nature Methods* 10, 737–740 (2013)

[75] Minsky, M.: Microscopy apparatus US3013467 A (1961)

[76] Cox, G. and Sheppard, C. J.: Practical limits of resolution in confocal and non-linear microscopy. *Microscopy Research and Technique* 63, 18–22 (2004)

[77] Hell, S. and Stelzer, E. H. K.: Properties of a 4Pi confocal fluorescence microscope. *Journal of the Optical Society of America A* 9, 2159 (1992)

[78] Pavani, S. R. P., Thompson, M. A., Biteen, J. S., Lord, S. J., Liu, N., et al.: Three-dimensional, single-molecule fluorescence imaging beyond the diffraction limit by using a double-helix point spread function. *Proceedings of the National Academy of Sciences* 106, 2995–2999 (2009)

[79] Lee, H.-L. D., Sahl, S. J., Lew, M. D., and Moerner, W. E.: The double-helix microscope super-resolves extended biological structures by localizing single blinking molecules in three dimensions with nanoscale precision. *Applied physics letters* 100, 153701–1537013 (2012)

[80] Shechtman, Y., Sahl, S. J., Backer, A. S., and Moerner, W. E.: Optimal Point Spread Function Design for 3D Imaging. *Physical Review Letters* 113, 133902 (2014)

[81] Shechtman, Y., Weiss, L. E., Backer, A. S., Sahl, S. J., and Moerner, W. E.: Precise Three-Dimensional Scan-Free Multiple-Particle Tracking over Large Axial Ranges with Tetrapod Point Spread Functions. *Nano Letters* 15, 4194–4199 (2015)

[82] Huisken, J., Swoger, J., Del Bene, F., Wittbrodt, J., and Stelzer, E. H. K.: Optical Sectioning Deep Inside Live Embryos by Selective Plane Illumination Microscopy. *Science* 305 (2004)

[83] Keller, P. J., Schmidt, A. D., Wittbrodt, J., and Stelzer, E. H.: Reconstruction of Zebrafish Early Embryonic Development by Scanned Light Sheet Microscopy. *Science* 322 (2008)

[84] Ahrens, M. B., Orger, M. B., Robson, D. N., Li, J. M., and Keller, P. J.: Whole-brain functional imaging at cellular resolution using light-sheet microscopy. *Nature Methods* 10, 413–420 (2013)

[85] Keller, P. J., Schmidt, A. D., Santella, A., Khairy, K., Bao, Z., et al.: Fast, high-contrast imaging of animal development with scanned light sheet–based structured-illumination microscopy. *Nature Methods* 7, 637–642 (2010)

[86] Planchon, T. A., Gao, L., Milkie, D. E., Davidson, M. W., Galbraith, J. A., et al.: Rapid three-dimensional isotropic imaging of living cells using Bessel beam plane illumination. *Nature methods* 8, 417–23 (2011)

[87] Vettenburg, T., Dalgarno, H. I. C., Nylk, J., Coll-Lladó, C., Ferrier, D. E. K., et al.: Light-sheet microscopy using an Airy beam. *Nature methods* 11, 541–4 (2014)

[88] Pitrone, P. G., Schindelin, J., Stuyvenberg, L., Preibisch, S., Weber, M., et al.: OpenSPIM: an open-access light-sheet microscopy platform. *Nature Methods* 10, 598–599 (2013)

[89] Marx, V.: Microscopy: OpenSPIM 2.0. *Nature Methods* 13, 979–982 (2016)

[90] Chen, B.-C., Legant, W. R., Wang, K., Shao, L., Milkie, D. E., et al.: Lattice light-sheet microscopy: Imaging molecules to embryos at high spatiotemporal resolution. *Science* 346, 1257998–1257998 (2014)

[91] Denk, W., Strickler, J., and Webb, W.: Two-photon laser scanning fluorescence microscopy. *Science* 248 (1990)

[92] Hoover, E. E. and Squier, J. A.: Advances in multiphoton microscopy technology. *Nature Photonics* 7, 93–101 (2013)

[93] Horton, N. G., Wang, K., Kobat, D., Clark, C. G., Wise, F. W., et al.: In vivo three-photon microscopy of subcortical structures within an intact mouse brain. *Nature Photonics* 7, 205–209 (2013)

[94] Reyes-Lamothe, R., Sherratt, D. J., and Leake, M. C.: Stoichiometry and architecture of active DNA replication machinery in Escherichia coli. *Science (New York, NY)* 328, 498–501 (2010)

[95] Watson, F.H.C and Crick, J.: A Structure for Deoxyribose Nucleic Acid. *Nature* 171, 737–738 (1953)

[96] Dickerson, R., Drew, H., Conner, B., Wing, R., Fratini, A., and Kopka, M.: The anatomy of A-, B-, and Z-DNA. *Science* 216 (1982)

[97] Berg, J., Tymoczko, J., and Stryer, L.: *Biochemistry*. W.H. Freeman and company, fifth edn. (2002)

[98] Rose, A. S. and Hildebrand, P. W.: NGL Viewer: a web application for molecular visualization. *Nucleic Acids Research* 43, 576–579 (2015)

[99] Rose, A. S., Bradley, A. R., Valasatava, Y., Duarte, J. M., Prlić, A., and Rose, P. W.: Web-based molecular graphics for large complexes. In *Proceedings of the 21st International Conference on Web3D Technology - Web3D '16*, 185–186. ACM Press, New York, New York, USA (2016). ISBN 9781450344289

[100] Daniels, D., Schroeder, J., Szybalski, W., Sanger, F., Coulson, A., et al.: Appendix II: Complete Annotated Lambda Sequence. In Hendrix, R., Roberts, J., Stahl, F., and Weisberg, R., eds., *Lambda II*, chap. Appendix I, 519–676. Cold Spring Harbor (1983)

[101] Lander, E. S., Linton, L. M., Birren, B., Nusbaum, C., Zody, M. C., et al.: Initial sequencing and analysis of the human genome. *Nature* 409, 860–921 (2001)

[102] Crick, F.: The biological replication of macromolecules. In Society for Experimental Biology (Great Britain), ed., *Symposia of the Society for Experimental Biology, no.12*. New York Academic Press (1958)

[103] Crick, F.: Central Dogma of Molecular Biology. *Nature* 227, 561–563 (1970)

[104] Lopez-Lastra, M., Rivas, A., and Barria, M. I.: Protein synthesis in eukaryotes: The growing biological relevance of cap-independent translation initiation. *Biological Research* 38, 121–146 (2005)

[105] Champoux, J. J.: DNA Topoisomerases: Structure, Function, and Mechanism. *Annual Review of Biochemistry* 70, 369–413 (2001)

[106] Liu, L. F. and Wang, J. C.: Supercoiling of the DNA template during transcription. *Proceedings of the National Academy of Sciences* 84, 7024–7027 (1987)

[107] Gavathiotis, E., Sharman, G. J., and Searle, M. S.: Sequence-dependent variation in DNA minor groove width dictates orientational preference of Hoechst 33258 in A-tract recognition: solution NMR structure of the 2:1 complex with d(CTTTTGCAAAAG)(2). *Nucleic acids research* 28, 728–35 (2000)

[108] Moon, J. H., Kim, S. K., Sehlstedt, U., Rodger, A., and Nordén, B.: DNA structural features responsible for sequence-dependent binding geometries of Hoechst 33258. *Biopolymers* 38, 593–606 (1996)

[109] Pjura, P. E., Grzeskowiak, K., and Dickerson, R. E.: Binding of Hoechst 33258 to the minor groove of B-DNA. *Journal of Molecular Biology* 197, 257–271 (1987)

[110] Spink, N., Brown, D. G., Skelly, J. V., and Neidle, S.: Sequence-dependent effects in drug-DNA interaction: the crystal structure of Hoechst 33258 bound to the d(CGCAAATTTGCG)2 duplex. *Nucleic acids research* 22, 1607–12 (1994)

[111] Flors, C., Ravarani, C. N. J., and Dryden, D. T. F.: Super-resolution imaging of DNA labelled with intercalating dyes. *Chemphyschem : a European journal of chemical physics and physical chemistry* 10, 2201–4 (2009)

[112] Marko, J. F. and Siggia, E. D.: Stretching DNA. *Macromolecules* 28, 8759–8770 (1995)

[113] Rothemund, P. W. K.: Folding DNA to create nanoscale shapes and patterns. *Nature* 440, 297–302 (2006)

[114] Orozco, M., Pérez, A., Noy, A., and Luque, F. J.: Theoretical methods for the simulation of nucleic acids. *Chem Soc Rev* 32, 350–364 (2003)

[115] de Pablo, J. J.: Coarse-Grained Simulations of Macromolecules: From DNA to Nanocomposites. *Annual Review of Physical Chemistry* 62, 555–574 (2011)

[116] Doye, J. P. K., Ouldridge, T. E., Louis, A. A., Romano, F., Šulc, P., et al.: Coarse-graining DNA for simulations of DNA nanotechnology. *Physical Chemistry Chemical Physics* 15, 20395 (2013)

[117] Wollman, A. J. M., Miller, H., Foster, S., and Leake, M. C.: An automated image analysis framework for segmentation and division plane detection of single live Staphylococcus aureus cells which can operate at millisecond sampling time scales using bespoke Slimfield microscopy. *Physical Biology* 13, 055002 (2016)

[118] Churchman, L. S., Okten, Z., Rock, R. S., Dawson, J. F., and Spudich, J. a.: Single molecule high-resolution colocalization of Cy3 and Cy5 attached to macromolecules measures intramolecular distances through time. *Proceedings of the National Academy of Sciences of the United States of America* 102, 1419–23 (2005)

[119] Gebhardt, J. C. M., Suter, D. M., Roy, R., Zhao, Z. W., Chapman, A. R., et al.: Single-molecule imaging of transcription factor binding to DNA in live mammalian cells. *Nature methods* 10, 421–6 (2013)

[120] Di Paolo, D., Afanzar, O., Armitage, J. P., and Berry, R. M.: Single-molecule imaging of electroporated dye-labelled CheY in live Escherichia coli. *Philosophical Transactions of the Royal Society of London B: Biological Sciences* 371 (2016)

[121] Axelrod, D.: Cell-substrate contacts illuminated by total internal reflection fluorescence. *Journal of Cell Biology* 89, 141–145 (1981)

[122] Schmidt, T., Schütz, G. J., Baumgartner, W., Gruber, H. J., and Schindler, H.: Imaging of single molecule diffusion. *Proceedings of the National Academy of Sciences of the United States of America* 93, 2926–9 (1996)

[123] Guo, L., Har, J. Y., Sankaran, J., Hong, Y., Kannan, B., and Wohland, T.: Molecular Diffusion Measurement in Lipid Bilayers over Wide Concentration Ranges: A Comparative Study. *ChemPhysChem* 9, 721–728 (2008)

[124] Shim, S.-H., Xia, C., Zhong, G., Babcock, H. P., Vaughan, J. C., et al.: Super-resolution fluorescence imaging of organelles in live cells with photoswitchable membrane probes. *Proceedings of the National Academy of Sciences of the United States of America* 109, 13978–83 (2012)

[125] Barak, L. S. and Webb, W. W.: Diffusion of low density lipoprotein-receptor complex on human fibroblasts. *The Journal of cell biology* 95, 846–52 (1982)

[126] Cherry, R. J., Wilson, K. M., Triantafilou, K., O'Toole, P. J., Morrison, I. E. G., et al.: Detection of dimers of dimers of human leukocyte antigen (HLA)-DR on the surface of living cells by single-particle fluorescence imaging. *The Journal of cell biology* 140, 71–9 (1998)

[127] Vrljic, M., Nishimura, S. Y., Brasselet, S., Moerner, W. E., and McConnell, H. M.: Translational diffusion of individual class II MHC membrane proteins in cells. *Biophysical journal* 83, 2681–92 (2002)

[128] Sadler, E. E., Kapanidis, A. N., and Tucker, S. J.: Solution-Based Single-Molecule FRET Studies of K+ Channel Gating in a Lipid Bilayer. *Biophysical Journal* 110, 2663–2670 (2016)

[129] Giepmans, B. N. G., Adams, S. R., Ellisman, M. H., and Tsien, R. Y.: The Fluorescent Toolbox for Assessing Protein Location and Function. *Science* 312 (2006)

[130] Yang, T. T., Cheng, L., and Kain, S. R.: Optimized codon usage and chromophore mutations provide enhanced sensitivity with the green fluorescent protein. *Nucleic acids research* 24, 4592–3 (1996)

[131] Snapp, E.: Design and use of fluorescent fusion proteins in cell biology. *Current protocols in cell biology* Chapter 21, Unit 21.4 (2005)

[132] De Meulenaere, E., Nguyen Bich, N., de Wergifosse, M., Van Hecke, K., Van Meervelt, L., et al.: Improving the Second-Order Nonlinear Optical Response of Fluorescent Proteins: The Symmetry Argument. *Journal of the American Chemical Society* 135, 4061–4069 (2013)

[133] Shimomura, O., Johnson, F. H., and Saiga, Y.: Extraction, Purification and Properties of Aequorin, a Bioluminescent Protein from the Luminous Hydromedusan, Aequorea. *Journal of Cellular and Comparative Physiology* 59, 223–239 (1962)

[134] Chalfie, M., Tu, Y., Euskirchen, G., Ward, W., and Prasher, D.: Green fluorescent protein as a marker for gene expression. *Science* 263 (1994)

[135] Tsien, R. Y.: The Green Fluorescent Protein. *Annual Review of Biochemistry* 67, 509–544 (1998)

[136] Shaner, N. C., Steinbach, P. A., and Tsien, R. Y.: A guide to choosing fluorescent proteins. *Nature Methods* 2, 905–909 (2005)

[137] Brus, L. E.: Electron - electron and electron -hole interactions in small semiconductor crystallites: The size dependence of the lowest excited electronic state. *The Journal of Chemical Physics* 80, 4403–4409 (1984)

[138] Bruchez, M., Moronne, M., Gin, P., Weiss, S., and Alivisatos, A. P.: Semiconductor Nanocrystals as Fluorescent Biological Labels. *Science* 281 (1998)

[139] Chan, W. C. W. and Nie, S.: Quantum Dot Bioconjugates for Ultrasensitive Nonisotopic Detection. *Science* 281 (1998)

[140] Pinaud, F., Michalet, X., Bentolila, L. A., Tsay, J. M., Doose, S., et al.: Advances in fluorescence imaging with quantum dot bio-probes. *Biomaterials* 27, 1679–1687 (2006)

[141] Efros, A. L. and Nesbitt, D. J.: Origin and control of blinking in quantum dots. *Nature Nanotechnology* 11, 661–671 (2016)

[142] Mujumdar, R. B., Ernst, L. A., Mujumdar, S. R., Lewis, C. J., and Waggoner, A. S.: Cyanine dye labeling reagents: Sulfoindocyanine succinimidyl esters. *Bioconjugate Chemistry* 4, 105–111 (1993)

[143] Flors, C.: Super-resolution fluorescence imaging of directly labelled DNA: from microscopy standards to living cells. *Journal of microscopy* 251, 1–4 (2013)

[144] Panchuk-Voloshina, N., Haugland, R. P., Bishop-Stewart, J., Bhalgat, M. K., Millard, P. J., et al.: Alexa Dyes, a Series of New Fluorescent Dyes that Yield Exceptionally Bright, Photostable Conjugates. *Journal of Histochemistry & Cytochemistry* 47, 1179–1188 (1999)

[145] Berlier, J. E., Rothe, A., Buller, G., Bradford, J., Gray, D. R., et al.: Quantitative Comparison of Long-wavelength Alexa Fluor Dyes to Cy Dyes: Fluorescence of the Dyes and Their Bioconjugates. *Journal of Histochemistry & Cytochemistry* 51, 1699–1712 (2003)

[146] Shun'ko, E. V. and Belkin, V. S.: Treatment surfaces with atomic oxygen excited in dielectric barrier discharge plasma of O2 admixed to N2. *AIP Advances* 2, 022157 (2012)

[147] Harriman, O. L. J.: *A system-level approach to single-molecule live-cell fluorescence microscopy*. Ph.D. thesis, University of Oxford (2013)

[148] McMaster, G. K. and Carmichael, G. G.: Analysis of single- and double-stranded nucleic acids on polyacrylamide and agarose gels by using glyoxal and acridine orange. *Proceedings of the National Academy of Sciences of the United States of America* 74, 4835–8 (1977)

[149] Miller, H., Zhou, Z., Wollman, A. J. M., and Leake, M. C.: Superresolution imaging of single DNA molecules using stochastic photoblinking of minor groove and intercalating dyes. *Methods (San Diego, Calif)* 88, 81–88 (2015)

[150] Otsu, N.: A Threshold Selection Method from Gray-Level Histograms. *IEEE Transactions on Systems, Man, and Cybernetics* 9, 62–66 (1979)

[151] Weszka, J., Nagel, R., and Rosenfeld, A.: A Threshold Selection Technique. *IEEE Transactions on Computers* C-23, 1322–1326 (1974)

[152] Chow, C. and Kaneko, T.: Automatic boundary detection of the left ventricle from cineangiograms. *Computers and Biomedical Research* 5, 388–410 (1972)

[153] Zhou, Z., Miller, H., Wollman, A., and Leake, M.: Developing a New Biophysical Tool to Combine Magneto-Optical Tweezers with Super-Resolution Fluorescence Microscopy. *Photonics* 2, 758–772 (2015)

[154] Miller, H., Wollman, A. J. M., and Leake, M. C.: Designing a Single-Molecule Biophysics Tool for Characterising DNA Damage for Techniques that Kill Infectious Pathogens Through DNA Damage Effects. *Advances in experimental medicine and biology* 915, 115–27 (2016)

[155] Thompson, R. E., Larson, D. R., and Webb, W. W.: Precise nanometer localization analysis for individual fluorescent probes. *Biophysical journal* 82, 2775–83 (2002)

[156] Duffin, W.: *Electricity and Magnetism Fourth Edition*. McGraw Hill, fourth edn. (1990). ISBN 0-07-707209-X

[157] Axelrod, D., Burghardt, T. P., and Thompson, N. L.: Total Internal Reflection Fluorescence. *Annual Review of Biophysics and Bioengineering* 13, 247–268 (1984)

[158] Holonyak, N. and Bevacqua, S. F.: Coherent (visible) light emission from $Ga(As_{1-x}P_x)$ junctions. *Applied Physics Letters* 1, 82–83 (1962)

[159] Bormuth, V., Howard, J., and Schaffer, E.: LED illumination for video-enhanced DIC imaging of single microtubules. *Journal of Microscopy* 226, 1–5 (2007)

[160] Thornton, K. L., Findlay, R. C., Walrad, P. B., and Wilson, L. G.: Investigating the Swimming of Microbial Pathogens Using Digital Holography. 17–32. Springer International Publishing (2016)

[161] Diaz, E. and Knobl, M.: Prototyping optical systems with stock optic components. *Photonik International* (2012)

[162] Wessels, J. T., Pliquett, U., and Wouters, F. S.: Light-emitting diodes in modern microscopy-from David to Goliath? *Cytometry Part A* 81A, 188–197 (2012)

[163] Tanner, N. a. and van Oijen, A. M.: *Visualizing DNA replication at the single-molecule level.*, vol. 475. Elsevier Inc., 1 edn. (2010)

[164] Gorman, J., Plys, A. J., Visnapuu, M.-L., Alani, E., and Greene, E. C.: Visualizing one-dimensional diffusion of eukaryotic DNA repair factors along a chromatin lattice. *Nature Structural & Molecular Biology* 17, 932–938 (2010)

[165] Nöllmann, M., Stone, M. D., Bryant, Z., Gore, J., Crisona, N. J., et al.: Multiple modes of Escherichia coli DNA gyrase activity revealed by force and torque. *Nature structural & molecular biology* 14, 264–71 (2007)

[166] Liphardt, J., Onoa, B., Smith, S. B., Tinoco, I., and Bustamante, C.: Reversible Unfolding of Single RNA Molecules by Mechanical Force. *Science* 292 (2001)

[167] Smith, S. B., Cui, Y., and Bustamante, C.: Overstretching B-DNA: The Elastic Response of Individual Double-Stranded and Single-Stranded DNA Molecules. *Science* 271, 795–799 (1996)

[168] Neuman, K. C. and Nagy, A.: Single-molecule force spectroscopy: optical tweezers, magnetic tweezers and atomic force microscopy. *Nature methods* 5, 491–505 (2008)

[169] Lipfert, J., Kerssemakers, J. W. J., Jager, T., and Dekker, N. H.: Magnetic torque tweezers: measuring torsional stiffness in DNA and RecA-DNA filaments. *Nature methods* 7, 977–80 (2010)

[170] Flors, C.: DNA and chromatin imaging with super-resolution fluorescence microscopy based on single-molecule localization. *Biopolymers* 95, 290–7 (2011)

[171] Ullal, A. J., Pisetsky, D. S., and Reich, C. F.: Use of SYTO 13, a fluorescent dye binding nucleic acids, for the detection of microparticles in in vitro systems. *Cytometry Part A : the journal of the International Society for Analytical Cytology* 77, 294–301 (2010)

[172] van Zandvoort, M. A., de Grauw, C. J., Gerritsen, H. C., Broers, J. L., oude Egbrink, M. G., et al.: Discrimination of DNA and RNA in cells by a vital fluorescent probe: Lifetime imaging of SYTO13 in healthy and apoptotic cells. *Cytometry* 47, 226–235 (2002)

[173] Benke, A. and Manley, S.: Live-cell dSTORM of cellular DNA based on direct DNA labeling. *Chembiochem : a European journal of chemical biology* 13, 298–301 (2012)

[174] Larsson, A., Carlsson, C., and Jonsson, M.: Characterization of the binding of YO to [poly(dA-dT)]2 and [poly(dG-dC)]2, and of the fluorescent properties of YO and YOYO complexed with the polynucleotides and double-stranded DNA. *Biopolymers* 36, 153–67 (1995)

[175] Netzel, T. L., Nafisi, K., Zhao, M., Lenhard, J. R., and Johnson, I.: Base-Content Dependence of Emission Enhancements, Quantum Yields, and Lifetimes for Cyanine Dyes Bound to Double-Strand DNA: Photophysical Properties of Monomeric and Bichromomphoric DNA Stains. *The Journal of Physical Chemistry* 99, 17936–17947 (1995)

[176] Carlsson, C., Larsson, A., Jonsson, M., Albinsson, B., and Nordcn, B.: Optical and Photophysical Properties of the Oxazole Yellow DNA Probes YO and YOYO. *J Phys Chem* 98, 10313–10321 (1994)

[177] Larsson, A., Carlsson, C., Jonsson, M., and Albinsson, B.: Characterization of the Binding of the Fluorescent Dyes YO and YOYO to DNA by Polarized Light Spectroscopy. *Journal of the American Chemical Society* 116, 8459–8465 (1994)

[178] Kanony, C., Åkerman, B., and Tuite, E.: Photobleaching of Asymmetric Cyanines Used for Fluorescence Imaging of Single DNA Molecules. *Journal of the American Chemical Society* 123, 7985–7995 (2001)

[179] Biebricher, A. S., Heller, I., Roijmans, R. F. H., Hoekstra, T. P., Peterman, E. J. G., and Wuite, G. J. L.: The impact of DNA intercalators on DNA and DNA-processing enzymes elucidated through force-dependent binding kinetics. *Nature Communications* 6, 7304 (2015)

[180] Smith, S. B., Finzi, L., and Bustamante, C.: Direct mechanical measurements of the elasticity of single DNA molecules by using magnetic beads. *Science (New York, NY)* 258, 1122–6 (1992)

[181] Lerman, L.: Structural considerations in the interaction of DNA and acridines. *Journal of Molecular Biology* 3, 18–IN14 (1961)

[182] Vladescu, I. D., McCauley, M. J., Nuñez, M. E., Rouzina, I., and Williams, M. C.: Quantifying force-dependent and zero-force DNA intercalation by single-molecule stretching. *Nature Methods* 4, 517–522 (2007)

[183] Günther, K., Mertig, M., and Seidel, R.: Mechanical and structural properties of YOYO-1 complexed DNA. *Nucleic acids research* 38, 6526–32 (2010)

[184] Molecular Probes: Eugene, O.: Molecular Probes Handbook - Probes for the Nucleus—Section 12.5 (2010)

[185] Frey, T.: Nucleic acid dyes for detection of apoptosis in live cells. *Cytometry* 21, 265–274 (1995)

[186] Wojcik, K. and Dobrucki, J. W.: Interaction of a DNA intercalator DRAQ5, and a minor groove binder SYTO17, with chromatin in live cells-Influence on chromatin organization and histone-DNA interactions. *Cytometry Part A* 73A, 555–562 (2008)

[187] Zhao, H., Traganos, F., Dobrucki, J., Wlodkowic, D., and Darzynkiewicz, Z.: Induction of DNA damage response by the supravital probes of nucleic acids. *Cytometry Part A* 75A, 510–519 (2009)

[188] Tárnok, A.: SYTO dyes and histoproteins—Myriad of applications. *Cytometry Part A* 73A, 477–479 (2008)

[189] Dragan, A. I., Casas-Finet, J. R., Bishop, E. S., Strouse, R. J., Schenerman, M. A., and Geddes, C. D.: Characterization of PicoGreen interaction with dsDNA and the origin of its fluorescence enhancement upon binding. *Biophysical journal* 99, 3010–9 (2010)

[190] Singer, V. L., Jones, L. J., Yue, S. T., and Haugland, R. P.: Characterization of PicoGreen Reagent and Development of a Fluorescence-Based Solution Assay for Double-Stranded DNA Quantitation. *Analytical Biochemistry* 249, 228–238 (1997)

[191] Erickson, H. P.: Size and shape of protein molecules at the nanometer level determined by sedimentation, gel filtration, and electron microscopy. *Biological procedures online* 11, 32–51 (2009)

[192] Henriques, R., Lelek, M., Fornasiero, E. F., Valtorta, F., Zimmer, C., and Mhlanga, M. M.: QuickPALM: 3D real-time photoactivation nanoscopy image processing in ImageJ. *Nature methods* 7, 339–40 (2010)

[193] Högbom, J. A.: Aperture Synthesis with a Non-Regular Distribution of Interferometer Baselines. *Astronomy and Astrophysics Supplement* 15, 417–426 (1974)

[194] Rees, E. J., Erdelyi, M., Schierle, G. S. K., Knight, A. E., and Kaminski, C. F.: Elements of image processing in localization microscopy. *Journal of Optics* 15, 094012 (2013)

[195] Tycon, M. A., Dial, C. F., Faison, K., Melvin, W., and Fecko, C. J.: Quantification of dye-mediated photodamage during single-molecule DNA imaging. *Analytical biochemistry* 426, 13–21 (2012)

[196] Francis, K. and Palsson, B. O.: Effective intercellular communication distances are determined by the relative time constants for cyto/chemokine secretion and diffusion. *Proceedings of the National Academy of Sciences of the United States of America* 94, 12258–62 (1997)

[197] Widney, D. P., Breen, E. C., Boscardin, W. J., Kitchen, S. G., Alcantar, J. M., et al.: Serum Levels of the Homeostatic B Cell Chemokine, CXCL13, Are Elevated During HIV Infection. *Journal of Interferon & Cytokine Research* 25, 702–706 (2005)

[198] Ansel, K. M., Ngo, V. N., Hyman, P. L., Luther, S. A., Förster, R., et al.: A chemokine-driven positive feedback loop organizes lymphoid follicles. *Nature* 406, 309–314 (2000)

[199] Mori, S., Nakano, H., Aritomi, K., Wang, C.-R., Gunn, M. D., and Kakiuchi, T.: Mice Lacking Expression of the Chemokines CCL21-Ser and CCL19 (plt Mice) Demonstrate Delayed but Enhanced T Cell Immune Responses. *The Journal of Experimental Medicine* 193, 207–218 (2001)

[200] Reif, K., Ekland, E. H., Ohl, L., Nakano, H., Lipp, M., et al.: Balanced responsiveness to chemoattractants from adjacent zones determines B-cell position. *Nature* 416, 94–99 (2002)

[201] Pereira, J. P., Kelly, L. M., and Cyster, J. G.: Finding the right niche: B-cell migration in the early phases of T-dependent antibody responses. *International immunology* 22, 413–9 (2010)

[202] Rot, A. and von Andrian, U. H.: Chemokines in innate and adaptive host defense: basic chemokinese grammar for immune cells. *Annual Review of Immunology* 22, 891–928 (2004)

[203] Garside, P.: Visualization of Specific B and T Lymphocyte Interactions in the Lymph Node. *Science* 281, 96–99 (1998)

[204] Schulz, O., Hammerschmidt, S. I., Moschovakis, G. L., and Förster, R.: Chemokines and Chemokine Receptors in Lymphoid Tissue Dynamics. *Annual Review of Immunology* 34, 203–242 (2016)

[205] Colditz, I. G., Schneider, M. A., Pruenster, M., and Rot, A.: Chemokines at large: in-vivo mechanisms of their transport, presentation and clearance. *Thrombosis and Haemostasis* 97, 688–693 (2007)

[206] Kim, K.-S., Rajarathnam, K., Clark-Lewis, I., and Sykes, B. D.: Structural characterization of a monomeric chemokine: Monocyte chemoattractant protein-3. *FEBS Letters* 395, 277–282 (1996)

[207] Bennett, L. D., Fox, J. M., and Signoret, N.: Mechanisms regulating chemokine receptor activity. *Immunology* 134, 246–256 (2011)

[208] de Paz, J. L., Moseman, E. A., Noti, C., Polito, L., von Andrian, U. H., and Seeberger, P. H.: Profiling heparin-chemokine interactions using synthetic tools. *ACS chemical biology* 2, 735–744 (2007)

[209] Buschmann, V., Weston, K. D., and Sauer, M.: Spectroscopic Study and Evaluation of Red-Absorbing Fluorescent Dyes. *Bioconjugate Chemistry* 14, 195–204 (2003)

[210] Olivier, N., Keller, D., Gönczy, P., and Manley, S.: Resolution Doubling in 3D-STORM Imaging through Improved Buffers. *PLoS ONE* 8, e69004 (2013)

[211] Dempsey, G. T., Vaughan, J. C., Chen, K. H., Bates, M., and Zhuang, X.: Evaluation of fluorophores for optimal performance in localization-based super-resolution imaging. *Nature methods* 8, 1027–36 (2011)

[212] Nesmelova, I. V., Sham, Y., Dudek, A. Z., van Eijk, L. I., Wu, G., et al.: Platelet Factor 4 and Interleukin-8 CXC Chemokine Heterodimer Formation Modulates Function at the Quaternary Structural Level. *Journal of Biological Chemistry* 280, 4948–4958 (2005)

[213] Veldkamp, C. T., Kiermaier, E., Gabel-Eissens, S. J., Gillitzer, M. L., Lippner, D. R., et al.: Solution Structure of CCL19 and Identification of Overlapping CCR7 and PSGL-1 Binding Sites. *Biochemistry* 54, 4163–6 (2015)

[214] Einstein, A.: Über die von der molekularkinetischen Theorie der Wärme geforderte Bewegung von in ruhenden Flüssigkeiten suspendierten Teilchen. *Annalen der Physik* 322, 549–560 (1905)

[215] Cosgrove, J., Butler, J., Alden, K., Read, M., Kumar, V., et al.: Agent-Based Modeling in Systems Pharmacology. *CPT: pharmacometrics & systems pharmacology* 4, 615–29 (2015)

[216] Magde, D., Elson, E., and Webb, W. W.: Thermodynamic Fluctuations in a Reacting System—Measurement by Fluorescence Correlation Spectroscopy. *Physical Review Letters* 29, 705–708 (1972)

[217] Ehrenberg, M. and Rigler, R.: Rotational brownian motion and fluorescence intensify fluctuations. *Chemical Physics* 4, 390–401 (1974)

[218] Krichevsky, O. and Bonnet, G.: Fluorescence correlation spectroscopy: the technique and its applications. *Reports on Progress in Physics* 65, 251–297 (2002)

[219] Schwille, P., Meyer-Almes, F. J., and Rigler, R.: Dual-color fluorescence cross-correlation spectroscopy for multicomponent diffusional analysis in solution. *Biophysical journal* 72, 1878–86 (1997)

[220] Schwille, P., Haupts, U., Maiti, S., and Webb, W. W.: Molecular Dynamics in Living Cells Observed by Fluorescence Correlation Spectroscopy with One- and Two-Photon Excitation. *Biophysical Journal* 77, 2251–2265 (1999)

[221] Schwille, P.: Fluorescence Correlation Spectroscopy and Its Potential for Intracellular Applications. *Cell Biochemistry and Biophysics* 34, 383–408 (2001)

[222] Riley, K., Hobson, M., and Bence, S.: *Mathematical methods for physics and engineering*. Cambridge University Press, third edn. (2006)

[223] Patel, R. C., Kumar, U., Lamb, D. C., Eid, J. S., Rocheville, M., et al.: Ligand binding to somatostatin receptors induces receptor-specific oligomer formation in live cells. *Proceedings of the National Academy of Sciences of the United States of America* 99, 3294–9 (2002)

[224] Liu, P., Sudhaharan, T., Koh, R. M. L., Hwang, L. C., Ahmed, S., et al.: Investigation of the dimerization of proteins from the epidermal growth factor receptor family by single wavelength fluorescence cross-correlation spectroscopy. *Biophysical journal* 93, 684–98 (2007)

[225] Herrick-Davis, K., Grinde, E., Cowan, A., and Mazurkiewicz, J. E.: Fluorescence correlation spectroscopy analysis of serotonin, adrenergic, muscarinic, and dopamine receptor dimerization: the oligomer number puzzle. *Molecular pharmacology* 84, 630–42 (2013)

[226] Soumpasis, D.: Theoretical analysis of fluorescence photobleaching recovery experiments. *Biophysical Journal* 41, 95–97 (1983)

[227] Sprague, B. L., Pego, R. L., Stavreva, D. A., and McNally, J. G.: Analysis of Binding Reactions by Fluorescence Recovery after Photobleaching. *Biophysical Journal* 86, 3473–3495 (2004)

[228] Deschout, H., Hagman, J., Fransson, S., Jonasson, J., Rudemo, M., et al.: Straightforward FRAP for quantitative diffusion measurements with a laser scanning microscope. *Optics express* 18, 22886–905 (2010)

[229] Axelrod, D., Koppel, D., Schlessinger, J., Elson, E., and Webb, W.: Mobility measurement by analysis of fluorescence photobleaching recovery kinetics. *Biophysical Journal* 16, 1055–1069 (1976)

[230] Kang, M., Day, C. A., Drake, K., Kenworthy, A. K., and DiBenedetto, E.: A Generalization of Theory for Two-Dimensional Fluorescence Recovery after Photobleaching Applicable to Confocal Laser Scanning Microscopes. *Biophysical Journal* 97, 1501–1511 (2009)

[231] Macháň, R., Foo, Y. H., and Wohland, T.: On the Equivalence of FCS and FRAP: Simultaneous Lipid Membrane Measurements. *Biophysical Journal* 111, 152–161 (2016)

[232] Nenninger, A., Mastroianni, G., Robson, A., Lenn, T., Xue, Q., et al.: Independent mobility of proteins and lipids in the plasma membrane of Escherichia coli. *Molecular microbiology* 92, 1142–53 (2014)

[233] Andrecka, J., Ortega Arroyo, J., Takagi, Y., de Wit, G., Fineberg, A., et al.: Structural dynamics of myosin 5 during processive motion revealed by interferometric scattering microscopy. *eLife* 4, 393–414 (2015)

[234] Qian, H., Sheetz, M. P., and Elson, E. L.: Single particle tracking. Analysis of diffusion and flow in two-dimensional systems. *Biophysical journal* 60, 910–21 (1991)

[235] Saxton, M. J.: Lateral diffusion in an archipelago. Single-particle diffusion. *Biophysical journal* 64, 1766–80 (1993)

[236] Kusumi, A., Sako, Y., and Yamamoto, M.: Confined lateral diffusion of membrane receptors as studied by single particle tracking (nanovid microscopy). Effects of calcium-induced differentiation in cultured epithelial cells. *Biophysical Journal* 65, 2021–2040 (1993)

[237] Zawadzki, P., Stracy, M., Ginda, K., Zawadzka, K., Lesterlin, C., et al.: The Localization and Action of Topoisomerase IV in Escherichia coli Chromosome Segregation Is Coordinated by the SMC Complex, MukBEF. *Cell reports* 13, 2587–96 (2015)

[238] Shoulders, M. D. and Raines, R. T.: Collagen structure and stability. *Annual review of biochemistry* 78, 929–58 (2009)

[239] Stegemann, J. P. and Nerem, R. M.: Altered response of vascular smooth muscle cells to exogenous biochemical stimulation in two- and three-dimensional culture. *Experimental cell research* 283, 146–55 (2003)

[240] Butcher, J. T. and Nerem, R. M.: Porcine aortic valve interstitial cells in three-dimensional culture: comparison of phenotype with aortic smooth muscle cells. *The Journal of heart valve disease* 13, 478–85; discussion 485–6 (2004)

[241] Bozec, L. and Horton, M.: Topography and Mechanical Properties of Single Molecules of Type I Collagen Using Atomic Force Microscopy. *Biophysical Journal* 88, 4223–4231 (2005)

[242] Buehler, M. J.: Nature designs tough collagen: explaining the nanostructure of collagen fibrils. *Proceedings of the National Academy of Sciences of the United States of America* 103, 12285–90 (2006)

[243] Kramer, R. Z., Bella, J., Mayville, P., Brodsky, B., and Berman, H. M.: Sequence dependent conformational variations of collagen triple-helical structure. *Nature structural biology* 6, 454–7 (1999)

[244] Antoine, E. E., Vlachos, P. P., and Rylander, M. N.: Tunable collagen I hydrogels for engineered physiological tissue micro-environments. *PloS one* 10, e0122500 (2015)

[245] Branco, M. C., Pochan, D. J., Wagner, N. J., and Schneider, J. P.: Macromolecular diffusion and release from self-assembled beta-hairpin peptide hydrogels. *Biomaterials* 30, 1339–47 (2009)

[246] Amsden, B.: Solute Diffusion within Hydrogels. Mechanisms and Models. *Macromolecules* 31, 8382–8395 (1998)

[247] Ramanujan, S., Pluen, A., McKee, T. D., Brown, E. B., Boucher, Y., and Jain, R. K.: Diffusion and convection in collagen gels: implications for transport in the tumor interstitium. *Biophysical journal* 83, 1650–60 (2002)

[248] Campagnola, P. J., Wei, M.-d., Lewis, A., and Loew, L. M.: High-Resolution Nonlinear Optical Imaging of Live Cells by Second Harmonic Generation. *Biophysical Journal* 77, 3341–3349 (1999)

[249] Campagnola, P. J. and Loew, L. M.: Second-harmonic imaging microscopy for visualizing biomolecular arrays in cells, tissues and organisms. *Nature Biotechnology* 21, 1356–1360 (2003)

[250] Kleinman, D. A.: Theory of Second Harmonic Generation of Light. *Physical Review* 128, 1761–1775 (1962)

[251] Boyd, R. W.: The Nonlinear Optical Susceptibility. In *Nonlinear Optics*, 1–67. Elsevier (2008)

[252] Cox, G., Kable, E., Jones, A., Fraser, I., Manconi, F., and Gorrell, M. D.: 3-Dimensional imaging of collagen using second harmonic generation. *Journal of Structural Biology* 141, 53–62 (2003)

[253] Chen, X., Nadiarynkh, O., Plotnikov, S., and Campagnola, P. J.: Second harmonic generation microscopy for quantitative analysis of collagen fibrillar structure. *Nature Protocols* 7, 654–669 (2012)

[254] Leonard, D. and Meek, K.: Refractive indices of the collagen fibrils and extrafibrillar material of the corneal stroma. *Biophysical Journal* 72, 1382–1387 (1997)

[255] Barnes, A. L., Genever, P. G., Rimmer, S., and Coles, M. C.: Collagen–Poly(N -isopropylacrylamide) Hydrogels with Tunable Properties. *Biomacromolecules* 17, 723–734 (2016)

[256] ThermoFisher Scientific: Fluorescein (FITC) https://www.thermofisher.com/uk/en/home/life-science/... cell-analysis/fluorophores/fluorescein.html. *Date accessed: 2017-03-31*

[257] Putnam, F.: *The Plasma Proteins : Structure, Function, and Genetic Control.* Academic Press, New York, second edn. (1975). ISBN 9780323161732

[258] Saxton, M.: Single-particle tracking: the distribution of diffusion coefficients. *Biophysical Journal* 72, 1744–1753 (1997)

[259] Efron, B. and Tibshirani, R.: *An introduction to the bootstrap*. Chapman & Hall (1994). ISBN 9780412042317

[260] Asbury, C. L., Fehr, A. N., and Block, S. M.: Kinesin Moves by an Asymmetric Hand-Over-Hand Mechanism. *Science* 302 (2003)

[261] Hulmes, D. J.: Building Collagen Molecules, Fibrils, and Suprafibrillar Structures. *Journal of Structural Biology* 137, 2–10 (2002)

[262] Petrásek, Z. and Schwille, P.: Precise measurement of diffusion coefficients using scanning fluorescence correlation spectroscopy. *Biophysical journal* 94, 1437–48 (2008)

[263] Majer, G. and Melchior, J. P.: Characterization of the fluorescence correlation spectroscopy (FCS) standard Rhodamine 6G and calibration of its diffusion coefficient in aqueous solutions. *The Journal of Chemical Physics* 140, 094201 (2014)

[264] Squire, P. G., Moser, P., and O'Konski, C. T.: Hydrodynamic properties of bovine serum albumin monomer and dimer. *Biochemistry* 7, 4261–4272 (1968)

[265] Sobek, J., Aquino, C., and Schlapbach, R.: Analyzing Properties of Fluorescent Dyes Used for Labeling DNA in Microarray Experiments. *BioFiles (Sigma-Aldrich)* 6.3 (2011)

[266] Wollman, A. J. M. and Leake, M. C.: Millisecond single-molecule localization microscopy combined with convolution analysis and automated image segmentation to determine protein concentrations in complexly structured, functional cells, one cell at a time. *Faraday Discuss* 184, 401–424 (2015)

[267] Rashid, R., Chee, S. M. L., Raghunath, M., and Wohland, T.: Macromolecular crowding gives rise to microviscosity, anomalous diffusion and accelerated actin polymerization. *Physical Biology* 12, 034001 (2015)

[268] Axelsson, I.: Characterization of proteins and other macromolecules by agarose gel chromatography. *Journal of Chromatography A* 152, 21–32 (1978)

[269] Ikeda, S. and Nishinari, K.: Intermolecular Forces in Bovine Serum Albumin Solutions Exhibiting Solidlike Mechanical Behaviors. *Biomacromolecules* 1, 757–763 (2000)

[270] García-Sáez, A. J., Carrer, D. C., and Schwille, P.: Fluorescence correlation spectroscopy for the study of membrane dynamics and organization in giant unilamellar vesicles. *Methods in molecular biology (Clifton, NJ)* 606, 493–508 (2010)

[271] Chen, Y., Lagerholm, B. C., Yang, B., and Jacobson, K.: Methods to measure the lateral diffusion of membrane lipids and proteins. *Methods* 39, 147–153 (2006)

[272] Calizo, R. C. and Scarlata, S.: Discrepancy between fluorescence correlation spectroscopy and fluorescence recovery after photobleaching diffusion measurements of G-protein-coupled receptors. *Analytical Biochemistry* 440, 40–48 (2013)

[273] Adkins, E. M., Samuvel, D. J., Fog, J. U., Eriksen, J., Jayanthi, L. D., et al.: Membrane Mobility and Microdomain Association of the Dopamine Transporter Studied with Fluorescence Correlation Spectroscopy and Fluorescence Recovery after Photobleaching. *Biochemistry* 46, 10484–97 (2007)

[274] Lagerholm, B. C., Andrade, D. M., Clausen, M. P., and Eggeling, C.: Convergence of lateral dynamic measurements in the plasma membrane of live cells from single particle tracking and STED-FCS. *Journal of Physics D: Applied Physics* 50, 063001 (2017)

[275] Leake, M.: *The Elasticity of the Giant Muscle Protein Titin Investigated using a Laser-Tweezers Technique*. Ph.D. thesis, University of London (2001)

[276] Happel, J. and Brenner, H.: *Low Reynolds number hydrodynamics : with special applications to particulate media*. Springer Netherlands (1981). ISBN 9400983522

[277] Fischer, H., Polikarpov, I., and Craievich, A. F.: Average protein density is a molecular-weight-dependent function. *Protein science : a publication of the Protein Society* 13, 2825–8 (2004)

[278] Quillin, M. L. and Matthews, B. W.: Accurate calculation of the density of proteins. *Acta Crystallographica Section D Biological Crystallography* 56, 791–794 (2000)

[279] Willard-Mack, C. L.: Normal Structure, Function, and Histology of Lymph Nodes. *Toxicologic Pathology* 34, 409–424 (2006)

[280] Juette, M. F. and Bewersdorf, J.: Three-Dimensional Tracking of Single Fluorescent Particles with Submillisecond Temporal Resolution. *Nano Letters* 10, 4657–4663 (2010)

[281] Ashley, T. T., Gan, E. L., Pan, J., and Andersson, S. B.: Tracking single fluorescent particles in three dimensions via extremum seeking. *Biomedical optics express* 7, 3355–3376 (2016)

[282] van 't Hoff, M., de Sars, V., and Oheim, M.: A programmable light engine for quantitative single molecule TIRF and HILO imaging. *Optics Express* 16, 18495 (2008)

[283] Hiramoto-Yamaki, N., Tanaka, K. A. K., Suzuki, K. G. N., Hirosawa, K. M., Miyahara, M. S. H., et al.: Ultrafast Diffusion of a Fluorescent Cholesterol Analog in Compartmentalized Plasma Membranes. *Traffic* 15, 583–612 (2014)

[284] Seeman, N. C.: Nucleic acid junctions and lattices. *Journal of Theoretical Biology* 99, 237–247 (1982)

[285] Kallenbach, N. R., Ma, R.-I., and Seeman, N. C.: An immobile nucleic acid junction constructed from oligonucleotides. *Nature* 305, 829–831 (1983)

[286] Goodman, R. P., Berry, R. M., and Turberfield, A. J.: The single-step synthesis of a DNA tetrahedron. *Chemical Communications* 20, 1372 (2004)

[287] Praetorius, F. and Dietz, H.: Self-assembly of genetically encoded DNA-protein hybrid nanoscale shapes. *Science* 355 (2017)

[288] Hirst, A. M., Simms, M. S., Mann, V. M., Maitland, N. J., O'Connell, D., and Frame, F. M.: Low-temperature plasma treatment induces DNA damage leading to necrotic cell death in primary prostate epithelial cells. *British journal of cancer* 112, 1536–45 (2015)

[289] O'Connell, D., Cox, L. J., Hyland, W. B., McMahon, S. J., Reuter, S., et al.: Cold atmospheric pressure plasma jet interactions with plasmid DNA. *Applied Physics Letters* 98, 043701 (2011)

[290] Ostling, O. and Johanson, K.: Microelectrophoretic study of radiation-induced DNA damages in individual mammalian cells. *Biochemical and Biophysical Research Communications* 123, 291–298 (1984)

[291] Singh, N. P., McCoy, M. T., Tice, R. R., and Schneider, E. L.: A simple technique for quantitation of low levels of DNA damage in individual cells. *Experimental Cell Research* 175, 184–191 (1988)

[292] Gyori, B. M., Venkatachalam, G., Thiagarajan, P. S., Hsu, D., and Clement, M.-V.: OpenComet: an automated tool for comet assay image analysis. *Redox biology* 2, 457–65 (2014)

[293] Coons, A. H., Creech, H. J., Jones, R. N., and Berliner, E.: The Demonstration of Pneumococcal Antigen in Tissues by the Use of Fluorescent Antibody. *The Journal of Immunology* 45, 159–170 (1942)

[294] Coons, A. H. and Kaplan, M.: Localization of Antigen in tissue cells: II. Improvements in a method for the detection of antigen by means of fluorescent antibody. *Journal of Experimental Medicine* 91, 1–13 (1950)

[295] Hirst, A. M., Frame, F. M., Maitland, N. J., and O'Connell, D.: Low Temperature Plasma Causes Double-Strand Break DNA Damage in Primary Epithelial Cells Cultured From a Human Prostate Tumor. *IEEE Transactions on Plasma Science* 42, 2740–2741 (2014)

[296] Gavrieli, Y., Sherman, Y., and Ben-Sasson, S. A.: Identification of programmed cell death in situ via specific labeling of nuclear DNA fragmentation. *The Journal of cell biology* 119, 493–501 (1992)

[297] Pavliček, N. and Gross, L.: Generation, manipulation and characterization of molecules by atomic force microscopy. *Nature Reviews Chemistry* 1, 0005 (2017)

[298] Vogel, S., Rackwitz, J., Schürman, R., Prinz, J., Milosavljević, A. R., et al.: Using DNA origami nanostructures to determine absolute cross sections for UV photon-induced DNA strand breakage. *The journal of physical chemistry letters* 6, 4589–93 (2015)

[299] Chu, S.: Biology and polymer physics at the single–molecule level. *Philosophical Transactions of the Royal Society of London A: Mathematical, Physical and Engineering Sciences* 361 (2003)

[300] Dunn, K. E.: *DNA origami assembly*. Ph.D. thesis, University of Oxford (2014)

[301] Wickham, S.: *DNA origami : a substrate for the study of molecular motors*. Ph.D. thesis, University of Oxford (2011)

[302] Veneziano, R., Ratanalert, S., Zhang, K., Zhang, F., Yan, H., et al.: Designer nanoscale DNA assemblies programmed from the top down. *Science (New York, NY)* 352, 1534 (2016)

[303] Krisch, R. E., Flick, M. B., and Trumbore, C. N.: Radiation Chemical Mechanisms of Single- and Double-Strand Break Formation in Irradiated SV40 DNA. *Radiation Research* 126, 251 (1991)

[304] Zadeh, J. N., Steenberg, C. D., Bois, J. S., Wolfe, B. R., Pierce, M. B., et al.: NUPACK: Analysis and design of nucleic acid systems. *Journal of Computational Chemistry* 32, 170–173 (2011)

[305] Lerman, L. S.: The structure of the DNA-acridine complex. *Proceedings of the National Academy of Sciences of the United States of America* 49, 94–102 (1963)

[306] Sayed, M., Krishnamurthy, B., Pal, H., Hazra, P., Rajule, R. N., et al.: Unraveling multiple binding modes of acridine orange to DNA using a multispectroscopic approach. *Phys Chem Chem Phys* 18, 24642–24653 (2016)

[307] Johansen, F. and Jacobsen, J. P.: 1 H NMR Studies of the Bis-Intercalation of a Homodimeric Oxazole Yellow Dye in DNA Oligonucleotides. *Journal of Biomolecular Structure and Dynamics* 16, 205–222 (1998)

[308] Reuter, M. and Dryden, D. T. F.: The kinetics of YOYO-1 intercalation into single molecules of double-stranded DNA. *Biochemical and biophysical research communications* 403, 225–9 (2010)

[309] Spielmann, H. P., Wemmer, D. E., and Jacobsen, J. P.: Solution structure of a DNA complex with the fluorescent bis-intercalator TOTO determined by NMR spectroscopy. *Biochemistry* 34, 8542–53 (1995)

[310] Benvin, A. L., Creeger, Y., Fisher, G. W., Ballou, B., Waggoner, A. S., and Armitage, B. A.: Fluorescent DNA nanotags: supramolecular fluorescent labels based on intercalating dye arrays assembled on nanostructured DNA templates. *Journal of the American Chemical Society* 129, 2025–34 (2007)

[311] Alon, U.: *An introduction to systems biology : design principles of biological circuits*. Chapman & Hall/CRC (2007). ISBN 1584886420

[312] Leake, M. C.: *Single-Molecule Cellular Biophysics*. Cambridge University Press, first edn. (2013)

[313] Cosa, G., Focsaneanu, K.-S., McLean, J. R. N., McNamee, J. P., and Scaiano, J. C.: Photophysical Properties of Fluorescent DNA-dyes Bound

to Single- and Double-stranded DNA in Aqueous Buffered Solution¶. *Photochemistry and Photobiology* 73, 585 (2001)

[314] Geisse, N. A.: AFM and combined optical techniques. *Materials Today* 12, 40–45 (2009)

[315] He, Y., Lu, M., Cao, J., and Lu, H. P.: Manipulating Protein Conformations by Single-Molecule AFM-FRET Nanoscopy. *ACS Nano* 6, 1221–1229 (2012)

[316] Dobbie, I. M., Robson, A., Delalez, N., and Leake, M. C.: Visualizing single molecular complexes in vivo using advanced fluorescence microscopy. *Journal of visualized experiments : JoVE* 1508 (2009)

[317] Kellermayer, M. S., Karsai, Á., Kengyel, A., Nagy, A., Bianco, P., et al.: Spatially and Temporally Synchronized Atomic Force and Total Internal Reflection Fluorescence Microscopy for Imaging and Manipulating Cells and Biomolecules. *Biophysical Journal* 91, 2665–2677 (2006)

[318] Odermatt, P. D., Shivanandan, A., Deschout, H., Jankele, R., Nievergelt, A. P., et al.: High-Resolution Correlative Microscopy: Bridging the Gap between Single Molecule Localization Microscopy and Atomic Force Microscopy. *Nano Letters* 15, 4896–4904 (2015)

[319] Gumpp, H., Puchner, E. M., Zimmermann, J. L., Gerland, U., Gaub, H. E., and Blank, K.: Triggering Enzymatic Activity with Force. *Nano Letters* 9, 3290–3295 (2009)

[320] de Boer, P., Hoogenboom, J. P., and Giepmans, B. N. G.: Correlated light and electron microscopy: ultrastructure lights up! *Nature Methods* 12, 503–513 (2015)

[321] Schirra, R. T., Zhang, P., and Zhang, P.: Correlative fluorescence and electron microscopy. *Current protocols in cytometry* 70, 12.36.1–10 (2014)

[322] Brouwer, I., Sitters, G., Candelli, A., Heerema, S. J., Heller, I., et al.: Sliding sleeves of XRCC4–XLF bridge DNA and connect fragments of broken DNA. *Nature* 535, 566–569 (2016)

[323] Badieirostami, M., Lew, M. D., Thompson, M. a., and Moerner, W. E.: Three-dimensional localization precision of the double-helix point spread function versus astigmatism and biplane. *Applied physics letters* 97, 161103 (2010)

[324] Shechtman, Y., Weiss, L. E., Backer, A. S., Lee, M. Y., and Moerner, W. E.: Multicolour localization microscopy by point-spread-function engineering. *Nature Photonics* 10, 590–594 (2016)

[325] Cybulski, J. S., Clements, J., and Prakash, M.: Foldscope: Origami-Based Paper Microscope. *PLoS ONE* 9, e98781 (2014)

[326] Warhurst, D. C. and Williams, J. E.: Laboratory diagnosis of malaria. *J Clin Pathol* 49, 533–538 (1996)

[327] Roberts, T. M., Rudolf, F., Meyer, A., Pellaux, R., Whitehead, E., et al.: Identification and Characterisation of a pH-stable GFP. *Scientific Reports* 6, 28166 (2016)

[328] Kneen, M., Farinas, J., Li, Y., and Verkman, A.: Green Fluorescent Protein as a Noninvasive Intracellular pH Indicator. *Biophysical Journal* 74, 1591–1599 (1998)

[329] Chen, A. K., Cheng, Z., Behlke, M. A., and Tsourkas, A.: Assessing the sensitivity of commercially available fluorophores to the intracellular environment. *Analytical chemistry* 80, 7437–44 (2008)